

**SCANNING TUNNELING MICROSCOPY STUDIES ON THE STRUCTURE  
AND STABILITY OF MODEL CATALYSTS**

A Dissertation

by

FAN YANG

Submitted to the Office of Graduate Studies of  
Texas A&M University  
in partial fulfillment of the requirements for the degree of

DOCTOR OF PHILOSOPHY

December 2007

Major Subject: Chemistry

**SCANNING TUNNELING MICROSCOPY STUDIES ON THE STRUCTURE  
AND STABILITY OF MODEL CATALYSTS**

A Dissertation

by

FAN YANG

Submitted to the Office of Graduate Studies of  
Texas A&M University  
in partial fulfillment of the requirements for the degree of

DOCTOR OF PHILOSOPHY

Approved by:

|                     |                    |
|---------------------|--------------------|
| Chair of Committee, | D. Wayne Goodman   |
| Committee Members,  | Glenn Agnolet      |
|                     | James D. Batteas   |
|                     | Robert R. Lucchese |
| Head of Department, | David H. Russell   |

December 2007

Major Subject: Chemistry

**ABSTRACT**

Scanning Tunneling Microscopy Studies on  
the Structure and Stability of Model Catalysts.

(December 2007)

Fan Yang, B.S., Peking University (P. R. China)

Chair of Advisory Committee: Dr. D. Wayne Goodman

An atomic level understanding of the structure and stability of model catalysts is essential for surface science studies in heterogeneous catalysis. Scanning tunneling microscopy (STM) can operate both in UHV and under realistic pressure conditions with a wide temperature span while providing atomic resolution images. Taking advantage of the ability of STM, our research focuses on 1) investigating the structure and stability of supported Au catalysts, especially under CO oxidation conditions, and 2) synthesizing and characterizing a series of alloy model catalysts for future model catalytic studies.

In our study, Au clusters supported on  $\text{TiO}_2(110)$  have been used to model supported Au catalysts. Our STM studies in UHV reveal surface structures of  $\text{TiO}_2(110)$  and show undercoordinated Ti cations play a critical role in the nucleation and stabilization of Au clusters on  $\text{TiO}_2(110)$ . Exposing the  $\text{TiO}_2(110)$  surface to water vapor causes the formation of surface hydroxyl groups and subsequently alters the growth kinetics of Au clusters on  $\text{TiO}_2(110)$ . STM studies on Au/ $\text{TiO}_2(110)$  during CO oxidation demonstrate the real surface of a working catalyst. Au clusters supported on

TiO<sub>2</sub>(110) sinter rapidly during CO oxidation, but are mostly stable in the single component reactant gas, either CO or O<sub>2</sub>. The sintering kinetics of supported Au clusters has been measured during CO oxidation and gives an activation energy, which supports the mechanism of CO oxidation induced sintering. CO oxidation was also found to accelerate the surface diffusion of Rh(110). Our results show a direct correlation between the reaction rate of CO oxidation and the diffusion rate of surface metal atoms.

Synthesis of alloy model catalysts have also been attempted in our study with their structures successfully characterized. Planar Au-Pd alloy films has been prepared on a Rh(100) surface with surface Au and Pd atoms distinguished by STM. The growth of Au-Ag alloy clusters have been studied by *in-situ* STM on a cluster-to-cluster basis. Moreover, the atomic structure of a solution-prepared Ru<sub>3</sub>Sn<sub>3</sub> cluster has been resolved on an ultra-thin silica film surface. The atomic structure and adsorption sites of the ultra-thin silica film have also been well characterized in our study.

Dedicated to my parents, Jiang and Xiaoyun, and to my wife, Jing.

## ACKNOWLEDGEMENTS

In retrospect, graduate school has been both the most significant challenge and the most rewarding experience in my school life. Without the guidance, help and support from the following people, my long journey through graduate school could not have been completed.

First and foremost, I am deeply grateful to my advisor, Dr. D. Wayne Goodman, for giving me the opportunity to do research at the cutting edge of science, for his trust and patience to allow me to explore the research freely, for his guidance on both scientific and individual growth, and for his support and encouragement. I would like to thank my committee members, Dr. Glenn Agnolet, Dr. Robert R. Lucchese, Dr. James D. Batteas, and Dr. Richard M Crooks, for their advice and support.

I would also like to thank members of the Goodman group with whom I have interacted over the past six years. In particular, I would like to thank Dr. Mingshu Chen, who has been invaluable in his guidance and support on the instrumentation modification and in the fruitful discussion both scientifically and personally; Dr. Qinlin Guo, a senior PKU alumni and two-month project partner, who has generously shared his experience in both work and life; Dr. Patrick Han, both friend and 10-month project partner, who has broadened my knowledge on STM, scientific writing, and western culture; Dr. Jinhai Wang for his numerous help both in and out of the lab during my first two years of graduate school; Dr. Williams T. Wallace, Dr. Byoungkoun Min, and Kerrie Gath for keeping me cheerful after my many frustrating experimental failures in

the small and isolated basement room; Dr. Ashok K. Santra for easing me into the surface science research; Amy Liu for her secretarial assistance and warm support.

I am grateful to the staff in the machine and electronics shops at the Department of Chemistry and the electronic shop at the Department of Physics, Texas A&M University. More specifically, I want to thank Tony Montalbano, Mike Tullos, and Jason Caswell for not only helping me with the equipments, but also instructing me on the fundamentals of machining and electronics.

Last, but not least, I want to thank my family for their love and support. I am grateful to my father for supporting my decision to study science and encouraging me to look at the bigger picture. My mother has always been my biggest supporter and proud of what I do. My wife, Jing, who has been a constant support since we met, has made my time in graduate school much easier and joyful. Her editorial assistance has largely facilitated the writing of this dissertation.

## TABLE OF CONTENTS

|                         |                                                                    | Page |
|-------------------------|--------------------------------------------------------------------|------|
| ABSTRACT .....          |                                                                    | iii  |
| DEDICATION .....        |                                                                    | v    |
| ACKNOWLEDGEMENTS .....  |                                                                    | vi   |
| TABLE OF CONTENTS ..... |                                                                    | viii |
| LIST OF FIGURES .....   |                                                                    | x    |
| CHAPTER                 |                                                                    |      |
| I                       | INTRODUCTION.....                                                  | 1    |
|                         | Au clusters supported on TiO <sub>2</sub> (110) .....              | 8    |
|                         | Surface defects and Au growth on TiO <sub>2</sub> (110) .....      | 10   |
|                         | Au/TiO <sub>2</sub> (110) in the presence of reactant gases.....   | 13   |
|                         | W-J model of Ostwald ripening .....                                | 16   |
|                         | Synthesis and characterization of alloy model catalysts .....      | 21   |
| II                      | EXPERIMENTAL .....                                                 | 23   |
|                         | Instrumentation.....                                               | 23   |
|                         | Methods of analysis.....                                           | 29   |
|                         | Experimental considerations .....                                  | 35   |
| III                     | THE STRUCTURE AND STABILITY OF SUPPORTED GOLD                      |      |
|                         | CATALYSTS IN UHV .....                                             | 45   |
|                         | Surface structures of TiO <sub>2</sub> (110) .....                 | 45   |
|                         | TiO <sub>x</sub> species on TiO <sub>2</sub> (110) .....           | 50   |
|                         | Growth of Au clusters on TiO <sub>2</sub> (110) .....              | 55   |
|                         | Thermal stabilities of Au/TiO <sub>2</sub> (110) in UHV .....      | 65   |
|                         | Au clusters on hydroxylated TiO <sub>2</sub> (110) .....           | 71   |
|                         | Preparation of Au/TiO <sub>x</sub> on TiO <sub>2</sub> (110) ..... | 79   |
|                         | Size selected Au <sub>400</sub> clusters on HOPG .....             | 83   |



| CHAPTER |                                                                                              | Page |
|---------|----------------------------------------------------------------------------------------------|------|
| IV      | THE STRUCTURE AND STABILITY OF MODEL CATALYSTS<br>IN REACTANT GASES.....                     | 90   |
|         | Au clusters supported on TiO <sub>2</sub> (110) in O <sub>2</sub> or CO .....                | 90   |
|         | Chemical potentials of supported Au clusters.....                                            | 97   |
|         | Oxidation of Au clusters supported on TiO <sub>2</sub> (110) .....                           | 100  |
|         | Sintering of Au/TiO <sub>2</sub> (110) during CO oxidation .....                             | 106  |
|         | Model of Ostwald ripening for supported Au clusters during CO<br>oxidation.....              | 122  |
|         | Rh(110) during CO oxidation .....                                                            | 124  |
| V       | THE STRUCTURE AND STABILITY OF ALLOY MODEL<br>CATALYSTS.....                                 | 135  |
|         | The growth and structure of Au-Pd alloy on Rh(100) .....                                     | 135  |
|         | The growth of Ag-Au alloy clusters on TiO <sub>2</sub> (110) .....                           | 145  |
|         | The structure and adsorption sites of the ultra-thin silica film.....                        | 155  |
|         | The structure of Ru <sub>3</sub> Sn <sub>3</sub> clusters on the ultra-thin silica film..... | 169  |
| VI      | SUMMARY .....                                                                                | 178  |
|         | REFERENCES .....                                                                             | 181  |
|         | VITA .....                                                                                   | 203  |

## LIST OF FIGURES

|          |                                                                                                                                                                                                                                                                                                                                                                                                                                                                                                                  | Page |
|----------|------------------------------------------------------------------------------------------------------------------------------------------------------------------------------------------------------------------------------------------------------------------------------------------------------------------------------------------------------------------------------------------------------------------------------------------------------------------------------------------------------------------|------|
| Figure 1 | Schematic illustration of “material gap” and the efforts to bridge “material gap”. (a) A real catalyst. (b) The development of model catalysts .....                                                                                                                                                                                                                                                                                                                                                             | 5    |
| Figure 2 | Schematic drawing of the TiO <sub>2</sub> (110) surface. (a) A stoichiometric surface. (b) A defective surface with bridging oxygen vacancies. In the model, red balls represent Ti atoms and blue represent O atoms ....                                                                                                                                                                                                                                                                                        | 11   |
| Figure 3 | Schematic illustration of sintering modes: (a) cluster migration, and (b) Ostwald ripening.....                                                                                                                                                                                                                                                                                                                                                                                                                  | 15   |
| Figure 4 | Schematic view of the W-J model of Ostwald ripening. (a) and (b) represent the two-step treatment in W-J model. (a) shows the top view of a cluster in equilibrium with the surrounding monomer sea. (b) shows monomers detaching from the cluster and the relationship between the monomer concentration of clusters and the monomer concentration of bulk.....                                                                                                                                                 | 18   |
| Figure 5 | Schematic drawing of a surface analysis system for <i>in-situ</i> STM studies. (a) Side view of the surface analysis system. (b) 3D demonstration of the STM chamber for <i>in-situ</i> studies.....                                                                                                                                                                                                                                                                                                             | 24   |
| Figure 6 | Schematic drawing of a surface analysis system for high resolution STM studies.....                                                                                                                                                                                                                                                                                                                                                                                                                              | 28   |
| Figure 7 | Schematic illustration of (a) the operation principle of STM, and (b) the tunneling principle. Density of states (DOS) of the sample and the tip are shown in (b), where the filled states are shown in green. Application of a bias voltage to the sample will either raise or reduce the Fermi level of the sample with respect to the Fermi level of the tip. In the case of (b), the sample is negatively biased and allows for filled states of the sample to tunnel into the empty states of the tip ..... | 30   |
| Figure 8 | Schematic illustration of the Auger processes (KL <sub>1</sub> L <sub>2,3</sub> ). (a) Ionization of a core electron. (b) Excitation of an Auger electron.....                                                                                                                                                                                                                                                                                                                                                   | 34   |
| Figure 9 | The performance and vibration isolation of the RHK VT-UHV300 STM. (a) Atomic resolution STM images obtained by RHK VT-UHV300 STM. (b) Rule of thumb in the vibration isolation using New Port I-2000 air legs .....                                                                                                                                                                                                                                                                                              | 36   |

|           |                                                                                                                                                                                                                                                                                                                                                                                                                                                                                                                                                                                                                                                       |    |
|-----------|-------------------------------------------------------------------------------------------------------------------------------------------------------------------------------------------------------------------------------------------------------------------------------------------------------------------------------------------------------------------------------------------------------------------------------------------------------------------------------------------------------------------------------------------------------------------------------------------------------------------------------------------------------|----|
| Figure 10 | Methods of patterning the surface for <i>in-situ</i> STM studies. (a) Schematic of “shadow” technique. (b) STM image of the surface created by “shadow” technique. The shadow area uncovered by metal clusters is distinguished from the area covered with metal clusters by the white dash line. (c) Schematic of the tip manipulation. (d) STM image of the surface created by tip manipulation. The dash rectangle in (d) shows the area where most clusters are picked up by the STM tip. This area with lower cluster densities can be distinguished from the rest of the surface and serve as a nano-marker for <i>in-situ</i> STM studies..... | 44 |
| Figure 11 | STM images of the TiO <sub>2</sub> (110) surface. (a) 100 nm × 100 nm, V <sub>s</sub> = 2 V, I = 0.1 nA. Inset is the LEED image of TiO <sub>2</sub> (110) surface. (b) 5 nm × 5 nm, V <sub>s</sub> = 1.2 V, I = 1 nA .....                                                                                                                                                                                                                                                                                                                                                                                                                           | 46 |
| Figure 12 | High resolution STM images of the TiO <sub>2</sub> (110) surface. Both images have the same dimensions of 5 nm × 5 nm and same tunneling parameters of V <sub>s</sub> = 0.8 V and I = 4 nA.....                                                                                                                                                                                                                                                                                                                                                                                                                                                       | 48 |
| Figure 13 | STM images of TiO <sub>x</sub> on the TiO <sub>2</sub> (110) surface after annealing in UHV. Both images have the same dimensions of 200 nm × 200 nm and tunneling parameters of V <sub>s</sub> = 2 V and I = 0.1 nA. (a) A TiO <sub>2</sub> (110) surface annealed at 600 K for 10 min. (b) A TiO <sub>2</sub> (110) surface annealed at 750 K for 5 min .....                                                                                                                                                                                                                                                                                       | 52 |
| Figure 14 | STM images of TiO <sub>x</sub> on the TiO <sub>2</sub> (110) surface induced by O <sub>2</sub> exposure at room temperature. Both images are on the same area and have dimensions of 20 nm × 20 nm. Tunneling parameters are V <sub>s</sub> = 1.2 V and I = 0.3 nA. (a) A clean TiO <sub>2</sub> (110) surface. The bright protrusions are TiO <sub>x</sub> species remained on the surface after 900 K annealing. (b) The TiO <sub>2</sub> (110) surface in (a) exposed to 2 L O <sub>2</sub> at 1 × 10 <sup>-8</sup> Torr .....                                                                                                                     | 54 |
| Figure 15 | STM images of the same area of a TiO <sub>2</sub> (110) surface after the deposition of (a) 0.17 ML Au; (b) 0.34 ML Au; (c) 0.51 ML Au; (d) 0.69 ML Au; (e) 0.86 ML Au; and (f) 1.3 ML Au. All images have the same dimensions of 100 nm × 100 nm. The circle highlighted in white in each image indicates the identical area .....                                                                                                                                                                                                                                                                                                                   | 56 |
| Figure 16 | Histograms of the number of clusters as a function of diameter for the various Au coverage shown in Figure 15.....                                                                                                                                                                                                                                                                                                                                                                                                                                                                                                                                    | 57 |

|                                                                                                                                                                                                                                                                                                                                                                                                                                                                    | Page |
|--------------------------------------------------------------------------------------------------------------------------------------------------------------------------------------------------------------------------------------------------------------------------------------------------------------------------------------------------------------------------------------------------------------------------------------------------------------------|------|
| Figure 17 Cluster (a) number density, (b) diameter, and (c) height as a function of Au coverage taking into account the separate contributions of step-edges and terraces.....                                                                                                                                                                                                                                                                                     | 59   |
| Figure 18 The overall cluster density (right hand axis), diameter and height with respect to Au coverage .....                                                                                                                                                                                                                                                                                                                                                     | 60   |
| Figure 19 STM images of Au growth on TiO <sub>2</sub> (110) surfaces with different step edge termination. Both images have the same dimensions of 200 nm × 200 nm and tunneling parameters are, V <sub>s</sub> = 2 V, I = 0.1 nA. (a) Au growth on a TiO <sub>2</sub> (110) surface with straight steps running along the [001] direction, which have O termination. (b) Au growth on the same TiO <sub>2</sub> (110) surface with curved step edges present..... | 62   |
| Figure 20 STM images of Au growth on TiO <sub>2</sub> (110) surfaces with TiO <sub>x</sub> strands. Both images have the same dimensions of 100 nm × 100 nm and tunneling parameters, V <sub>s</sub> = 2 V, I = 0.1 nA. (a) Au growth on a TiO <sub>2</sub> (110) surface with mainly single strands. (b) Au growth on a TiO <sub>2</sub> (110) surface with mainly double strands .....                                                                           | 63   |
| Figure 21 <i>In-situ</i> STM images of Au clusters supported on the TiO <sub>2</sub> (110) surface before and after thermal treatments. Both images have dimensions of 100 × 100 nm and tunneling parameters are V <sub>s</sub> = 2 V and I = 0.1 nA. (a) Images taken at the same area before and after annealing at 450 K for 10 min. (b) Images taken at the same area before and after annealing at 600 K for 10 min .....                                     | 66   |
| Figure 22 Large scale STM image of Au clusters supported on TiO <sub>2</sub> (110) after 600 K annealing. The white dotted line separates the shadow area with Au covered area. The image has dimensions of 1000 nm × 1000 nm and the tunneling parameters are V <sub>s</sub> = 2 V and I = 0.1 nA. Inset shows a zoom-in image of the shadow area after annealing and has dimensions of 20 nm × 20 nm.....                                                        | 68   |
| Figure 23 STM images of Au growth on hydroxylated TiO <sub>2</sub> (110). (a) Clean TiO <sub>2</sub> (110). (b) TiO <sub>2</sub> (110) after exposed to 2 L H <sub>2</sub> O at 300 K. (c) 0.25 ML Au deposited on the hydroxylated TiO <sub>2</sub> (110). (d) 0.42 ML Au deposited on the hydroxylated TiO <sub>2</sub> (110). All images are taken on the same area, 100 nm × 100 nm in size. Tunneling parameters are V <sub>s</sub> = 2 V and I = 0.1 nA..... | 72   |

|           |                                                                                                                                                                                                                                                                                                                                                                                                                                                                                                                                                                                                                           |    |
|-----------|---------------------------------------------------------------------------------------------------------------------------------------------------------------------------------------------------------------------------------------------------------------------------------------------------------------------------------------------------------------------------------------------------------------------------------------------------------------------------------------------------------------------------------------------------------------------------------------------------------------------------|----|
| Figure 24 | STM images of Au growth on hydroxylated and annealed TiO <sub>2</sub> (110) surfaces. (a) The surface of Figure 23(d) annealed at 600 K for 10 min. (b) 0.17 ML Au deposited on the surface of (a). (a) and (b) are the same area as in Figure 23. (c) The shadow area of the hydroxylated TiO <sub>2</sub> (110) surface after annealing at 600 K for 10 min. TiO <sub>x</sub> species show up on the surface after annealing. (d) 0.17 ML Au deposited on the surface of (c). (c) and (d) are the same area. All images are 100 nm × 100 nm in size. Tunneling parameters are V <sub>s</sub> = 2 V and I = 0.1 nA ..... | 74 |
| Figure 25 | STM images of Au growth on TiO <sub>2</sub> (110) after the removal of hydroxyl groups by annealing at 600 K. (a) 0.34 ML Au deposited on the shadow area of the annealed TiO <sub>2</sub> (110). (b) 0.34 ML Au deposited on the Au covered area of the annealed TiO <sub>2</sub> (110). Both images are 100 nm × 100 nm in size .....                                                                                                                                                                                                                                                                                   | 75 |
| Figure 26 | Comparison of the number densities of Au clusters as a function of Au coverage on the surface of (a) and (b) clean TiO <sub>2</sub> (110); (c) and (d) TiO <sub>2</sub> (110) exposed to 2 L H <sub>2</sub> O (hydroxylated TiO <sub>2</sub> (110)); (e) and (f) TiO <sub>2</sub> (110) exposed to 2 L H <sub>2</sub> O and annealed at 600 K for 10 minutes (TiO <sub>2</sub> (110) covered with TiO <sub>x</sub> ) .....                                                                                                                                                                                                | 77 |
| Figure 27 | STM images of 1 ML Au/TiO <sub>2</sub> (110) (a) before and (b) after annealing in 5 × 10 <sup>-8</sup> Torr H <sub>2</sub> at 800 K for 10 min. Both images have the same dimensions of 100 nm × 100 nm and tunneling parameters of V <sub>s</sub> = 2 V and I = 0.1 nA .....                                                                                                                                                                                                                                                                                                                                            | 80 |
| Figure 28 | STM images of 0.8 ML Au/TiO <sub>2</sub> (110) after reduction in H <sub>2</sub> at 800 K. (a) 0.8 ML Au deposited on the TiO <sub>2</sub> (110) within 5 × 10 <sup>-8</sup> Torr H <sub>2</sub> at 700 K. (b) The surface of (a) annealed in 5 × 10 <sup>-6</sup> Torr H <sub>2</sub> at 700 K for 10 min. Profile of the white line marked in the images are shown at the side of each STM image. Both STM images have the same dimensions of 100 nm × 100 nm and tunneling parameters of V <sub>s</sub> = 2 V and I = 0.1 nA.....                                                                                      | 82 |
| Figure 29 | STM images of size selected Au clusters supported on HOPG. The size of deposited Au clusters varies from 100 to 1000 atoms per cluster. The majority of Au clusters have ~ 400 atoms. (a) 200 nm × 200 nm STM image with tunneling parameters of V <sub>s</sub> = 1 V and I = 0.2 nA. (b) 50 nm × 50 nm STM image with tunneling parameters of V <sub>s</sub> = 1 V and I = 2 nA. Inset shows the line profile of cluster A .....                                                                                                                                                                                         | 85 |

|           | Page                                                                                                                                                                                                                                                                                                                                                                                                                                                                                                                                                                                                              |
|-----------|-------------------------------------------------------------------------------------------------------------------------------------------------------------------------------------------------------------------------------------------------------------------------------------------------------------------------------------------------------------------------------------------------------------------------------------------------------------------------------------------------------------------------------------------------------------------------------------------------------------------|
| Figure 30 | High resolution STM images of size selected Au clusters supported on HOPG. Au clusters penetrate into HOPG and leave a pit on the surface. (a) $4.3 \text{ nm} \times 4.3 \text{ nm}$ STM image with tunneling parameters of $V_s = 0.6 \text{ V}$ and $I = 2 \text{ nA}$ . (b) 3D view of (a) ..... 87                                                                                                                                                                                                                                                                                                           |
| Figure 31 | STM images of the HOPG surface after Au clusters fully penetrate into HOPG, leaving holes and amorphous Carbon clusters on the surface. Both STM images have tunneling parameters of $V_s = 1 \text{ V}$ and $I = 0.5 \text{ nA}$ . The image sizes are (a) $8.2 \text{ nm} \times 8.2 \text{ nm}$ , and (b) $7.8 \text{ nm} \times 8.0 \text{ nm}$ . Inset shows the line profile of cluster A ..... 89                                                                                                                                                                                                          |
| Figure 32 | $75 \text{ nm} \times 75 \text{ nm}$ <i>in-situ</i> STM images of 0.5 ML Au clusters supported on the $\text{TiO}_2(110)$ surface (a) in UHV at 300 K, (b) after 1.5 hours in 0.1 Torr $\text{O}_2$ at 300 K, (c) in UHV at 300 K, and (d) after 2 hours in 3 Torr CO at 300 K. Tunneling parameters are $V_s = 2 \text{ V}$ and $I = 0.1 \text{ nA}$ .. 91                                                                                                                                                                                                                                                       |
| Figure 33 | $75 \text{ nm} \times 75 \text{ nm}$ <i>in-situ</i> STM images of 0.3 ML Au clusters supported on the $\text{TiO}_2(110)$ surface at 600 K in (a) UHV, (b) $10^{-8}$ Torr $\text{O}_2$ , (c) $10^{-6}$ Torr $\text{O}_2$ , and (d) $10^{-5}$ Torr $\text{O}_2$ . Tunneling parameters are $V_s = 2 \text{ V}$ and $I = 0.1 \text{ nA}$ ..... 93                                                                                                                                                                                                                                                                   |
| Figure 34 | STM images of 0.5 ML Au clusters supported on the $\text{TiO}_2(110)$ surface in the presence of $\sim 5$ Torr $\text{O}_2$ . Tunneling parameters are $V_s = 2 \text{ V}$ and $I = 0.1 \text{ nA}$ . (a) Surface of Figure 32(b) right after the $\text{O}_2$ pressure is raised to 10 Torr. (b) Profile of the white line in (a) is plotted in red. The blue dotted line shows the profile of the same Au clusters in the presence of $\sim 0.5$ Torr $\text{O}_2$ ..... 96                                                                                                                                     |
| Figure 35 | Calculated chemical potentials of Au clusters supported on $\text{TiO}_2(110)$ . The calculations are based on different theoretical models: (a) G-T relation; (b) MBA model; (c) DFT model. In the calculation based on DFT model, the number of oxygen vacancies underneath each cluster is set at 9..... 98                                                                                                                                                                                                                                                                                                    |
| Figure 36 | Plots of the equilibrium $\text{O}_2$ pressure versus temperature in van't Hoff format for the oxidation of Au clusters supported on $\text{TiO}_2(110)$ , assuming the oxidation state as $\text{Au}_2\text{O}_3$ . The plots are calculated based on the chemical potential of supported Au clusters, which were estimated from (a) G-T relationship, (b) MBA model, and (c) DFT model. In each plot, the top line is experimental data for the formation of bulk $\text{Au}_2\text{O}_3$ . The two lower lines are predicted for Au clusters with 2 and 1 nm radius supported on $\text{TiO}_2(110)$ ..... 101 |

- Figure 37 Plot of the equilibrium O<sub>2</sub> pressure versus cluster radius for the oxidation of Au clusters supported on TiO<sub>2</sub>(110), assuming the oxidation state as Au<sub>2</sub>O<sub>3</sub>. The plot is derived based on chemical potentials of supported Au clusters, which are calculated from (a) G-T relationship, (b) MBA model, and (c) DFT model. The blue line shows the O<sub>2</sub> partial pressure of 1 bar to note the difference in predictions, which are based on different chemical potential models... 103
- Figure 38 75 nm × 75 nm *in-situ* STM images of 0.5 ML Au clusters supported on the TiO<sub>2</sub>(110) surface in the presence of 0.1 Torr CO and O<sub>2</sub> mixture at 300 K. (a) - (f) are consequently taken at the same surface area. The time intervals are: (a) 0 min; (b) 28 min; (c) 42 min; (d) 63 min; (e) 120 min; (f) 280 min. Tunneling parameters are V<sub>s</sub> = 2 V and I = 0.1 nA..... 107
- Figure 39 75 nm × 75 nm *in-situ* STM images of 0.2 ML Au clusters supported on the TiO<sub>2</sub>(110) surface in the presence of 0.1 Torr CO and O<sub>2</sub> mixture gas at 300 K. (a) - (d) are consequently taken at the same surface area. The time intervals are: (a) 0 min; (b) 21 min; (c) 63 min; (d) 120 min. Tunneling parameters are V<sub>s</sub> = 2 V and I = 0.1 nA ..... 109
- Figure 40 75 nm × 75 nm *in-situ* STM images of 0.65 ML Au clusters supported on the TiO<sub>2</sub>(110) surface in the presence of 0.1 Torr CO and O<sub>2</sub> mixture gas at 410 K. (a) - (f) are consequently taken at the same surface area. The time intervals are: (a) 0 min; (b) 21 min; (c) 42 min; (d) 63 min; (e) 80 min; (f) 120 min. Tunneling parameters are V<sub>s</sub> = 2 V and I = 0.1 nA ..... 110
- Figure 41 Height distributions of Au clusters supported on TiO<sub>2</sub>(110) before and after 2 hours of CO oxidation (The total gas pressure is 0.1 Torr with P<sub>CO</sub>: P<sub>O<sub>2</sub></sub> = 1:1). (a) 0.5 ML Au/TiO<sub>2</sub>(110), 300 K. (b) 0.65 ML Au/TiO<sub>2</sub>(110), 410 K. (c) 0.2 ML Au/TiO<sub>2</sub>(110), 300 K..... 112
- Figure 42 75 nm × 75 nm *in-situ* STM images of 0.5 ML Au clusters supported on the TiO<sub>2</sub>(110) surface in (a) UHV at 500 K, (b) 2.1 Torr CO/O<sub>2</sub> (2:1) mixture gas at 500 K for 0.5 h, (c) 10<sup>-5</sup> Torr CO/O<sub>2</sub> (1:1) mixture gas at 600 K, and (d) 0.6 Torr CO/O<sub>2</sub> (10:1) mixture gas for 1 h. (a) and (b) are on the same surface area. (c) and (d) are on the same surface area. Tunneling parameters are V<sub>s</sub> = 2 V and I = 0.1 nA..... 113

|                                                                                                                                                                                                                                                                                                                                                                                                                                                                                                                                                                                                     | Page |
|-----------------------------------------------------------------------------------------------------------------------------------------------------------------------------------------------------------------------------------------------------------------------------------------------------------------------------------------------------------------------------------------------------------------------------------------------------------------------------------------------------------------------------------------------------------------------------------------------------|------|
| Figure 43 Arrhenius plot for the decay of supported Au clusters. The decay rates are achieved from Au clusters with a diameter around 3 nm. The solid line gives the best least square fit.....                                                                                                                                                                                                                                                                                                                                                                                                     | 121  |
| Figure 44 STM images of Rh (110) in (a) UHV at 300 K, (b) 12 Torr CO/O <sub>2</sub> (1:2) at 300 K, (c) UHV at 525 K, and (d) 8 Torr O <sub>2</sub> at 525 K. (a) and (b) are on the same area and have dimensions of 180 nm × 180 nm. The image size of (c) and (d) is 100 nm × 100 nm.....                                                                                                                                                                                                                                                                                                        | 126  |
| Figure 45 Plot of the total pressure versus time during CO oxidation on Rh(110) at 525 K. The ratio of CO:O <sub>2</sub> is 1:2. The reaction process is divided into four time periods, during which STM images and I-V curves are taken on the Rh(110) surface. These time periods are marked as A, B, C and D in the plot .....                                                                                                                                                                                                                                                                  | 128  |
| Figure 46 STM images of Rh(110) during CO oxidation. (a) Rh(110) in UHV at 300 K. (b) Rh(110) in 12 Torr CO/O <sub>2</sub> (1:2) at 475 K. (c) - (f) Rh(110) in 12 Torr CO/O <sub>2</sub> (1:2) at 525 K. (c) - (f) correspond to the time period A, B, C and D in Figure 45 respectively. (a), (b), (d), (e) and (f) have dimensions of 100 nm × 100 nm. The size of (c) is 80 nm × 110 nm.....                                                                                                                                                                                                    | 129  |
| Figure 47 I-V curves measured during CO oxidation at 525 K. The total pressure is 12 Torr and the ratio of CO:O <sub>2</sub> is 1:2. (a) corresponds to the time period A and B in Figure 45. (b) corresponds to the time period C <sub>1</sub> in Figure 45. (c) corresponds to the time period C <sub>2</sub> in Figure 45. (d) corresponds to the time period D in Figure 45. The tunneling gap is fixed at I = 0.1 nA and V <sub>s</sub> = 1.1 V. I-V curves for the different time periods of the reaction are based on the average behavior of I-V data sampled during each time period ..... | 131  |
| Figure 48 STM images and corresponding I-V curves of characteristic Rh (110) surfaces. (a) and (b) are Rh(110) in the presence of 10 <sup>-6</sup> Torr CO at 300 K. (c) and (d) are Rh(110) in the presence of 10 <sup>-6</sup> Torr O <sub>2</sub> at 300 K. (e) and (f) are on Rh(110) after being annealed in 10 <sup>-6</sup> Torr O <sub>2</sub> at 750 K, when a surface oxide layer is produced. For I-V curve measurements, the tunneling gap is fixed at I = 0.1 nA and V <sub>s</sub> = 1.1 V                                                                                            | 133  |
| Figure 49 STM images of (a) Rh(100) and (b) 2 ML Au on Rh(100). Both (a) and (b) have dimensions of 200 nm × 200 nm. Inset is a zoom-in image of Au surface layer, which has a size of 4.4 nm × 4.4 nm. Tunneling parameters are V <sub>s</sub> = -0.2 V and I = 1 nA .....                                                                                                                                                                                                                                                                                                                         | 138  |



- Figure 50 STM images of Au on Rh(100). (a) 2 ML Au on Rh(100). (b) 3 ML Au on Rh(100). (c) Zoom-in image in the reconstructed area of (a). (d) Zoom-in image of (b). (a) and (b) have dimensions of 50 nm  $\times$  50 nm. (c) and (d) have dimensions of 7 nm  $\times$  7 nm. Tunneling parameters are  $V_s = -0.1$  V and  $I = 2$  nA..... 139
- Figure 51 STM images of Au/Pd alloy on Rh(100). (a) 2 ML Pd deposited on 2 ML Au/Rh(100) at 300 K. (b) 2 ML Pd deposited on 2 ML Au/Rh(100) at 300 K and annealed at 800 K. (c) 0.5 ML Pd deposited on 2 ML Au/Rh(100) at 600 K. (d) 1 ML Pd deposited on 2 ML Au/Rh(100) at 600 K. All images have dimensions of 100 nm  $\times$  100 nm. Tunneling parameters are  $V_s = -0.1$  V and  $I = 1$  nA ..... 142
- Figure 52 High resolution STM images of Au/Pd alloy on Rh(100). (a) 0.5 ML Pd deposited on 2 ML Au/Rh(100) at 600 K. (b) Schematic representation of (a) for clarity. The red circle corresponds to the bright spots in (a). (c) 1 ML Pd deposited on 2 ML Au/Rh(100) at 600 K. (d) Schematic representation of (c) for clarity. The red circle corresponds to the bright spots in (c). All images have dimensions of 5 nm  $\times$  5 nm. Tunneling parameters are  $V_s = -6$  mV and  $I = 5$  nA..... 144
- Figure 53 High resolution STM images of Au/Pd alloy on Rh(100). (a) 2 ML Pd deposited on 2 ML Au/Rh(100) at 300 K and annealed at 800 K for 10 min. (b) 2 ML Pd deposited on 2 ML Au/Rh(100) at 300 K and annealed at 1000 K for 10 min. The image sizes are: (a) 7 nm  $\times$  7 nm, (b) 10 nm  $\times$  10 nm. Tunneling parameters are  $V_s = -20$  mV and  $I = 5$  nA..... 146
- Figure 54 STM images (100 nm  $\times$  100 nm) during Au deposition on a Ag pre-covered (0.08 ML) TiO<sub>2</sub>(110) surface after deposition of (a) 0.08 ML Ag, (b) 0.17, (c) 0.34, (d) 0.85, (e) 1.53 and (f) 2.04 ML Au 148
- Figure 55 Histograms of the number density of clusters for various Au covered surfaces shown in Figure 54 as a function of their diameter. In plots (b) – (f), black bars are obtained from plot (a) and are shown side-by-side to demonstrate how the size distribution changes as a function of Au coverage with respect to that of a Ag pre-covered TiO<sub>2</sub>(110) surface ..... 149

|           |                                                                                                                                                                                                                                                                                                                                                                                                                                                                                                                                                                                                                                                             |     |
|-----------|-------------------------------------------------------------------------------------------------------------------------------------------------------------------------------------------------------------------------------------------------------------------------------------------------------------------------------------------------------------------------------------------------------------------------------------------------------------------------------------------------------------------------------------------------------------------------------------------------------------------------------------------------------------|-----|
| Figure 56 | STM images (100 x 100 nm) during Au deposition on Ag pre-covered (0.033ML) TiO <sub>2</sub> (110) surface after deposition of (a) 0.033ML Ag, (b) 0.17, (c) 0.34, (d) 0.51, (e) 0.85 and (f) 1.53 ML Au. The white circles in image (a) and (b) show the appearance of new Au clusters ..                                                                                                                                                                                                                                                                                                                                                                   | 151 |
| Figure 57 | Histograms of the number density of clusters for various Au covered surfaces shown in Figure 56 as a function of their diameter. In plots (b) – (f), black bars are obtained from plot (a) and are shown side-by-side to demonstrate how the size distribution changes as a function of Au coverage with respect to that of a Ag pre-covered TiO <sub>2</sub> (110) surface .....                                                                                                                                                                                                                                                                           | 152 |
| Figure 58 | Au coverage dependent plots for two different Ag pre-covered (0.08 and 0.033 ML) TiO <sub>2</sub> (110) surfaces after isolating the contributions of step edges from those of terraces as a function of: (a) number density, (b) diameter and (c) height. Open and solid symbols are used for the 0.08 and 0.033 ML Ag pre-covered surfaces, respectively. The dotted line indicates the sharp increase in the number of clusters after 0.17 ML of Au deposition. Number density at terraces is expressed in the number of clusters/cm <sup>2</sup> while that at steps is expressed in the number of clusters/cm (i.e., per unit length of the step)..... | 154 |
| Figure 59 | STM images of SiO <sub>2</sub> (1ML)/Mo(112) at various sample bias voltages. All images have dimensions of 5 nm × 5 nm. Tunneling parameters are (a) V <sub>s</sub> = -0.6 V, I = 2 nA, (b) V <sub>s</sub> = -0.3 V, I = 2 nA, (c) V <sub>s</sub> = 0.3 V, I = 2 nA, and (d) V <sub>s</sub> = 1 V, I = 2 nA .....                                                                                                                                                                                                                                                                                                                                          | 157 |
| Figure 60 | Top-view and side-view of the structural model of isolated [SiO <sub>4</sub> ] for SiO <sub>2</sub> (1 ML)/ Mo(112). In the ball model, white represents Mo, red represents Si, and blue represents O.....                                                                                                                                                                                                                                                                                                                                                                                                                                                  | 161 |
| Figure 61 | STM images of 0.01 ML Pd deposited on SiO <sub>2</sub> (1 ML)/Mo(112). All images have dimensions of 10 nm × 10 nm. Tunneling parameters are (a) V <sub>s</sub> = -0.4 V, I = 1 nA, (b) V <sub>s</sub> = -0.2 V, I = 1 nA, (c) V <sub>s</sub> = 0.3 V, I = 1 nA, and (d) V <sub>s</sub> = 1 V, I = 1 nA .....                                                                                                                                                                                                                                                                                                                                               | 163 |
| Figure 62 | STM images of 0.03 ML Pd deposited on SiO <sub>2</sub> (1 ML)/Mo(112). All images have dimensions of 10 nm × 10 nm. Tunneling parameters are (a) V <sub>s</sub> = -1 V, I = 0.5 nA, (b) V <sub>s</sub> = 1 V, I = 0.5 nA, (c) V <sub>s</sub> = 1 V, I = 0.5 nA, and (d) V <sub>s</sub> = -1 V, I = 0.5 nA .....                                                                                                                                                                                                                                                                                                                                             | 165 |

|           |                                                                                                                                                                                                                                                                                                                                                                                                                                         |     |
|-----------|-----------------------------------------------------------------------------------------------------------------------------------------------------------------------------------------------------------------------------------------------------------------------------------------------------------------------------------------------------------------------------------------------------------------------------------------|-----|
| Figure 63 | STM images of Pd adsorption on SiO <sub>2</sub> (1 ML)/Mo(112) at various bias voltages. Size and tunneling parameters are (a) 4 nm × 4 nm, V <sub>s</sub> = -1.2 V, I = 4 nA, (b) 5 nm × 5 nm, V <sub>s</sub> = -0.4 V, I = 4 nA, (c) 5 nm × 5 nm, V <sub>s</sub> = -0.2 V, I = 4 nA, and (d) 5 nm × 5 nm, V <sub>s</sub> = -1 V, I = 4 nA .....                                                                                       | 166 |
| Figure 64 | STM image of 0.1 ML Pd on SiO <sub>2</sub> (1 ML)/Mo(112). The image size is 80 nm × 80 nm. Tunneling parameters are V <sub>s</sub> = -1.2 V and I = 4 nA. The line profile shows cross section along the white line in the STM image .....                                                                                                                                                                                             | 168 |
| Figure 65 | STM images of Ru <sub>3</sub> Sn <sub>3</sub> alloy clusters deposited on SiO <sub>2</sub> (1 ML)/Mo(112). The surface was annealed at 450 K for 10 min before STM images are taken at room temperature. Tunneling parameters and image sizes are (a) V <sub>s</sub> = 1 V, I = 0.1 nA, 100 nm × 100 nm, and (b) V <sub>s</sub> = 1 V, I = 0.2 nA, 20 nm × 20 nm .....                                                                  | 171 |
| Figure 66 | Schematics of (a) the structure of Ru <sub>3</sub> (CO) <sub>9</sub> (μ-SnPh <sub>2</sub> ) <sub>3</sub> precursor, and (b) top-view of a Ru <sub>3</sub> Sn <sub>3</sub> cluster supported on SiO <sub>2</sub> (1 ML)/ Mo(112). The isolated [SiO <sub>4</sub> ] model was used to construct the SiO <sub>2</sub> substrate. Color representations of the ball model are: Mo – white; Si – red; O – blue; Sn – Purple; Ru – Green..... | 173 |
| Figure 67 | High resolution STM images of Ru <sub>3</sub> Sn <sub>3</sub> alloy clusters supported on SiO <sub>2</sub> (1 ML)/Mo(112). Tunneling parameters and image sizes are (a) V <sub>s</sub> = 0.6 V, I = 1 nA, 6 nm × 4 nm, and (b) V <sub>s</sub> = 1 V, I = 1 nA, 6 nm × 6 nm. Inset is the section profile of the line in (b) .....                                                                                                       | 174 |
| Figure 68 | STM images of Ru <sub>3</sub> Sn <sub>3</sub> alloy clusters supported on SiO <sub>2</sub> (1 ML)/Mo(112) after annealing at 700 K for 10 min. Tunneling parameters and image sizes are (a) V <sub>s</sub> = 1 V, I = 0.1 nA, 100 nm × 100 nm, and (b) V <sub>s</sub> = 1 V, I = 0.2 nA, 20 nm × 20 nm .....                                                                                                                            | 177 |

## CHAPTER I

### INTRODUCTION

The study of heterogeneous catalysis has been a major subject in the field of surface science since the early twentieth century [1]. In heterogeneous catalysis, the catalytic reaction occurs on the surface of catalysts, which is well suited to the focus of surface science. Starting from the pioneering work by Langmuir [2] on the adsorption of gases on catalyst surfaces in the 1910s, surface science has served as the fundamental approach to understand and develop heterogeneous catalysis.

A major focus of surface science research in heterogeneous catalysis is to correlate the elemental composition and the electronic and geometric structure of catalyst surfaces with their catalytic reactivity in specific chemical processes. Since the early 1970s, ultra high vacuum (UHV) surface science techniques have been developed to provide spectroscopic and structural information of catalyst surfaces at the atomic level. The integration of UHV surface science techniques with conventional catalytic studies has improved our understanding of heterogeneous catalysis and facilitated the discovery and design of new catalysts. Some difficulties remain, however, in connecting the information obtained from UHV surface science studies to the real world catalytic reactions. These difficulties have often been termed as the material gap and the pressure gap.

The material gap refers to the gap between the surface structure of metal single crystals usually studied in surface science and surfaces of real catalysts. The real catalysts

---

This dissertation follows the style and format of Surface Science.

usually consist of small metal clusters ranging from 1-100 nm in size and dispersing finely on a high-surface-area oxide support. These metal clusters of finite size can have structures and properties that are quite different from the bulk metal. In catalysis research, it is well documented that the reactivity and selectivity of catalysts often depend on the size of supported metal clusters [3]. Meanwhile, the presence of oxide support can modify the structure and properties of supported metal clusters. For example, in the late 1970s, Tauster et al. [4-6] discovered the unusual properties of group VIII metal, e.g., Pt and Ir, when they are supported on TiO<sub>2</sub> and reduced at relatively high temperatures. The Pt and Ir clusters supported on TiO<sub>2</sub> then show a suppressed CO and H<sub>2</sub> chemisorption and increased methanation reactivity. “Strong metal support interaction” (SMSI) has since been introduced to describe the unusual properties of group VIII metal supported on TiO<sub>2</sub>. Apparently, the effect of cluster size and metal support interaction, cannot be addressed from surface science studies on the well-defined single crystal metal surfaces.

The pressure gap refers to the fact that whereas surface science studies are conducted under UHV conditions ( $10^{-10}$ - $10^{-14}$  bar), the industrial catalysis reactions usually take place at high pressures (1-1000 bar). Thermodynamically, when the pressure of reactants is raised from  $10^{-10}$  bar to 1 bar, the chemical potential of reactants is increased by an amount of 27 kJ/mol at room temperature. Over 10 orders of magnitude of difference in the pressure of reactant gases can drastically change the chemisorption and interaction of reactants on the catalyst surface, which is essential to the catalytic reaction. Moreover, chemisorption can often cause metal atoms on the catalyst surface to change positions. In the early 1980s, Somorjai et al. [7-9] demonstrated that adsorbates could induce the reconstruction of catalyst surfaces. Ertl et al. [10-12] showed a parallel

between the restructuring of Pt surfaces and an oscillation in CO oxidation, which also occurs on other noble metals. In order to relate the structural information obtained on single crystal metal surfaces to their catalytic performance at high pressures, specially designed chemical reactors allowing high pressure reaction studies have been attached to UHV chambers. The model catalyst could thus be characterized before and after reaction in the coupled UHV chamber. However, the question remains on whether the surface structure observed in UHV is the working phase during high pressure catalytic reactions. This has been a big challenge for surface science studies in heterogeneous catalysis.

Over the past three decades, tremendous efforts have been devoted to bridge these two gaps. Studies have shown these gaps might not be so important for some specific catalysts and reactions. Goodman et al. [13-15] demonstrated the material gap might be trivial in the catalytic methanation reaction ( $\text{CO} + 3\text{H}_2 = \text{CH}_4 + \text{H}_2\text{O}$ ). In a set of experiments, they measured the activity on surfaces of Ni single crystals and compared to that of supported Ni catalysts under identical conditions. The reactivity of Ni single crystal surfaces is essentially the same as that of the small Ni clusters supported on a high-surface-area  $\text{Al}_2\text{O}_3$  in the methanation reaction. Stoltze and Norskov [16] illustrated the pressure gap might not be a problem for the catalytic synthesis of ammonia ( $\text{N}_2 + 3\text{H}_2 = 2\text{NH}_3$ ). Based on the kinetic parameters measured by Ertl et al. [17] on well-defined metal single crystals under UHV conditions, Stoltz and Norskov successfully reproduced the reaction rates for ammonia synthesis under industrial conditions.

In the past decade, progress in bridging these gaps has been made as a result of the development of model systems and high pressure surface science techniques. To

bridge the material gap, a new type of model catalyst, i.e. supported model catalyst, has been introduced into surface science studies (Figure 1). Supported metal catalyst is constituted of small metal clusters supported on planar surfaces, allowing precise characterization as in the case of single crystal metal surfaces. Methodologies on the synthesis of supported model catalysts have been reported extensively in the last decade [18-26].

In supported model catalysts, oxide single crystal or oxide thin film coated on a metal single crystal is used as the planar support. Metals of interest are then deposited onto the support mainly via either 1) the evaporation of metal atoms in UHV, 2) deposition of size selected metal clusters in UHV, 3) nanolithography, or 4) chemical deposition of metal-organic precursors. Among these methods of metal deposition, evaporation of metal atoms under UHV has been the most convenient and is used frequently in the preparation of supported model catalysts. Deposition of size selected metal clusters can produce supported metal clusters with uniform size, which has been of great interest in probing the size effect in catalysis. Supported model catalysts synthesized via size selected cluster deposition have just emerged in recent years. In these model catalysts, the size of selected metal clusters has been limited by their cluster sources and mass filters to  $N < 100$ , where  $N$  is the total number of atoms in each cluster. Nano-lithography can prepare supported model catalysts with uniform cluster shape and separation. However, supported metal clusters prepared by nano-lithography are relatively large so far, ranging from 10-100 nm in size. The deposition of metal-organic precursors onto the planar oxide support could be carried out by either evaporation in UHV or wet-impregnation in ambient conditions. The latter case is most close to the



Figure 1. Schematic illustration of “material gap” and the efforts to bridge “material gap”.  
(a) A real catalyst. (b) The development of model catalysts.



preparation of industrial catalysts, but has rarely been used to prepare model catalysts for UHV studies because of contaminations and erosions when model catalysts are exposed to ambient pressures and solutions.

The progress in bridging the pressure gap has mostly benefited from the development of surface science techniques. In recent years, the development of high pressure surface science techniques, which can work at realistic operating temperatures and pressures, has provided an opportunity to reveal the nature of working catalysts.

The high pressure surface science techniques can be divided into three groups. The first group of techniques is developed by integrating the differential pumping stages with conventional UHV surface science techniques based on electrons, ions, or molecular beams. Conventional surface science techniques have been limited to operate in UHV because the mean free path of electrons, ions, and molecules is not long enough to reach the detector under high pressures. Therefore, by lowering the pressure between the sample surface and the detector, the pressure range of these techniques, such as low-energy ion scattering (LEIS), transmission electron microscopy (TEM), and X-ray photoelectron spectroscopy (XPS), has been extended up to several mbar [27-29]. The second group of the techniques is surface sensitive optical probes emerged in the last two decades. The application of optical probes is less limited by ambient pressures. Techniques such as polarization modulation infrared adsorption spectroscopy (PM-RAIRS) and sum frequency generation spectroscopy (SFG), can provide spectroscopic information of the surface at atmospheric pressures [30-38]. Taking advantage of the high brilliance X-ray beams from synchrotron radiation, surface X-ray diffraction (SXRD) has been developed to determine the structural parameters of model catalyst surfaces at

atmospheric pressures [39-42]. The third group of techniques is the family of scanning probe microscope (SPM), such as scanning tunneling microscope (STM) and atomic force microscope (AFM). STM has greatly facilitated the development of surface science since its invention, because it can give atomic-scale structural information of the surface in both vacuum and atmosphere.

The application of STM to high pressure catalysis studies started in the 1990s with the work by Somorjai, Salmeron and co-workers [43-45], in which they demonstrated that catalytic surfaces can be imaged at high temperatures and in the presence of high pressure reactant gases. Since then, a series of high pressure STM studies have been conducted on both metal single crystals and supported model catalysts [43-72]. Most of these studies have been focusing on the adsorbate structure and surface reconstruction on single crystal metal surfaces in the presence of single-component gases. High pressure STM studies of model catalysts under reaction conditions have emerged recently and delivered promising information to reveal the surface structure of working catalysts.

In the early 1990s, a hypothesis proposed by Somorjai [73-77], termed as the “flexible surface”, promoted the idea that metal surfaces exhibit high flexibility under reaction conditions. The low coordination number of metal atoms on a planar or curved-cluster surface can cause high diffusivity of these metal atoms and thus the morphological reconstruction of metal surfaces. To support his hypothesis, Somorjai has referred to the high activity of surface defect sites or rough surfaces, generally observed in surface science studies. In this hypothesis, it is critical to determine the time-scale and energetics of surface diffusion of metal atoms with their catalytic reactivity. In other

words: To what extent does the surface flexibility impact the catalysis? Are the moving metal atoms (metal complex) or the reconstructed but rigid surface doing the catalysis? High pressure STM is an excellent tool to conduct *in-situ* and real time studies on the surface of working catalysts, and thus provides a great opportunity to test this hypothesis.

In this dissertation, taking advantage of the development of supported model catalysts and high pressure STM, we have investigated the working principles of supported Au catalysts. Using Au clusters supported on  $\text{TiO}_2(110)$  as a model system, *in-situ* STM has been applied to study supported Au clusters both in UHV and under realistic conditions. The surface of  $\text{Au/TiO}_2(110)$  during CO oxidation has been further compared to that of  $\text{Rh}(110)$  to reveal the active phase of Au for CO oxidation. In addition, we have also explored the synthesis and characterization of supported alloy catalysts. STM has shown many advantages in determining structures of the alloy model catalysts.

### **Au clusters supported on $\text{TiO}_2(110)$**

Au clusters supported on high-surface-area titania have been found to be an active catalyst for low temperature CO oxidation and selective hydrogenation reactions[78, 79]. The unusual catalytic reactivity of supported Au clusters has been of great interest in both fundamental and applied research because (1) neither bulk Au nor the  $\text{TiO}_2$  support alone exhibits catalytic reactivity in these reactions, and (2) this catalyst has great technological potential in applications, such as preventing CO poisoning of proton exchange membrane fuel cells. In particular, supported Au clusters in the 2-4 nm size range show a remarkable catalytic reactivity in low temperature CO oxidation [80-83]. Meanwhile, the support

effect is generally present in supported Au catalysts. Au clusters exhibit better reactivity when they are supported on reducible oxides, e.g.,  $\text{TiO}_2$  and  $\text{Fe}_2\text{O}_3$ , than on non-reducible oxides, such as  $\text{MgO}$ ,  $\text{Al}_2\text{O}_3$ , and  $\text{SiO}_2$  [84-86]. Although the cause of the extraordinary activity of Au clusters is still under debate, it is clear that a supported Au model catalyst needs to be used in surface science studies to address the phenomenal size and support effect in supported Au catalysts.

Au clusters supported on a planar  $\text{TiO}_2(110)$  single crystal have been used as the model system to investigate the origin of the reactivity of Au catalysts during CO oxidation. Early studies on Au deposited on  $\text{TiO}_2(110)$  and Au on high-surface-area titania have shown a similar correlation between the Au cluster size and the catalytic activity for CO oxidation [80, 81].  $\text{TiO}_2$  supported Au catalysts with cluster size of 3 nm exhibit the highest reactivity. Several suggestions have been put forward to speculate the origin of catalytically active Au. Valden et al. [81] highlighted the size and band structure effect because the measured onset of reactivity corresponds to the transition of supported Au clusters from metallic to non-metallic state. Chen et al. [87, 88] further emphasized that bi-layer Au supported on a reduced  $\text{TiO}_x$  film exhibit an optimum reactivity in CO oxidation while the population of Au clusters in the 3 nm size peaked with Au clusters of 2 layer thickness [87, 88, 91]. Meanwhile, Pietron et al. [92] observed high reactivity for Au- $\text{TiO}_2$  aerogels with large cluster sizes and proposed that the enlargement of the Au/ $\text{TiO}_2$  contact area is critical. Among these speculations, it is generally agreed that the  $\text{TiO}_2$  support tunes the structure and reactivity of supported Au clusters. It is thus important to find out the Au binding sites and their structure on  $\text{TiO}_2$  in order to elucidate the origin of catalytically active Au.

### Surface defects and Au growth on TiO<sub>2</sub>(110)

TiO<sub>2</sub> has been the most investigated metal oxide by surface science techniques, because of 1) its great technological potentials in areas, such as photocatalysis and micro-electronics, and 2) its transparency to electron probes making it approachable by most surface science techniques. Mineral TiO<sub>2</sub> usually has many different phase structures, such as rutile, anatase, and brookite [93]. The rutile phase is the most stable phase of TiO<sub>2</sub> and readily available for research and technological development. In particular, the rutile-TiO<sub>2</sub> (110) crystal with a (1 × 1) surface has been studied most extensively by surface science techniques. The rutile phase is assumed in the following discussions regarding TiO<sub>2</sub>(110).

Figure 2 demonstrates the structural model of TiO<sub>2</sub>(110)- (1 × 1) surfaces, both stoichiometric and defective. From Figure 2(a), the (1 × 1) surface of TiO<sub>2</sub>(110) contains two different types of Titanium atoms, which form rows along the [001] crystal orientation. Rows of 6-fold coordinated Ti ions alternate with the 5-fold terminal Ti ions, which are missing a single O atom ligand perpendicular to the surface. The surface also contains two kinds of oxygen atoms, i.e., 3-fold coordinate oxygen atoms sitting within the surface plane and bridging oxygen atoms sitting above the surface plane and bonded to two 6-fold coordinated Ti atoms in the surface plane. The different positions and bondings of Ti and O atoms should make their stability different. Under-saturated bridging oxygen atoms are subjected to surface reaction and can be easily removed from the surface by thermal annealing, electron bombardment, or ion sputtering. The TiO<sub>2</sub>(110) surface can thus accommodate a range of sub-stoichiometry while undergoing oxygen loss, which has also been observed on other reducible oxides [94]. Bridging oxygen vacancies are the most common and well-defined defects on the TiO<sub>2</sub>(110) surface (Figure 2(b)). Surface science

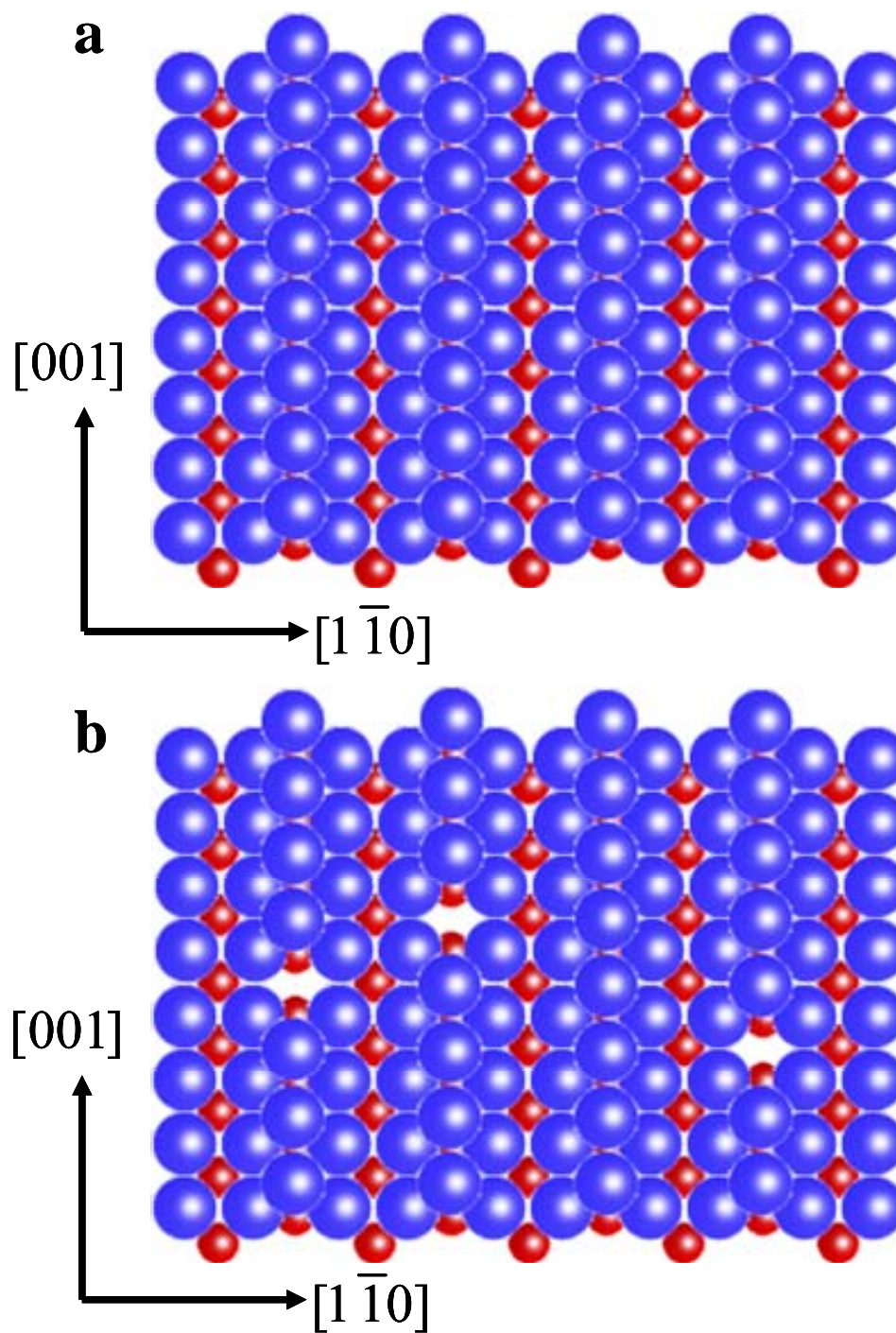


Figure 2. Schematic drawing of the  $\text{TiO}_2(110)$  surface. (a) A stoichiometric surface. (b) A defective surface with bridging oxygen vacancies. In the model, red balls represent Ti atoms and blue represent O atoms.

studies have also revealed other types of defects on the  $\text{TiO}_2(110)$  surface, such as step edges,  $\text{TiO}_x$  strands, and shear plan dislocations. However, the detailed structure of these defects remains largely unknown. The coordination number of atoms in these defects might vary with different surface preparation conditions and thus affect the overall surface chemistry.

In general, the nucleation and growth of Au on  $\text{TiO}_2(110)$  is an interplay between thermodynamics and kinetics of metal atom adsorption, surface diffusion, nucleation, and island growth. Campbell et al. [25] have reviewed the growth of late transition metals on oxide surfaces. The review show that 1) at low temperature, the growth of metal on oxide is controlled by kinetics leading to a flat 2D island, and 2) at high temperature or under equilibrium condition, it is controlled by thermodynamics leading to 3D shapes. Lai et al. [95] have further confirmed in their STM study that Au grows as three dimensional (3D) hemispherical clusters on  $\text{TiO}_2(110)$ , while 2D island formation is observed at low Au coverages ( $< 0.1\text{ML}$ ).

Moreover, studies have suggested that the nucleation and growth of Au on  $\text{TiO}_2(110)$  are primarily influenced by surface defects, such as oxygen vacancies and step edges. Using STM, Lai et al. [95] found Au clusters prefer to grow at step edges of  $\text{TiO}_2(110)$  after UHV annealing. STM and DFT studies by Wahlstrom et al. [96] show bridging oxygen vacancies bind Au most strongly on surface terraces of  $\text{TiO}_2(110)$ . A different opinion has recently been brought up by Matthey et al. [97]. In their study, the thermal stability of Au clusters was compared on  $\text{TiO}_2(110)$  surfaces with different pretreatments. They found Au clusters exhibit better stabilities on the  $\text{TiO}_2(110)$  surface pretreated with  $\text{O}_2$ , and thus concluded Au binds more strongly on an oxygen covered  $\text{TiO}_2(110)$  surface due to the formation of Au-O-Ti bonds. Indeed, the thermal stability of

Au/TiO<sub>2</sub>(110) has been studied extensively using a variety of surface science techniques. However, discrepancies remain in studies on the thermal stability of Au/TiO<sub>2</sub>(110). In this dissertation, we scrutinized surface structures of TiO<sub>2</sub>(110) after a variety of pretreatments and their influence on the growth and stability of Au clusters supported on TiO<sub>2</sub>(110). Our studies reveal the strongest Au binding sites of TiO<sub>2</sub>(110) and can explain the discrepancies among previous studies.

### **Au/TiO<sub>2</sub>(110) in the presence of reactant gases**

The morphology of supported metal clusters can change dramatically upon exposure to adsorbate gases due to the low coordination number and high surface chemical potential of metal clusters. For example, CO, NO and O<sub>2</sub> have been reported to promote the dissociation of Rh and Ir clusters into metal atoms at room temperature [98-100]. At 1000 K, O<sub>2</sub> promoted the disappearance of Pt clusters supported on alumina [101]. For supported Au catalysts, the presence of reactant gases has caused a major problem for their technological application. The major problem for the commercialization of supported Au catalysts is that these catalysts deactivate rapidly [78, 79, 81]. The fast deactivation of a Au catalyst consisting of Au clusters supported on TiO<sub>2</sub>(110) has been attributed to the sintering of Au clusters induced by O<sub>2</sub> [81, 95]. This is a typical example of pressure gap since Au/TiO<sub>2</sub>(110) is stable in UHV while it is susceptible to sintering in the presence of reactant gases.

Sintering of supported metal catalysts has been central for catalysis research. Metal particles of several nanometers in size, supported on oxide surfaces are often efficient catalysts [18, 19, 22, 25, 79, 102]. These catalysts, however, frequently



deactivate as the average size of the supported metal particles increases via sintering [79, 81, 103]. Numerous studies have addressed the sintering of supported nanoparticles in order to understand the sintering mechanisms and to formulate kinetic models that allow the prediction of the sintering kinetics of supported nanoparticles [101, 103-106].

A fundamental issue in sintering kinetics is to determine the dominating mass transport process. The sintering of supported nanoclusters can occur in essentially two modes, either by the migration and coalescence of whole clusters or by the migration of monomers (single metal atoms or metal complexes). These modes are illustrated in Figure 3. In the first mode, known as cluster migration, metal atoms diffusing on the cluster surface accumulate on one side by random fluctuations, causing the cluster to advance. These events repeated over time cause Brownian motion of the clusters on the substrate, that then coalesce with neighboring clusters. The second mode, known as Ostwald ripening, entails monomers dissociating from small clusters, which then diffuse to and coalesce with large ones. Kinetic models of the sintering of supported metal clusters have been developed based on these two modes [105, 106].

Previous experimental studies [101, 103] have tried to determine the predominant mass transport mode, as well as the kinetic parameters of sintering, by fitting the average cluster size distribution or average cluster size with theoretical kinetic models. These models provide the rate equation of sintering for a single cluster, which is then generalized to clusters on the whole surface with approximation. On the other hand, previous kinetic studies focused on the behavior of the whole cluster ensemble, such as average cluster dispersion and average cluster size, rather than on individual clusters.

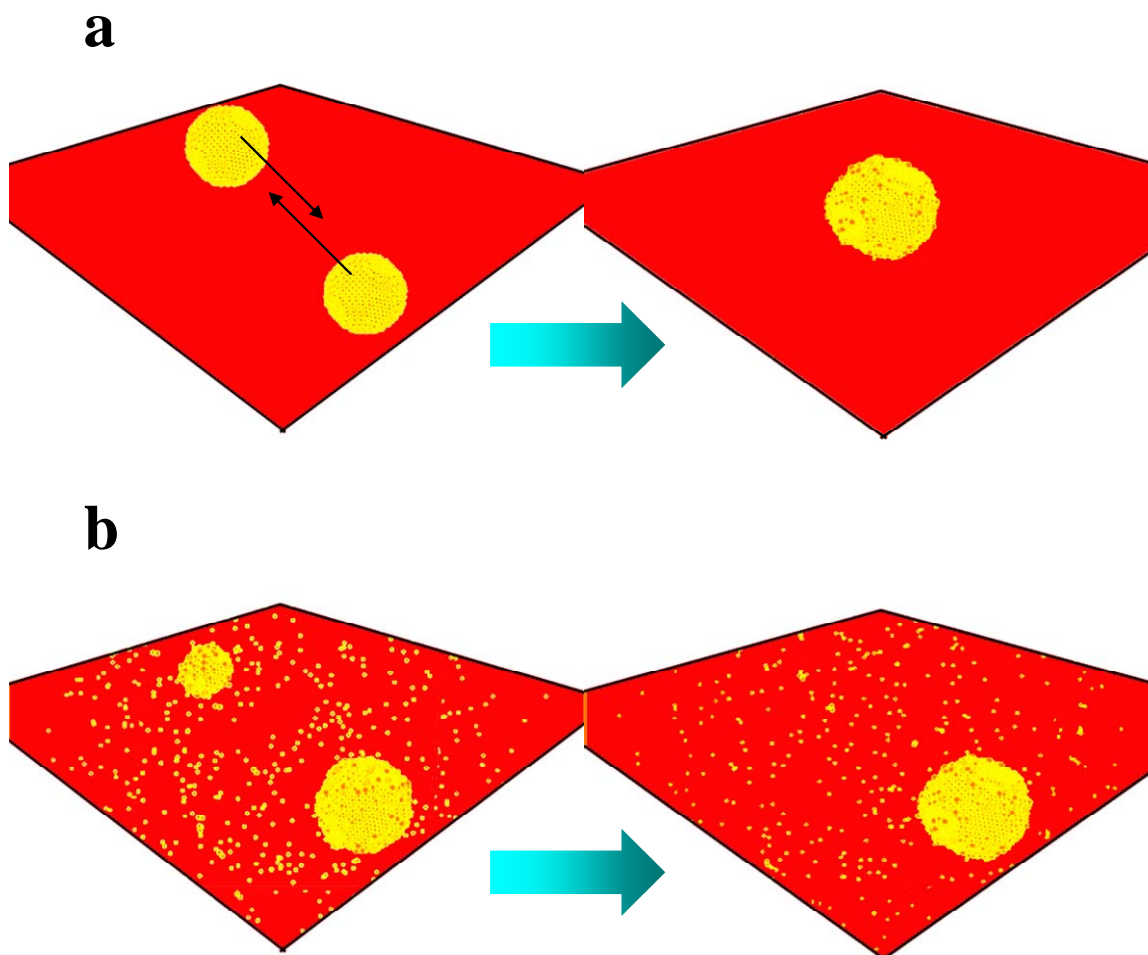


Figure 3. Schematic illustration of sintering modes: (a) cluster migration, and (b) Ostwald ripening.

Discrepancies exist between the kinetics predicted by these theoretical models and experimental results on the sintering of supported metal clusters [101, 107].

*In-situ* STM presents a great opportunity to monitor individual clusters under realistic conditions and directly determine the controlling mass transport mode. Continuous STM snap shots of certain clusters could reveal which mode is dominating the sintering process. Moreover, STM measurements on volume change of supported metal clusters as a function of time at constant temperature could directly provide the most accurate rate data for the simulation of sintering kinetics and the determination of activation energy of sintering. *In-situ* STM studies on supported metal clusters have been limited [64, 65, 108], due to experimental difficulties, such as tip instability in the reactive environment and scan drifts caused by ambient pressure/temperature changes. Methods to overcome these difficulties have been addressed in preceding studies [65, 108, 109]. In this dissertation, we report an *in-situ* kinetic study on the sintering of Au clusters supported on TiO<sub>2</sub>(110) in the presence of reactant gases. In addition to the sintering kinetics of Au/TiO<sub>2</sub>(110), *in-situ* STM studies can also reveal the active phase of catalytically active Au.

### **W-J model of Ostwald ripening**

In this dissertation, the theoretical model of Ostwald ripening is used to analyze the sintering kinetics of Au/TiO<sub>2</sub>(110) during CO oxidation. The theoretical model of Ostwald ripening for supported metal clusters has been developed by Wynblatt and Gjostein [106] (“W-J” model). The rate equation of sintering is derived based on two kinetic processes: the diffusion of monomers across the surface and the detachment of

monomers, as shown in Figure 4. The main elements of the model of Ostwald ripening [106] are rewritten as below, considering two corrections addressed by Campbell et al.[107]

For a metal cluster supported on an oxide surface, the sintering rate of the metal cluster is determined by two kinetic processes: the detachment of monomers across the edge of metal clusters and the diffusion of monomers on the surrounding terraces of metal clusters.

For a spherical cap shape cluster labeled with index  $i$  (Figure 4), the net flux of monomers coming on to the metal cluster can be given by the vicinity area,  $2\pi r_i a$ , times the difference of concentration between monomers attaching to the cluster and monomers leaving the cluster,  $\frac{D}{l^2}(C_i' - C_i)$ :  $J_{i,c} = \frac{2\pi r_i a D}{l^2}(C_i' - C_i)$ . (1)

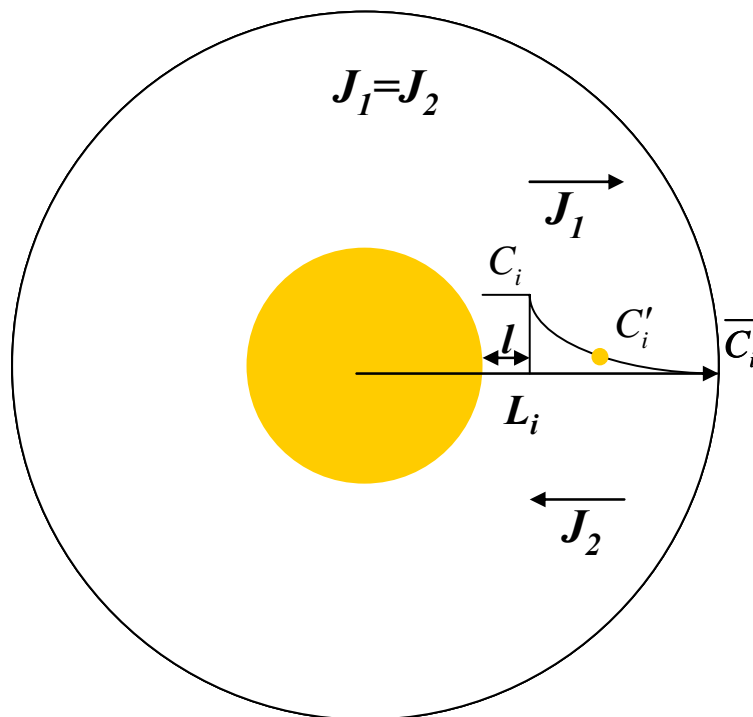
Here  $D$  is diffusion coefficient of monomers,  $r_i$  is the effective radius of the metal cluster,  $a$  is the lattice constant of metal clusters and  $l$  is the monomer jumping length on the terrace.  $C_i'$  denotes the monomer concentration adjacent to the metal cluster and  $C_i$  denotes the monomer concentration detached from the cluster. At steady state, the flux  $J_{i,c}$  matches the net flux of monomers coming towards the metal cluster,  $J_{i,s}$ , which is

$$\text{given by } J_{i,s} = \frac{2\pi D}{\ln(L_i / r_i)}(\bar{C}_i - C_i'). \quad (2)$$

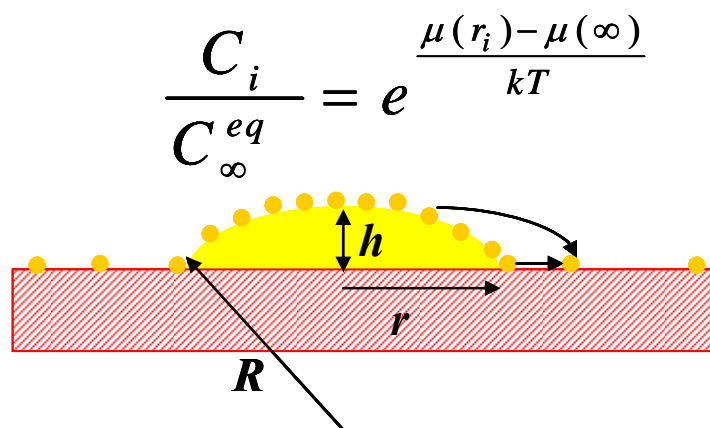
Here  $L_i$  specifies the length for monomer concentration to reach far field equilibrium,  $\bar{C}_i$ .

Since  $J_i = J_{i,c} = J_{i,s}$ , the rate equation of the cluster volume can thus be yielded to

$$\frac{dV_i}{dt} = J_i \Omega = \frac{2\pi \Omega D}{\ln(L_i / r_i) + l^2 / r_i a}(\bar{C}_i - C_i), \quad (3)$$



**(a) diffusion process**



**(b) detachment process**

Figure 4. Schematic view of the W-J model of Ostwald ripening. (a) and (b) represent the two-step treatment in W-J model. (a) shows the top view of a cluster in equilibrium with the surrounding monomer sea. (b) shows monomers detaching from the cluster and the relationship between the monomer concentration of clusters and the monomer concentration of bulk.

where  $\Omega$  is the volume of a metal atom. Not considering the influence of adsorbates, the detachment of monomers from the cluster can be treated as a 2D evaporation process and equal to the equilibrium 2D vapor pressure of the cluster,

$$C_i = C_\infty^{eq} e^{\frac{\mu(r_i) - \mu(\infty)}{kT}}. \quad (4)$$

Here  $C_\infty^{eq}$  is the equilibrium 2D vapor pressure of an infinite size cluster supported on an oxide,  $\mu(r_i)$  is the chemical potential of the cluster  $i$ , and  $\mu(\infty)$  is the bulk chemical potential. Thus, Equation (3) can be expressed as

$$\frac{dV_i}{dt} = \frac{2\pi \Omega DC_\infty^{eq}}{\ln(L_i / r_i) + l^2 / r_i a} \left[ e^{\frac{\mu(r_i^*) - \mu(\infty)}{kT}} - e^{\frac{\mu(r_i) - \mu(\infty)}{kT}} \right]. \quad (5)$$

Here  $r_i^*$  is the critical radius of the cluster that neither decays nor grows at diffusion equilibrium. The cluster with a radius of  $r_i^*$  has a monomer concentration leaving the cluster equal to the far field monomer concentration,  $\bar{C}_i = C_\infty^{eq} e^{\frac{\mu(r_i^*) - \mu(\infty)}{kT}}$ . Assuming clusters on the surface in equilibrium with the same far field monomer concentration (mean field approximation),  $r_i^*$  is the average radius of all clusters and increases as a function of time.

Equation (5) yields two kinetic limits for the sintering of nanoclusters. If the diffusion of monomers is much slower than the detachment of monomers, i.e.

$\ln(L_i / r_i) \gg l^2 / r_i a$ , the rate of cluster sintering is completely determined by the monomer diffusion on the terrace and the situation is termed as “diffusion control”.

Equation (5) is thus simplified to

$$\frac{dV_i}{dt} = \frac{2\pi \Omega DC_\infty^{eq}}{\ln(L_i / r_i)} \left[ e^{\frac{\mu(r_i^*) - \mu(\infty)}{kT}} - e^{\frac{\mu(r_i) - \mu(\infty)}{kT}} \right]. \quad (6)$$

If the flux across the edge of clusters is the rate limiting step, i.e.  $\ln(L_i / r_i) \ll l^2 / r_i a$ , the situation is termed as “interface control”. Equation (5) is simplified to

$$\frac{dV_i}{dt} = \frac{2\pi \Omega r_i a D C_\infty^{eq}}{l^2} \left[ e^{\frac{\mu(r_i^*) - \mu(\infty)}{kT}} - e^{\frac{\mu(r_i) - \mu(\infty)}{kT}} \right]. \quad (7)$$

The diffusion coefficient  $D$  equals to  $l^2 \nu_s \exp(-\frac{S_m^s}{k}) \exp(-\frac{H_m^s}{kT})$  assuming isotropic diffusion. Here  $\nu_s$  is the vibrational frequency of monomer on the substrate site,  $S_m^s$  is the entropy of monomer diffusion on the substrate, and  $H_m^s$  is the enthalpy for monomer diffusion on the substrate. The equilibrium 2D vapor pressure of an infinite size cluster supported on an oxide,  $C_\infty^{eq}$ , equals to  $\frac{\nu_c}{a^2 \nu_s} \exp(-\frac{E_t}{kT})$ , where  $\nu_c$  is the vibrational frequency of monomer on the cluster edge. The detachment activation energy,  $E_t$ , equals to  $\Delta H_{sub} - E_{ad}^s$ , where  $\Delta H_{sub}$  is the sublimation enthalpy of bulk metal, and  $E_{ad}^s$  is the adsorption energy of a monomer on the substrate. The contributions from entropies are neglected in  $C_\infty^{eq}$ , because they are very small compared with the enthalpies for metal clusters. Therefore, the equation (6) for diffusion control limit can be expressed as,

$$\frac{dV_i}{dt} = \frac{K_{dc}}{\ln(L_i / r_i)} e^{\frac{E_{tot}}{kT}} \left[ e^{\frac{\mu(r_i^*) - \mu(\infty)}{kT}} - e^{\frac{\mu(r_i) - \mu(\infty)}{kT}} \right]. \quad (8)$$

And the equation (7) for interface control limit can be rewrote as,

$$\frac{dV_i}{dt} = K_{ic} r_i e^{\frac{E_{tot}}{kT}} \left[ e^{\frac{\mu(r_i^*) - \mu(\infty)}{kT}} - e^{\frac{\mu(r_i) - \mu(\infty)}{kT}} \right]. \quad (9)$$

$K_{dc}$  and  $K_{ic}$  are prefactors.  $E_{tot}$  equals to  $\Delta H_{sub} - E_{ad}^s + H_m^s$ , the summation of detachment activation energy and diffusion activation energy.

In conventional treatments of the W-J model, the chemical potential of supported metal clusters,  $\mu(r)$ , was expressed by Gibbs-Thomson (G-T) relationship,

$$\mu(r) - \mu(\infty) = 2\gamma\Omega / r, \quad (10)$$

where  $\gamma$  is the surface free energy of the bulk metal and  $r$  is the radius of the cluster. The rate equation was then simplified by Taylor expansion, assuming the chemical potential of clusters is much smaller than  $kT$ . These simplifications were void as addressed by Campbell et al.[107]. Their microcalorimetric studies on supported metal clusters suggested that the chemical potentials of nanoclusters are much higher than the values estimated from G-T relationship.

### **Synthesis and characterization of alloy model catalysts**

In recent years, the development of model catalysts has further expanded to a more complex system, i.e., supported alloy catalysts. Supported alloy clusters are used for several industrially important heterogeneously catalyzed reactions [110-112]. Extensive studies of alloy catalysts by Sinfelt et al. [110, 113-115] have demonstrated the reactivity and selectivity of alloy clusters can change drastically as the cluster composition changes for hydrogenolysis and dehydrogenation reactions. Meanwhile, tuning alloy composition can often prepare catalysts with reactivity and selectivity superior to monometallic catalysts. The enhanced properties of alloy catalysts are generally attributed to either ensemble or electronic effects although other factors related to cluster size effects, matrix effects, and catalyst stability have been invoked [111].



Studies on model systems consisting of small alloy clusters supported on planar surfaces is still in its infancy due to the difficulties in preparation and characterization [19]. The methods of metal deposition described above have caused some difficulties for the characterization of supported alloy clusters. For instance, evaporation of metal atoms in UHV can be a simple and convenient way to make clusters. However, it is difficult to prove that two metals form alloy clusters. Deposition of metal-organic precursors and subsequent annealing to remove organic ligands can make alloy clusters of uniform size and structure. However, same as the preparation of monometallic model catalysts using wet-impregnation, contamination and erosions cause difficulties in surface characterization.

In this dissertation, supported alloy model catalysts have been synthesized via the evaporation of metal atoms in UHV and wet impregnation of metal-organic precursors. In the case of UHV deposition of metal atoms, we have successfully applied *in-situ* STM to verify the formation of alloy clusters. In the case of wet impregnation of metal-organic precursors, we have been able to obtain the atomic structure of Ru<sub>3</sub>Sn<sub>3</sub> alloy cluster supported on a thin silica film. STM has provided great opportunities for the atomic understanding of complex heterogeneous catalysts.

## CHAPTER II

### EXPERIMENTAL

In this chapter, we describe our experimental setups, summarize the related theories, and discuss experimental considerations for both *in-situ* and high resolution STM studies.

#### Instrumentation

Two experimental setups are employed to study the structure and stability of model catalysts. The first setup, named as “*in-situ* STM system”, can conduct *in-situ* STM studies on model catalysts both in UHV and under realistic reaction conditions. The second setup mainly focuses on resolving the surface atomic structures of model catalysts and is thus termed as “high resolution STM system” in following discussions.

The *in-situ* STM system consists of three parts: 1) an UHV analysis chamber equipped with Auger electron spectroscopy (AES) and quadrupole mass spectrometry (QMS), 2) a commercial (RHK VT-UHV300) variable temperature STM chamber, and 3) a fast loadlock transfer chamber. A 60 inch long linear rotary feedthrough is used to transfer the sample between the UHV analysis chamber and the STM chamber while a 10 inch long linear feedthrough is used to transfer the sample or STM tip holders between the STM chamber and the loadlock chamber. A schematic of the entire system is shown in Figure 5a. The entire system is supported by a steel frame which rests on three pneumatic air legs (Newport Laminar Flow Isolators, I-2000 Series) for primary vibration isolation.

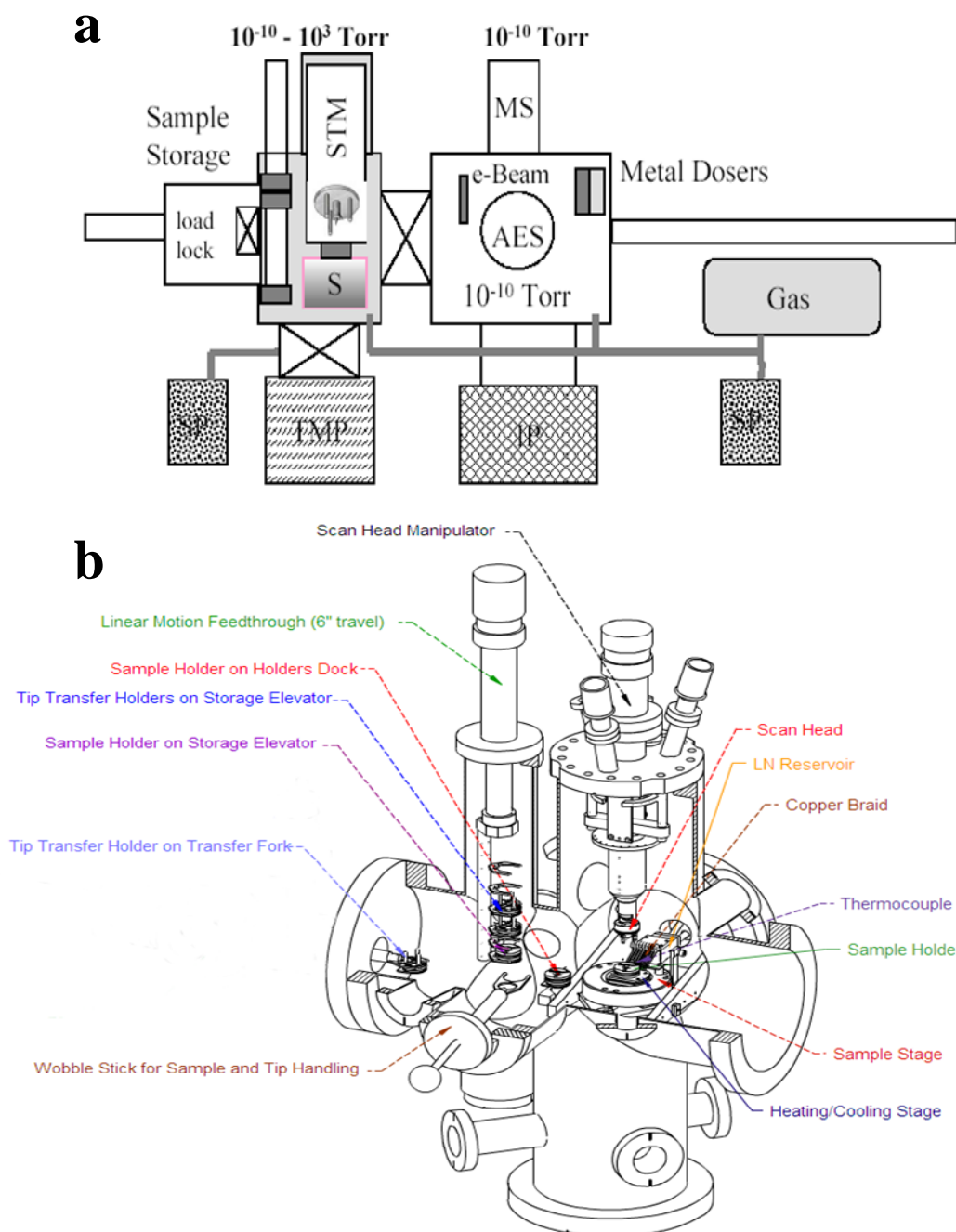


Figure 5. Schematic drawing of a surface analysis system for *in-situ* STM studies. (a) Side view of the surface analysis system. (b) 3D demonstration of the STM chamber for *in-situ* studies.

The base pressure of the *in-situ* STM system is typically  $< 2.0 \times 10^{-10}$  Torr. The UHV is achieved and maintained through three stages of pumping systems. The first stage is a mechanical rotary pump (Alcatel), which allows the system to be pumped down from atmospheric pressure into milliTorr pressure range. The second stage is a 330 l/s turbo molecular pump (Balzers–Pfeiffer, Model TPU 330) attached below the STM chamber. The turbo molecular pump, backed up by the mechanical rotary pump, can achieve an operating vacuum of  $10^{-9}$  Torr. The third stage is a 220 l/s ion pump (Perkin-Elmer) and a titanium sublimation pump (TSP), which are attached below the UHV analysis chamber and provide a working base pressure  $< 2 \times 10^{-10}$  Torr. The ion pump does not need to be backed once the operating pressure is reached below  $10^{-6}$  Torr, resulting in a cleaner UHV environment with respect to the turbo molecular pump. Additional efficiency is provided by TSP, which utilizes a reactive titanium film to remove active gas molecules, such as  $H_2$ ,  $H_2O$ , and  $O_2$ . During STM experiments in UHV, both the first and second stage of pumping systems are turned off to reduce the vibration.

The STM chamber is equipped with RHK variable temperature STM (RHK VT-UHV300), as shown in Figure 5b. The microscope is Besocke-type, with compact construction and high thermal stability [116], and can be applied to conduct *in-situ* STM experiments at temperature ranges between 100-600 K. The sample stage is mounted on three viton spacers, which provide secondary vibration isolation for STM measurements. The STM chamber can be isolated from the UHV system via gate valves and pressurized with gases from a gas manifold to 1 atmosphere while the UHV analysis chamber and the loadlock remain in vacuum. As the pressure in the STM chamber is increased, STM tip can remain in tunneling range and keep scanning the same area of the surface. Under

tunneling conditions, the STM chamber can also be evacuated with a sorption pump (ULTEK), attached below the STM chamber, to  $10^{-3}$  Torr without inducing vibrations that could crash the STM tip.

For sample preparation, an ion sputtering gun (PHI 20-015) is equipped in the STM chamber with the gun head facing the sample storage. The bottom storage fork on the sample storage is modified to be rotary so that the sample can be rotated to face the sputtering gun with adjustable angles. Two methods are available for the sample annealing in UHV. The first method is electron beam heating in the UHV analysis chamber. An electron beam filament is mounted on a linear feedthrough, which is perpendicular to the sample manipulator in the UHV analysis chamber. The filament can be moved close to the back of the sample while heating, and it can be retracted away afterwards. The second method is resistive heating, which uses a highly doped Si wafer attached to the back of the sample and sandwiched in the sample holder. In order to heat the sample in high pressures, the sample stage is equipped with a 30 W halogen filled quartz bulb. While heating, the bulb is raised to the back of the sample, keeping an approximately 1 mm distance between the top of the bulb and the back of the sample. This provides radiative heating without causing additional vibration to the STM stage. Depending on the sample size, the bulb can usually be used to heat the sample up to 600 K in pressures up to 1 atm. The sample temperature can be measured by a type K thermocouple mounted in the sample holder through ceramic tube leads and held in place by screw. The bare thermocouple wires protrude from the sample holder and have an efficient contact with the spring clips of thermocouple leads on the sample stage.

The high resolution STM system consists of an UHV STM chamber, an UHV sample preparation chamber, an UHV analysis chamber, and a loadlock chamber. Detailed schematics of this system are shown in Figure 6. The UHV STM chamber is equipped with an Omicron room temperature STM (STM-1) for surface structure characterization. The UHV analysis chamber is equipped with a double-pass cylindrical mirror analyzer (PHI model 25-255) for AES measurements and a set of low energy electron diffraction (LEED) optics (Perkin-Elmer). The sample preparation chamber contains an array of metal and semiconductor evaporators (Au, Pd, Ag, Ti, Si). These evaporators are used to deposit metal clusters or oxide thin films onto the planar support by resistive heating. A Ta sample holder is attached to the end of a linear rotary sample manipulator, which is used to transfer the sample between the UHV analysis chamber and the UHV preparation chamber. A W filament is implemented to the back of the Ta sample holder for electron beam heating. With a wobble-stick, the sample can be transferred between from the Ta sample holder to the STM chamber, and vice versa. Besides AES and LEED, the UHV analysis chamber is also equipped with an ion gun for Ar<sup>+</sup> sputtering. The sample can be moved in for surface cleaning or spectroscopic studies. A loadlock chamber is located at one end of the system. This design enables the sample to be linearly transferred into the loadlock chamber for high-pressure exposures.

The base pressure of the high resolution STM system is typically  $< 1.0 \times 10^{-10}$  Torr. The UHV is achieved and maintained through a series of pumping systems, which consist of a mechanical roughing pump (Alcatel), a 170 l/s turbo molecular pump (Balzers-Pfeiffer), two ion pumps (PE model, 500 l/s and 60 l/s), and a TSP. The 500 l/s ion pump is used to maintain the base pressure of the whole system below  $10^{-10}$  Torr. The

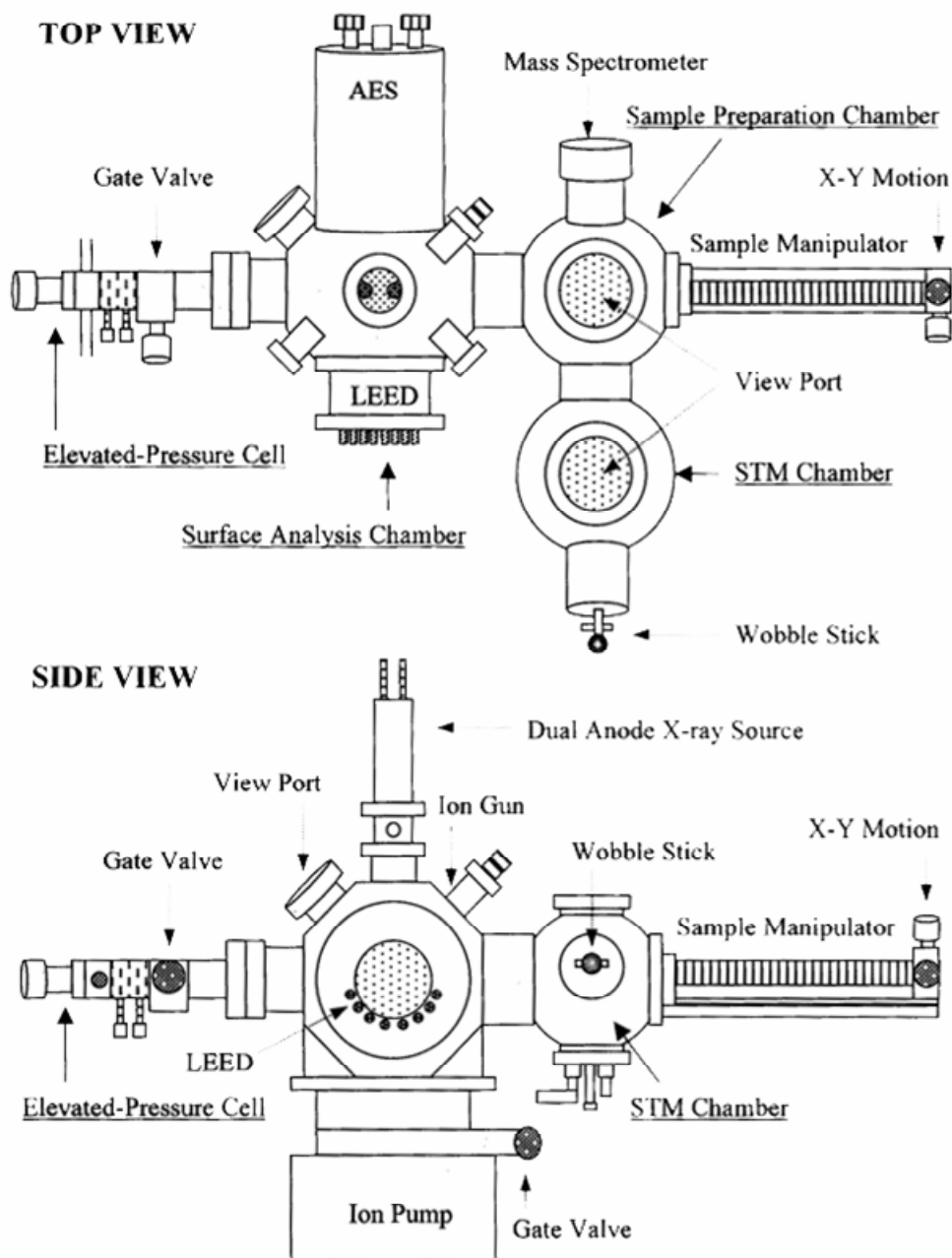


Figure 6. Schematic drawing of a surface analysis system for high resolution STM studies.

60 l/s ion pump is located at the sliding seal of the sample manipulator and differentially pumps the manipulator and the bellow. The TSP can be cooled using liquid nitrogen, which enhances the efficiency in removing residue  $H_2$  and  $H_2O$  from the vacuum chamber.

### **Methods of analysis**

In this section, we summarize the operation principles of STM, introduce the mechanisms of image contrast in STM, and describe the theory of AES.

#### **Scanning Tunneling Microscopy (STM)**

Scanning tunneling microscope was invented in 1982 by Binnig and Rohrer [117, 118], for which they were awarded the Nobel prize in physics in 1986. The operation principle of the STM is fundamentally based on the effect of quantum electron tunneling (Figure 7a). As an atomically sharp metal tip is brought within a few Angstroms above the sample, electron tunneling begins between the tip and sample due to their work function difference. When a bias voltage is applied between the tip and sample, an electronic current flows. As the tip scans across the surface, this current can be measured as a function of xy coordinates and reflects the tip-surface separation, or to be precise, tip-surface interaction. A STM image can thus be created while the image contrast represents the tip-surface interaction. There are essentially two principal modes of image acquisition. The first and most common mode, i.e., constant current mode, applies a feedback to the z piezo to keep the tunneling current constant and thus measures the z displacement as a function of xy coordinates. The second mode is termed as constant



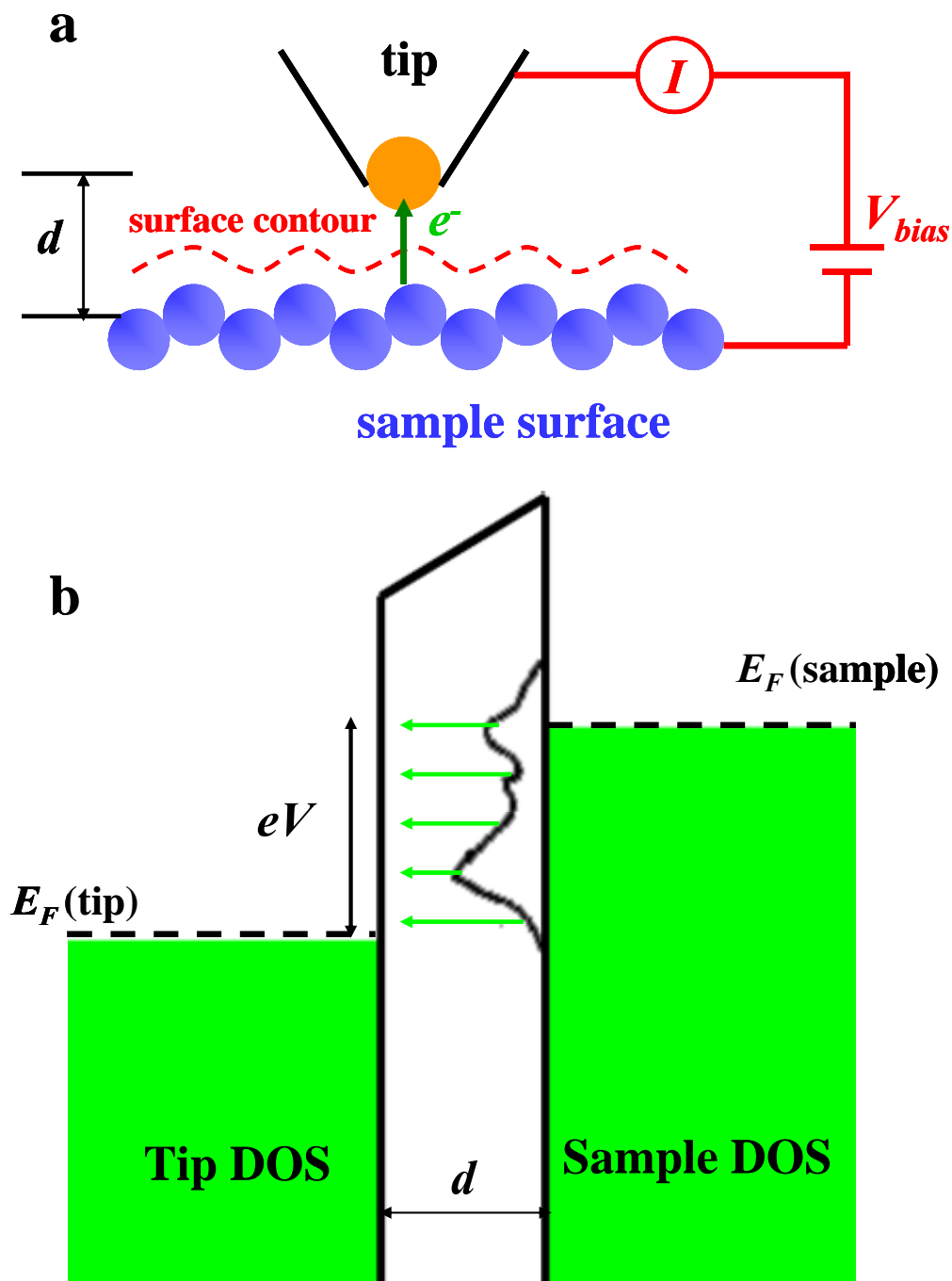


Figure 7. Schematic illustration of (a) the operation principle of STM, and (b) the tunneling principle. Density of states (DOS) of the sample and the tip are shown in (b), where the filled states are depicted in green. Application of a bias voltage to the sample will either raise or reduce the Fermi level of the sample with respect to the Fermi level of the tip. In the case of (b), the sample is negatively biased and allows for filled states of the sample to tunnel into the empty states of the tip.

height mode, which directly measures the tunneling current as a function of xy coordinates.

The origin of image contrast can be demonstrated by the equation of tunneling current. Assuming the bias voltage is small compared to the tunnel barrier height, we could estimate the tunneling current as [119],  $I = cV \exp(-\sqrt{\Phi}z)$ , where  $c$  is a constant,  $V$  is the bias voltage,  $\Phi$  is the tunnel barrier height (work function of tip or sample, depending on the direction of tunneling) and  $z$  is the tip-surface separation. The tunneling current decreases exponentially with the tip-surface separation, which enables the STM to be extremely sensitive to surface corrugation. A more sophisticated treatment of the tunneling current based on WKB approximation gives the tunneling equation as

$$[120], I = \int_0^{eV} \rho_s(r, E) \rho_t(r, \pm eV \mp E) T(E, eV, r) dE, \text{ where } \rho_s(r, E) \text{ and } \rho_t(r, E) \text{ are the}$$

density of states of the sample and the tip at location  $r$  and energy level  $E$ , the upper signs corresponds to positive sample bias ( $eV > 0$ ), the lower signs corresponds to negative sample bias ( $eV < 0$ ), and  $T$  is the tunneling transmission probability. This equation clearly shows the tunneling current is proportional to the surface local density of states (LDOS), evaluated at the location of the tip. Meanwhile, the equation reveals the tunneling current depends only on the DOS within  $eV$  above or below the Fermi level. The first derivative of tunneling current with respect to bias voltage will give the DOS at  $eV$  above or below the Fermi level (Figure 7b). Therefore, in addition to obtain the topography of a surface, STM is capable of measuring LDOS by recording the tunneling current while ramping the bias voltage at a fixed tip position.

The origin of image contrast on surfaces with adsorbates might be a little more sophisticated. Thin oxide films supported on metal surfaces, self-assembled monolayers, and surface metal oxides can all be deemed as surface adsorbates. In many cases, especially when these adsorbates are not interacting with the metal substrate strongly, they may not contribute a significant number of states to the surface electronic structure or cause the shifts of energy level at near the Fermi level. Nevertheless, STM has been successful in resolving the surface geometry of these adsorbates. The general nature of image contrast on these adsorbates can be illustrated using the case of Xe on Ni [121]. Xe atoms on Ni(110) can be well resolved although not a single Xe adsorbate state lies within several eV of the Fermi level. As evaluated at the position of tip, the presence of Xe has a significant influence on the LDOS, simply due to its lower tunneling barrier height than the vacuum, which allows the surface wavefunction to extend further out in the vacuum. The existence of adsorbates can also enhance the transport rate of electrons across the tunneling junction, as recently reported by Nazin et al. [122] Therefore, STM can provide a topographic map of insulating adsorbates, especially on the topmost atoms.

### **Auger Electron Spectroscopy (AES)**

Auger electron spectroscopy (AES) can be used to determine the chemical composition of solid surfaces. Even though the phenomenon of Auger electron excitation was described by Auger in 1925 [123], the process of Auger transitions was not identified until 1953 by Lander [124], using electron bombardment on solid surfaces in a vacuum chamber. The AES technique for surface chemical analysis was not developed until 1968,

when Harris [125] demonstrated that electronic differentiation of the secondary electron energy distribution could greatly enhance the sensitivity of Auger signal.

The Auger effect is an intrinsic property of the ionized atom. An Auger transition can be excited by photons, electrons, or high energy ions. Figure 8 illustrates the process of Auger electron excitation. The incident electron ionizes the atom and creates a core hole. To reduce the potential energy of the ionized atom, an electron from the outer shell relaxes into the vacant hole. The energy released from this relaxation process can be transmitted to an electron (Auger electron) in the outer shell and cause the emission of Auger electron. Using the  $KL_1L_{2,3}$  Auger process as an example, the kinetic energy of the emitted Auger electron can be approximated to  $E_{KL_1L_{2,3}} = E_K - E_{L_1} - E_{L_{2,3}} - \Phi$ , where  $E_K$ ,  $E_{L_1}$ , and  $E_{L_{2,3}}$  are the binding energy of an electron in the K, L<sub>1</sub>, or L<sub>2,3</sub> shells, and  $\Phi$  is the work function. Therefore, the Auger electron provides information regarding the emitting atom's core level electronic structure, which varies with different elements. The typical AES operating range is between 50-2500 eV, where the intensity of Auger electrons dominates. Since the Auger process involves three electrons, AES can only be used to detect and examine surface elements with atomic number  $> 2$ .

In AES spectra, Auger electrons form small peaks on a large and continuous secondary electron background. Differentiation is thus used to emphasize the Auger signal. The peak to trough height of the derivative Auger signal can be used for quantitative concentration analysis of surface elements. A primary advantage of AES is its high surface sensitivity ( $\sim 1\%$  of a monolayer).

In our studies, AES is mainly used to qualitatively identify surface species both before and after STM experiments. Quantitative analysis is also conducted during a few

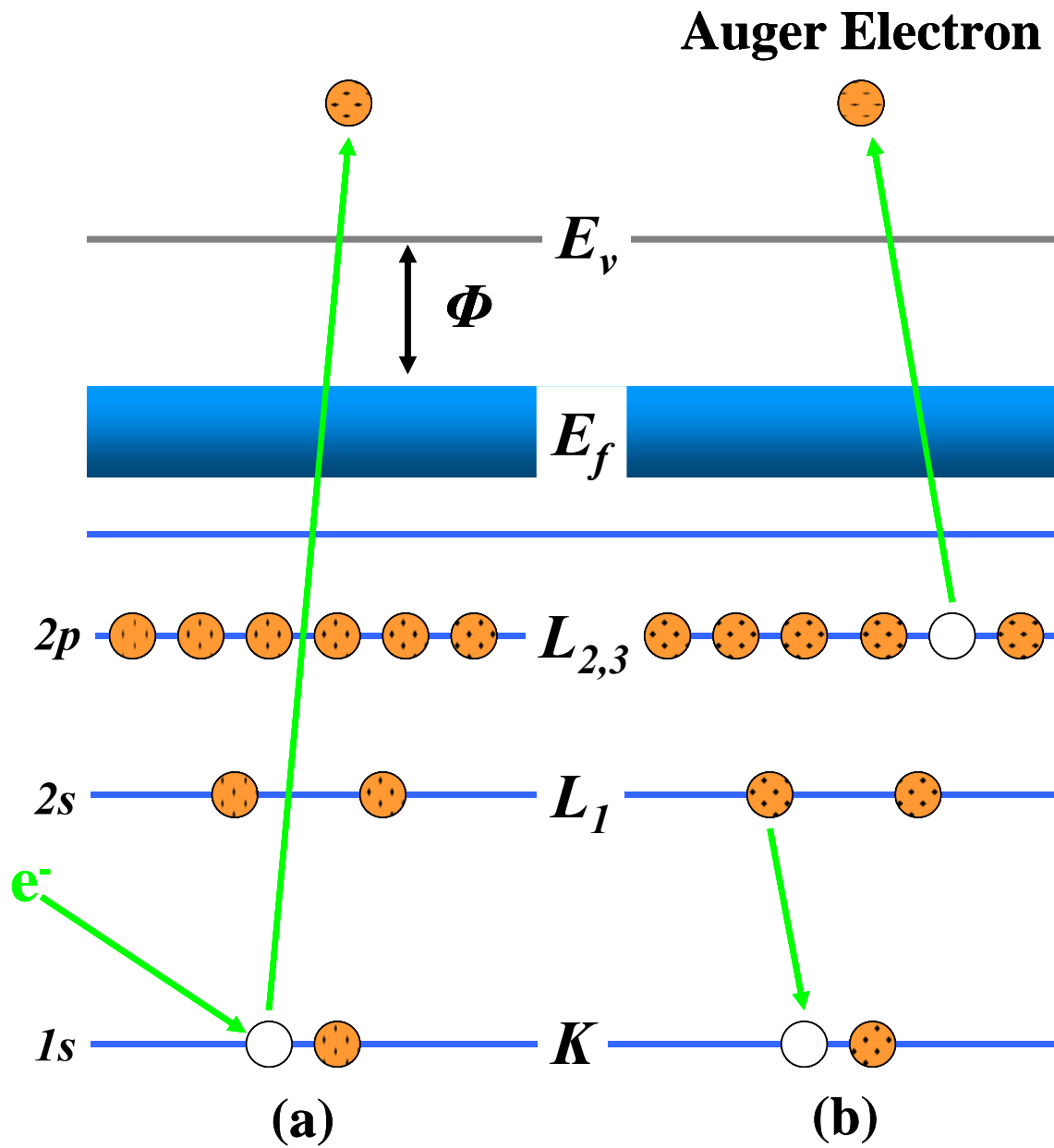


Figure 8. Schematic illustration of the Auger processes ( $KL_1L_{2,3}$ ). (a) Ionization of a core electron. (b) Excitation of an Auger electron.

growth studies to determine the surface coverage of specific elements by comparing the relative peak intensity of these elements to that of the substrate.

### **Experimental considerations**

In this section, we discuss the practical considerations in applying STM for *in-situ* or high resolution studies. We start with the performance and weakness of our current instruments and then proceed to address the challenges in *in-situ* and high resolution studies and methods to overcome these challenges.

The *in-situ* STM system is equipped with an RHK STM (VT-UHV300), which is very accessible for modification. The high resolution STM system is equipped with an Omicron STM (STM-1), which is probably one of the most stable commercial STM ever built. High resolution STM images can also be achieved on the RHK STM (Figure 9a), however, its stability remains to be improved, especially on its vibration isolation.

The vibration noises and electronic noises are two major noise sources in STM measurements, and are critical for the performance of STM. Vibration noises can affect the STM measurement in basically two ways: (1) changing the tip-sample separation, resulting in an exponential change in the tunneling current, and (2) causing capacitive coupling noises by inducing the vibration of BNC junction of the pre-amp and the motion of the wire between the tip and the pre-amp. In general, the main vibration source in a quiet lab room is the floor vibration, which is on the order of  $10^{-7}$  m. Meanwhile, in order to resolve the atomic surface corrugation, the fluctuation of tip-sample separation must be controlled to within a few pm. Therefore, an effective vibration isolation system for STM must have a vibration isolation factor of at least  $10^{-5}$ .

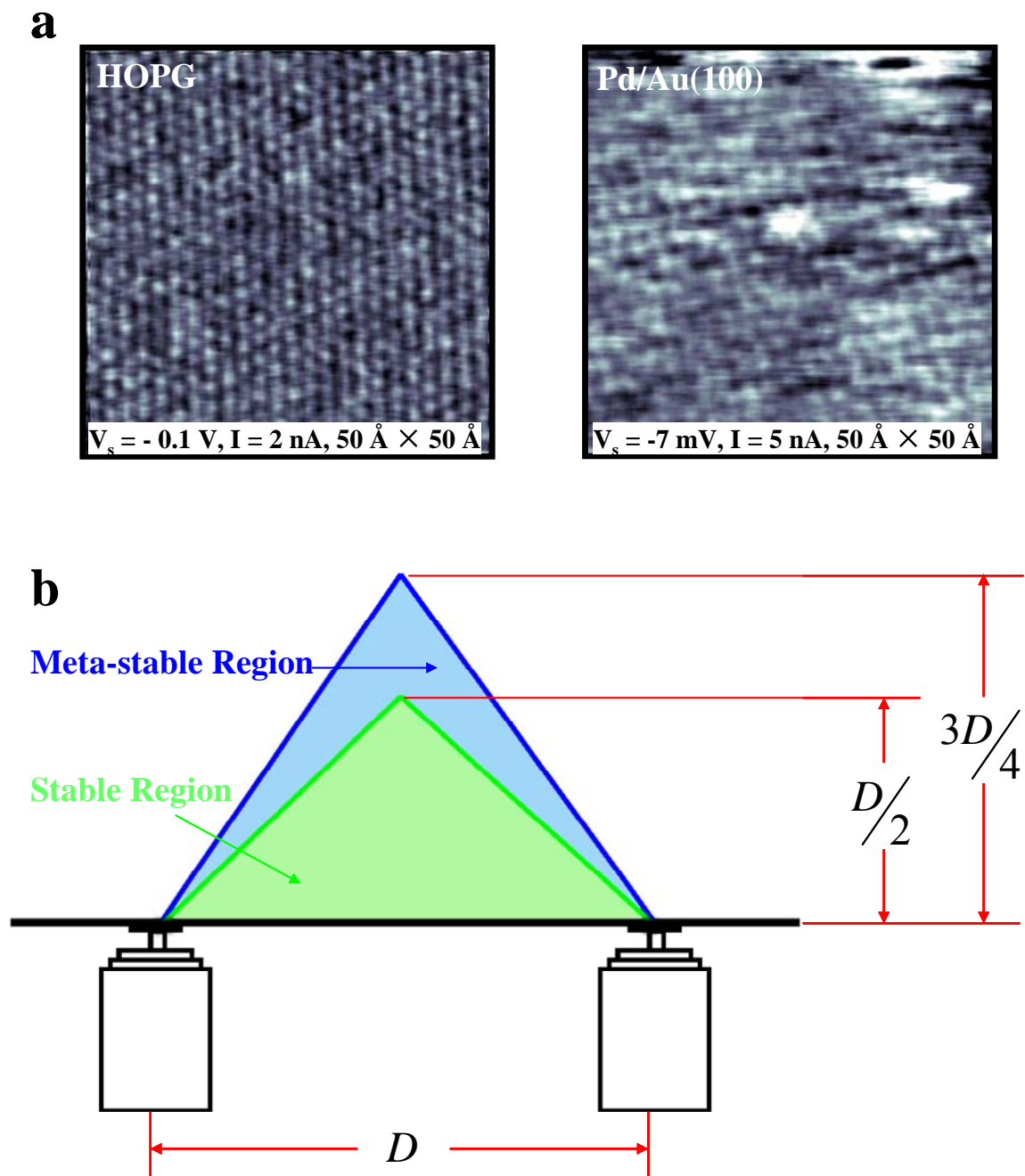


Figure 9. The performance and vibration isolation of the RHK VT-UHV300 STM. (a) Atomic resolution STM images obtained by RHK VT-UHV300 STM. (b) Rule of thumb in the vibration isolation using New Port I-2000 air legs.

The vibration isolation of STM is accomplished in two steps. The first step is the design of a rigid and compact tunneling unit, including both the scan head and the sample. The rigid and compact design results in a high resonant frequency of the tunneling unit. The second step is the application of external vibration stages with very low resonant frequencies, such as the pneumatic support and viton spacers for our RHK STM and the eddy current damping system for our Omicron STM. The overall transfer function for the vibration isolation is a multi-peak curve, where the best vibration isolation is at intermediate frequencies between the high resonant frequency of the tunneling unit and the low resonant frequency of external vibration isolation stages. The efficiency of vibration isolation depends solely on the resonant frequency ratio of external vibration isolation stages and the tunneling unit. Therefore, it is desirable to have a minimum resonant frequency for external vibration isolation stages while having a maximum resonant frequency for the tunneling unit.

For our RHK STM, due to the limited compression length of viton spacers, the resonant frequency of viton spacers is around 10-100 Hz. Thus the external vibration isolation relies mainly on the pneumatic support (New Port, I-2000 series), which can have resonant frequencies as low as 1 Hz in both horizontal and vertical directions. To reach its lowest resonant frequency, we tried to reduce the Young's modulus of those air springs by increasing their lengths. This adjustment has a drawback of longer response time, but can help decrease the amplitude of low frequency vibration noises. Further, low center of mass is most critical in the installation of pneumatic supports. A rule of thumb for the installation of pneumatic support is shown in Figure 9b. In our experimental setup, to reduce the center of mass, 500 pounds of lead bricks were added to the bottom of steel



frame, which can efficiently attenuate the low frequency vibration noises by near an order of magnitude.

Indeed, even with the above adjustments, the pneumatic supports (New Port, I-2000 series) can not sufficiently satisfy the vibration isolation requirements at low frequencies, considering its vibration isolation factor is only  $10^{-2}$  at  $\sim 10$  Hz. Other research groups have also made some successful adjustments on the external vibration isolation of the RHK STM chamber. For instance, the Salmeron group used a wooden frame to lower the resonant frequency [56]. The Polanyi group added a set of piezo legs to the bottom of pneumatic supports for active control, as the non-pneumatic part of pneumatic supports were cut off to prevent raising up the center of mass.

The design of the tunneling unit in our RHK STM also has some inherent weakness for vibration isolation. In spite of its excellent thermal stability, the Besocke type STM has a major disadvantage in its mechanical stability, which is at the coupling point between the scan head and the walking ramp of sample holder. Although the scan head itself has a high resonant frequency, the lowest resonant frequency of the tunneling unit is determined by the mechanical coupling between the scan head and the sample holder. Since the scan head is made small to ensure a high resonant frequency, the contact force between the scan head and the sample holder is very weak, resulting in a much lowered resonant frequency of the tunneling unit. Moreover, during sample preparation, extended  $\text{Ar}^+$  sputtering might increase surface roughness microscopically on the walking ramp of the sample holder, which further deteriorates the point contacts between the scan head and the sample holder. During experiments, we could often see large noise peaks at around a few hundred Hz. By moving the scan head around on top

of the sample holder, these noises peaks of a few hundred Hz could be removed, indicating the noise is due to bad contacts between the scan head and the sample holder. A better sample stage and sample holder design might help reduce this noise and improve the mechanical stability of the tunneling unit. It is better to fix the walking ramp on the sample stage and use a much smaller sample holder, which can be decoupled from the walking ramp for sample preparation and re-inserted for STM measurements. Doing so might also improve the RHK sample holder in thermal and electrical isolation and for sample preparation, which are compromised in order to pack the resistive heater, thermocouple, and sample all together in a small copper block.

The design of Omicron STM-1 system is free of the above mechanical problems. Also, the eddy current damping stage in Omicron STM-1 system is more effective for vibration isolation. By allowing enough spring extension, the resonant frequency of eddy current damping stage can be pushed well below 1 Hz. Meanwhile, the wire carrying tunneling currents is very short between the STM tip and the pre-amp. The short length reduces the capacitive coupling of the tunneling wire with its environment.

The electronic noise is usually not as large a problem as the vibration noise for commercial STM systems. Most common electronic noises seen in STM measurements are the 60 Hz noise and its harmonics, often caused by ground loops or bad shielding on the wire carrying tunneling currents. The most difficult part to remove or reduce this 60 Hz noise is usually to identify the noise source. In general, all STM electronics are required to be plugged into the same power line to ensure a common ground. To identify the source of the 60 Hz noise, power transformer, fluorescent lamps, ion pumps, and other nearby electrical equipments should be turned off one by one. The shielding of

tunneling current wire is also critical and has to be taken care of when the STM head is removed from the chamber. Most STMs measure the tunneling current from the tip and shield the tunneling current by holding the tip at ground, since it is more effective to shield the tip than a much larger sample.

Besides the 60 Hz noise, another major electronic noise concerned in the tunneling circuit is the Johnson noise due to fluctuations in voltage across a resistor. The magnitude of Johnson noise is flat as a function of frequency and can be calculated using the equation,  $\Delta V = \sqrt{4k_B TR \Delta f}$ , where  $R$  is the resistance and  $\Delta f$  is the band width frequency. The RHK preamplifier (IVP 300) has a typical gain setting at  $10^9$ , which means the resistance of feedback is  $1 \text{ G}\Omega$  and thus gives the Johnson noise at room temperature as  $0.13\sqrt{RnV} / \sqrt{Hz} = 4.11\mu V / \sqrt{Hz}$ . The bandwidth of RHK preamplifier (IVP 300) is 5 kHz, resulting in the rms noise of 0.29 mV, or a tunneling current noise of 0.29 pA. Considering the setpoint of the tunneling current is usually on the order of nA, the Johnson noise is not a problem for STM measurements. The concern of Johnson noise might rise when ultra-fast scan rate is desired, which requires a large bandwidth on the order of MHz [126]. Imperfections in the electronics might cause other types of electronic noises, such as  $1/f$  noise and interference noise. However, these have not been a concern in our experimental studies.

In addition to the instrumental performance, the STM tip is of primary importance for *in-situ* and high-resolution STM measurements. The importance of the STM tip is addressed in two aspects: 1) tip selection and 2) tip preparation and *in-situ* tip regeneration.

The selection of tip materials is of critical importance, especially for STM studies under high pressure and high temperature conditions. To ensure continuous DOS near the Fermi level, transition metals are usually selected to prepare STM tips. For general high resolution STM studies in UHV, W tips are most widely used due to its convenient fabrication and hardness, which maintain the tip structure highly resistant against accidental tip crashes. For spectroscopic studies at low temperature, the Ho group often uses Ag tips, which are not an option at room temperature due to their poor chemical and thermal stability. In the presence of reactant gases, especially under high pressure and high temperature conditions, the chemical and thermal stability of STM tip becomes the ultimate limit for reaction studies and thus the major concern in tip selection. W tips are very stable in CO, but perform poorly in the presence of O<sub>2</sub> or mixtures of CO and O<sub>2</sub>. Pt or Pt alloy tips are stable in O<sub>2</sub>, but suffer in CO, especially when the sample surface temperature is at above 550 K. The noblest metal, Au, is stable in both CO and O<sub>2</sub>, but unstable at high temperatures, especially in the presence of water. Indeed, H<sub>2</sub>O or the humidity of high pressure reactant gases is found in our practice to cause not only the instability of Au tip, but also the electrical breakdown during the introduction of reactant gases to the STM chamber [127]. Purification of all reactant gases using liquid N<sub>2</sub> can greatly improve the operating pressure range for our high pressure reaction studies and prevent the electrical breakdown when backfilling the STM chamber.

Methods for the preparation of STM tips have been studied extensively, with a goal to prepare an atomically sharp tip [128-139]. The actual method adopted for tip preparation varies with different STM groups. Some groups simply cut the tip and directly put the cut tip into the vacuum. Other groups prefer the electrochemically etched

tip and apply a series of cleaning procedures before putting the tip into the vacuum. Due to the mysterious geometry of STM tips, either freshly prepared or transferred into the vacuum, it is difficult to define a superior method for tip preparation. In our practice, we found the etched tip is usually much better than the cut tip for STM imaging, especially on curved surfaces, e.g., surfaces with supported clusters. We also attempted a combination of methods in order to improve the performance and stability of etched tips. We found the two-step etching process [128, 129] can improve the tip quality in general. A more precise etching control using function generator or sputtering the tip using  $\text{Ar}^+$  did not show apparent improvement in tip quality through our STM studies. Indeed, *in-situ* tip regeneration or cleaning is also critical for our STM studies, especially in the presence of high pressure reactant gases. *In-situ* tip regeneration refers to the method of applying a large voltage pulse (from 3 volts to hundreds of volts) between tip and sample while the tip is in tunneling range. This method induces field emission, which cleans and regenerates the STM tip. *In-situ* tip regeneration has been essential to the success of high pressure STM studies because the STM tip is susceptible to pick up some poorly conducting layers during extended measurements at elevated pressures. In our study, *in-situ* voltage pulsing of a few volts has helped to expand the pressure ranges of *in-situ* kinetic studies to a few Torr. Wintterlin and coworkers [66] recently reported a high pressure STM study, in which they used W tips to study ethylene oxidation on Ag (111) and the tip could be recovered by applying high voltages to the tip (e.g. +300 V). This high-voltages-pulse method might help to further expand the pressure range of *in-situ* studies and can be adapted to our *in-situ* STM system by switching the RHK pre-amp

with a pre-amp with low gain. After the *in-situ* tip regeneration, the pre-amp with low gain can be switched back to the RHK pre-amp for STM measurements.

Another major challenge for *in-situ* STM studies is the loss of pre-selected surface area, often caused by tunnel junction instabilities and sample drifts. To overcome this challenge and find the lost surface area, it is important to develop experimental approaches that pattern the surface without influencing the kinetics and dynamics of studies surface areas. A “shadowing” technique (Figure 10a) has been developed, in which metal is dosed when the STM tip is already in the tunneling position. Metal flux from a collimated doser thus creates a shadow of the tip on the substrate [108, 127]. For an oxide surface supported with metal clusters, tip manipulation might be another method of choice (Figure 10b), which is to remove clusters from a specific area through aggressive scanning. Using the STM tip to pattern the surface, we imaged the pre-selected individual clusters at elevated temperatures while changing the gas pressure over twelve orders of magnitude.

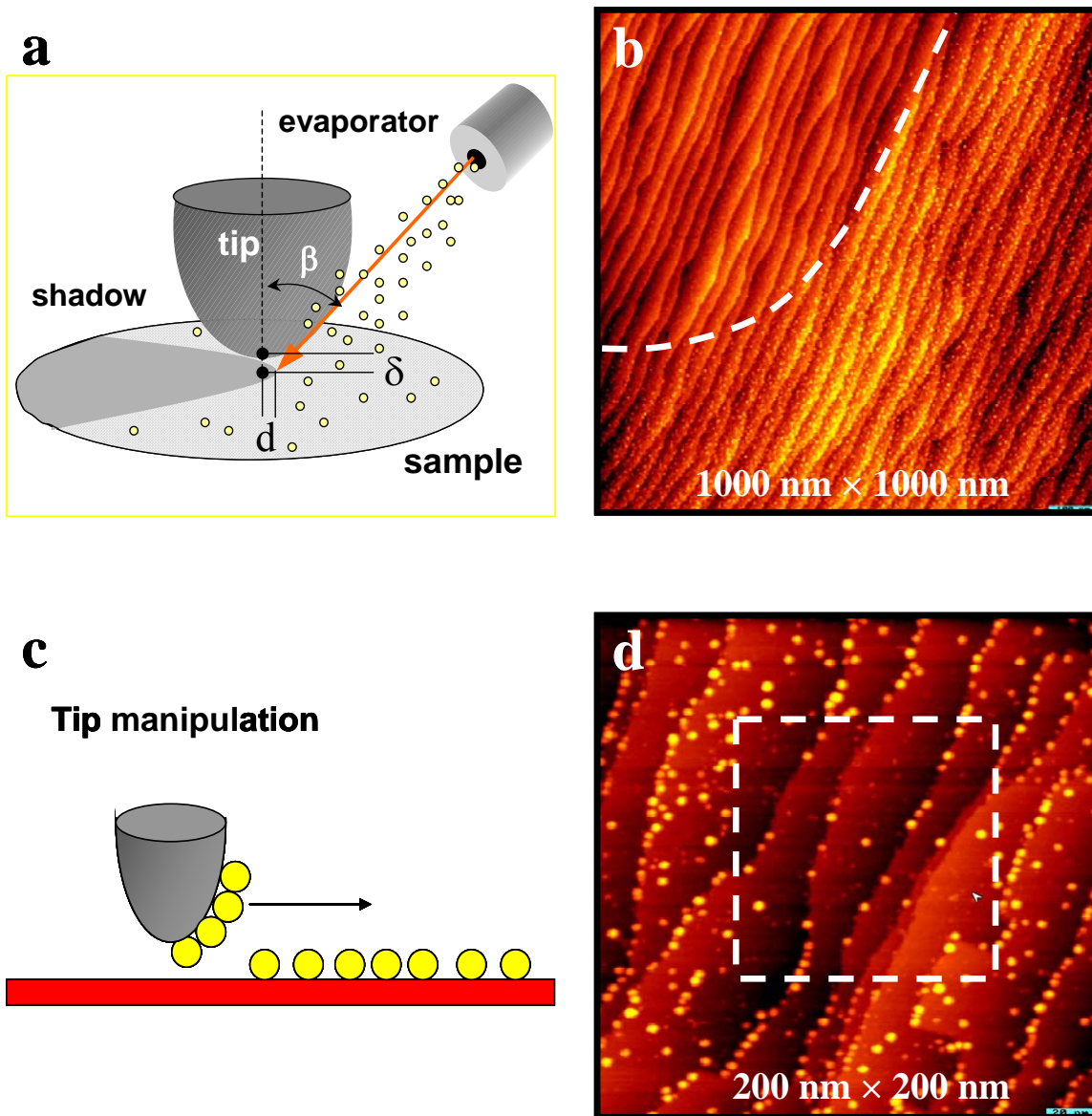


Figure 10. Methods of patterning the surface for *in-situ* STM studies. (a) Schematic of "shadow" technique. (b) STM image of the surface created by "shadow" technique. The shadow area uncovered by metal clusters is distinguished from the area covered with metal clusters by the white dash line. (c) Schematic of the tip manipulation. (d) STM image of the surface created by tip manipulation. The dash rectangle in (d) shows the area where most clusters are picked up by the STM tip. This area with lower cluster densities can be distinguished from the rest of the surface and serve as a nano-marker for *in-situ* STM studies.

### CHAPTER III

#### THE STRUCTURE AND STABILITY OF SUPPORTED GOLD CATALYSTS IN UHV

In this chapter, we study the nucleation and stabilization of supported Au clusters in UHV. In particular, we have focused on the growth and thermal stabilities of Au clusters supported on  $\text{TiO}_2(110)$ . The growth and thermal stabilities of Au clusters are compared on  $\text{TiO}_2(110)$  surfaces with different pre-treatments in order to reveal the strongest Au binding sites on  $\text{TiO}_2(110)$ . The morphology of size selected Au clusters is also examined on a HOPG surface to compare with Au clusters supported on  $\text{TiO}_2(110)$ .

#### Surface structures of $\text{TiO}_2(110)$

Structures of the  $\text{TiO}_2(110)$  surface depend strongly on the preparation procedure. The annealing temperature, sputtering intensity and preceding sample history all play a role in the surface morphology of  $\text{TiO}_2(110)$  [138, 139]. In general, cycles of  $\text{Ar}^+$  sputtering and subsequent annealing at temperatures above 900 K produce a smooth surface of  $\text{TiO}_2(110)$  with large surface terraces (Figure 11). Terraces of the prepared surface are several 10 nm in width separated by monatomic steps. The surface structure of  $\text{TiO}_2(110)$  depends heavily on the annealing temperature. In our preparation, the surface is usually annealed between 900 and 1100 K, which produces the  $(1 \times 1)$  phase of  $\text{TiO}_2(110)$ . Inset of Figure 11 shows  $(1 \times 1)$  LEED pattern of the  $\text{TiO}_2(110)$  surface.

Figure 11b shows an empty state STM image of the  $\text{TiO}_2(110)$  surface with  $(1 \times 1)$  phase. The image was obtained at sample bias of +1.2 V and tunneling current set of 1



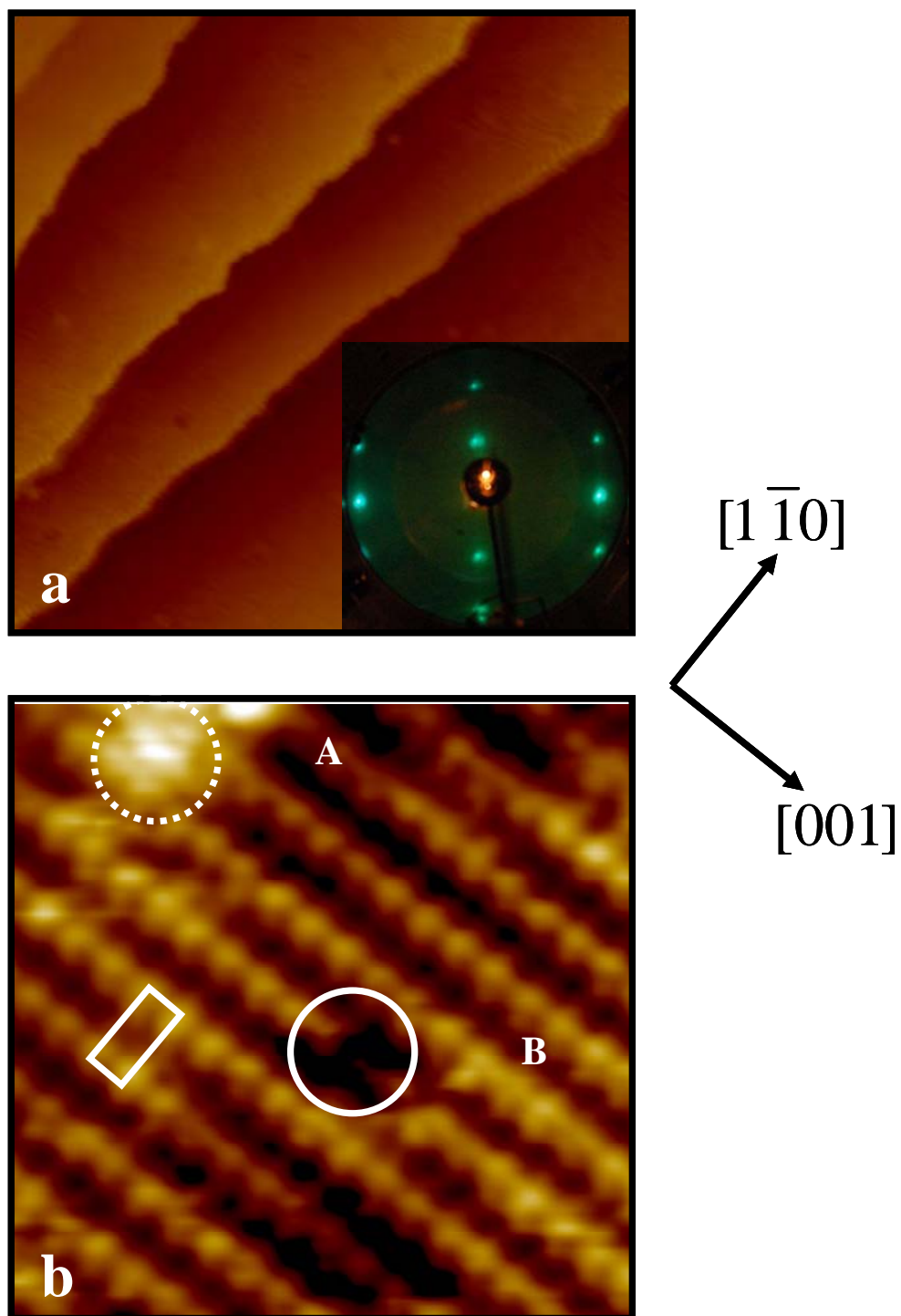


Figure 11. STM images of the  $\text{TiO}_2(110)$  surface. (a)  $100 \text{ nm} \times 100 \text{ nm}$ ,  $V_s = 2 \text{ V}$ ,  $I = 0.1 \text{ nA}$ . Inset is the LEED image of  $\text{TiO}_2(110)$  surface. (b)  $5 \text{ nm} \times 5 \text{ nm}$ ,  $V_s = 1.2 \text{ V}$ ,  $I = 1 \text{ nA}$ .

nA. In the image, both bright and dark rows run along the [001] direction. The distance between the bright rows is  $\sim 6.5 \text{ \AA}$  while the distance between bright protrusions along the bright row is measured to be  $3.0 \text{ \AA}$ . The distances match the lengths of  $(1 \times 1)$  unit cell, shown as a white rectangle in Figure 11b. Assignment of these bright and dark rows has been subjected to debate in the past decade. The debate was settled after the publication of STM studies on the adsorption sites of the  $\text{TiO}_2(110)$  surface [142-145], as well as DFT calculations on the electronic structure of  $\text{TiO}_2(110)$  [145, 146]. It is generally agreed now that the bright rows correspond to lines of fivefold coordinated Ti ions and the dark row corresponds to lines of bridging oxygen atoms.

Two types of point defects were also seen in the STM image, labeled as A and B in Figure 11b. Type “A” defect, the bright spot centered on the dark row (labeled A), was usually assigned as oxygen vacancies or H adatoms in STM experiments [147-150]. The appearance of H adatoms was due to the dissociation of background water at bridging oxygen vacancies. Using water as a probe molecule, these STM experiments showed H adatoms appear larger and brighter than the oxygen vacancies. The height of type “A” defect was measured to be  $1.5 \text{ \AA}$ , same as the apparent height of H adatoms measured by Wendt et al. [148, 149]. Thus, Type “A” defect in Figure 11 was H adatoms formed by the dissociation of background water. Type “B” defect, the dark spot on the bright rows (labeled B), was also observed in previous STM experiments [93, 146], and assigned as subsurface oxygen vacancy.

High resolution images of  $\text{TiO}_2(110)$  were obtained when the sample bias was lowered to below +1 V (Figure 12). Two features, dark and bright protrusions, were observed in each surface unit cell (Figure 12a). Comparing the position of these two

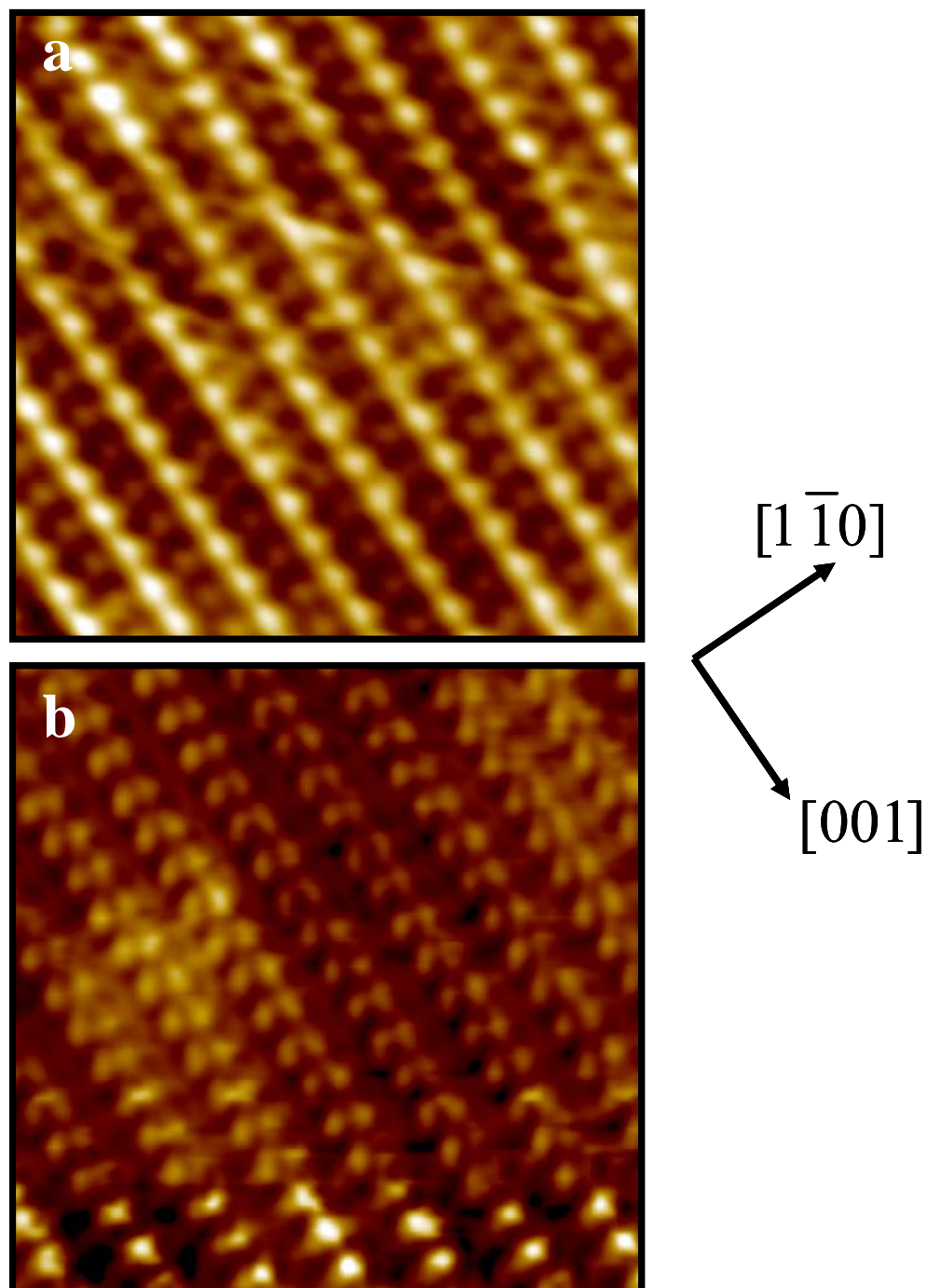


Figure 12. High resolution STM images of the  $\text{TiO}_2(110)$  surface. Both images have the same dimensions of  $5 \text{ nm} \times 5 \text{ nm}$  and same tunneling parameters of  $V_s = 0.8 \text{ V}$  and  $I = 4 \text{ nA}$ .

features with the structural model of the  $\text{TiO}_2(110)$  surface, we could assign the bright protrusion as the fivefold coordinated Ti ions and the dark protrusion as the bridging oxygen atoms. Although the empty state image of  $\text{TiO}_2(110)$  is in principal due to the electronic contrast from Ti atoms, theoretical studies [145, 151] predicted bridging O atoms could also be resolved due to the additional topographic contrast ( $\sim 1 \text{ \AA}$  above the surface), when the tip-sample separation was reduced. An early STM study by Xu et al. [152] showed a STM image with both Ti and oxygen atoms resolved. However, the similar apparent height of Ti and O, image noises due to the instability of tunneling junctions, and the tunneling parameters they used, create speculation that the enhanced resolution could be caused by a double tip [153]. The dark protrusions resolved in our study, shown in Figure 12a, were centered between the bright rows and parallel with neighboring fivefold Ti atoms. Positions of the dark and bright protrusions were in good agreement with the structural model of  $\text{TiO}_2(110)$ .

During STM scanning, the STM tip can often change when it adsorbs a molecule at the front end of tip, inducing an extended tip state that overlaps with the sample state and thus enhancing the resolution of STM images [154]. Figure 12b shows a STM image that resolved the unoccupied states of  $\text{TiO}_2(110)$ . A tip change occurred in the middle of scanning and caused an enhanced resolution. The bright protrusions of Ti atoms splitted into two lobes after the tip change. This enhanced resolution was stable with continuous scanning. The pattern of resolved Ti atoms could hardly be explained by tip artifacts and could be reproduced on different surface areas. Comparing Figure 12b with the electronic structure of  $\text{TiO}_2(110)$  calculated by Munnix et al. [155], we found Figure 12b might

have revealed the shape of  $t_{2g}$  symmetry orbitals which sit close to the conductance band minimum (CBM).

Theoretical studies by Munnix et al. [155] showed that the unoccupied states of  $\text{TiO}_2(110)$  surface are mostly formed by Ti 3d orbitals whereas the occupied states of  $\text{TiO}_2(110)$  are derived mostly from O 2p orbitals. The hybridization of O 2p and Ti 3d orbitals causes the crystal-field splitting of the Ti 3d orbitals into two different symmetries,  $t_{2g}$  and  $e_g$ . Unoccupied states, which are  $\sim 1-2$  eV above the Fermi level, mainly consist of  $t_{2g}$  symmetry orbitals and are probed by the tunneling condition used in Figure 12b. The  $t_{2g}$  symmetry orbitals are formed by  $\pi$  type bonding between the  $d_{xy}$ ,  $d_{xz}$  and  $d_{yz}$  orbitals of Ti and the p orbitals of O. The direction of  $d_{xy}$ ,  $d_{xz}$  and  $d_{yz}$  orbitals is normal to the O ligand in agreement with our STM observation. Unoccupied states derived from  $e_g$  symmetry orbitals are  $\sim 3-4$  eV above the Fermi level, which are not probed in Figure 12b. Local electronic structure of  $t_{2g}$  symmetry orbitals on  $\text{TiO}_2(110)$  remains unclear. Further DFT calculation should help to verify the structure observed in Figure 12b.

### **$\text{TiO}_x$ species on $\text{TiO}_2(110)$**

Before we proceed to the growth of Au clusters on  $\text{TiO}_2(110)$ , the formation of  $\text{TiO}_x$  species are discussed here which is critical for the growth and stabilization of Au clusters on  $\text{TiO}_2(110)$ . The formation of  $\text{TiO}_x$  species have been observed extensively during the re-oxidation of  $\text{TiO}_2(110)$  at elevated temperatures in  $\text{O}_2$  [156-158].  $\text{TiO}_x$  refers to surface features on  $\text{TiO}_2$  that have undercoordinated Ti cations, i.e., the molar ratio of  $\text{Ti}:\text{O} < 2$ . STM studies from various research groups [156-158] have shown  $\text{TiO}_x$

species were formed by Ti interstitials diffusing to the surface and being surrounded by ambient oxygen at elevated temperatures. These  $\text{TiO}_x$  species would further transform into the row structure during oxidation and serve as nucleation sites for the re-growth of surfaces. A precursor in the formation of  $\text{TiO}_x$  species is Ti interstitials caused by the reduction of  $\text{TiO}_2$  in vacuum. Vacuum annealing of  $\text{TiO}_2(110)$  removes oxygen from the surface lattice and causes the reduction of  $\text{TiO}_2$  [93]. Meanwhile, to minimize surface free energy, excess Ti cations would diffuse into the bulk at high temperatures and stay as Ti interstitials while the stoichiometry of  $\text{TiO}_2$  surface was restored [159]. We found these Ti interstitials were not stable and would diffuse back to the surface, forming  $\text{TiO}_x$  species even in vacuum.

Figure 13a shows the morphology of a  $\text{TiO}_2(110)$  surface after being annealed at 600 K for 10 minutes in UHV. Bright spots showed up with a very homogeneous size of 1-2 nm and oriented along the [001] direction. These spots were well distributed over the terrace and covered 40% of whole surface. AES showed no contamination on this surface. The bright spots are thus assigned as  $\text{TiO}_x$  species, formed via the diffusion and adhesion of Ti interstitials to surface oxygen. Compared with the formation of  $\text{TiO}_x$  species in  $\text{O}_2$  at 600 K, only a small amount of  $\text{TiO}_x$  species were formed at the diffusion equilibrium due to the lack of ambient oxygen.

These  $\text{TiO}_x$  species would transform into  $\text{TiO}_x$  strands at higher temperatures. Figure 13b shows the morphology of the  $\text{TiO}_2(110)$  surface after being annealed at 750 K for 5 minutes. Bright strands running along the [001] direction formed on the surface, as well as some bright spots. The concentration of bright spots is less than that in Figure 13a. These bright strands are assigned as  $\text{TiO}_x$  strands formed by  $\text{TiO}_x$  species coalescing

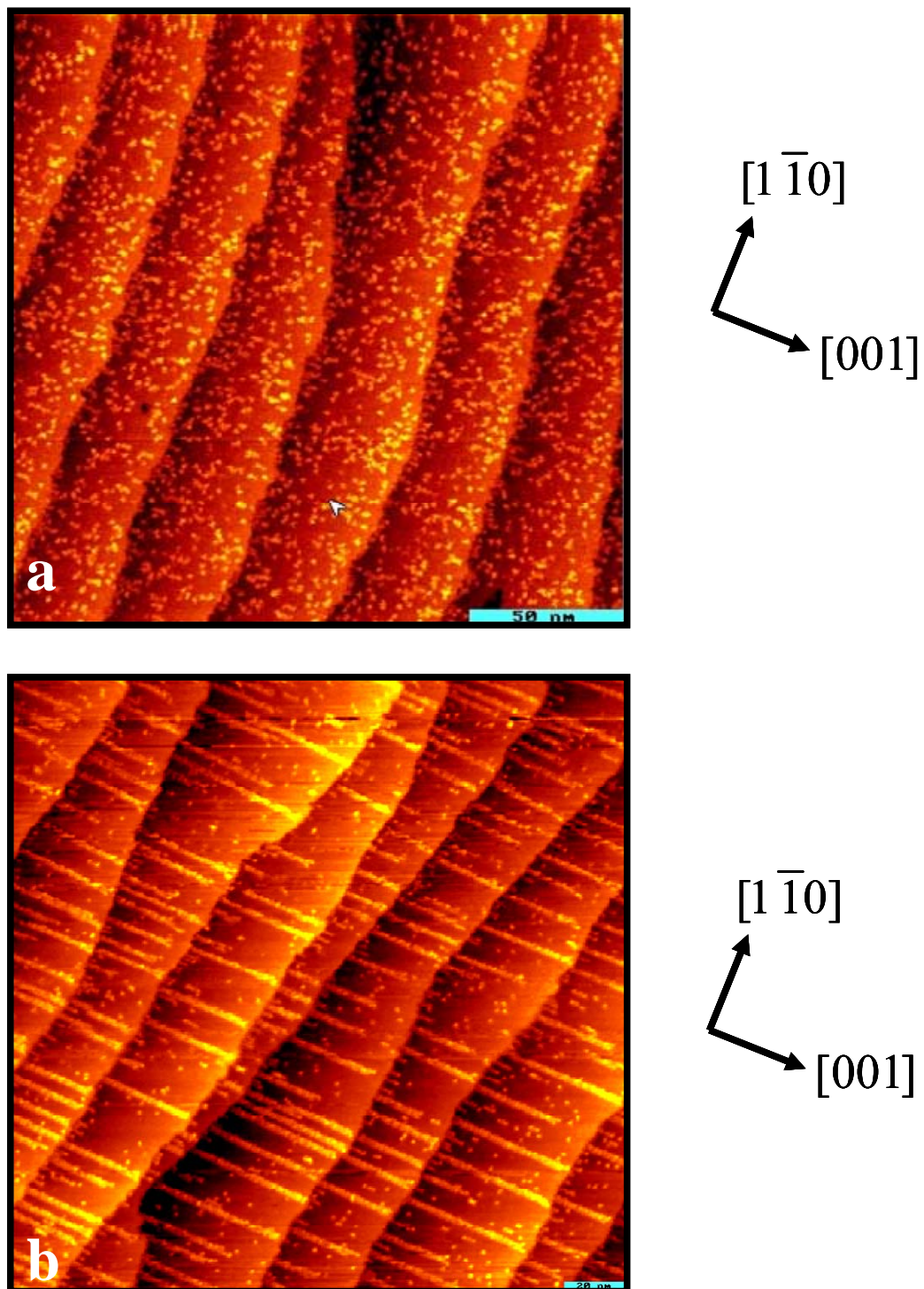


Figure 13. STM images of  $\text{TiO}_x$  on the  $\text{TiO}_2(110)$  surface after annealing in UHV. Both images have the same dimensions of  $200 \text{ nm} \times 200 \text{ nm}$  and tunneling parameters of  $V_s = 2 \text{ V}$  and  $I = 0.1 \text{ nA}$ . (a) A  $\text{TiO}_2(110)$  surface annealed at 600 K for 10 min. (b) A  $\text{TiO}_2(110)$  surface annealed at 750 K for 5 min.

along the [001] direction, which have also been observed in previous STM studies [93, 140, 152] when  $\text{TiO}_2(110)$  was annealed in vacuum between 700-800 K.

The formation of  $\text{TiO}_x$  species in vacuum was supported by the study by Henderson using static secondary ion mass spectrometry (SSIMS) [159]. His results, on the diffusion species of  $\text{TiO}_2(110)$  during vacuum annealing, show, 1) between 400-700 K, both oxygen anions and interstitial Ti cations diffuse to the surface; and 2) above 700 K, as oxygen leaving the surface, Ti cations diffuse back to the bulk from the surface. Bright spots on  $\text{TiO}_2(110)$  formed during vacuum annealing were also observed in recent STM studies by Park et al. [160, 161]. Combining DFT calculations, they suggested these bright spots were  $\text{TiO}_x$  species, which serves as the building block for the re-growth of  $\text{TiO}_2(110)$  surface.

Indeed, in the presence of oxygen, the formation of  $\text{TiO}_x$  species is much accelerated and starts as low as room temperature. Figure 14 shows the formation and growth of  $\text{TiO}_x$  species when the  $\text{TiO}_2(110)$  surface was exposed to  $1 \times 10^{-8}$  Torr  $\text{O}_2$  at room temperature. Figure 14b was obtained in the presence of  $\text{O}_2$  at room temperature. After  $\text{O}_2$  exposure, small bright spots appeared on the bright rows, as was observed in previous STM studies of oxygen adsorption on  $\text{TiO}_2(110)$  [148, 162]. These atomic spots were explained as the adsorption of oxygen atoms on top of the fivefold Ti cations. In Figure 14b, protrusions larger than the single atomic spots were also observed to grow along the [001] direction. These protrusions were due to the formation of  $\text{TiO}_x$  species. In the presence of  $\text{O}_2$ , Ti interstitials were drawn out from the bulk and to react with  $\text{O}_2$  on the surface, leading to the formation of  $\text{TiO}_x$  species. Larger  $\text{TiO}_x$  clusters were formed when these  $\text{TiO}_x$  species aggregated and grew along the [001] direction. The appearance



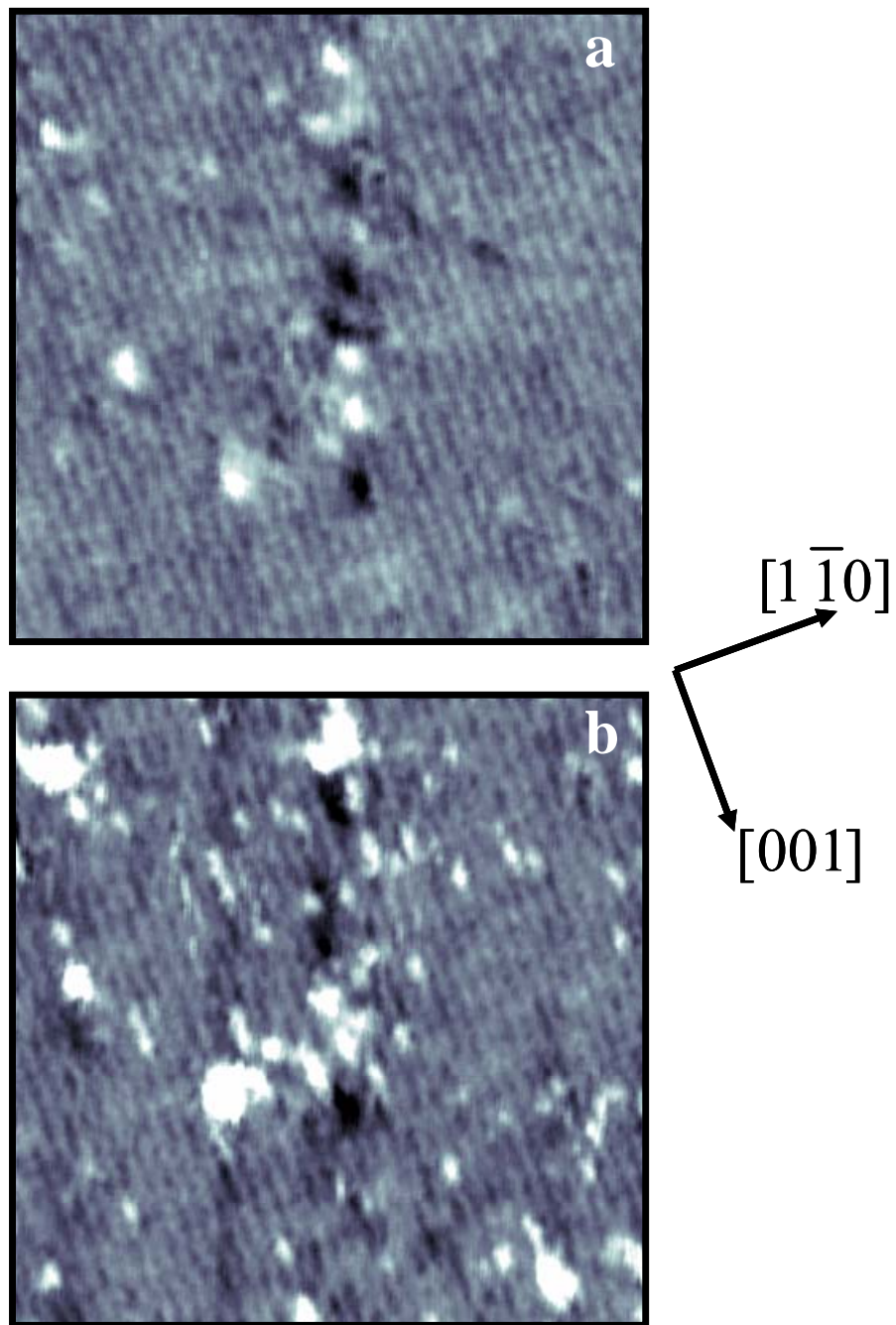


Figure 14. STM images of  $\text{TiO}_x$  on the  $\text{TiO}_2(110)$  surface induced by  $\text{O}_2$  exposure at room temperature. Both images are on the same area and have dimensions of  $20 \text{ nm} \times 20 \text{ nm}$ . Tunneling parameters are  $V_s = 1.2 \text{ V}$  and  $I = 0.3 \text{ nA}$ . (a) A clean  $\text{TiO}_2(110)$  surface. The bright protrusions are  $\text{TiO}_x$  species remained on the surface after 900 K annealing. (b) The  $\text{TiO}_2(110)$  surface in (a) exposed to 2 L  $\text{O}_2$  at  $1 \times 10^{-8}$  Torr.

of these  $\text{TiO}_x$  species after  $\text{O}_2$  exposure was also observed in the recent STM experiments by Park et al. [160]. They found  $\text{TiO}_x$  species preferentially agglomerated on surface defect sites including step edges.

### **Growth of Au clusters on $\text{TiO}_2(110)$**

An early STM study [95] by Lai et al. has demonstrated the overall growth mode of Au clusters on the  $\text{TiO}_2(110)$  surface. Contrasting their focus on the overall growth behavior, this article describes an *in-situ* STM study which follow the growth of identical sets of Au clusters, and analyze the growth of Au clusters on a cluster-by-cluster basis.

In this study, a series of STM images as a function of increasing Au coverage (Figure 15) were obtained on the same area of a  $\text{TiO}_2(110)$  surface at room temperature. The  $\text{TiO}_2(110)$  surface has a relatively larger terraces with step edges running perpendicular to the [001] direction. At the very early stages of growth, Au clusters preferentially decorate the step edges (Figure 15a). With an increase in Au coverage, the prevailing role of the step edges as major nucleation sites decreases, whereas new clusters begin to nucleate on terraces.

A quantitative analysis of the cluster distribution is shown in histogram form in Figure 16. It is very clear from these histograms that even at lower coverages, Au clusters have a wide range of size distributions (1 – 5 nm). With increasing Au coverage, the number of Au clusters with larger diameters increases leading to an increase in the average size distribution. However, from these histograms and the STM images of Figure 15, a bimodal size distribution is apparent for the growth of clusters at step edges and terraces.

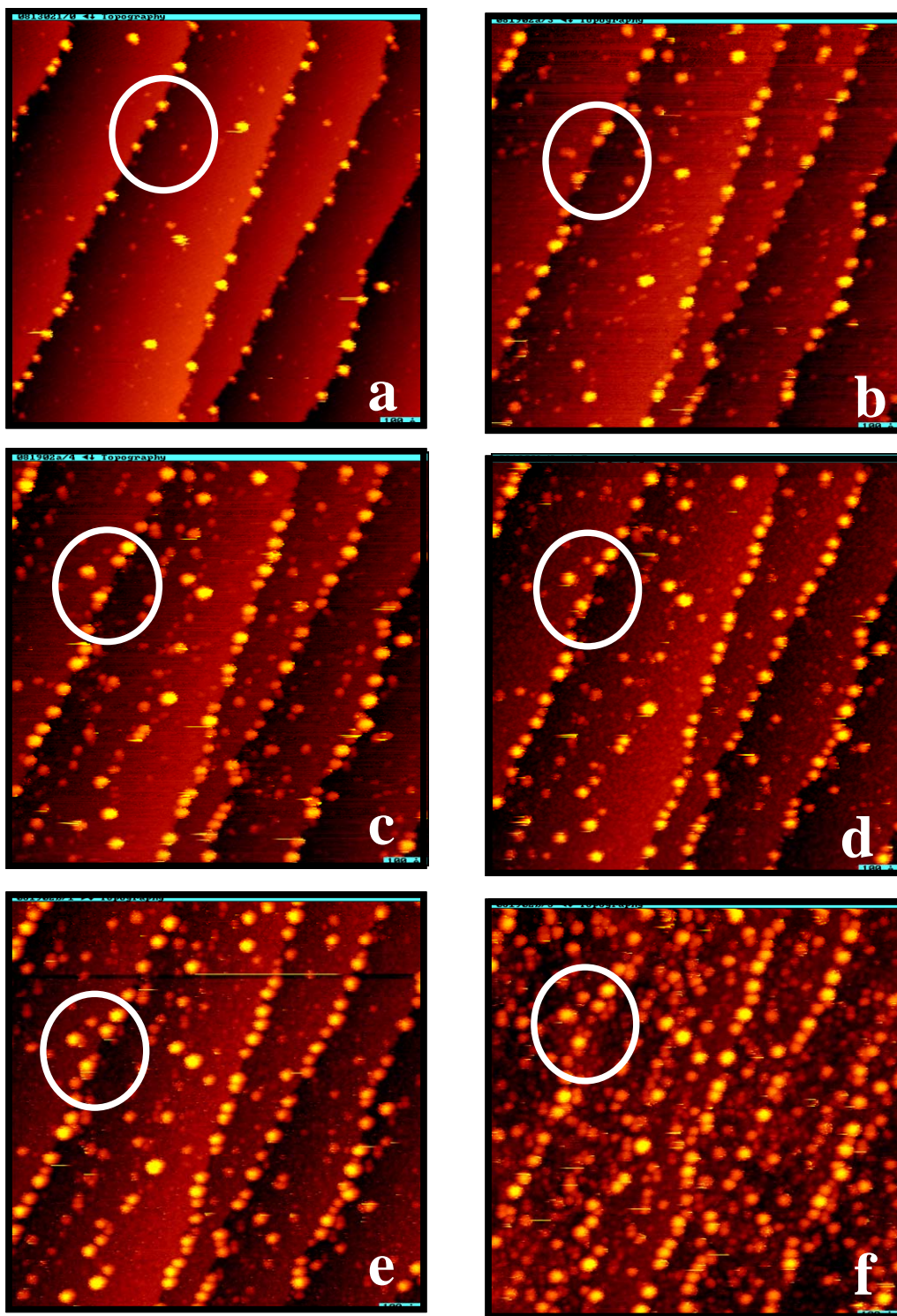


Figure 15. STM images of the same area of a TiO<sub>2</sub>(110) surface after the deposition of (a) 0.17 ML Au; (b) 0.34 ML Au; (c) 0.51 ML Au; (d) 0.69 ML Au; (e) 0.86 ML Au; and (f) 1.3 ML Au. All images have the same dimensions of 100 nm × 100 nm. The circle highlighted in white in each image indicates the identical area.

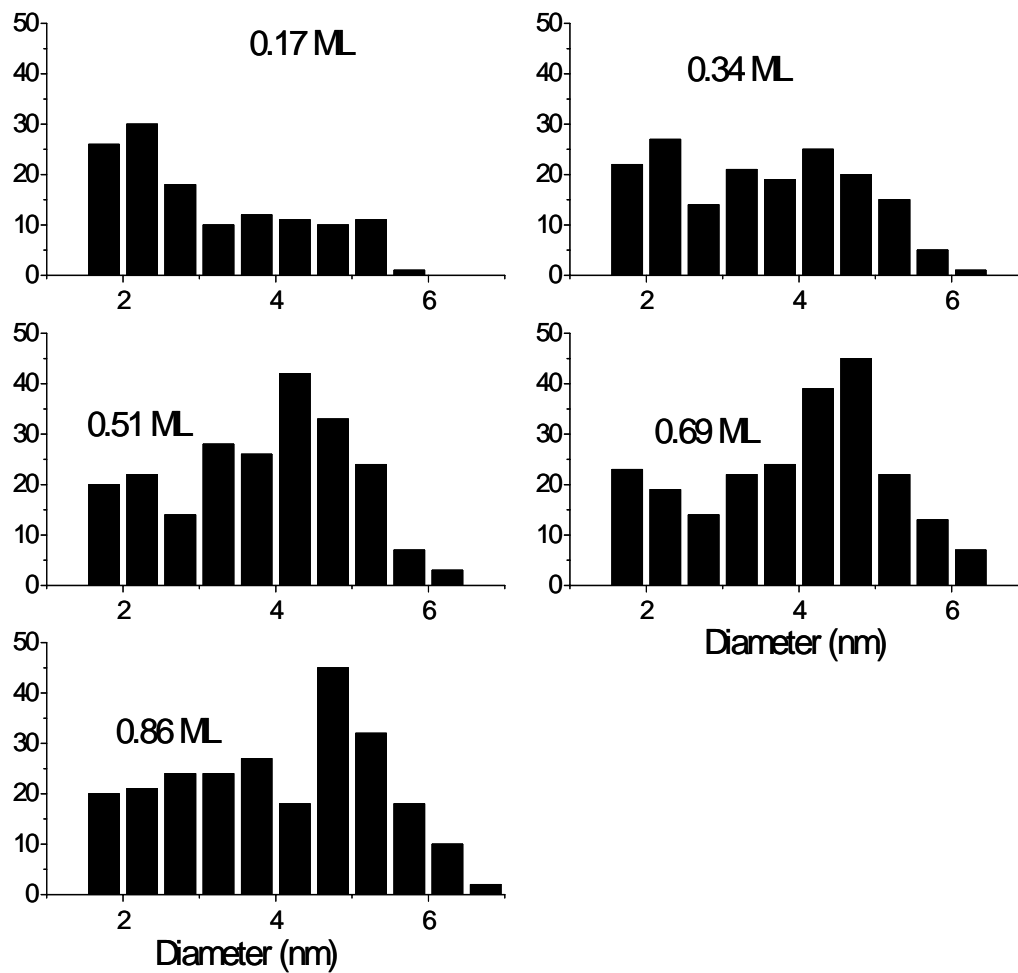


Figure 16. Histograms of the number of clusters as a function of diameter for the various Au coverage shown in Figure 15.

*In-situ* studies allow the growth mode to be followed on a cluster-to-cluster basis, the behavior of clusters grown at step edges can be isolated from those grown at terraces. Figure 17a shows how the cluster number density changes as a function of Au coverage. As was observed in Figure 17, the number density at the step-edges rapidly reaches saturation compared to the number density at the terraces. The average diameter (Figure 17b) at the step edges quickly reaches the maximum, as compared to the terraces, confirming the preferential growth of clusters at step-edges. These data also show that the metal atom diffusion length at room temperature is sufficient for preferential nucleation at relatively strongly bound sites. The average cluster height (Figure 17c) increases at a much faster rate at the step edges compared to terraces indicating that the overall volume of the clusters increases more rapidly at the step-edges.

The overall nucleation and growth kinetics acquired from this set of data are shown in Figure 18. The average of the cluster diameter grows quickly at the onset of deposition and reaches approximately 80% of its saturation at an Au coverage of 0.2 ML. The cluster height, on the other hand, has a positive slope even at an Au coverage of 0.7 ML. The cluster density increases relatively slowly after reaching a density of  $N \sim 2.2 \times 10^{12} \text{ cm}^{-2}$  at 0.5 ML.

The above growth study of Au on  $\text{TiO}_2(110)$  has demonstrated that step edges play a dominant role in the growth of Au clusters on  $\text{TiO}_2(110)$  at room temperature. Now the question comes to where, or which sites, Au binds at the step edge.

Based on the surface structure of  $\text{TiO}_2(110)$ , terraces on a  $\text{TiO}_2(110)$  surface could terminate with a mixture of both Ti and O atoms at the step, except when the step run parallel to the [001] direction. STM study by Diebold et al. [146] categorize the

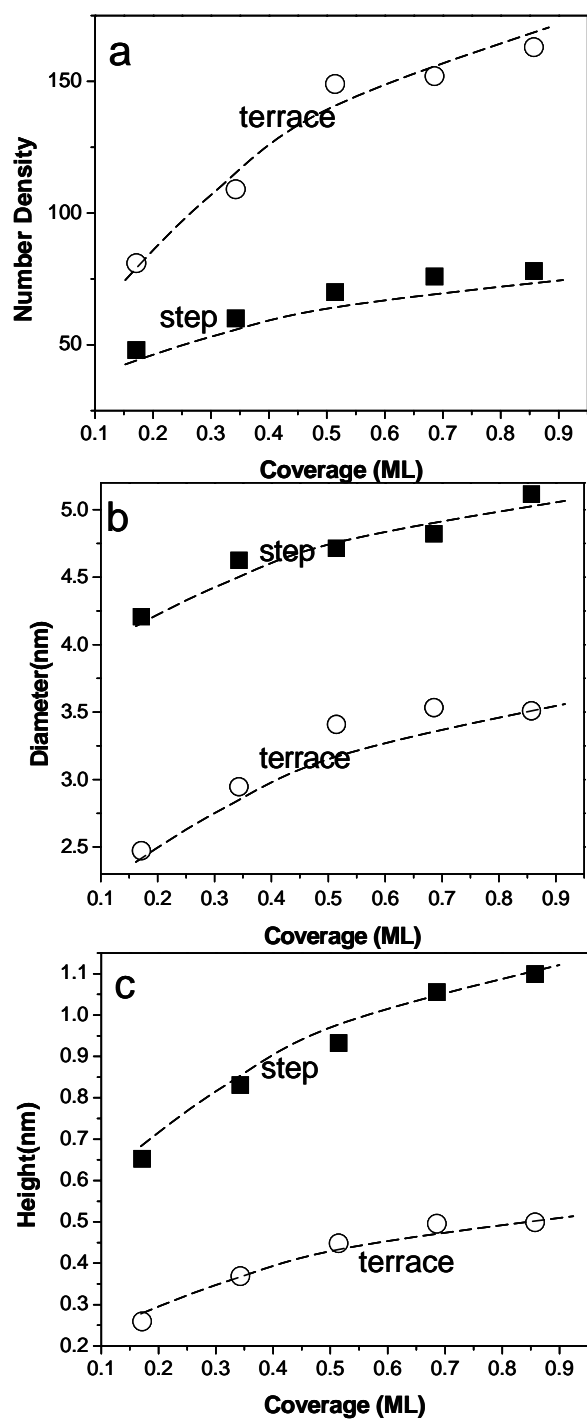


Figure 17. Cluster (a) number density, (b) diameter, and (c) height as a function of Au coverage taking into account the separate contributions of step-edges and terraces.

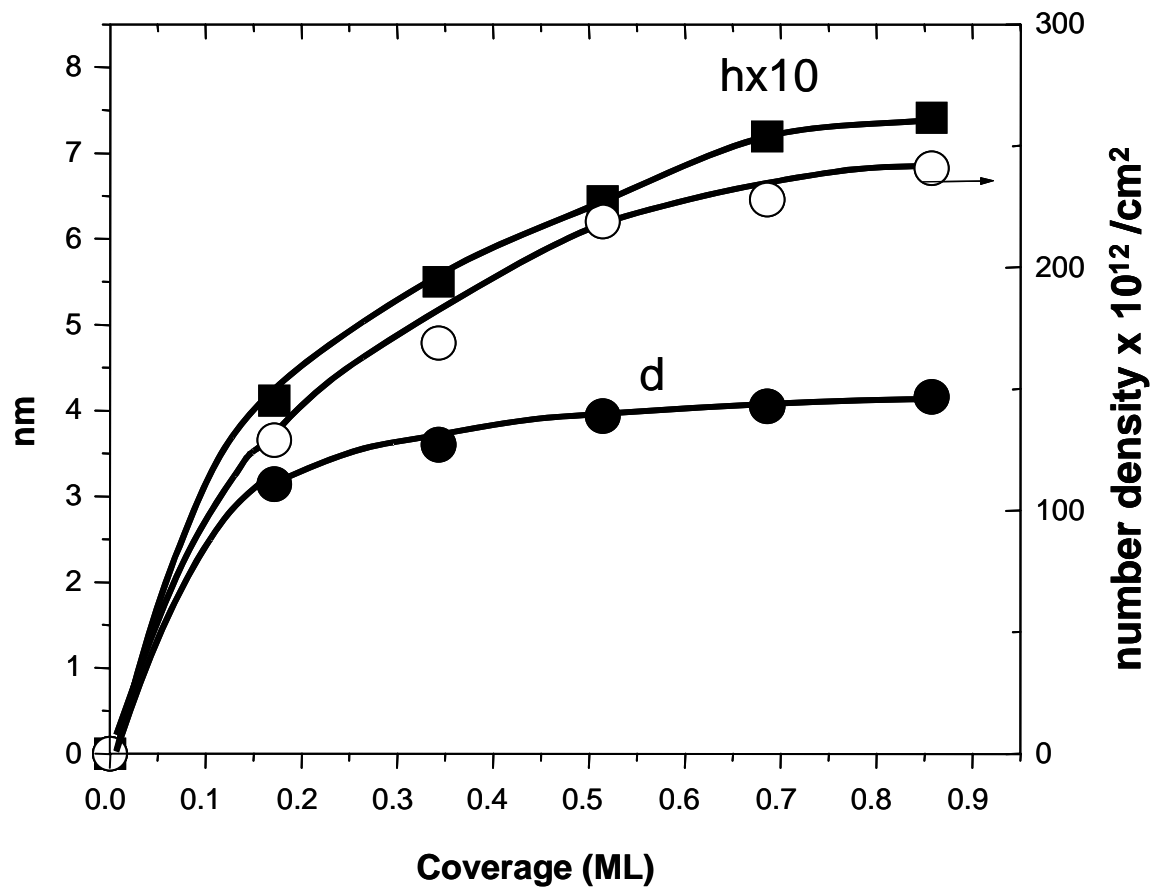


Figure 18. The overall cluster density (right hand axis), diameter and height with respect to Au coverage.

surface steps of  $\text{TiO}_2(110)$  into two types, based on whether the step run parallel or non-parallel to the  $[001]$  direction. Their study found a smooth step that run parallel to the  $[001]$  direction, termed as  $\langle 001 \rangle$ -type step, was terminated with a bridging oxygen row.

The growth of Au clusters was then examined in our experiment on a  $\text{TiO}_2(110)$  surface with oxygen terminated,  $\langle 001 \rangle$ -type steps (Figure 19a) . On a surface area with mainly  $\langle 001 \rangle$ -type steps, Au clusters did not exhibit a preferential growth at the step edges. Instead, the clusters were found to grow homogeneously on the terraces instead of adhering the step edges. On the same surface, where the steps run non-parallel to the  $[001]$  direction, Au clusters were found to decorate the step edges preferentially, as shown in Figure 19b. The contrast behavior of cluster growth on the same surface suggests that the step sites that bind Au clusters strongly are not sites with oxygen termination.

The growth of Au clusters was further studied on  $\text{TiO}_2(110)$  surfaces with  $\text{TiO}_x$  strands. Recent STM and DFT studies [93, 160, 161] have suggested these  $\text{TiO}_x$  strands have undercoordinated Ti ions at both ends. By annealing in vacuum at 750 K for 5 minutes, two  $\text{TiO}_2(110)$  surfaces were prepared with supported  $\text{TiO}_x$  strands while one surface has mainly single strands (Figure 20a) and the other has mainly double strands (Figure 20b). Single strands and double strands have been observed extensively in STM studies on the  $\text{TiO}_2(110)$  surface [93]. They were termed based on their width over the length of  $(1 \times 1)$  unit cell. The single strand has one Ti row along the  $[001]$  whereas the double strands have two Ti rows running along the  $[001]$  direction. The growth of Au clusters on these surfaces was compared in Figure 20. On both surfaces, it is clearly shown Au clusters prefer to grow at the end of these  $\text{TiO}_x$  strands. In Figure 20a, Au clusters were found to grow preferentially at both ends of the  $\text{TiO}_x$  strands, forming a



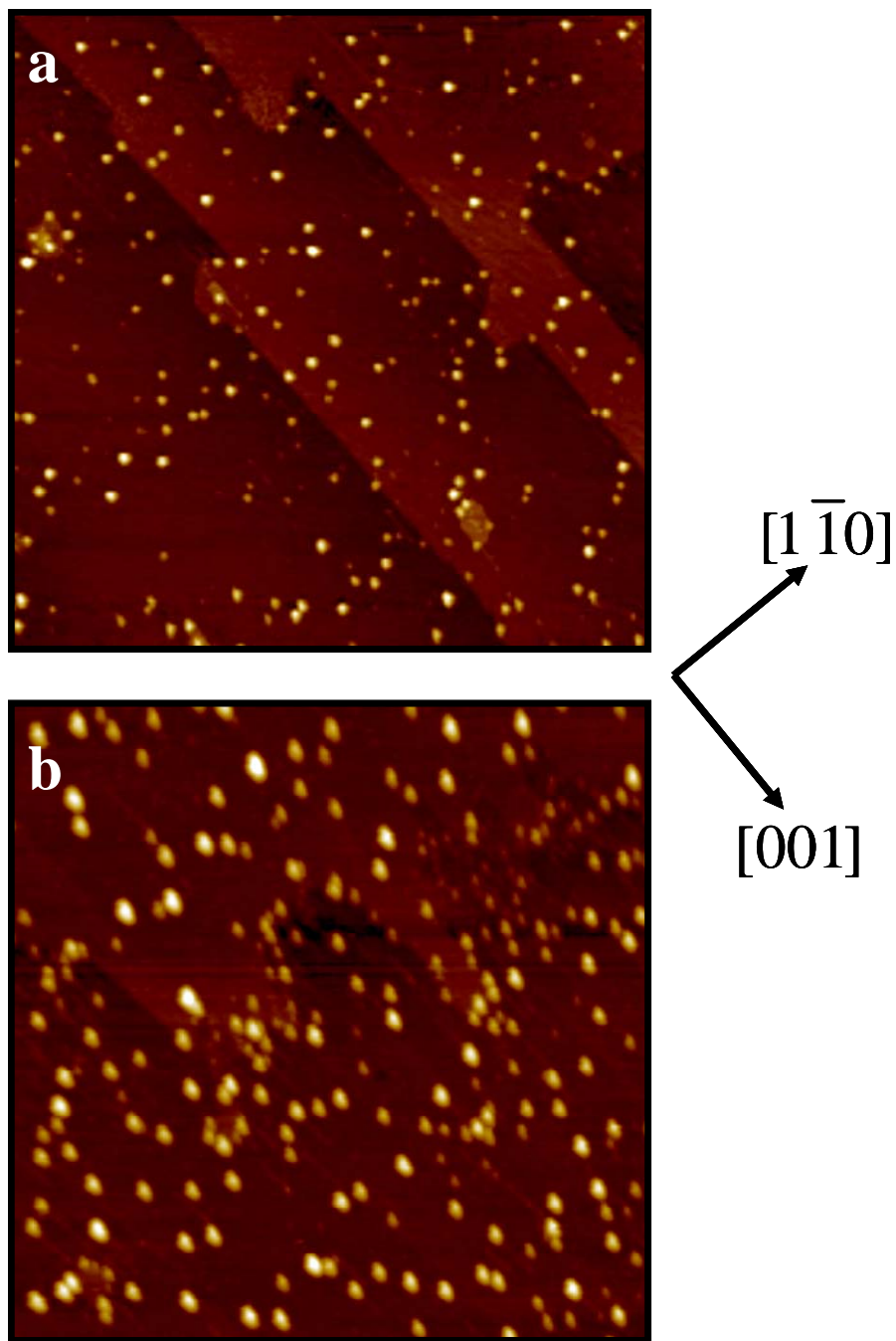


Figure 19. STM images of Au growth on  $\text{TiO}_2(110)$  surfaces with different step edge termination. Both images have the same dimensions of  $200 \text{ nm} \times 200 \text{ nm}$  and tunneling parameters are,  $V_s = 2 \text{ V}$ ,  $I = 0.1 \text{ nA}$ . (a) Au growth on a  $\text{TiO}_2(110)$  surface with straight steps running along the  $[001]$  direction, which have O termination. (b) Au growth on the same  $\text{TiO}_2(110)$  surface with curved step edges present.

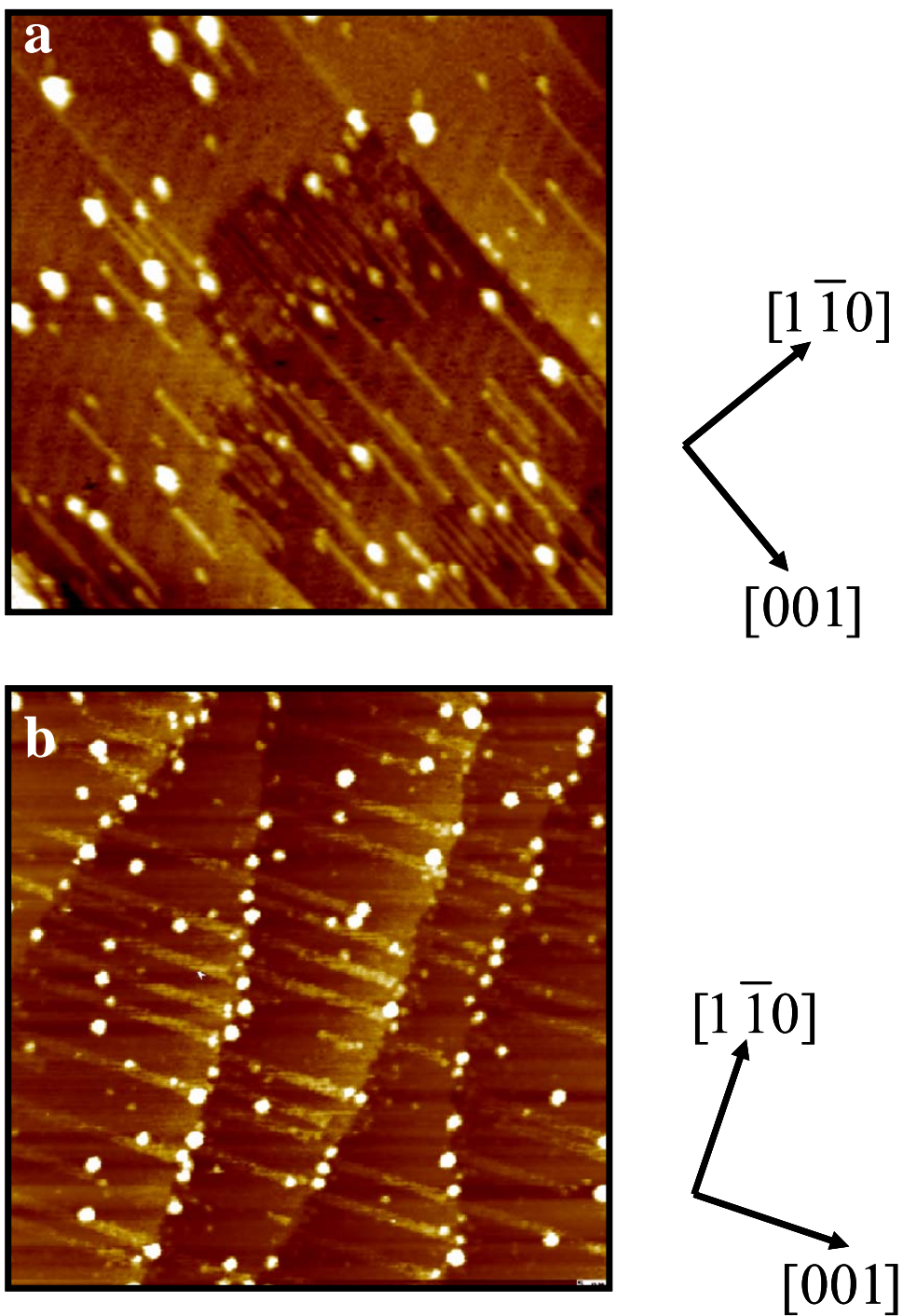


Figure 20. STM images of Au growth on TiO<sub>2</sub>(110) surfaces with TiO<sub>x</sub> strands. Both images have the same dimensions of 100 nm × 100 nm and tunneling parameters,  $V_s = 2$  V,  $I = 0.1$  nA. (a) Au growth on a TiO<sub>2</sub>(110) surface with mainly single strands. (b) Au growth on a TiO<sub>2</sub>(110) surface with mainly double strands.

dumb-bell structure, rather than growing at the  $\langle 001 \rangle$ -type steps. In Figure 20b, Au clusters were found to grow at step edges, as well as the end of  $\text{TiO}_x$  strands. Similar to the behavior of  $\langle 001 \rangle$ -type steps, Figure 20 also shows the edges of  $\text{TiO}_x$  strands, parallel to the  $[001]$  direction, had little affinity to Au clusters.

Overall, the results suggest  $\text{TiO}_x$  strands behave similarly in growing Au clusters as the step edges. Undercoordinated Ti ions at the ends of these  $\text{TiO}_x$  strands were the sites where Au clusters nucleate. Since these  $\text{TiO}_x$  strands were the building blocks for the growth of  $\text{TiO}_2(110)$  surfaces, step edges that run non-parallel to the  $[001]$  direction could be deemed as an ensemble of undercoordinated Ti ions. Therefore, it is concluded that the origin of preferential Au growth at step edges is due to the high density of undercoordinated Ti ions at step edges.

STM studies by Besenbacher et al. [96] also demonstrated bridging oxygen vacancies on  $\text{TiO}_2(110)$  to be strong Au binding sites. These oxygen vacancies are essentially another form of undercoordinated Ti ions where one oxygen is removed from the Ti octahedral. Our studies suggest step edges bind Au much stronger than bridging oxygen vacancies, indicating a lower coordination number of Ti at step edges than that of Ti underneath the bridging oxygen vacancy.

The dominant role that undercoordinated Ti cations play in the surface structure of Au/ $\text{TiO}_2(110)$  would be further illustrated in following studies through  $\text{TiO}_x$  species and their role in the nucleation and stabilization of Au clusters on  $\text{TiO}_2(110)$ .

### Thermal stabilities of Au/TiO<sub>2</sub>(110) in UHV

Thermal stability of Au clusters supported on TiO<sub>2</sub>(110) has been studied using LEIS[107, 163, 164] XPS [163-166], AFM [165, 166] and STM [108, 167, 168]. The conclusions on the stability of Au clusters supported on TiO<sub>2</sub>(110) have varied with annealing temperatures and substrate conditions. LEIS studies show the surface fraction of Au clusters start to attenuate at temperatures above 400 K whereas AFM and STM studies suggested appreciable change of cluster size/density was only observed for Au/TiO<sub>2</sub>(110) after being heated to above 800 K. *In-situ* STM has allowed us to follow the growth of individual clusters at elevated temperatures and thus provides an opportunity to settle the debate over thermal stability of Au/TiO<sub>2</sub>(110).

Figure 21 shows the evolution of surface morphology of Au/TiO<sub>2</sub>(110) after thermal treatments. Low surface Au coverage (< 0.3 ML) was used in this *in-situ* study because, at this coverage, the size of supported Au clusters ranges from 2-4 nm, which is the active phase of Au/TiO<sub>2</sub>(110) catalyst, and thus of our best interest. For Au clusters larger than 4 nm, no appreciable change has been observed from our *ex-situ* STM study, consistent with previous STM and AFM results [165, 168]. In Figure 21a, after being annealed at 450 K for 10 minutes, most Au clusters remain stable on the surface. Changes in cluster size were not apparent before and after annealing. Also, no change of cluster positions was detected at 450 K for Au clusters of 2-4 nm in size. Upon annealing at 600 K (Figure 21b), a few small clusters with a size around 2 nm disappeared while the majority of Au clusters remained static on the surface. Au clusters which disappeared after annealing at 600 K were marked by the dashed circles in Figure 21b. At 600 K,

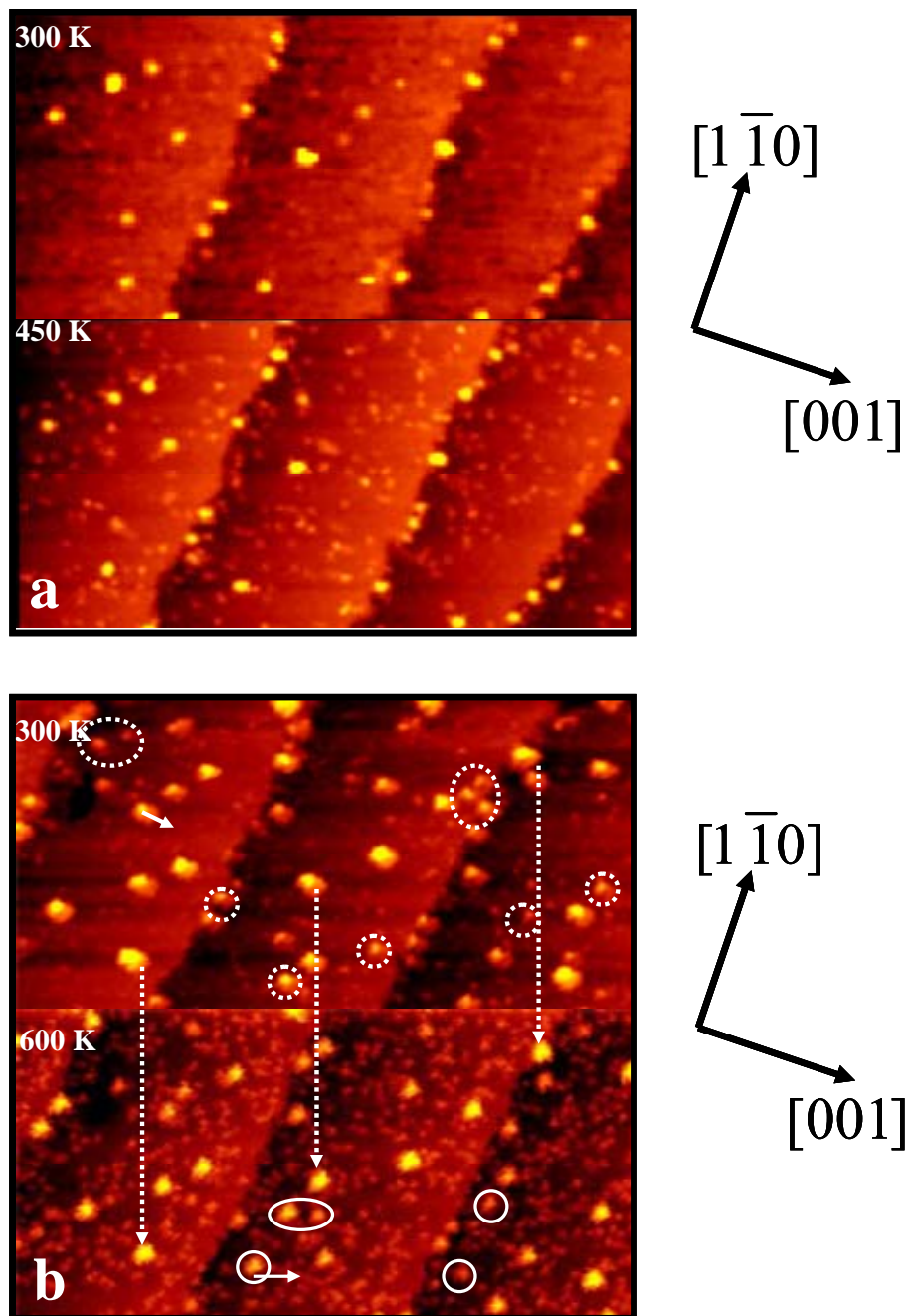


Figure 21. *In-situ* STM images of Au clusters supported on the TiO<sub>2</sub>(110) surface before and after thermal treatments. Both images have dimensions of  $100 \times 100$  nm and tunneling parameters are  $V_s = 2$  V and  $I = 0.1$  nA. (a) Images taken at the same area before and after annealing at 450 K for 10 min. (b) Images taken at the same area before and after annealing at 600 K for 10 min.

several new Au clusters appeared on terraces, as marked in the solid circles. The dashed arrows show three stationary large clusters, which exhibited a height increase.

After annealing, small bright spots appeared on the surface and enriched around the vicinity of Au clusters (Figure 21). These bright spots had a length of around 1-2 nm and a height of 0.1-0.2 nm, lower than the apparent height of Au clusters nucleated on  $\text{TiO}_2(110)$ . In this experiment, a tip silhouette area uncovered by Au clusters was created and these bright dots also appeared on the uncovered shadow area with a similar density (Figure 22). The above studies of  $\text{TiO}_2(110)$  surfaces after vacuum annealing suggest these bright dots were  $\text{TiO}_x$  species. The higher density of  $\text{TiO}_x$  around the edge of Au clusters indicates oxygen enriches at the edge of Au clusters, attracts Ti interstitials to diffuse towards the clusters and forms  $\text{TiO}_x$  species at the edge of cluster. Unlike Pt or Pd on  $\text{TiO}_2(110)$  [169-172], the encapsulation of Au clusters were not observed upon annealing.

*In-situ* STM study by Kolmakov et al.[108] have examined the stability of Au/ $\text{TiO}_2(110)$  after thermal treatment at 950K. Drastic morphological changes have been observed. Accompanying the decomposition of surface steps, the density of Au clusters decreased by 20%, whereas the volume of Au clusters increased. Most Au clusters changed their positions on the  $\text{TiO}_2(110)$  surface.

The above *in-situ* studies on the thermal stability of Au/ $\text{TiO}_2(110)$  reveal 1) Au clusters were mostly stable on  $\text{TiO}_2(110)$  upon thermal treatment up to 600 K, and 2) substantial changes of supported Au clusters happened only when the  $\text{TiO}_2$  substrate became unstable. This suggests the  $\text{TiO}_2$  substrate play a major role in the stabilization of Au clusters supported on  $\text{TiO}_2(110)$ .

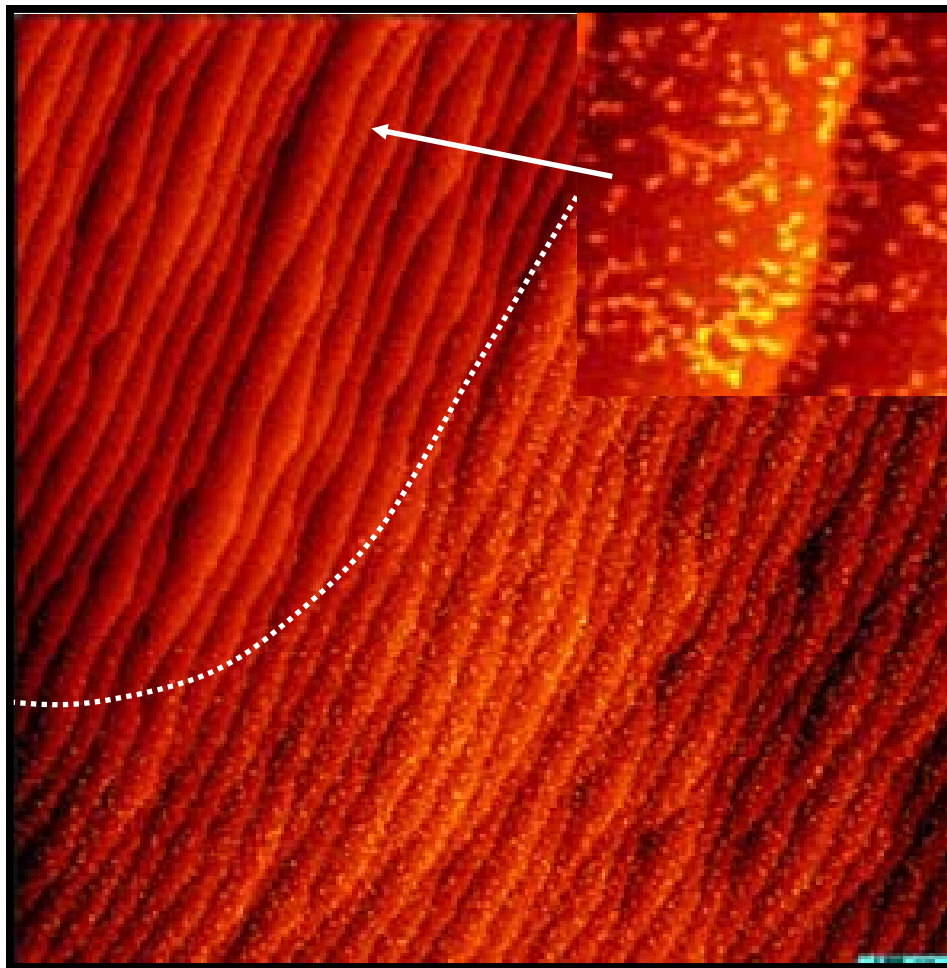


Figure 22. Large scale STM image of Au clusters supported on  $\text{TiO}_2(110)$  after 600 K annealing. The white dotted line separates the shadow area with Au covered area. The image has dimensions of  $1000 \text{ nm} \times 1000 \text{ nm}$  and the tunneling parameters are  $V_s = 2 \text{ V}$  and  $I = 0.1 \text{ nA}$ . Inset shows a zoom-in image of the shadow area after annealing and has dimensions of  $20 \text{ nm} \times 20 \text{ nm}$ .

The thermal stability of  $\text{TiO}_2(110)$  in UHV can be categorized into two temperature ranges based on STM and LEIS studies by Diebold et al.[158], as well as SSIMS study by Henderson [159]. Below 750 K, Ti interstitials would diffuse onto the surface and form  $\text{TiO}_x$  species. Above 750 K, the matrix of surface terraces is not stable and would start to decompose at steps, which eventually leads to the formation of larger terraces. STM study by Bennett et al. also demonstrated the decomposition of surface steps of  $\text{TiO}_2(110)$  at 1000 K [172]. The removal of O and Ti ions indicated Ti diffuse into the bulk and become interstitial cations. The thermal stability of Au clusters supported on  $\text{TiO}_2(110)$  can be divided into these temperature ranges accordingly. Below 750 K, Au clusters with size larger than 2 nm are mostly stable due to the enrichment of  $\text{TiO}_x$  species around the periphery of Au clusters. Above 750 K, accompanying the decomposition of  $\text{TiO}_x$  and step edges, Au clusters become mobile on the surface.

Our *in-situ* studies could also resolve the discrepancy among previous studies on the thermal stability of Au/ $\text{TiO}_2(110)$ . The attenuation of Au signals or Au/Ti ratios observed in previous XPS and LEIS studies, was probably due to 1) the diffusion of Ti interstitials onto the surface which increase the concentration of Ti cations at and near the surface; and 2) the enrichment of  $\text{TiO}_x$  around the periphery of Au clusters which decreased the accessibility of probe ions to Au.

Another question that could be answered by our *in-situ* STM studies is the mode of thermally induced sintering. While most previous studies[173, 174] attempted to elucidate the mode of sintering by fitting cluster distributions with theoretical models, we here benefited from the capability to follow individual clusters before and after thermal treatments and could directly look into the mode of sintering.



In Figure 21, most Au clusters were static on the surface after thermal treatment. New Au clusters appeared on the surface after annealing at 600 K. Most of these new clusters were smaller than their neighbor Au clusters, but much larger than  $\text{TiO}_x$  species on the surface. These phenomena explicitly show Ostwald ripening is the operative mode during thermally induced sintering at 600 K. The migration of whole Au clusters might be difficult due to the surrounding  $\text{TiO}_x$  species, which on the other hand traps diffusing Au monomers and lead to the formation of new clusters on the surface.

Besides the snapshots of before and after thermal treatments, STM experiments at constant temperatures were also conducted to investigate the thermal stability of supported Au clusters. We have been able to scan the same area of supported Au clusters for hours at temperatures of 400 K, 450 K and 600 K. (Due to thermal drifts of the scan head, 600 K is the upper limit for scanning at high temperature and the scan head generally got stabilized within less than 20 minutes in UHV.) Au clusters supported on  $\text{TiO}_2(110)$  were found stable within 2-3 hours of scanning.

Mitchell et al. studied Au clusters supported on  $\text{TiO}_2(110)$  at  $\sim 750$  K as a function of time [167]. Their STM results show Au clusters are mostly static while some small clusters with size below 3 nm will diffuse along the surface. The diffusion of small clusters does not behave in a continuous manner. Instead, the clusters stick for a long time before taking a sudden jump. This unconventional diffusion of clusters, termed as Levy flight, was not observed in our experiments at or below 600 K. Small clusters observed in the study by Mitchell et al. might as well be small  $\text{TiO}_x$  islands nucleated on the terrace, which started to get destabilized at 750 K.

### **Au clusters on hydroxylated TiO<sub>2</sub>(110)**

Surface defects of TiO<sub>2</sub>(110) play a dominant role in the nucleation and stabilization of Au clusters. These surface defects might be influenced by the presence of adsorbate gases and their affinities in binding Au clusters might be altered.

Figure 23 shows the growth of Au nanoclusters on a hydroxylated TiO<sub>2</sub>(110) surface. The hydroxylated TiO<sub>2</sub>(110) surface was prepared by exposing TiO<sub>2</sub>(110) to water vapor at  $1 \times 10^{-7}$  Torr. The total exposure was 2 L (assuming  $1 \text{ L} = 10^{-6} \text{ Torr}\cdot\text{s}$ ). TPD, HREELS and STM studies have shown H<sub>2</sub>O dissociates and forms hydroxyl groups at defect sites on the TiO<sub>2</sub>(110) surface [148-150, 175, 176]. In TPD studies by Henderson [176], a high temperature tail (between 300 - 500K) was attributed to the recombination of surface hydroxyl groups that are formed through water dissociation at surface defects. The formation of hydroxyl groups at surface defects was also observed in HREELS and STM experiments [150, 176]. In our study, water exposure at room temperature caused changes in the surface morphology of TiO<sub>2</sub>(110) due to the appearance of small protrusions (Figure 23b). These protrusions were less than 2 Å in height and elongated along the [001] direction. The morphology of these protrusions suggests these protrusions were TiO<sub>x</sub> species. Similar to the O<sub>2</sub>-induced formation of TiO<sub>x</sub> observed in Figure 14 and by Park et al.[160], Ti interstitials were drawn out the bulk to form TiO<sub>x</sub> which preferentially aggregate on defect sites such as step edges. STM studies by Uetsuka et al. [177] show severe erosion and roughening of the TiO<sub>2</sub>(110) surface when exposing the surface to water solution. The erosion caused by water solution might be similar to the formation of TiO<sub>x</sub> induced by water vapor exposure, but to a more intensive degree.

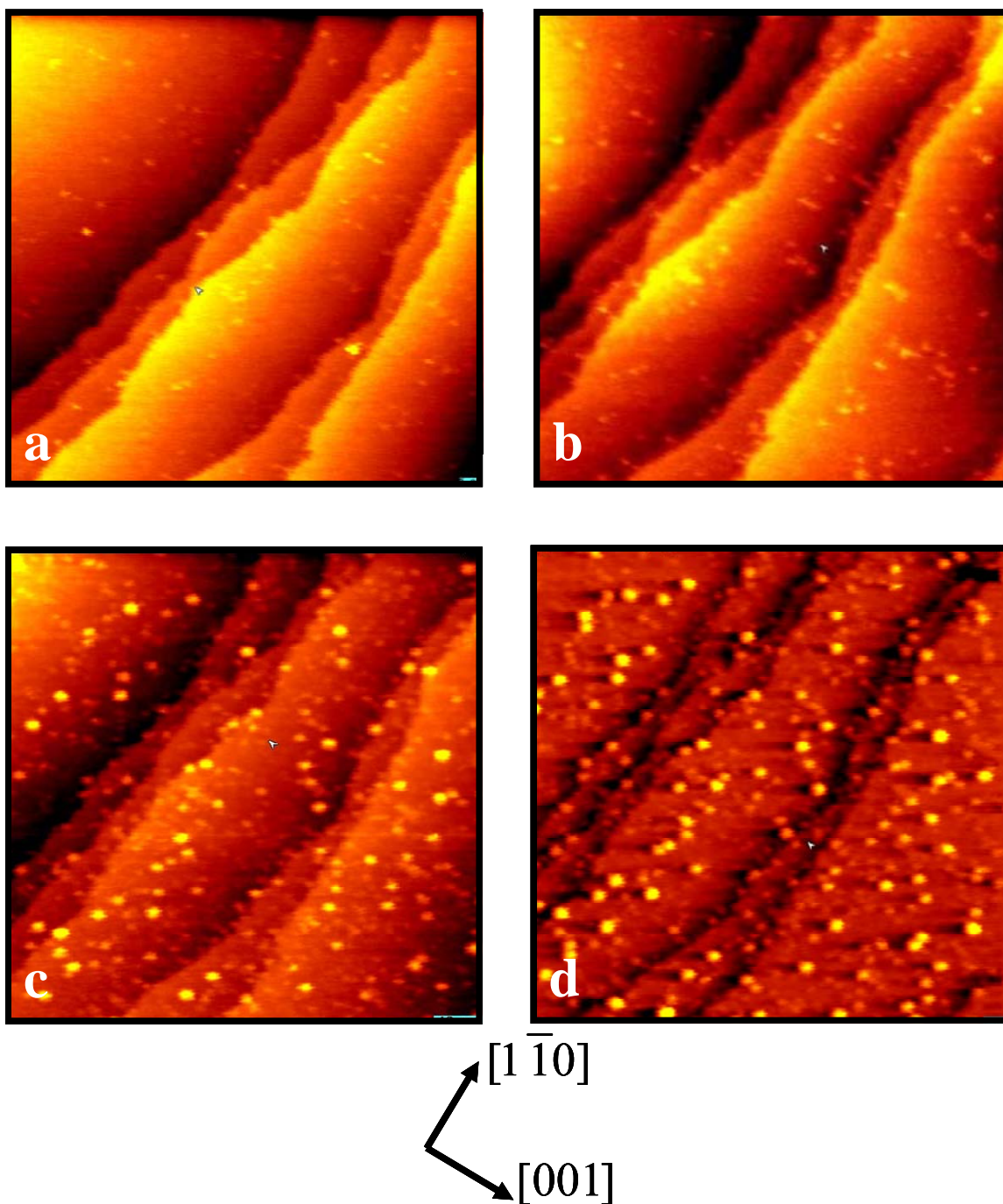


Figure 23. STM images of Au growth on hydroxylated  $\text{TiO}_2(110)$ . (a) Clean  $\text{TiO}_2(110)$ . (b)  $\text{TiO}_2(110)$  after exposed to 2 L  $\text{H}_2\text{O}$  at 300 K. (c) 0.25 ML Au deposited on the hydroxylated  $\text{TiO}_2(110)$ . (d) 0.42 ML Au deposited on the hydroxylated  $\text{TiO}_2(110)$ . All images are taken on the same area,  $100 \text{ nm} \times 100 \text{ nm}$  in size. Tunneling parameters are  $V_s = 2 \text{ V}$  and  $I = 0.1 \text{ nA}$ .

Au growth on the hydroxylated  $\text{TiO}_2$  surface exhibits a different growth mode from Au growth on the clean  $\text{TiO}_2$  surface. At room temperature, small Au clusters nucleated on the terraces homogeneously (Figure 23c) instead of the preferential nucleation at step edges observed in Au growth on clean  $\text{TiO}_2(110)$ . This indicates that water dissociates at the step sites and forms hydroxyl groups which block the growth of Au at these sites. Meanwhile, surface  $\text{TiO}_x$  species also play a role serving as nucleation sites for Au clusters. Following deposition of Au on the same surface (Figure 23d), an increase in the cluster size was observed, accompanying a slight increase in the cluster density. This is also different from the Au growth behavior on clean  $\text{TiO}_2$  surface, where the cluster density on terraces increased tremendously at this surface coverage level.

Following an anneal at 600K, Au clusters on the terraces grew, but these clusters did not move to step edges (Figure 24a). This might be due to the high concentration of  $\text{TiO}_x$  species formed after annealing, which serve as diffusion barriers and resist the diffusion of Au. The concentration of  $\text{TiO}_x$  species was much higher than that on a clean  $\text{TiO}_2(110)$  surface after being annealed at 600 K (Figure 24b). Subsequent deposition of Au on this annealed surface resulted in an increase in both the cluster density and the cluster size. In this experiment, a shadow area uncovered by Au clusters was created prior to the annealing at 600 K. Figure 24c shows the morphology of this shadow area after the annealing at 600 K.  $\text{TiO}_x$  species were observed with a density approximating that on a clean  $\text{TiO}_2(110)$  surface after being annealed at 600 K (Figure 24b). Comparing Figure 24a, 24c and Figure 21b, the results suggest surface hydroxyl groups greatly facilitated the formation of  $\text{TiO}_x$  species when Au clusters were supported on the surface. After the annealing at 600 K, STM tip was moved to allow the shadow area in Figure 24c to be

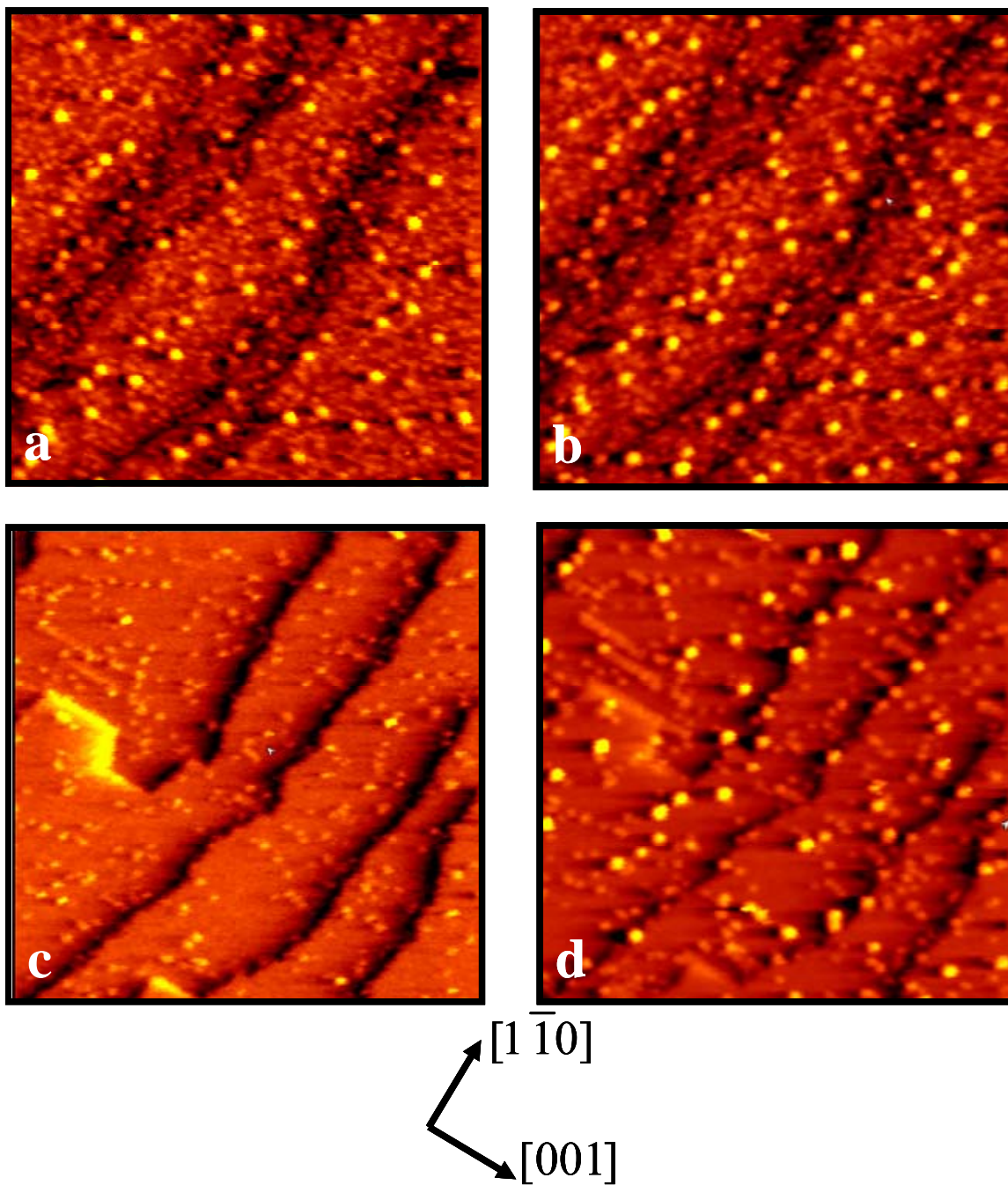


Figure 24. STM images of Au growth on hydroxylated and annealed  $\text{TiO}_2(110)$  surfaces. (a) The surface of Figure 23(d) annealed at 600 K for 10 min. (b) 0.17 ML Au deposited on the surface of (a). (a) and (b) are the same area as in Figure 23. (c) The shadow area of the hydroxylated  $\text{TiO}_2(110)$  surface after annealing at 600 K for 10 min.  $\text{TiO}_x$  species show up on the surface after annealing. (d) 0.17 ML Au deposited on the surface of (c). (c) and (d) are the same area. All images are  $100 \text{ nm} \times 100 \text{ nm}$  in size. Tunneling parameters are  $V_s = 2 \text{ V}$  and  $I = 0.1 \text{ nA}$ .

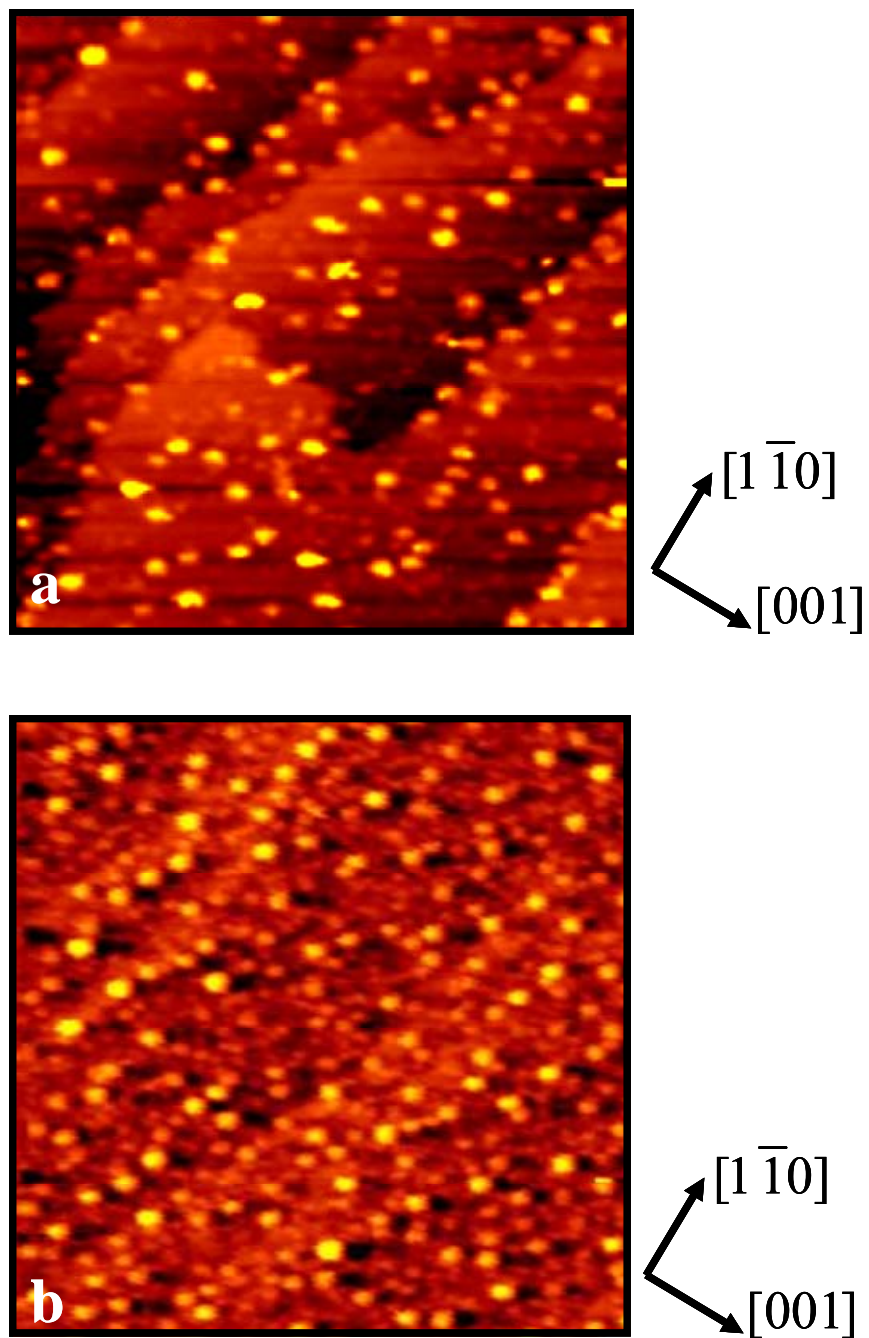


Figure 25. STM images of Au growth on  $\text{TiO}_2(110)$  after the removal of hydroxyl groups by annealing at 600 K. (a) 0.34 ML Au deposited on the shadow area of the annealed  $\text{TiO}_2(110)$ . (b) 0.34 ML Au deposited on the Au covered area of the annealed  $\text{TiO}_2(110)$ . Both images are  $100 \text{ nm} \times 100 \text{ nm}$  in size.

exposed to Au flux. Au clusters were found to grow on both step edges and terraces on the shadow area (Figure 24d). The decoration of Au clusters at step edges were apparent as the surface coverage of Au clusters increased on the shadow area (Figure 25a). On surfaces with high  $\text{TiO}_x$  concentration, the growth of Au clusters remained homogeneous at increased Au coverages (Figure 25b).

Figure 26 compares the density of Au clusters as a function of Au coverage on different surfaces of  $\text{TiO}_2(110)$ . The shadow area in Figure 24c were termed as a  $\text{TiO}_2(110)$  surface supported with  $\text{TiO}_x$ . The statistics of Au growth on a clean  $\text{TiO}_2(110)$  was obtained from Figure 15. On a clean  $\text{TiO}_2(110)$  surface, the growth mode at steps differ drastically with that on terraces. While Au clusters quickly saturate the steps, the density of Au cluster increase continuously on the terraces. On a  $\text{TiO}_2(110)$  surface covered with  $\text{TiO}_x$ , the increases of cluster densities on steps and terraces exhibit a similar slope, indicating homogeneous Au growth on this surface. This is because surface  $\text{TiO}_x$  species behave similarly as step edges in binding Au clusters. On a hydroxylated  $\text{TiO}_2(110)$  surface, Au growth at step edges was greatly inhibited. At the same Au coverage, the density of Au clusters on the terraces was much higher than that on the other two surfaces. The total density of Au clusters on the hydroxylated surface was also higher than that on the other two surfaces at the same Au coverage, indicating a smaller average cluster size on the hydroxylated surface. Since the flux rate of Au did not change in these studies, a higher cluster density and a smaller average size suggest an inhibited diffusion of Au atoms on the hydroxylated surface. The inhibited diffusion could be due to either the increase of surface defect densities induced by hydroxyl groups or an

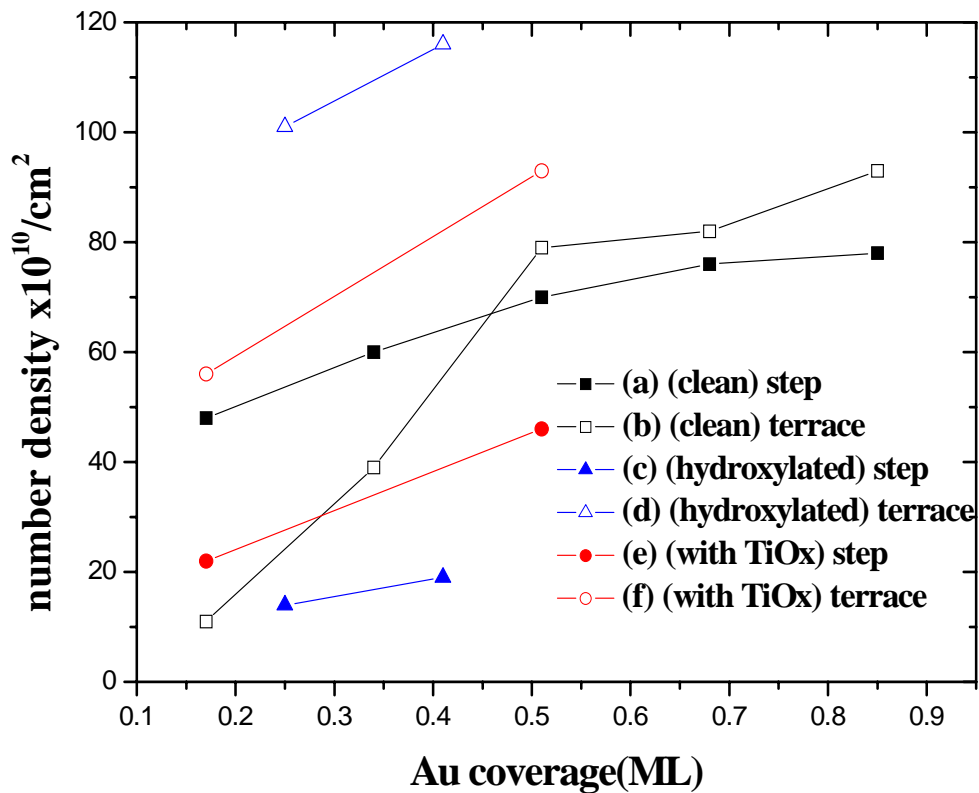


Figure 26. Comparison of the number densities of Au clusters as a function of Au coverage on the surface of (a) and (b) clean  $\text{TiO}_2(110)$ ; (c) and (d)  $\text{TiO}_2(110)$  exposed to 2 L  $\text{H}_2\text{O}$  (hydroxylated  $\text{TiO}_2(110)$ ); (e) and (f)  $\text{TiO}_2(110)$  exposed to 2 L  $\text{H}_2\text{O}$  and annealed at 600 K for 10 minutes ( $\text{TiO}_2(110)$  covered with  $\text{TiO}_x$ ).



increased diffusion barrier caused by the interaction between adsorbed hydroxyl groups and the diffusing Au atoms.

Recent STM and DFT studies by Matthey et al. [97] suggest that the adhesion of Au clusters is strongest on the oxidized support based on their comparison of the cluster distribution on reduced, hydroxylated or oxidized  $\text{TiO}_2(110)$  surfaces. In their study, the oxidized or hydroxylated  $\text{TiO}_2(110)$  surfaces were prepared by exposing the surface to a few Langmuir of  $\text{O}_2$  or  $\text{H}_2\text{O}$  accordingly. Au clusters supported on an oxidized  $\text{TiO}_2(110)$  surface showed the best stability after being heated to 68 °C. Their DFT calculations explain the stabilization of Au on the oxidized  $\text{TiO}_2(110)$  as the formation of strong Au-O-Ti bonds. A perception in their study has been that  $\text{O}_2$  exposure leads to the decrease of surface defects, even on a reduced  $\text{TiO}_2(110)$  surface.

Our above studies have found exposure of  $\text{O}_2$  would induce the diffusion of Ti interstitials to the surface, followed with the formation of  $\text{TiO}_x$  species. These  $\text{TiO}_x$  species behave similarly to step edges in the stabilization of Au. Studies by Park et al. [160, 161] also reveal adsorbed oxygen would increase the surface concentration of  $\text{TiO}_x$  species, especially at elevated temperatures. Therefore, instead of quenching surface defects, the initial stage of  $\text{O}_2$  exposure increases the density of surface defects, i.e.  $\text{TiO}_x$  species. Our studies have also shown these  $\text{TiO}_x$  species were fairly small with a height around or lower than 2 Å. The majority of Au clusters used in the study by Matthey et al. [97] had a height around 2 Å, which made the height distribution of Au clusters ambiguous.

Indeed, earlier STM study from our group [81] has also shown the increased stability of Au clusters on a  $\text{TiO}_2(110)$  surface pretreated with  $\text{O}_2$ . Through the above

growth studies, we found this increased stability was due to the increased density of surface defects, i.e.,  $\text{TiO}_x$  species. Thermodynamically,  $\text{O}_2$  exposure would lead to the removal of undercoordinated Ti cations. However, the above studies show the oxidation kinetics of the  $\text{TiO}_2(110)$  surface is via 1) the increase in surface concentration of undercoordinated Ti cations and 2) subsequent oxidation to remove these undercoordinated Ti cations.

On the hydroxylated  $\text{TiO}_2(110)$  surface, Matthey et al. studied the stability of Au clusters from cryogenic temperatures to room temperature, while their studies on the other two surfaces were performed at room temperature and above. It is not surprising to see that the growth and stability of Au clusters deposited at cryogenic temperatures differed with those of Au clusters grown at room temperature. In our study, similar to  $\text{O}_2$ , hydroxyl groups induce the formation of surface  $\text{TiO}_x$  species at room temperature, whereas the diffusion of Ti interstitials was mostly inhibited at cryogenic temperatures.

### **Preparation of Au/ $\text{TiO}_x$ on $\text{TiO}_2(110)$**

Our studies have shown undercoordinated Ti cations or  $\text{TiO}_x$  species play a vital role in the growth and stabilization of Au clusters on  $\text{TiO}_2(110)$ . Meanwhile, Chen et al. [88, 89, 91] have provided another excellent evidence via the synthesis of Au films on a reduced  $\text{TiO}_x$  surface. The reduced  $\text{TiO}_x$  film was prepared on a  $\text{Mo}(112)$  surface. Deposition of Au with subsequent annealing at 900 K results a complete wetting layer of Au on top of the  $\text{TiO}_x$ - $\text{Mo}(112)$  surface. Parallel to this idea, if we could heavily reduce the  $\text{TiO}_2(110)$  surface, it is possible to make flat Au films on top of  $\text{TiO}_2(110)$ .

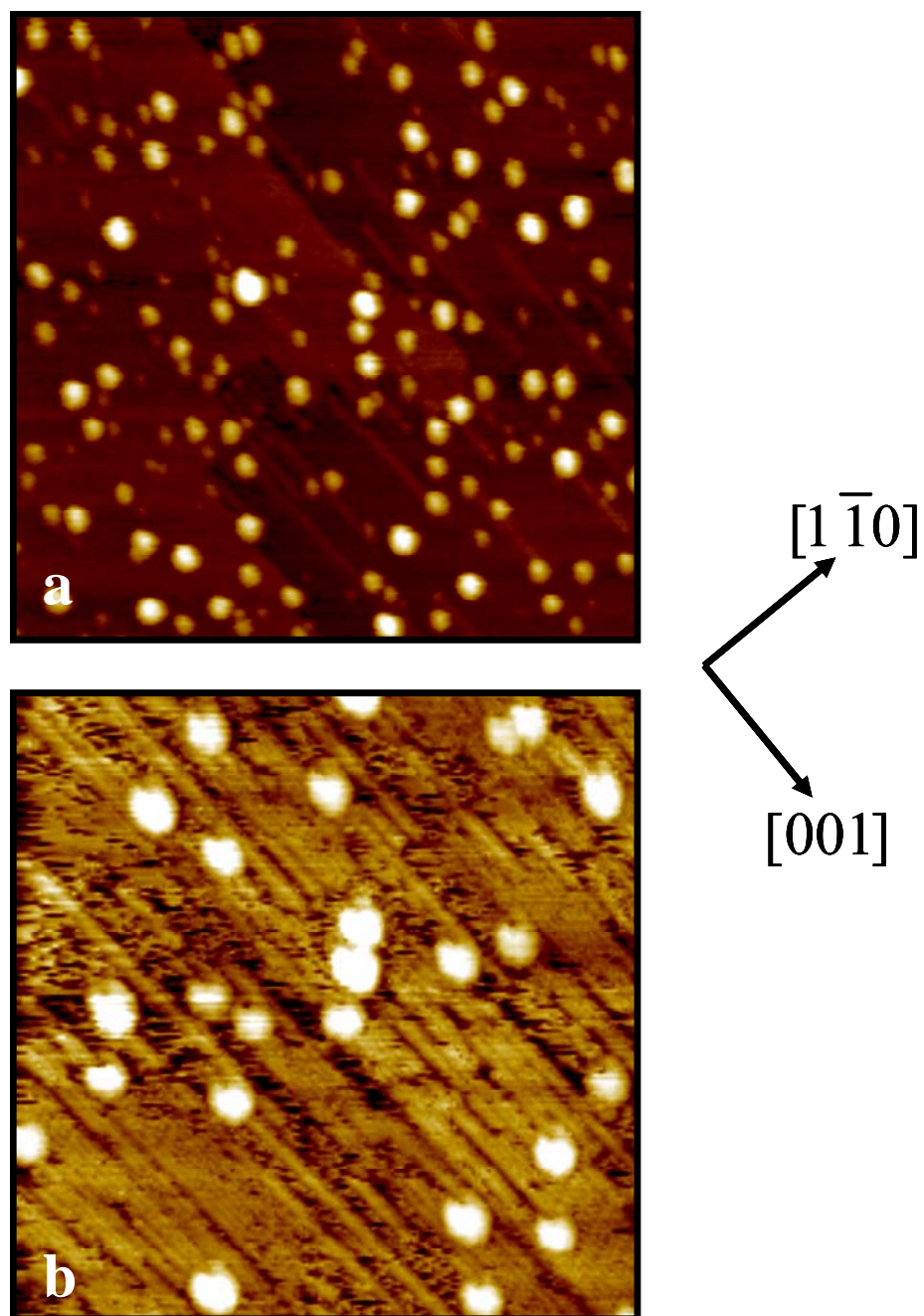


Figure 27. STM images of 1 ML Au/TiO<sub>2</sub>(110) (a) before and (b) after annealing in  $5 \times 10^{-8}$  Torr H<sub>2</sub> at 800 K for 10 min. Both images have the same dimensions of 100 nm × 100 nm and tunneling parameters of  $V_s = 2$  V and  $I = 0.1$  nA.

H<sub>2</sub> was used as the reducing agent in this study to remove surface oxygen from TiO<sub>2</sub>(110). Figure 27 shows the surface morphology of ~ 1 ML Au supported on TiO<sub>2</sub>(110) before and after annealing in the  $5 \times 10^{-8}$  Torr H<sub>2</sub> at 800 K. After annealing, the cluster density decreased by 85% while the size of clusters increased drastically. STM revealed a significant modification of the substrate morphology. The whole surface was roughened with bright added rows and protrusions extending along the [001] direction.

The preparation of a reduced TiO<sub>x</sub> layer on a TiO<sub>2</sub>(110) surface differs with the preparation of a TiO<sub>x</sub> film on the metal surface in their thermodynamic feasibilities. Surface free energy of an oxide surface is usually much lower than that of a metal surface. For instance, the surface free energy of TiO<sub>2</sub> is  $\sim 35 \mu\text{J} / \text{cm}^2$  [178], much lower than that of Au ( $\sim 140 \mu\text{J} / \text{cm}^2$  [178]). Thus, it is thermodynamically favorable to make a reduced TiO<sub>x</sub> film on a Mo surface. The reduced TiO<sub>x</sub> has a higher surface free energy than the stoichiometric TiO<sub>2</sub> and is thus not stable on the TiO<sub>2</sub>(110) surface. The diffusion study by Henderson [159] has shown TiO<sub>x</sub> species dissolve into the bulk at temperature above 700 K, restoring the surface stoichiometry. Meanwhile, the growth of Au on TiO<sub>2</sub>(110) favors the separation between Au and TiO<sub>2</sub> thermodynamically, which has been displayed by the VW mode of Au growth.

However, to prepare flat Au film on a reduced TiO<sub>2</sub>(110) surface might be kinetically feasible. In Figure 27b, the roughened TiO<sub>2</sub> surface with added rows and protrusions suggests it is kinetically possible to maintain reduced TiO<sub>x</sub> on the TiO<sub>2</sub>(110) surface at a certain level. However, the annealing temperature might be too high and caused the agglomeration of Au clusters. Our studies on the thermal stabilities of Au/TiO<sub>2</sub>(110) have shown the rapid migration of Au clusters when the TiO<sub>2</sub> substrate

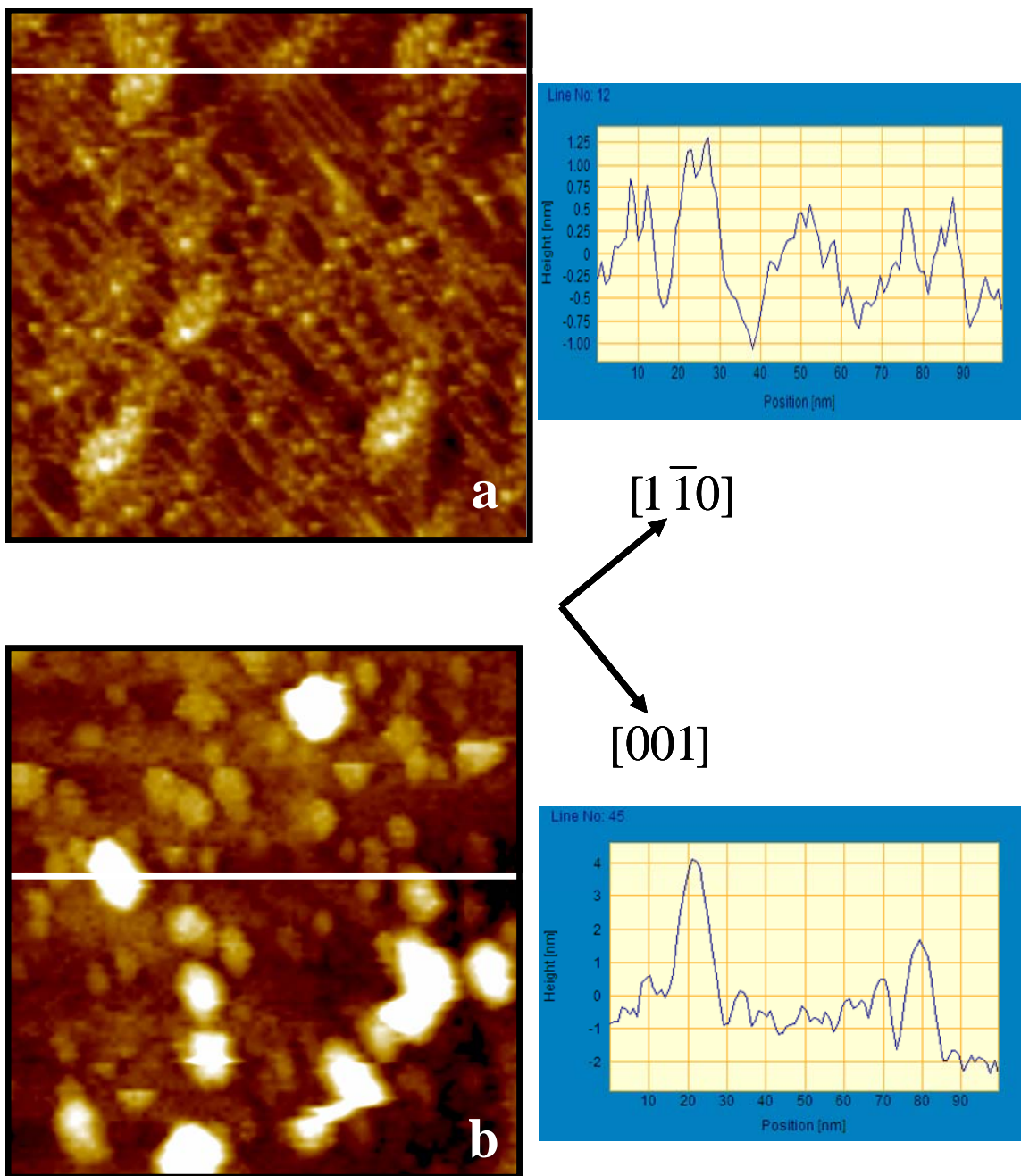


Figure 28. STM images of 0.8 ML Au/TiO<sub>2</sub>(110) after reduction in H<sub>2</sub> at 800 K. (a) 0.8 ML Au deposited on the TiO<sub>2</sub>(110) within  $5 \times 10^{-8}$  Torr H<sub>2</sub> at 700 K. (b) The surface of (a) annealed in  $5 \times 10^{-6}$  Torr H<sub>2</sub> at 700 K for 10 min. Profile of the white line marked in the images are shown at the side of each STM image. Both STM images have the same dimensions of 100 nm  $\times$  100 nm and tunneling parameters of  $V_s = 2$  V and  $I = 0.1$  nA.

becomes unstable in UHV at above 700 K. The cluster migration favors the agglomeration and de-wetting of Au clusters from the TiO<sub>2</sub>(110) surface.

To prevent the formation and migration of Au clusters, we deposited Au while reducing the TiO<sub>2</sub>(110) surface at elevated temperatures. Figure 28a shows the surface morphology when 0.8 ML Au were evaporated onto the TiO<sub>2</sub>(110) surface at 700 K and in the presence of  $5 \times 10^{-8}$  Torr H<sub>2</sub>. The line profile shows although Au did not completely wet the surface, Au clusters prepared this way are very small with heights no more than 3 layer thickness. Further annealing at higher H<sub>2</sub> partial pressure caused the presence of large clusters on the TiO<sub>2</sub>(110) surface (Figure 28b). The clusters ranges from 10-20 nm in size and elongated along the [001] direction. The line profile shows the surface of clusters was curved, instead of a planar surface observed on the clusters of Pt/TiO<sub>x</sub> and Pd/TiO<sub>x</sub>. This suggests Au is at the surface of these clusters and has not faceted yet.

### **Size selected Au<sub>400</sub> clusters on HOPG**

The growth of Au clusters was mediated by surface defects of TiO<sub>2</sub>(110), when Au atoms was deposited onto the surface with low impact energies. The size of Au clusters prepared this way exhibited a wide distribution. The number density of Au clusters was a function of Au flux, as well as the density of surface defects. Probing the size effect of supported nanoclusters often requires a more precise control over the size and density of supported metal clusters.

Recent development in vapor phase deposition of size-selected clusters has provided an opportunity to prepare supported metal clusters of uniform size. In our study,

Au<sub>400</sub> clusters were produced through a liquid metal ion source, selected by a mass filter and then deposited onto a highly oriented pyrolytic graphite (HOPG) surface. The nucleation of these Au clusters was not influenced by the substrate.

Gold ions were generated in a liquid metal ion source. In the source, Au and Si eutectic were heated to the eutectic point in a tungsten reservoir. An extraction voltage was applied to the needle tip of the reservoir to extract Au ions out of the source. Au cluster ions (Au<sub>n</sub><sup>q+</sup>) containing 1 up to 1000 (n=1-1000) atoms with 1 to 10 charges (q=1-10) could be produced in the source. The Au ions mixture was introduced into a series of focus lens and to a Wien filter, where they were separated according to their mass to charge ratio. In this study, heavy Au cluster with a mass to charge ratio of 20,000 was selected. Under this condition, the actual distribution of Au clusters ranged from 100 atoms to 1000 atoms. On average, each cluster contained 400 Au atoms and four positive charges (Au<sub>400</sub><sup>4+</sup>). In below discussion, Au<sub>400</sub> is used to represent the whole distribution of size selected clusters used in this study.

The intensity of Au cluster beam was measured by a Faraday cup located at the outlet of the ion source. In our study, the total beam intensity was 15 pA and the focal area of the ion beam was ~2.6 mm<sup>2</sup>. With a total irradiation time of 10 min, surface coverage of Au<sub>400</sub> clusters was reached to around  $5.4 \times 10^{11}$  projectiles per cm<sup>2</sup>. The total impact energy of the Au cluster beam is 34 qkeV, where q is the charge the specific cluster bears. For an Au<sub>400</sub><sup>4+</sup> cluster, the impact energy was 340 eV/atom.

Figure 29 shows STM images of these Au<sub>400</sub><sup>4+</sup> clusters supported on the HOPG surface. Unlike Au atoms deposited on the TiO<sub>2</sub>(110) through thermal evaporation, these Au clusters were highly dispersed and spreaded evenly on the surface. The density

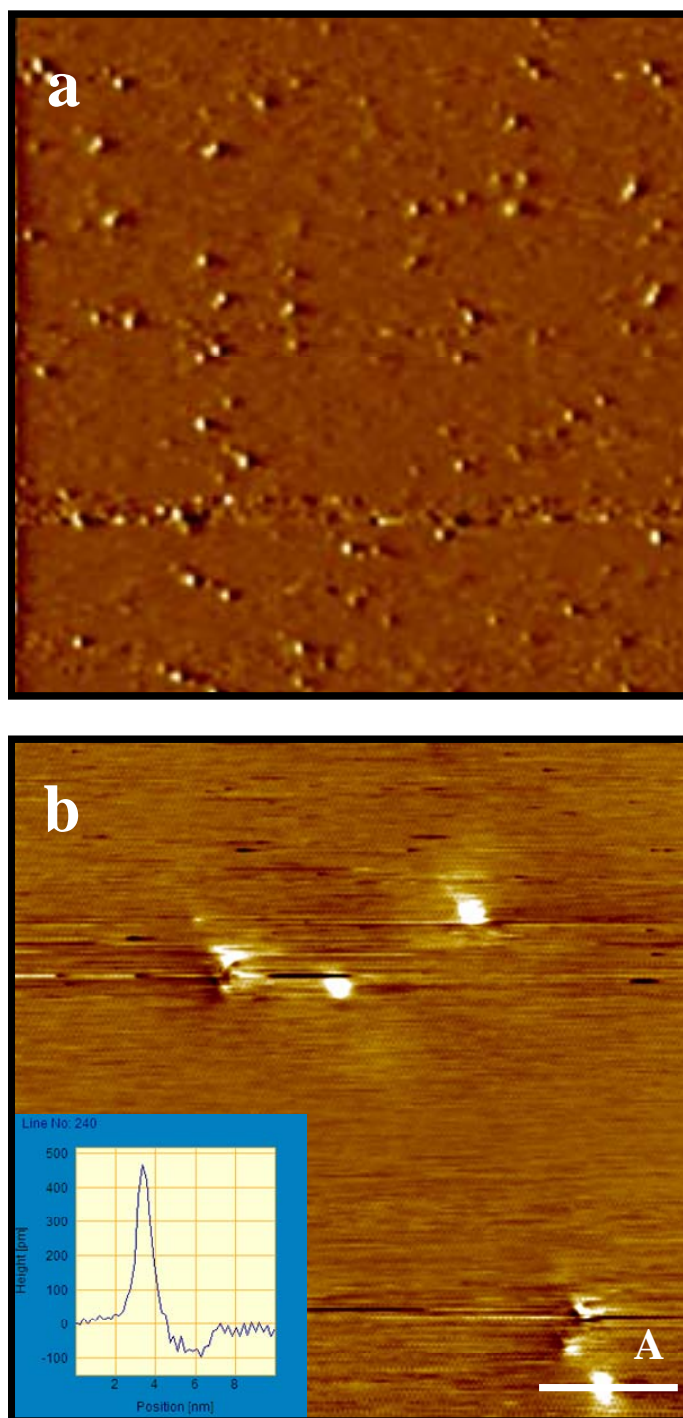


Figure 29. STM images of size selected Au clusters supported on HOPG. The size of deposited Au clusters varies from 100 to 1000 atoms per cluster. The majority of Au clusters have  $\sim 400$  atoms. (a)  $200 \text{ nm} \times 200 \text{ nm}$  STM image with tunneling parameters of  $V_s = 1 \text{ V}$  and  $I = 0.2 \text{ nA}$ . (b)  $50 \text{ nm} \times 50 \text{ nm}$  STM image with tunneling parameters of  $V_s = 1 \text{ V}$  and  $I = 2 \text{ nA}$ . Inset shows the line profile of cluster A.



of Au clusters obtained from Figure 29a was around  $4 \times 10^{11}$  projectiles per  $\text{cm}^2$ , in approximation to the Au ion flux measured from Faraday cup. The diameter of Au clusters ranged between 2.0-3.5 nm. Assuming a spherical shape, Au clusters in the diameter range of 2.0-3.5 nm consist of around 250 to 1300 Au atoms. The number of Au atoms estimated from STM measurement was reasonable with the size selection set by Wien filter, considering the positive offset caused by tip convolution in the STM measurement of cluster diameters. The high impact energy of  $\text{Au}_{400}$  clusters also caused minor damage to the HOPG surface. Figure 29b shows holes were created by Au clusters penetrating into the surface. Meanwhile, Au clusters with relatively lower impact energies would remain on the surface but created a crater along the direction of incoming trajectory, as evidenced in the inset line profile.

High resolution STM images were obtained on some Au clusters when they were partially buried into the HOPG surface (Figure 30). In Figure 30a, the distance between atoms on top of the protrusion was  $\sim 2.8 \text{ \AA}$ , which corresponds to the atomic distance on Au (111). The arrangement of atoms on top of the protrusion demonstrates the hexagonal pattern. The atomic distance and the atom arrangement suggest the protrusion in Figure 30a is fcc-stacked Au clusters with [111] orientation. Cosandey et al. [179] used electron backscattered diffraction (EBSD) in combination with high resolution scanning electron microscope (HRSEM) to determine the orientation of Au/ $\text{TiO}_2(110)$  and suggested that Au microcrystals grow with a [111] orientation. Figure 30 shows the fcc-stacking of Au atoms and [111] surface orientation are energetically favored even for small  $\text{Au}_{400}$  clusters. Au clusters in Figure 30 elongated along the direction of incoming trajectory. This is because when Au clusters were injected onto the HOPG surface, carbon atoms

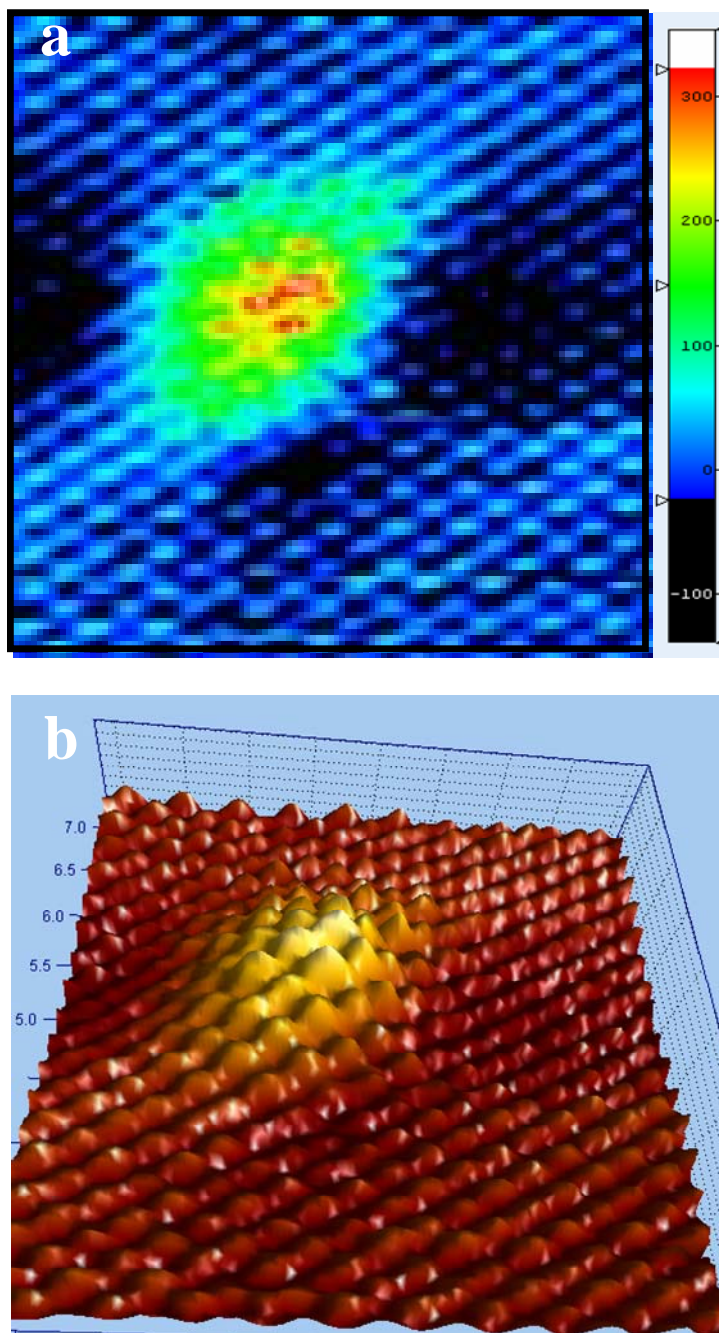


Figure 30. High resolution STM images of size selected Au clusters supported on HOPG. Au clusters penetrate into HOPG and leave a pit on the surface. (a)  $4.3 \text{ nm} \times 4.3 \text{ nm}$  STM image with tunneling parameters of  $V_s = 0.6 \text{ V}$  and  $I = 2 \text{ nA}$ . (b) 3D view of (a).

along the direction of incoming trajectory were pushed up and caused surface protrusions along the direction of trajectory.

The impact energy varies with the size and charge of incoming Au clusters. Figure 31 shows high resolution STM images of the holes on the HOPG surface created by Au clusters with high impact energy. Carbons atoms were pushed out and accumulated along the direction of the trajectory of Au clusters. Unlike Au clusters, these carbon clusters were amorphous and subjected to movements induced by tip scanning.

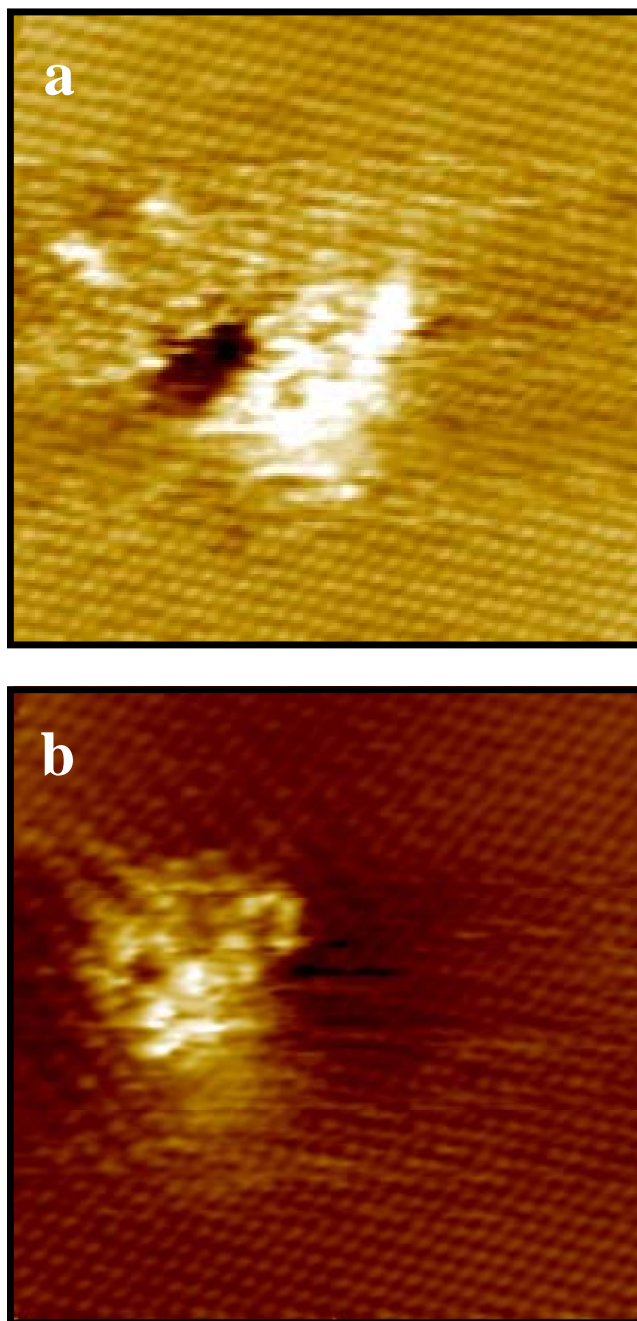


Figure 31. STM images of the HOPG surface after Au clusters fully penetrate into HOPG, leaving holes and amorphous Carbon clusters on the surface. Both STM images have tunneling parameters of  $V_s = 1$  V and  $I = 0.5$  nA. The image sizes are (a)  $8.2$  nm  $\times$   $8.2$  nm, and (b)  $7.8$  nm  $\times$   $8.0$  nm. Inset shows the line profile of cluster A.

## CHAPTER IV

### THE STRUCTURE AND STABILITY OF MODEL CATALYSTS IN REACTANT GASES

In this chapter, we present our studies on the surface morphologies of Au/TiO<sub>2</sub>(110) and Rh(110) in the presence of reactant gases. In particular, we have focused on the oxidation state and sintering kinetics of Au clusters supported on TiO<sub>2</sub>(110) in the presence of O<sub>2</sub> or during CO oxidation. The morphology and oxidation state of the Rh(110) surface during CO oxidation are also studied to help reveal the nature of catalytically active Au.

#### **Au clusters supported on TiO<sub>2</sub>(110) in O<sub>2</sub> or CO**

To investigate the influence of adsorbates on the surface morphology of Au/TiO<sub>2</sub>(110), *in-situ* STM has been applied to follow identical sets of Au clusters in the presence of O<sub>2</sub> or CO. The influence of O<sub>2</sub> exposure is compared in Figure 32a and 32b. Minimal changes were observed for 0.5 ML Au clusters supported on TiO<sub>2</sub>(110) after an exposure of 0.1 Torr O<sub>2</sub> for 1.5 hour at 300 K. In the presence of 0.1 Torr O<sub>2</sub>, most Au clusters with a height above 2.3 Å remain stable on the surface and the number density of Au clusters was  $1.5 \times 10^{12}/\text{cm}^2$  after O<sub>2</sub> exposure. Au clusters of monolayer thickness were not stable in O<sub>2</sub> and disappeared after the exposure of 0.1 Torr O<sub>2</sub>. No change of cluster positions has been apparent and the growth of new clusters was not observed. At 300 K, exposure of 0.1 Torr O<sub>2</sub> did not change the principal appearance of the TiO<sub>2</sub> surface. The density of surface TiO<sub>x</sub> species was low after extended O<sub>2</sub> exposure because

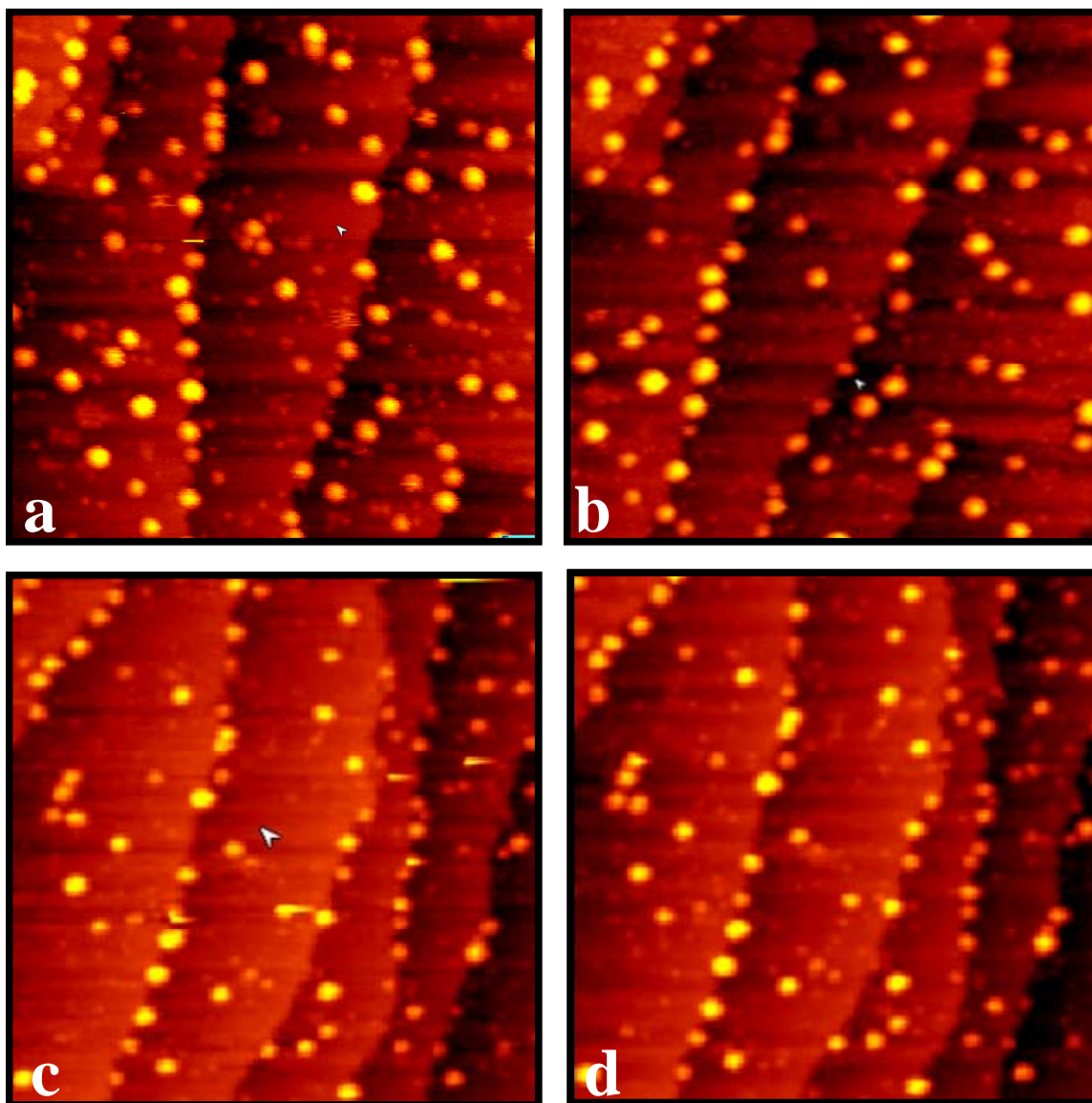


Figure 32.  $75 \text{ nm} \times 75 \text{ nm}$  *in-situ* STM images of 0.5 ML Au clusters supported on the  $\text{TiO}_2(110)$  surface (a) in UHV at 300 K, (b) after 1.5 hours in 0.1 Torr  $\text{O}_2$  at 300 K, (c) in UHV at 300 K, and (d) after 2 hours in 3 Torr CO at 300 K. Tunneling parameters are  $V_s = 2 \text{ V}$  and  $I = 0.1 \text{ nA}$ .

Ti interstitials diffuse onto the terraces via surface defects, which were covered by Au prior to O<sub>2</sub> exposure. The influence of CO exposure on 0.5 ML Au clusters supported on TiO<sub>2</sub>(110) was compared in Figure 32c and 32d. The exposure of 3 Torr CO at 300 K did not result in any noticeable change in either the TiO<sub>2</sub> substrate or supported Au clusters for 2 hours.

STM studies [64, 180] by Lai et al. observed an increase of the average diameter of Au clusters supported on TiO<sub>2</sub>(110) after Au/TiO<sub>2</sub>(110) was exposed to 10 Torr O<sub>2</sub> for 1 hour [180]. AFM study by Kielbassa et al. [165] found no apparent change in the size or density of Au clusters supported on a fully oxidized TiO<sub>2</sub>(110) surface in the presence of 50 mbar O<sub>2</sub>. The size of Au clusters prepared in their study was generally larger than 3 nm. Through our study, Au clusters with a size larger than 3 nm were found stable in the presence of O<sub>2</sub>, whereas some smaller clusters disappeared upon O<sub>2</sub> exposure. Thus, the discrepancy between early STM and AFM studies is due to the size dependency of sintering of Au clusters in O<sub>2</sub>.

The sintering mode of Au/TiO<sub>2</sub>(110) in the presence of O<sub>2</sub> can also be revealed through our *in-situ* STM study. At room temperature, a gradual increase of the size of large Au clusters were observed at the expense of small Au clusters, which indicates Au clusters sinter via atom diffusion between clusters. No cluster movement was detected through the consecutive images on the same surface area, which suggests no cluster migration happened on the surface. Therefore it could be concluded that O<sub>2</sub> induce the sintering of Au clusters via Ostwald ripening at room temperature.

The influence of O<sub>2</sub> on the surface morphology of Au/TiO<sub>2</sub>(110) was also investigated at elevated temperatures. Figure 33 shows the evolution of surface

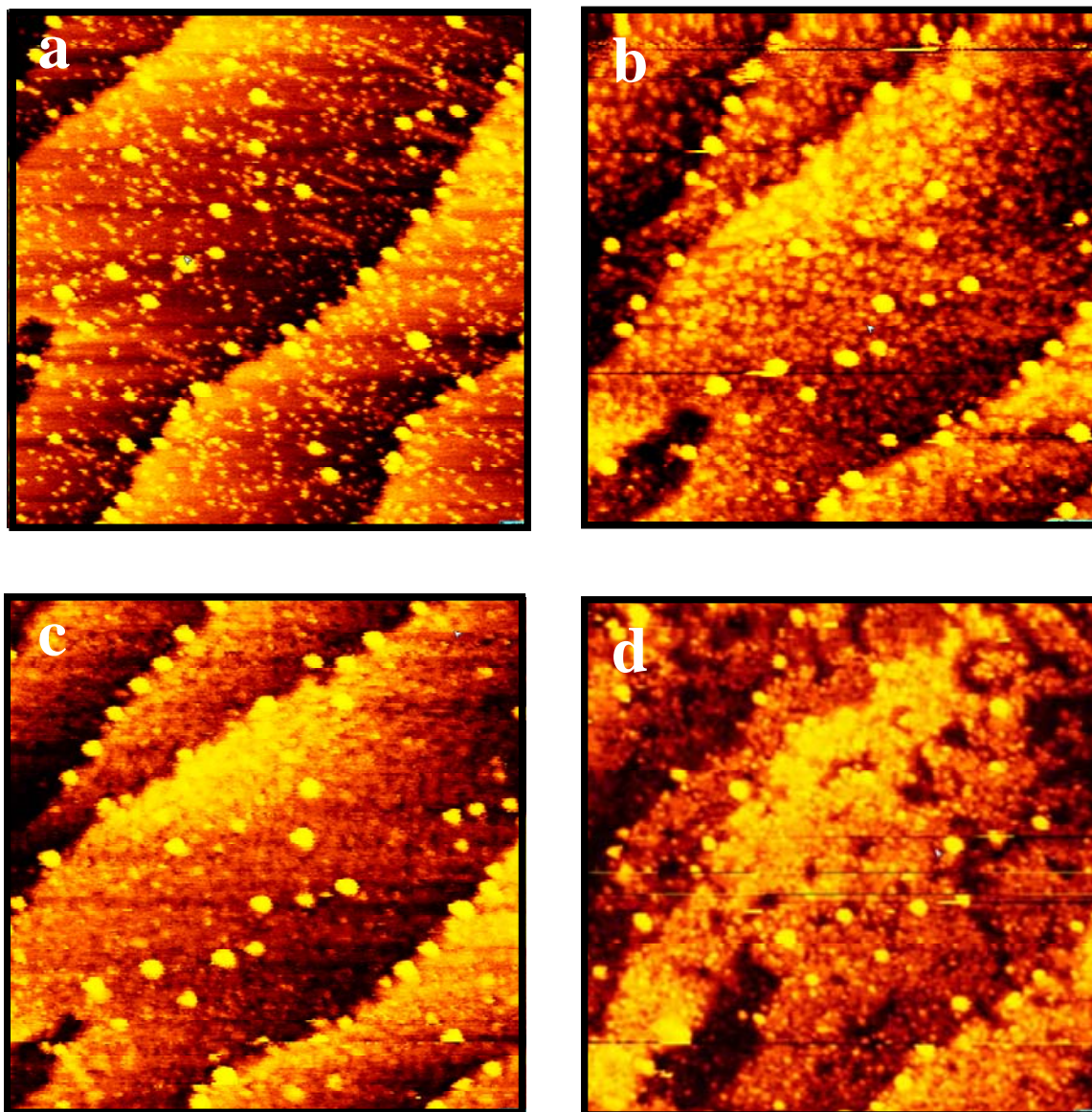


Figure 33.  $75 \text{ nm} \times 75 \text{ nm}$  *in-situ* STM images of 0.3 ML Au clusters supported on the  $\text{TiO}_2(110)$  surface at 600 K in (a) UHV, (b)  $10^{-8}$  Torr  $\text{O}_2$ , (c)  $10^{-6}$  Torr  $\text{O}_2$ , and (d)  $10^{-5}$  Torr  $\text{O}_2$ . Tunneling parameters are  $V_s = 2 \text{ V}$  and  $I = 0.1 \text{ nA}$ .



morphology of Au/TiO<sub>2</sub>(110) at 600 K and elevated O<sub>2</sub> pressures. STM images in Figure 33 were taken on the same surface area. In these images, the formation TiO<sub>x</sub> overlayers was observed via the rapid diffusion of Ti interstitials onto the surface, surrounded by oxygen and coalesced with neighboring TiO<sub>x</sub> species. When the pressure of O<sub>2</sub> was increased to 10<sup>-5</sup> Torr, oxidation of the substrate was much accelerated. Instead of taking a layer by layer growth at lower O<sub>2</sub> pressure, three dimensional TiO<sub>x</sub> clusters were also seen on the surface. Meanwhile, Au clusters remain static on the re-oxidized TiO<sub>2</sub>(110) surface at 600 K. No growth or decay of Au clusters was apparent from Figure 33. Similar to Au/TiO<sub>2</sub>(110) in UHV at 600 K, Au clusters were stabilized by the continuous enrichment of TiO<sub>x</sub> at the periphery of Au clusters. Extended exposure in 10<sup>-5</sup> Torr O<sub>2</sub> caused the instability of the tunneling junction and eventually the loss of tunneling currents.

Bennett et al. studied the re-oxidation process of Pd clusters supported on the reduced TiO<sub>2</sub>(110) [172, 181]. TiO<sub>x</sub> overlayer was found to grow preferentially around the periphery and on top of the flat Pd clusters. By measuring the height of clusters, the authors claimed over 5 layers of TiO<sub>2</sub> covered the cluster. In Figure 33d, no complete covering of Au clusters has been apparent even though a more drastic substrate oxidation has happened. Since both Au and Pd have a higher surface free energy than the TiO<sub>2</sub> oxide or TiO<sub>x</sub> species [160, 178], a complete covering of these metal clusters by TiO<sub>x</sub> is thermodynamically favored. However, compared to Pd, Au clusters have a lower affinity to TiO<sub>x</sub> and thus have a larger diffusion barrier for TiO<sub>x</sub> to climb up the cluster and stay stabilized. The increase of surface temperature to 600 K does not cause an apparent change in the morphology of support Au clusters at oxygen partial pressure of 10<sup>-5</sup> Torr.

Meanwhile, a drastic change in the size of Au clusters was observed at elevated O<sub>2</sub> pressures. Figure 34 shows a sudden increase in the size of Au clusters when the ambient O<sub>2</sub> pressure was increased to 10 Torr. Figure 34a was taken on the same surface area as Figure 32b. The enlargement of Au clusters was apparent comparing Figure 34a and 32b. The line profiles in Figure 34b compare the size and height of Au clusters in the presence of ~ 0.5 Torr and ~ 5 Torr O<sub>2</sub>. It is evident from the line profiles that small Au clusters with a size below 4 nm underwent a size increase when the pressure of O<sub>2</sub> was raised to ~5 Torr. Au clusters with a size larger than 5 nm remain not changed at elevated pressures. Figure 34b also suggested the size increase in Figure 34a was not due to a tip artifact but a real morphological change, because the tip artifact would usually cause similar size increase on all clusters. It is noteworthy that the tunneling junction became instable 2-3 minutes after Figure 34a was taken and caused the loss of image resolution. Infusing 3 Torr CO into the chamber could re-stabilize the tunneling junction. But the area in Figure 34a has been contaminated and covered by large particles, which were probably released from the STM tip during the loss of image resolution. STM images were then taken on other areas of the same surface. The average size of Au clusters observed in those areas was similar to that observed in Figure 34a. Because the density of small Au clusters was lower than in Figure 34a, it is hard to conclude whether CO would reduce the size of Au clusters. Nevertheless, all these observations suggest Au clusters with a size below 4 nm might have undergone a change in their oxidation states in the presence of 5 Torr O<sub>2</sub> at room temperature. Below we discuss the thermodynamic feasibility of oxidation of these supported Au clusters.

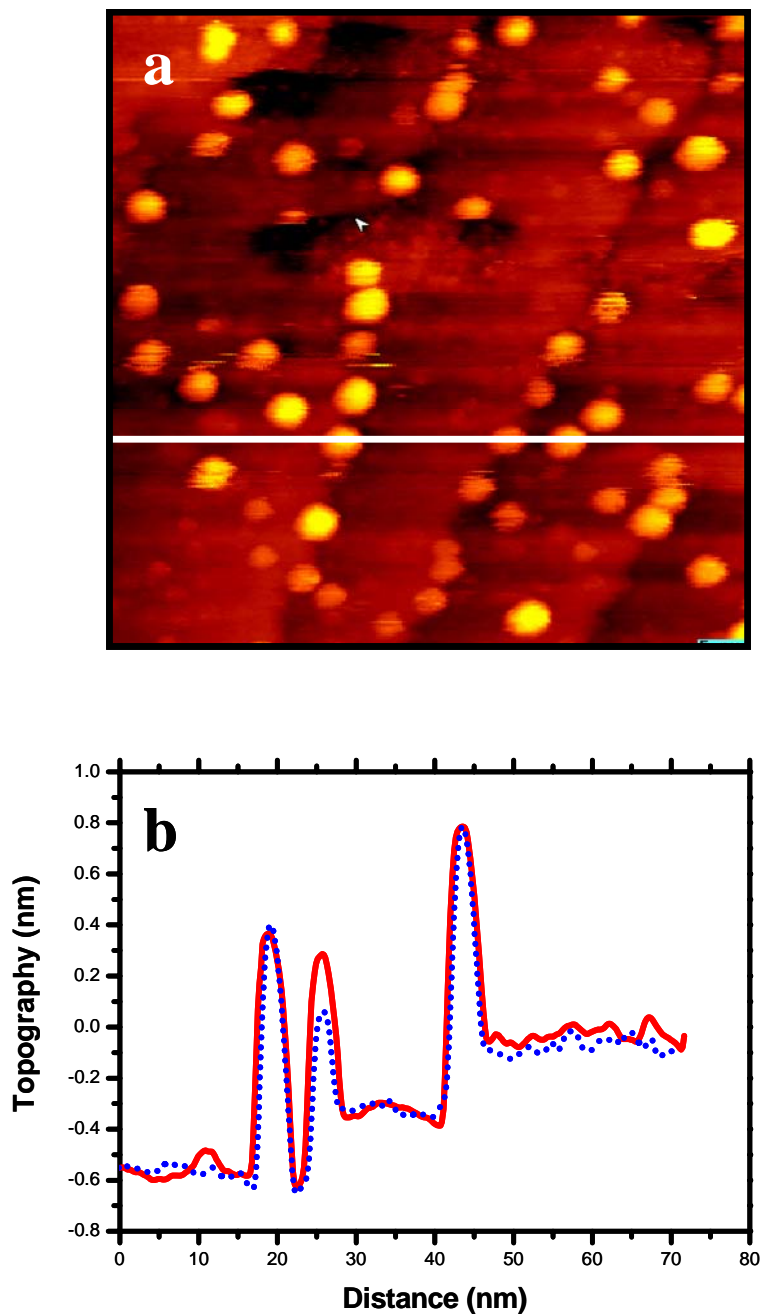


Figure 34. STM images of 0.5 ML Au clusters supported on the  $\text{TiO}_2(110)$  surface in the presence of  $\sim 5$  Torr  $\text{O}_2$ . Tunneling parameters are  $V_s = 2$  V and  $I = 0.1$  nA. (a) Surface of Figure 32(b) right after the  $\text{O}_2$  pressure is raised to 10 Torr. (b) Profile of the white line in (a) is plotted in red. The blue dotted line shows the profile of the same Au clusters in the presence of  $\sim 0.5$  Torr  $\text{O}_2$ .

### Chemical potentials of supported Au clusters

Chemical potentials (partial molar free energy) of supported Au clusters need be estimated before our discussion on the thermodynamics of supported Au clusters.

Experimental measurements on the chemical potential of nanoclusters have been rare due to difficulties in characterizing these clusters of limited size [107, 182, 183]. However, theoretical models have been developed to estimate the chemical potential of supported nanoclusters.

Three theoretical models have been available to calculate the chemical potential of supported metal clusters. Based on these models, chemical potentials of Au clusters supported on TiO<sub>2</sub>(110) were calculated and plotted in Figure 35. In conventional treatments, G-T relationship [106] is often used to describe the chemical potential of supported metal clusters. For an isotopic circular cluster, G-T relationship describes the chemical potential of the cluster as,  $\mu(r) - \mu(\infty) = 2\gamma\Omega/r$ , where  $\gamma$  is the surface free energy of the bulk metal and  $r$  is the radius of the cluster (Figure 35a).

A modified pairwise bond-additivity (MBA) model has been proposed by Campbell et al. [107, 184] considering the low coordination number of nanoclusters. The clusters are built by adding successive hexagonal close-packed layers in fcc packing. Each underlayer provides a threefold hollow site for each atom in the layer above. The effective radius  $r$  is calculated from the volume of the cluster assuming hemispherical shape. The chemical potential of clusters can be calculated assuming

$$\mu(r) - \mu(\infty) = -[H_{sub}(r) - H_{sub}(\infty)],$$

where the entropy difference between the nanocluster and the bulk metal is neglected.

$H_{sub}(r)$  is the molar sublimation enthalpy of metal clusters and can be approximated as

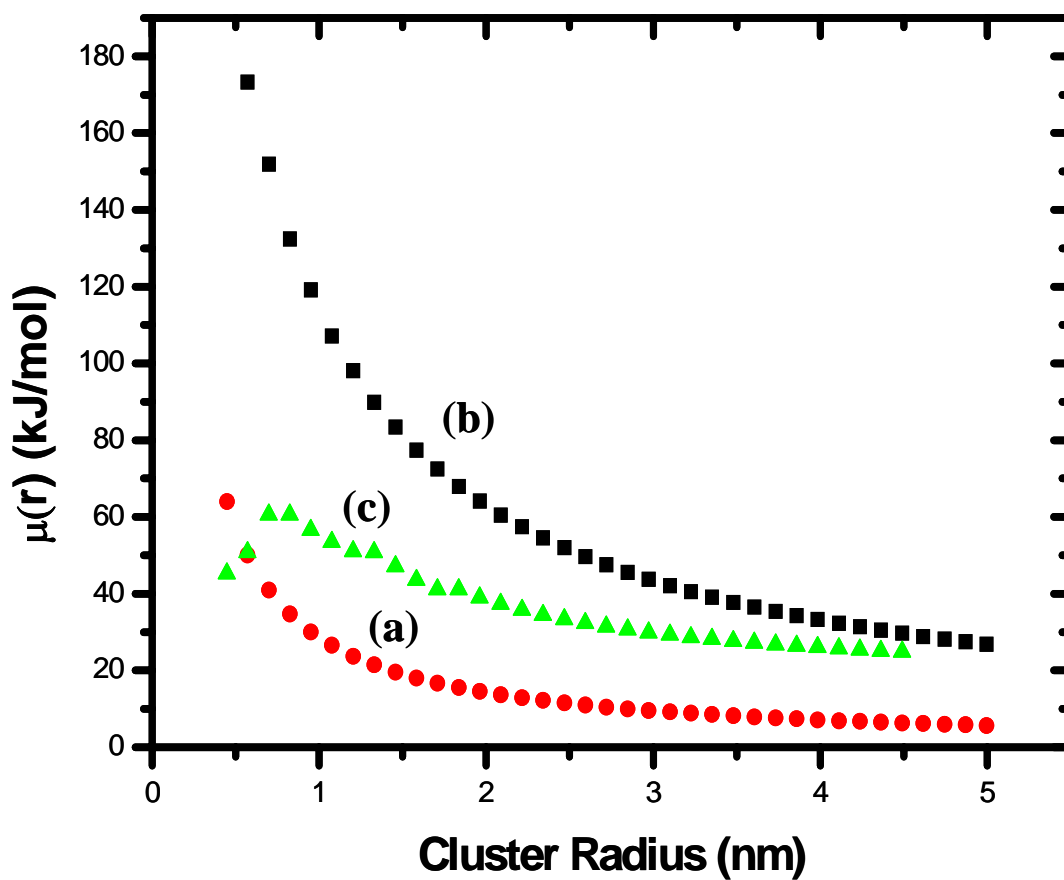


Figure 35. Calculated chemical potentials of Au clusters supported on  $\text{TiO}_2(110)$ . The calculations are based on different theoretical models: (a) G-T relation; (b) MBA model; (c) DFT model. In the calculation based on DFT model, the number of oxygen vacancies underneath each cluster is set at 9.

the metal-metal bond energy (bulk value) multiplying with the total bond number in the cluster (Figure 35b). In these two models, the influence of surface defects, such as oxygen vacancies and step edges, has not been included.

Recent studies on Au clusters supported on TiO<sub>2</sub>(110) [95, 179, 185] show these Au clusters exhibit a flat cap shape due to the strong bonding between surface defects and Au clusters. Lopez et al. [185] have constructed an equation to calculate the chemical potential of Au clusters supported on a TiO<sub>2</sub>(110) surface, taking into account the influence of oxygen vacancies. The total energy of a multilayer cluster is given by

$$E^{LML} = \gamma_0^{LML} \frac{2N}{L} + n_d E_d^{LML} + 4\pi \sqrt{\frac{N}{L}} E_{edge,top-bottom}^{LML} + 2(L-2)\pi \sqrt{\frac{N}{L}} E_{edge,central}^{LML},$$

where N is the number of atoms in a cluster, L is the total number of layers.  $\gamma_0^{LML}$ ,  $E_d^{LML}$ ,

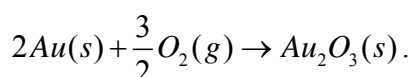
$E_{edge,top-bottom}^{LML}$  and  $E_{edge,central}^{LML}$  are surface energy, defect energy, edge energy for atoms in

the top and bottom layer and edge energy for the central layers respectively. In this equation for the calculation of free energy, each layer of the cluster is assumed to be circular and have no corner atoms. In this equation, parameters such as surface energy of Au atoms, edge energy of Au atoms and the defect energy of oxygen vacancies have been calculated by DFT. The equation is thus termed as the DFT model in following discussions. The number of defects underneath an Au cluster varies with the shape of the Au cluster, which could be estimated by correlating the cluster shape measured from our STM study with the shape diagram calculated by Lopez et al. [185]. Based on the DFT model, the chemical potential of supported Au clusters is plotted in Figure 35c. In this plot, the number of surface defects underneath each Au cluster is set at 9.

### Oxidation of Au clusters supported on TiO<sub>2</sub>(110)

Gold, known as the most inert metal to O<sub>2</sub>, requires high temperature and high O<sub>2</sub> pressure to form oxide [186]. Thermodynamically, oxidation of supported Au clusters might undergo at much lower temperature and oxygen partial pressure than the oxidation of bulk Au. Au<sub>2</sub>O<sub>3</sub> is the most stable Au oxide in bulk form [186] and is used here as the oxidative state of Au to discuss minimum thermodynamic requirements for the oxidation of supported Au clusters.

The formation of Au<sub>2</sub>O<sub>3</sub> is illustrated by the following reaction:



Unlike other metals, the oxidation of Au has a positive standard free energy of formation of Au<sub>2</sub>O<sub>3</sub> ( $\Delta G_{298}(Au_2O_3) = 79.8 \text{ kJ/mol}$ ) at room temperature [186]. For bulk Au, the

free energy of the above reaction can be expressed as  $\Delta G = RT \ln K^{eq} = \frac{3}{2}RT \ln P_{O_2} / P^\ominus$ ,

where  $K^{eq}$  is equilibrium constant of the oxidation reaction,  $P_{O_2}$  is the partial pressure of O<sub>2</sub>, and  $P^\ominus$  is the standard pressure of 1 bar. For Au clusters, the influence of curvature

to the free energy of Au has to be considered. The free energy change of the reaction can

be expressed as,  $\Delta G(r) = \Delta G_{298}(Au_2O_3) - 2\mu_{Au}(r) = \frac{3}{2}RT \ln P_{O_2} / P^\ominus$ , where  $\mu_{Au}(r)$  is the

chemical potential (partial molar free energy) of Au clusters with radius  $r$ .

Based on the chemical potentials of Au clusters supported on TiO<sub>2</sub>(110) (Figure 35), the equilibrium O<sub>2</sub> pressure for Au oxidation versus temperature are plotted in Figure 36, as in van't Hoff format. Based on the chemical potential of supported Au clusters calculated from G-T relationship, the formation of Au<sub>2</sub>O<sub>3</sub> was not possible in 1 bar O<sub>2</sub>

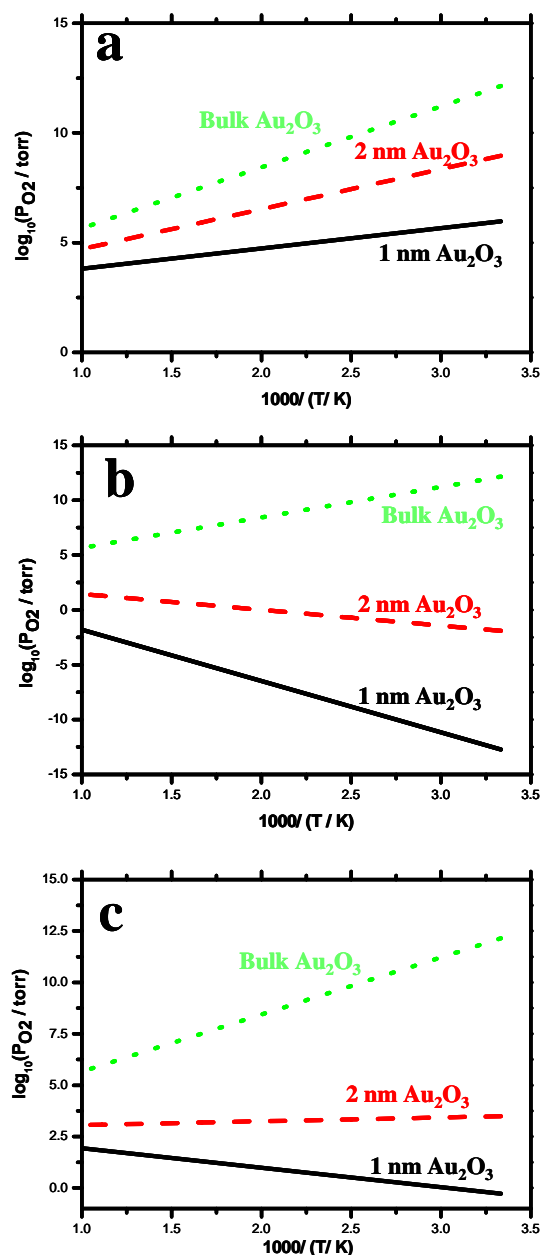


Figure 36. Plots of the equilibrium  $\text{O}_2$  pressure versus temperature in van't Hoff format for the oxidation of Au clusters supported on  $\text{TiO}_2(110)$ , assuming the oxidation state as  $\text{Au}_2\text{O}_3$ . The plots are calculated based on the chemical potential of supported Au clusters, which were estimated from (a) G-T relationship, (b) MBA model, and (c) DFT model. In each plot, the top line is experimental data for the formation of bulk  $\text{Au}_2\text{O}_3$ . The two lower lines are predicted for Au clusters with 2 and 1 nm radius supported on  $\text{TiO}_2(110)$ .



even for Au clusters of 1 nm radius (Figure 36a). If the chemical potential of supported Au clusters were predicted using MBA model, Au clusters of 1 nm radius would form oxides at room temperature even in UHV. For Au clusters of 2 nm radius, an O<sub>2</sub> partial pressure of around 1 Torr or above is required for the formation of Au<sub>2</sub>O<sub>3</sub> (Figure 36b). According to the chemical potentials calculated using the DFT model (Figure 36c), the oxidation of small Au clusters (1-2 nm radius) requires an O<sub>2</sub> partial pressure ranging from 1 Torr to a few bars. At 300 K, 1 Torr O<sub>2</sub> is ready to oxidize Au clusters of 1 nm radius.

Figure 37 plots the required P<sub>O<sub>2</sub></sub> pressure for the formation of Au<sub>2</sub>O<sub>3</sub> as a function of Au cluster radius at room temperature. The blue line represents the partial pressure of O<sub>2</sub> at 1 bar. In 1 bar O<sub>2</sub> and room temperature, Au clusters with radius around 3 nm or below, i.e., diameter < 6 nm, could be oxidized and form Au<sub>2</sub>O<sub>3</sub> according to the predictions using the MBA model. The calculation based on the DFT model predicts the formation of Au<sub>2</sub>O<sub>3</sub> is feasible for Au clusters with radius below 1.8 nm, whereas the calculation based on G-T relationship suggests only very small Au clusters with radius smaller than 0.7 nm (d < 1.4 nm) could be oxidized in 1 bar O<sub>2</sub> and at room temperature.

Among the predictions based on different chemical potential models, the prediction based on the DFT model is most close to our experimental observations. The prediction based on DFT model matches our observation that Au clusters could not be oxidized between 300-600 K in low O<sub>2</sub> pressure (P<sub>O<sub>2</sub></sub>=10<sup>-5</sup> Torr). Our experimental observation also suggests Au clusters with radius smaller than 2 nm could be oxidized in the presence a few Torr O<sub>2</sub> at room temperature, whereas the prediction based on DFT model suggests Au clusters with radius smaller than 1.6 nm be oxidized under the same

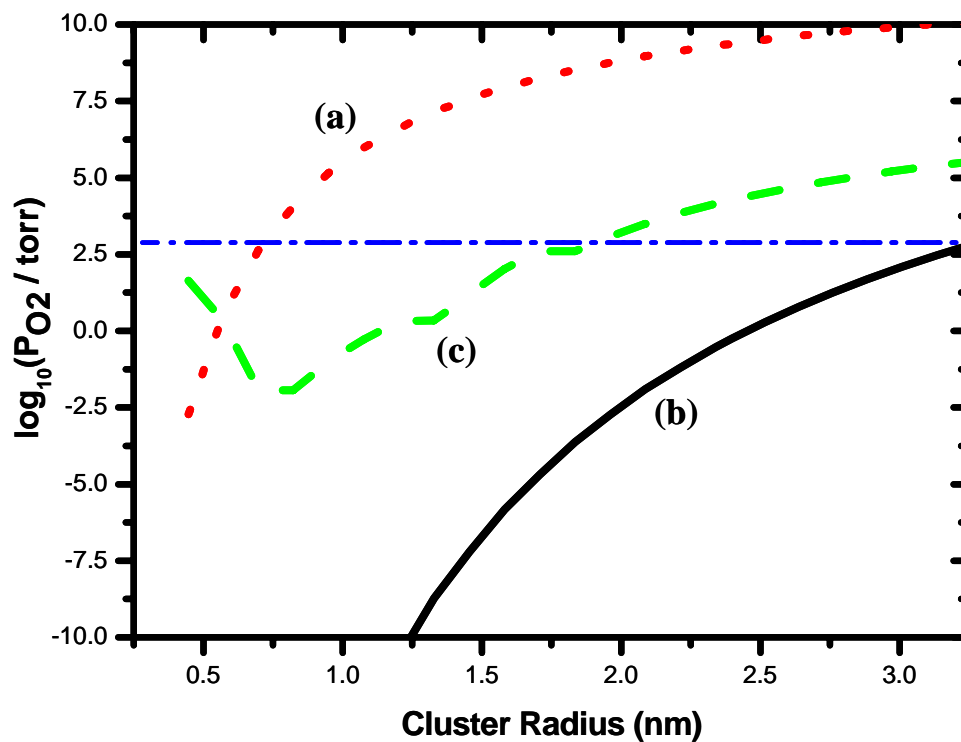


Figure 37. Plot of the equilibrium  $O_2$  pressure versus cluster radius for the oxidation of Au clusters supported on  $TiO_2(110)$ , assuming the oxidation state as  $Au_2O_3$ . The plot is derived based on chemical potentials of supported Au clusters, which are calculated from (a) G-T relationship, (b) MBA model, and (c) DFT model. The blue line shows the  $O_2$  partial pressure of 1 bar to note the difference in predictions, which are based on different chemical potential models.

conditions. The prediction based on G-T relationship or the MBA model contradicts our experimental observations. The prediction based on G-T relationship suggests the oxidation of Au clusters with radius above 0.7 nm is not possible at room temperature and above in 1 bar O<sub>2</sub>. On the other hand, the prediction based on the MBA model suggests even Au clusters with 3 nm radius can be readily oxidized into Au<sub>2</sub>O<sub>3</sub> in the presence of 1 bar O<sub>2</sub> at room temperature. Moreover, the prediction based on MBA model shows Au clusters of 1.5 nm radius could be oxidized even in 10<sup>-10</sup> Torr O<sub>2</sub>, which is apparently not correct based on our UHV studies.

Therefore, chemical potentials of Au clusters calculated from the DFT model could be used to estimate the thermodynamic behavior of Au clusters supported on TiO<sub>2</sub>(110). G-T relationship and MBA model have estimated the chemical potential of supported Au clusters too low or too high, which is probably due to the absence of substrate effect in these models. It should also be noted here that the chemical potential increase due to the curvature of Au<sub>2</sub>O<sub>3</sub> has not been considered yet. Thus, the O<sub>2</sub> partial pressure predicted in Figure 36 and 37 might be the lower limit for the oxidation of Au clusters supported on TiO<sub>2</sub>(110).

The possible change in the oxidation state of Au in the presence of O<sub>2</sub> is very interesting because it might provide insightful information to settle the long debate on the oxidation state of Au clusters supported on the oxide during CO oxidation. UHV studies and theoretical calculations [88-91, 187-189] have suggested that electronic charge is transferred from the oxide support to Au yielding anionic Au, whereas steady-state catalysis studies and post-reaction surface analysis identified the appearance of cationic

Au, suggesting cationic Au responsible for the catalytic reactivity during CO oxidation [190-193].

Hammer et al. [194] reviewed the extensive studies, both experimentally and theoretically, on the charge state of oxide supported Au clusters. In their review, they attributed the discrepancy to the difference between the oxidation state of the oxide used in UHV studies and that of the oxide used in catalysis studies. Through their DFT calculation, Hammer et al. [194] suggested Au is anionic on a reduced  $\text{TiO}_2(110)$  surface, i.e. the support used in UHV studies, whereas cationic Au show up on a fully oxidized  $\text{TiO}_2(110)$  surface, i.e. the support used in steady-state catalysis studies. A recent work on the thermal stability of Au clusters supported on different  $\text{TiO}_2(110)$  surfaces [97] has been used by Hammer et al. [194] to support their suggestion. In that work, Au clusters are found to bind most strongly on an oxygen covered  $\text{TiO}_2(110)$  surface. In our above studies (chapter I), however, we have found the strong binding is due to the increased surface defects, i.e.,  $\text{TiO}_x$  species, rather than the formation of Au-O-Ti bonds, as interpreted by Matthey et al [97]. In this study, our results suggest Au clusters might undergo a change in the oxidation state in the presence of  $\text{O}_2$ . The presence of cationic Au in catalysis studies might simply be due to the oxidation of Au in an  $\text{O}_2$ -rich atmosphere, rather than the different oxidation states of  $\text{TiO}_2(110)$  support.

The question now comes to which state of Au is the active phase for CO oxidation. Is the active phase anionic as observed in UHV studies, or cationic as observed in catalysis studies? We then studied the surface morphology of Au/ $\text{TiO}_2(110)$  during CO oxidation under a variety of conditions.

### **Sintering of Au/TiO<sub>2</sub>(110) during CO oxidation**

Early STM studies [65, 81, 95] have shown Au clusters supported on TiO<sub>2</sub>(110) sinter during CO oxidation. In this study, we have further measured the sintering kinetics of Au/TiO<sub>2</sub>(110) during CO oxidation between 300-600 K. We found the sintering of Au could be separated into two temperature ranges between 300-600 K. The first range is between 300-410 K, when we found surface TiO<sub>x</sub> growth was not apparent at the initial stage of Au sintering. The second range is at 500 K and above, when we found overlayer TiO<sub>x</sub> growth accompanying the sintering of Au clusters. The study of sintering kinetics will be focused on the temperature between 300-410 K.

Figure 38 shows the morphological changes of 0.5 ML Au clusters supported on TiO<sub>2</sub>(110) in the presence of CO/O<sub>2</sub> at 300 K. Under UHV condition, Au clusters stayed immobile and showed no detectable change of either cluster size or shape for more than 4 hours. Sintering of Au clusters started immediately upon the infusing of CO and O<sub>2</sub> mixture gas. 0.1 Torr CO/O<sub>2</sub> gas mixture (1:1 ratio) was infused into the chamber with the STM tip in tunneling. Consecutive images were then taken on the same surface area as a function of time. Figure 38 shows no apparent change of cluster positions before and after gas exposure. Instead, small Au clusters gradually decayed whereas large Au clusters grew. The gradual change in cluster size and static cluster positions manifested an Ostwald ripening process. As captured in the series of images, Au clusters with a height around 2.3 Å disappeared within 28 minutes after the infusing of mixture gas. Most Au clusters with a height around 4.6 Å or less (assuming the height of Au clusters of 2 layer thickness is 4.6 Å [179]) disappeared within 2 hours of CO oxidation reaction.

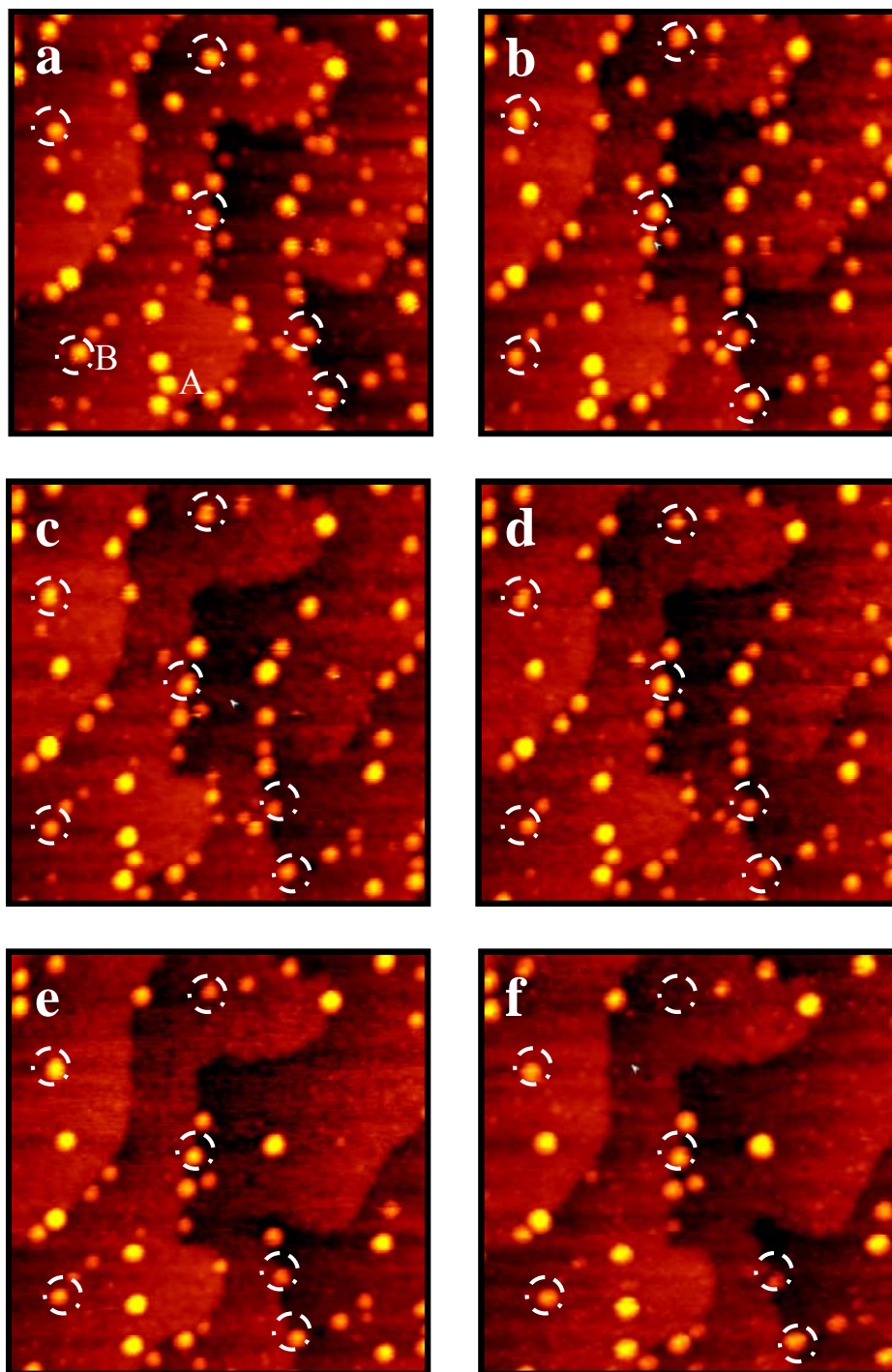


Figure 38.  $75 \text{ nm} \times 75 \text{ nm}$  *in-situ* STM images of 0.5 ML Au clusters supported on the  $\text{TiO}_2(110)$  surface in the presence of 0.1 Torr CO and  $\text{O}_2$  mixture at 300 K. (a) - (f) are consequently taken at the same surface area. The time intervals are: (a) 0 min; (b) 28 min; (c) 42 min; (d) 63 min; (e) 120 min; (f) 280 min. Tunneling parameters are  $V_s = 2 \text{ V}$  and  $I = 0.1 \text{ nA}$ .

The number density of Au clusters decreased to  $6.9 \times 10^{11}/\text{cm}^2$  after 2 hours of CO oxidation and decreased slowly afterwards.

Figure 39 shows the sintering of 0.2 ML Au/TiO<sub>2</sub>(110) in the presence of 0.1 Torr CO/O<sub>2</sub> (1:1) at 300 K. Similar to Figure 38, large Au clusters grew at the expense of small Au clusters and no change of cluster position was apparent through the consecutive images of the same surface. Most Au clusters with a height of 4.6 Å or less disappeared within 2 hours of CO oxidation. The density of Au clusters decreased to  $7.1 \times 10^{11}/\text{cm}^2$  within 2 hours and decreased slowly afterwards.

At elevated temperatures, CO oxidation induced sintering of supported Au clusters was observed at an increased sintering rate. Figure 40 summarizes the morphological changes of 0.65 ML Au/TiO<sub>2</sub>(110) at 410 K in 0.1 Torr CO/O<sub>2</sub> (1:1). Similar to Figure 38, Au clusters were found to sinter via Ostwald ripening. Most Au clusters with a height less than 4.6 Å disappeared within 1 hour of CO oxidation reaction. The total cluster density decreased by 60% to  $6.9 \times 10^{11}/\text{cm}^2$  within 1 hour of CO oxidation and decreased slowly afterwards. Adsorbate-induced change of the substrate morphology became apparent at elevated temperatures. The density of small protrusions with a height around 1-2 Å increased during the reaction. These protrusions were TiO<sub>x</sub> species formed on the TiO<sub>2</sub>(110) surface during CO oxidation. In the presence of oxygen, interstitial Ti cations would diffuse to the surface and form TiO<sub>x</sub> species which serves as the precursor of surface regrowth. These protrusions were not likely to be small Au atoms because Au clusters of monolayer thickness were unstable and would decay rapidly in the presence of 0.1 Torr CO/O<sub>2</sub>, as shown in Figure 38.

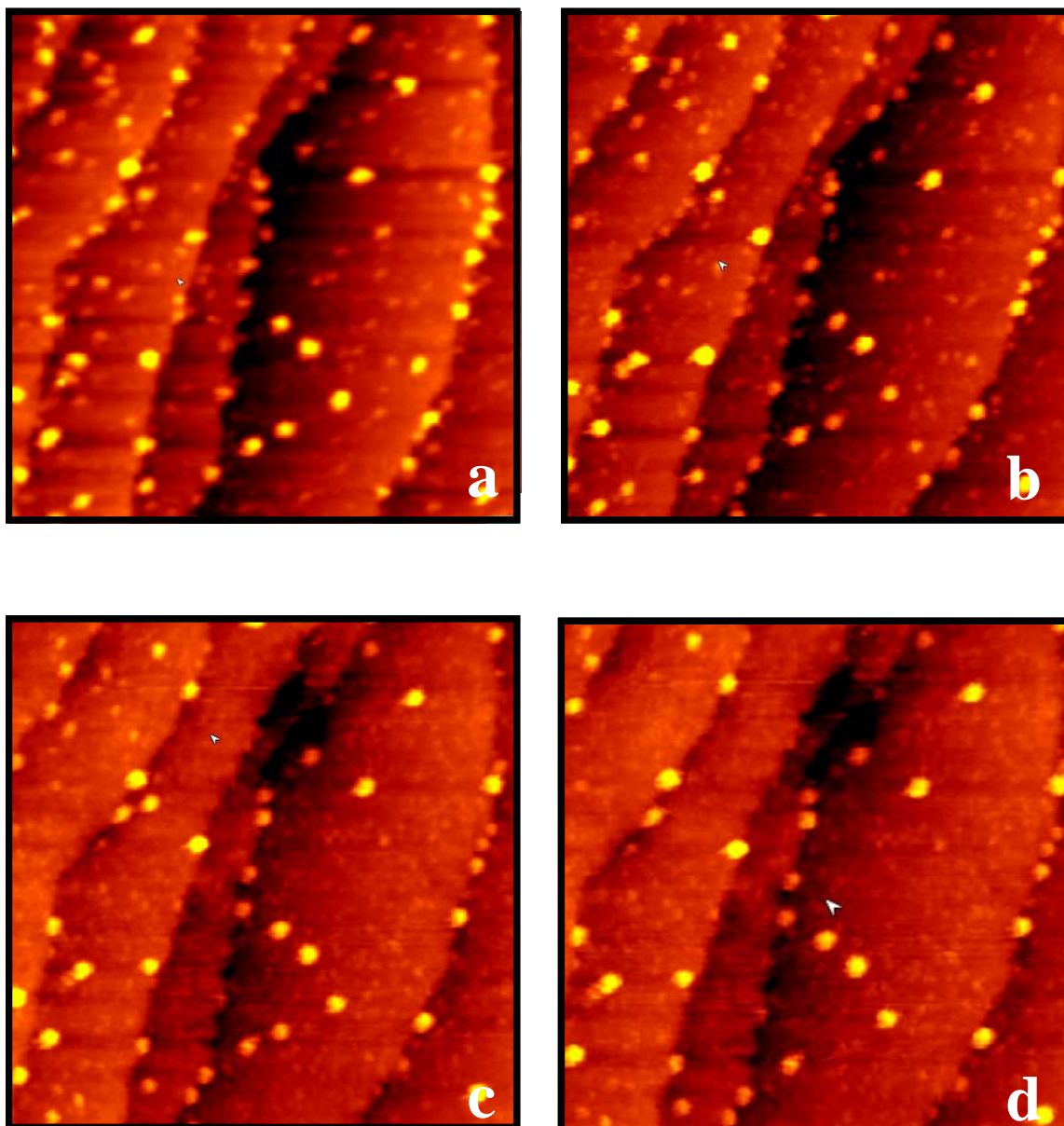


Figure 39.  $75 \text{ nm} \times 75 \text{ nm}$  *in-situ* STM images of 0.2 ML Au clusters supported on the  $\text{TiO}_2(110)$  surface in the presence of 0.1 Torr CO and  $\text{O}_2$  mixture gas at 300 K. (a) - (d) are consequently taken at the same surface area. The time intervals are: (a) 0 min; (b) 21 min; (c) 63 min; (d) 120 min. Tunneling parameters are  $V_s = 2 \text{ V}$  and  $I = 0.1 \text{ nA}$ .



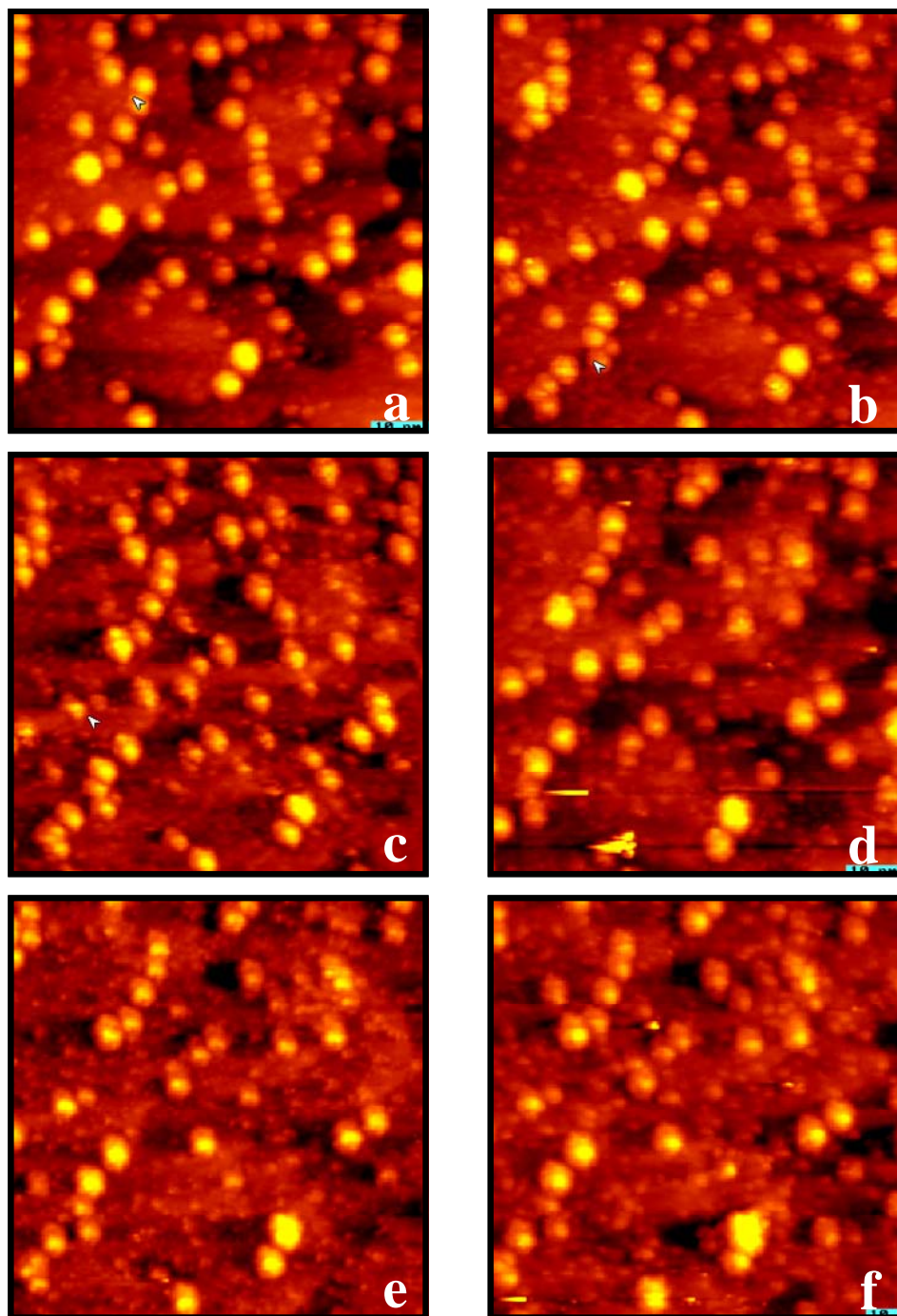


Figure 40.  $75\text{nm} \times 75\text{nm}$  *in-situ* STM images of 0.65 ML Au clusters supported on the  $\text{TiO}_2(110)$  surface in the presence of 0.1 Torr CO and  $\text{O}_2$  mixture gas at 410 K. (a) - (f) are consequently taken at the same surface area. The time intervals are: (a) 0 min; (b) 21 min; (c) 42 min; (d) 63 min; (e) 80 min; (f) 120 min. Tunneling parameters are  $V_s = 2\text{V}$  and  $I = 0.1\text{nA}$ .

Figure 41 compares the height distribution of Au clusters before and after 2 hours of CO oxidation at 300 K and 410 K. The number density of Au clusters with height taller than the median height would grow whereas the number density of Au clusters with height smaller than the median height would decrease. For Au clusters of the same size, the decay rates of Au clusters increased as the surface temperature or the surface coverage increased. The sintering of Au clusters with height less than 4.6 Å were very rapid and less influenced by the surface Au coverage. For Au clusters of different coverages, in the presence of 0.1 Torr CO/O<sub>2</sub>, the decrease of cluster density became very slow after the total cluster density dropped to around  $7 \times 10^{11}/\text{cm}^2$ .

Figure 42 summarizes the sintering of 0.5 ML Au/TiO<sub>2</sub>(110) at 500 K and 600 K during CO oxidation. At temperatures above 500 K, the growth of TiO<sub>x</sub> overlayers became apparent. Figure 42a and 42b compare surface morphology of Au/TiO<sub>2</sub>(110) before and after CO oxidation. The total pressure used in this experiment was 2.1 Torr, higher than 0.1 Torr CO/O<sub>2</sub> mixture used in the above studies between 300-410 K. However, the sintering rate at 500 K was slower than the sintering observed at 410 K (Figure 40). This might be due to the formation of TiO<sub>x</sub> overlayers, which decelerated the Ostwald ripening of Au clusters. The influence of TiO<sub>x</sub> overlayers is more evident during the sintering at 600 K, as shown in Figure 42c and 42d. At 600 K, no sintering was apparent on these Au clusters in the presence of 0.6 Torr CO/O<sub>2</sub> mixture gas for ~ 1 hour. To prevent the rapid surface re-growth of TiO<sub>2</sub>(110) at 600 K, high CO/O<sub>2</sub> ratio (10:1) was used in this experiment to maintain a monolayer of TiO<sub>x</sub> during CO oxidation. However, due to the oxidation of TiO<sub>2</sub>(110) bulk, the tunneling current was lost after ~ 1 hour of CO/O<sub>2</sub> exposure at 600 K. The slowed Au sintering at 500 K and 600 K might be

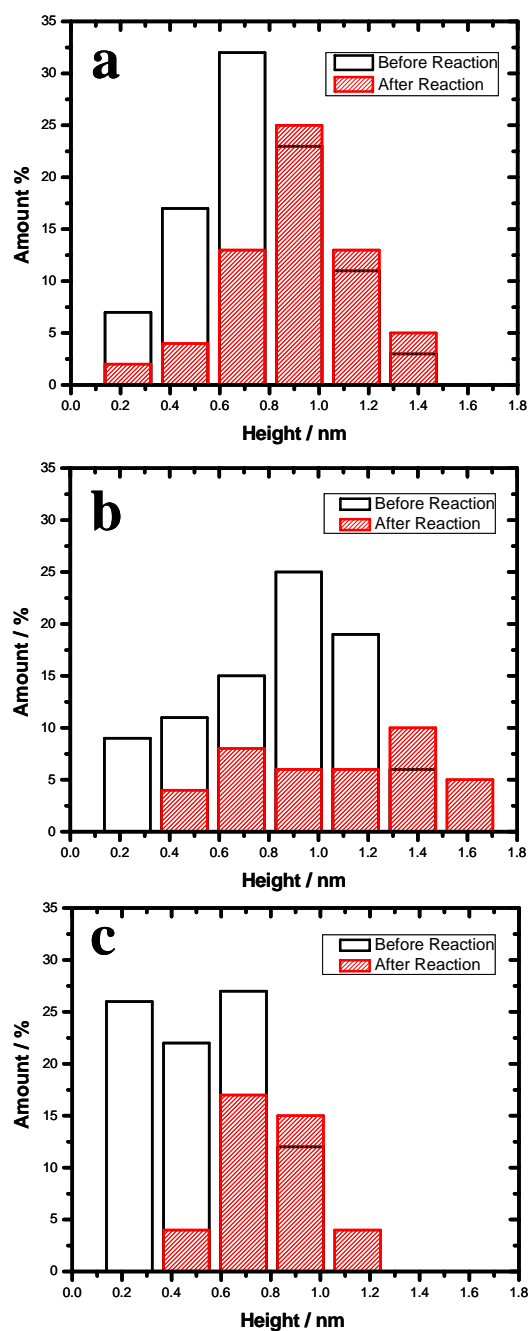


Figure 41. Height distributions of Au clusters supported on TiO<sub>2</sub>(110) before and after 2 hours of CO oxidation (The total gas pressure is 0.1 Torr with P<sub>CO</sub>: P<sub>O<sub>2</sub></sub> = 1:1). (a) 0.5 ML Au/TiO<sub>2</sub>(110), 300 K. (b) 0.65 ML Au/TiO<sub>2</sub>(110), 410 K. (c) 0.2 ML Au/TiO<sub>2</sub>(110), 300 K.

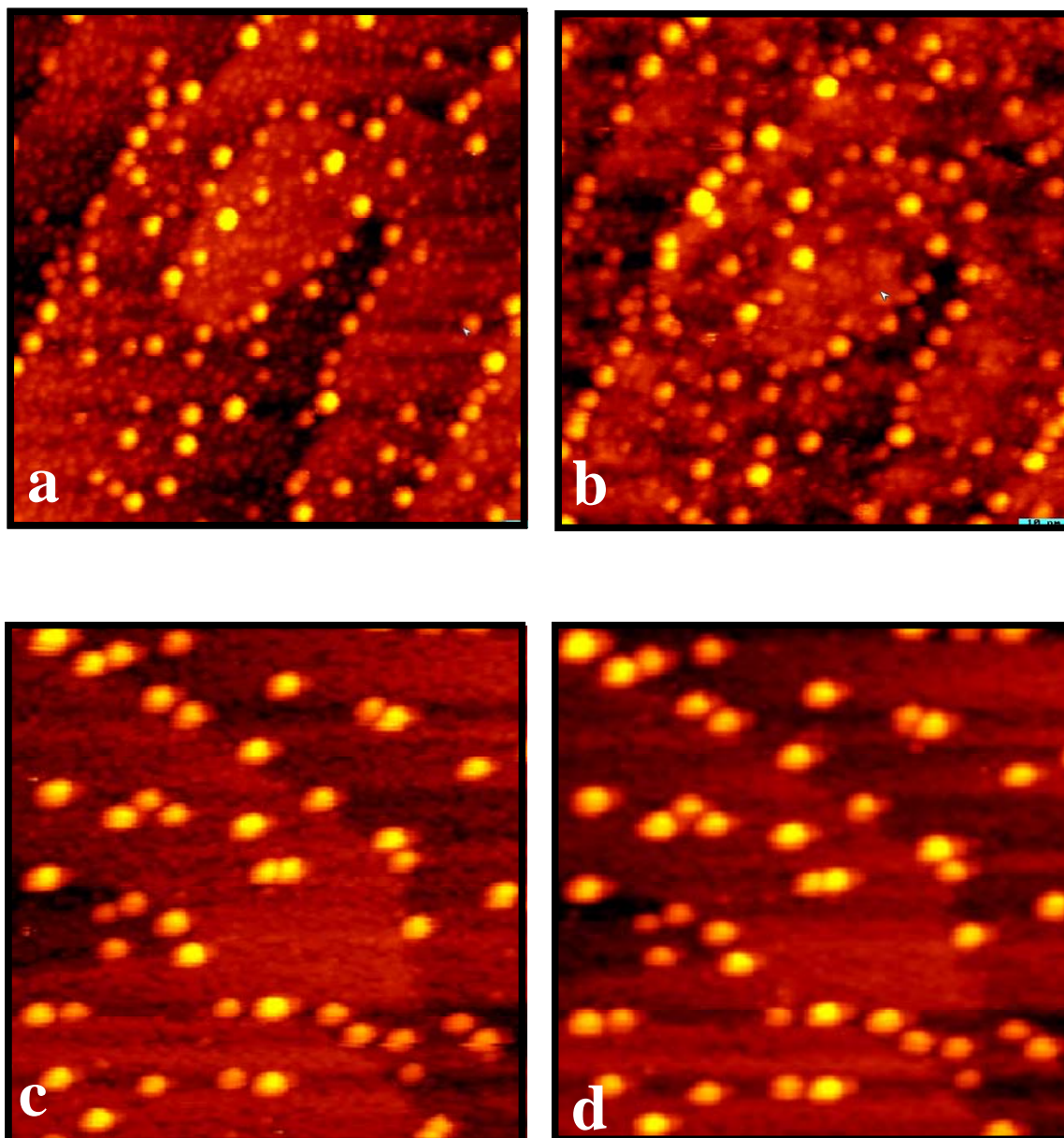


Figure 42.  $75 \text{ nm} \times 75 \text{ nm}$  *in-situ* STM images of 0.5 ML Au clusters supported on the  $\text{TiO}_2(110)$  surface in (a) UHV at 500 K, (b) 2.1 Torr  $\text{CO/O}_2$  (2:1) mixture gas at 500 K for 0.5 h, (c)  $10^{-5}$  Torr  $\text{CO/O}_2$  (1:1) mixture gas at 600 K, and (d) 0.6 Torr  $\text{CO/O}_2$  (10:1) mixture gas for 1 h. (a) and (b) are on the same surface area. (c) and (d) are on the same surface area. Tunneling parameters are  $V_s = 2 \text{ V}$  and  $I = 0.1 \text{ nA}$ .

caused by two factors, the formation of  $\text{TiO}_x$  overlayer and the increased CO partial pressure. The appearance of  $\text{TiO}_x$  overlayer complicates the sintering kinetics of supported Au clusters during CO oxidation. In the following discussion, we focus on the sintering kinetics at 300-410 K, where the influence of  $\text{TiO}_x$  can be neglected.

Adsorbate-induced changes in surface morphology have been observed extensively for supported metal clusters [64, 65, 81, 93, 98, 99, 101, 165, 166, 195-197]. For example, CO and NO have been reported to promote the dissociation of Rh and Ir clusters into metal atoms at room temperature [98, 99, 198-200]. At high temperatures ( $> 600$  °C), an accelerated sintering of supported metal catalysts were often observed within an oxidative environment [101, 106, 201]. These studies have often attributed the decay of metal clusters to the formation of volatile metal-adsorbate complex, which results in the disintegration of metal clusters. The sintering of supported Au clusters induced by  $\text{O}_2$  or during CO oxidation can not be simply explained by the formation of metal-adsorbate complex. Au clusters supported on  $\text{TiO}_2(110)$  are stable in pure CO gas (Figure 32) and have a much slower sintering rate in pure  $\text{O}_2$  (Figure 32) than during CO oxidation. If the formation of metal-oxygen complex is the reason for sintering, the existence of CO should reduce the concentration of metal-oxygen complex and result in a slower rather than accelerated sintering rate.

Our studies on the growth of Au clusters on  $\text{TiO}_2(110)$ , as well as previous STM and DFT studies [88, 91, 95, 185, 202, 203], have shown substrate defects play a major role in the stabilization of Au clusters. These studies demonstrate Au clusters prefer to nucleate at surface defects such as oxygen vacancies and step edges. Surface defects of  $\text{TiO}_2(110)$  determine the shape and distribution of Au clusters. DFT calculation also

shows the binding energy of Au atoms to an oxygen vacancy in TiO<sub>2</sub> is about 1.6 eV. Therefore, the detachment of Au atoms from Au clusters needs to overcome the interface bonding between defects and Au. O<sub>2</sub>-induced sintering of Au clusters supported on TiO<sub>2</sub>(110) might be explained by the influence of O<sub>2</sub> on the interface bonding. Various studies have postulated O<sub>2</sub> adsorb and dissociate on Au clusters or at the interface of Au/TiO<sub>2</sub>(110) [78, 204-206]. Thermodynamically, the adsorption and dissociation of O<sub>2</sub> can heal the surface defect and lead to the break down of interface bond between defects and Au. Small Au clusters are thus destabilized due to its low coordination numbers. The stabilization of Au clusters with a height taller than 4.6 Å is less dependent on the interface bond and thus less influenced by oxygen induced breakdown of the interface bond.

The synergetic effect of CO and O<sub>2</sub> mixture might be explained in a reaction induced mechanism. DFT studies by Liu et al. [207] suggested CO oxidation on Au/TiO<sub>2</sub>(110) can proceed with high efficiency without O<sub>2</sub> dissociation. The barrier for the direct bi-molecular pathway to produce CO<sub>2</sub> is 0.10 eV, much lower than the dissociation barrier of O<sub>2</sub> on Au/TiO<sub>2</sub>(110), 0.52 eV. The production of each CO<sub>2</sub> molecule releases an energy of 2.9 eV [208, 209]. The energy generated from CO oxidation could be transferred to electrons at the surface of Au clusters and excite hot electrons. Ji et al. [208-210] have demonstrated that hot electrons were generated on metal films supported on TiO<sub>2</sub> during CO oxidation. The energy of hot electrons was larger than the Schottky barrier at the metal-oxide interface (around 0.7-1.2 eV) and the density of hot electrons was proportional to the rate of CO oxidation. Hot electrons

generated by CO oxidation might induce surface chemistries, such as inducing the dissociation of Au monomers to leave supported Au clusters.

Indeed, the above sintering kinetic studies gave an activation energy of sintering, which tracked the activation energy of CO oxidation on Au/TiO<sub>2</sub> and supported the reaction induced mechanism.

The kinetics of sintering could be understood using the model of Ostwald ripening developed by Wynblatt and Gjostein [106] (“W-J” model). The rate equation of sintering of supported metal clusters was derived based on the steady state equilibrium of monomers (either metal atoms or metal-adsorbate complex) diffusing across the surface. Recent calorimetric studies by Campbell et al. [183, 184] suggested the free energy of metal nano-clusters were much higher than conventionally predicted by G-T relationship. With this correction, the rate equation in W-J model could be rewritten as:

$$\frac{dV_i}{dt} = Ke^{-\frac{E_{tot}}{kT}} \left[ e^{\frac{\mu(r_i^*) - \mu(\infty)}{kT}} - e^{\frac{\mu(r_i) - \mu(\infty)}{kT}} \right]$$

where  $K$  is the prefactor depending on the controlling kinetic process of diffusion,  $E_{tot}$  is the total activation energy for bulk metal,  $\mu(r_i)$  is the chemical potential (partial molar free energy) of the cluster  $i$  with radius of  $r_i$  and  $\mu(\infty)$  is the chemical potential of bulk metal. Here  $r_i^*$  is the critical radius of the cluster that neither decays nor grows at diffusion equilibrium. Assuming clusters on the surface are in equilibrium with the same far field monomer concentration (mean field approximation),  $r_i^*$  is the average radius of all clusters and increases as a function of time during the sintering. Clusters with radius smaller than  $r_i^*$  would decay, whereas clusters with radius larger than  $r_i^*$  would grow.

Their sintering rates depend on their chemical potentials, as well as the chemical potential of  $\mu(r_i^*)$ .

The chemical potential of metal clusters decreases as their radius increases. Higher surface cluster coverage would in general result in a higher  $r_i^*$  and thus a smaller  $\mu(r_i^*)$ . For clusters with radius smaller than  $r_i^*$ , their decay rates increase with the decrease of  $\mu(r_i^*)$ . Thus the decay rates of Au clusters smaller than  $r_i^*$  increase with the surface coverage. For supported metal clusters with positive activation energies, the rate of sintering would increase as the surface temperature increases.

In the rate equation of sintering, the prefactor K varies depending on the kinetic limits of surface diffusion. Two kinetic limits were described in the W-J model, which are interface control limit and diffusion control limit. In the interface control limit, where the detachment of monomers from clusters is the rate limiting step, K is only a function of cluster radius. As the distance between clusters increases and mass transport becomes more and more dependent on the surface diffusion of monomers, K would become a function of cluster radius as well as the diffusion length of monomers. The rate equation would become diffusion limited when the distances between clusters are long enough that the rate of sintering is decided by the rate of monomers diffusing across the surface. In our kinetic studies of sintering, the decrease of number densities became very slow when it dropped to around  $7 \times 10^{11}/\text{cm}^2$ , regardless of surface Au coverage or temperature. The decrease of number density indicates the increase of average distance between clusters and suggests surface diffusion became more critical in the later stage of sintering.

Size dependent activation energies of sintering could be extrapolated for clusters of different radius by analyzing the sintering rates of individual clusters. Small Au



clusters, with height around 4.6 Å or less, exhibited similar decay rates at the same temperature. However, intermediate-sized Au clusters, with height around the median height of cluster distribution, showed various sintering rate depending on their local cluster configuration. For example, in the sintering of 0.5 ML Au/TiO<sub>2</sub>(110) at 300 K, clusters of similar sizes (clusters in dashed circles in Figure 38) sintered at different rates when they were around the average size (with heights of 0.7-0.9 nm and diameters around 4 nm). At different areas, even their tendency of sintering could be different. Depending on the size of neighbor clusters, a larger cluster (e.g. cluster A in Figure 38) could decay while a smaller cluster (e.g. cluster B in Figure 38) grew in different local environments.

In the W-J model, the mean field approximation enables the rate equation of sintering to be applied to all clusters on the surface. With this approximation, for a certain model system at constant temperature, the rate equation gives the same sintering rate for clusters of the same radius. The above behavior cannot be understood by the mean field approximation, but can be explained by the differences in size and position of clusters in the local vicinity, i.e., local effect. Indeed, the breakdown of mean field approximation is most likely for real system since long range equilibrium only exists in the two kinetic limits described in the W-J model. Deviations from these limits lead to gradients in the monomer density and thus local effects. Meanwhile, structural defects, such as step edges, are huge diffusion barriers to break the diffusion equilibrium across the surface. Decay or growth rates of an individual cluster are thus decided by the location and size of neighboring clusters.

The failure of mean field approximation has also been observed in the ripening of 2D islands on flat metal surfaces and semiconductor surfaces [211-214]. Local effects dominated their process of Ostwald ripening. A simplified analytical approach, “nearest neighbor approach”, has been proposed to extrapolate the controlling kinetic parameters assuming the sintering of a cluster is decided by its nearest neighbor clusters [212-217]. Mathematically, all clusters on the surface could be simulated by the W-J model. However, for each cluster,  $r_i^*$  varies with the spatial configuration of its neighbor clusters. For clusters of the same size, the tendency or rate of sintering can be different depending on whether they are larger or smaller than  $r_i^*$  in their certain local environment.

The rate of sintering is exponential to the chemical potential of clusters. For supported metal clusters of a few nanometer size, high chemical potentials suggested by Campbell et al. [107, 184], i.e.  $\mu(r_i) - \mu(\infty) \gg kT$  and  $\mu(r_i^*) - \mu(\infty) \gg kT$ , indicate a huge dependency of sintering rates in  $r_i^*$  and thus a prominent local effect. In real catalysis, these local effects could be more prominent due to the curvature of substrate and structural defects. The dominance of local effects explained the broader size distribution observed in real catalysts, as well as the deviation of power law simulation between experimental data and theoretical prediction [101, 103, 218, 219].

For Au clusters with a height of 4.6 Å or less, their decay rates are rapid and the least dependent on the local spatial configuration of Au clusters. Their independence of decay rates to local environments is due to the huge difference of chemical potentials between small clusters and clusters with radius of  $r_i^*$ . Chemical potential difference

between clusters of different size could lead to  $e^{\frac{\mu(r_i^*) - \mu(\infty)}{kT}} \ll e^{\frac{\mu(r_i) - \mu(\infty)}{kT}}$ . Therefore, the rate equation for small clusters would be mainly decided by the monomer concentration near

the cluster and could be simplified as:  $\frac{dV_i}{dt} = -Ke^{\frac{E_{tot} + \mu(r_i) - \mu(\infty)}{kT}}$ . The decay rates of small clusters are independent of  $r_i^*$  and thus of local cluster distribution. This simplification could be justified by the chemical potentials of Au clusters supported on TiO<sub>2</sub>(110), calculated from either the MBA model or the DFT model (Figure 35). No matter which model is used, the difference of chemical potentials between clusters with size close to the critical radius (diameters around 4-5 nm) and small clusters (diameters around 3 nm) always satisfies  $(\mu(r^*) - \mu(\infty)) - (\mu(r) - \mu(\infty)) < -10 \text{ kJ/mol}$ , which results

$e^{\frac{\mu(r^*) - \mu(\infty)}{kT}} \ll e^{\frac{\mu(r) - \mu(\infty)}{kT}}$ . For small Au clusters, the rate equation could be simplified as

$$\frac{dV_i}{dt} = -Ke^{\frac{E_{tot} + \mu(r_i) - \mu(\infty)}{kT}}$$

Therefore, for small Au clusters, the plot of  $\ln(dV_i / dt)$  vs  $1/T$  gave the activation energy of sintering,  $E_{tot} + \mu(r_i) - \mu(\infty)$ . Volumes of Au clusters during CO oxidation were calculated by the volume equation for a spherical cap,  $V = \frac{1}{6}\pi h(3r^2 + h^2)$ , where  $r$  and  $h$  are radius and height of clusters measured from STM images. Figure 43 gives the activation energy for Au clusters with diameters around 3 nm to be  $10 \pm 2 \text{ kJ/mol}$ .

Previous studies showed a size dependent reactivity in CO oxidation and the apparent activation energy of CO oxidation is 14 kJ/mol for Au clusters with an average diameter of 3 nm supported on the TiO<sub>2</sub>(110) [80]. Because the apparent activation energy of CO oxidation was an average value for Au clusters with a size distribution, the actual apparent activation energy could be lower for Au clusters of 3 nm size. Therefore, the

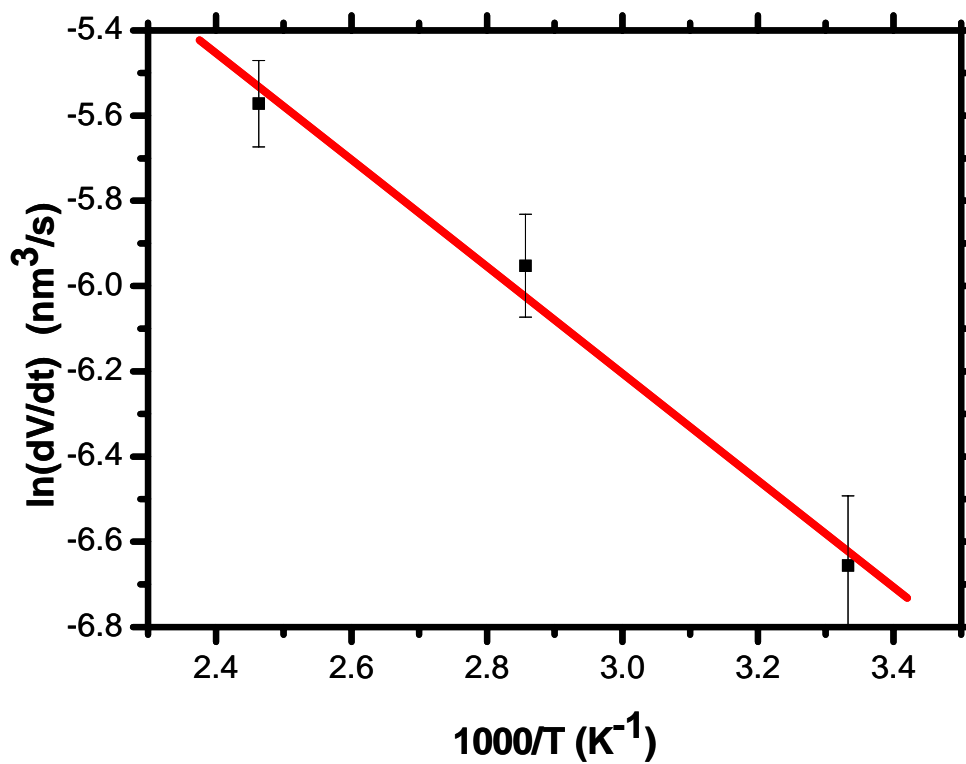


Figure 43. Arrhenius plot for the decay of supported Au clusters. The decay rates are achieved from Au clusters with a diameter around 3 nm. The solid line gives the best least square fit.

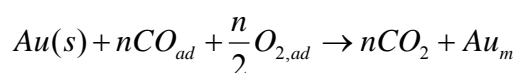
activation energy of sintering tracks the activation energy of CO oxidation on supported Au clusters.

Campbell et al. estimated the activation energy of sintering for Au clusters supported on TiO<sub>2</sub>(110) in UHV [107, 184]. The activation energy for Au clusters with diameters around 3 nm was around ~310 kJ/mol. The huge difference in the activation energy of sintering between under UHV and during CO oxidation demonstrates the magnificence of CO oxidation induced sintering, which might also be general for the other supported metal catalyst during CO oxidation.

### **Model of Ostwald ripening for supported Au clusters during CO oxidation**

The W-J model was used directly in the above discussion of sintering kinetics of supported Au clusters during CO oxidation. Rigorously, the W-J model only applies to the situation when the influence of adsorbates is not included. In our study, however, the sintering of Au clusters is induced by CO oxidation. To validate the application of W-J model to the Au sintering induced by CO oxidation, it is necessary to extend the W-J model to include the influence of reaction in its atomic description of the Ostwald ripening process.

Here we extend the W-J model for the reaction induced Ostwald ripening adopting a similar approach to that of Wynblatt and Gjostein. In the above proposed mechanism for CO oxidation induced sintering, hot electrons induce the sintering by breaking down the detachment barriers. The total reaction can be illustrated as:



where  $Au_m$  denotes the Au monomer leaving the Au cluster during CO oxidation, and  $n$  denotes the turn over number of CO oxidation required to make the monomer to leave the cluster. The monomer concentration leaving the cluster can be expressed as,

$C_i = k(r_i)p_{co}^x p_{o_2}^y$ . Here, the rate equation is simplified in a power law form where  $k(r_i)$  is the rate constant of the reaction dependent on the size of Au clusters, and  $x$  and  $y$  denote the power number for pressure of CO and O<sub>2</sub>, respectively.

In the above kinetic discussion, we have shown vapor phase transfer via the formation of volatile Au-O complex is not the case for the sintering of Au clusters during CO oxidation. Therefore, the detachment process is still treated as a monomer dissociated from the edge of the cluster in our extension. Replacing  $C_i$  in equation (3) of the W-J model with  $k(r_i)p_{co}^x p_{o_2}^y$ , the rate equation of sintering can be reached as,

$$\frac{dV_i}{dt} = \frac{2\pi \Omega p_{co}^x p_{o_2}^y D}{\ln(L_i / r_i) + l^2 / r_i a} [k(r^*) - k(r_i)] \quad (11)$$

where  $k(r^*)$  is the rate constant for reaction occurring on a cluster with radius  $r^*$  that neither shrinks or grows. The rate constant  $k(r^*)$  and  $k(r_i)$  can be expressed as

$$k(r^*) = p_1 e^{-\frac{E_a(r^*)}{kT}} \text{ and } k(r_i) = p_1 e^{-\frac{E_a(r_i)}{kT}}, \text{ where } p_1 \text{ is the prefactor of the reaction and } E_a$$

is the activation barrier. Equation (11) can thus be rewritten as

$$\frac{dV_i}{dt} = \frac{2\pi \Omega p_{co}^x p_{o_2}^y D p_1}{\ln(L_i / r_i) + l^2 / r_i a} \left[ e^{-\frac{E_a(r^*)}{kT}} - e^{-\frac{E_a(r_i)}{kT}} \right] \quad (12)$$

Comparing with Equation 5, the rate equation of supported Au clusters during CO oxidation simulates the equation derived by W-J in its general form as,

$$\frac{dV_i}{dt} = K_i p_{co}^x p_{o_2}^y e^{\frac{H_m^*}{kT}} \left[ e^{-\frac{E_a(r^*)}{kT}} - e^{-\frac{E_d(r_i)}{kT}} \right],$$

where  $K_i$  is the prefactor. However, the prefactor is changed by the inclusion of reaction probability. The sintering energetics is also altered to track the reaction activation energy.

### **Rh(110) during CO oxidation**

Before we discuss the oxidation state of Au clusters supported on TiO<sub>2</sub>(110) during CO oxidation, we would like to describe the surface morphology of Rh(110) during CO oxidation first. The evolution of surface morphology of Rh(110) during CO oxidation would increase our understanding toward the surface states of supported metal clusters.

Surface morphology of Rh(110) changes upon the exposure of reactant gases. The adsorbate-induced reconstruction of Rh(110) surfaces have been studied extensively in UHV [220-251]. Meanwhile, using high pressure STM, Rider et al. [58, 60] demonstrated a more condensed CO and NO layer formed on the Rh(111) surface in the presence of a few Torr CO and NO, as compared to the adsorption of CO and NO under UHV. High pressure STM studies by Hendriksen et al. [59, 61, 70, 252] depicted the morphological change of single crystal surfaces of Pt, Pd and Ru during CO oxidation. However, at their surface temperatures (< 500 K), the rate of CO oxidation was usually very low. In our study, we looked at the surface of Rh(110) during CO oxidation at 525 K, which could give the TOF of CO<sub>2</sub> as high as 1100 molecules/s and thus better represent the surface of a working catalyst.

First, we show the surface morphology of Rh(110) changed readily upon the exposure of CO and O<sub>2</sub> (Figure 44). Figure 44a shows a clean Rh(110) surface with large islands appearing on the terraces in UHV. These islands grew right upon the exposure of 12 Torr CO/O<sub>2</sub> mixture gas at room temperature (Figure 44b). The mixture gas was introduced into the chamber through a Nupro valve and the pressure in the chamber was balanced within seconds. In the presence of 12 Torr CO/O<sub>2</sub>, the Rh(110) surface did not show continuous changes, but was rather stable during the one hour we scanned on this surface. Figure 44c and 44d compare the surface morphology of Rh(110) before and after O<sub>2</sub> exposure at 525 K. The Rh(110) surface was stable in UHV at 525 K. The sharp step edge of Rh(110) suggests the step fluctuation was not rapid at 525 K. Figure 44d shows the Rh(110) surface after exposure of 8 Torr O<sub>2</sub> at 525 K. The Rh(110) surface was roughened within a few minutes upon the exposure of 8 Torr O<sub>2</sub>. Similar to the exposure of CO/O<sub>2</sub> mixture gas at room temperature, no continuous change of the Rh(110) surface had been apparent in the presence of 8 Torr O<sub>2</sub> at 525 K. This is probably due to the formation of RhO<sub>x</sub> oxide, which inhibited the diffusion of oxygen into the bulk or Rh atoms onto the surface.

The evolution of surface morphology of Rh(110) was then studied during CO oxidation at 525 K. At this temperature, CO oxidation happened rapidly on the Rh(110) surface. Since the production of CO<sub>2</sub> molecule is proportional to the decrease of CO pressure, the reaction rate could be measured from the total pressure change during CO oxidation. The decrease of 1 Torr in total pressure corresponds to the production of 0.5 Torr CO<sub>2</sub>. The total pressure change during CO oxidation was measured from a baratron attached to the STM chamber and plotted in Figure 45 as a function of time. The total



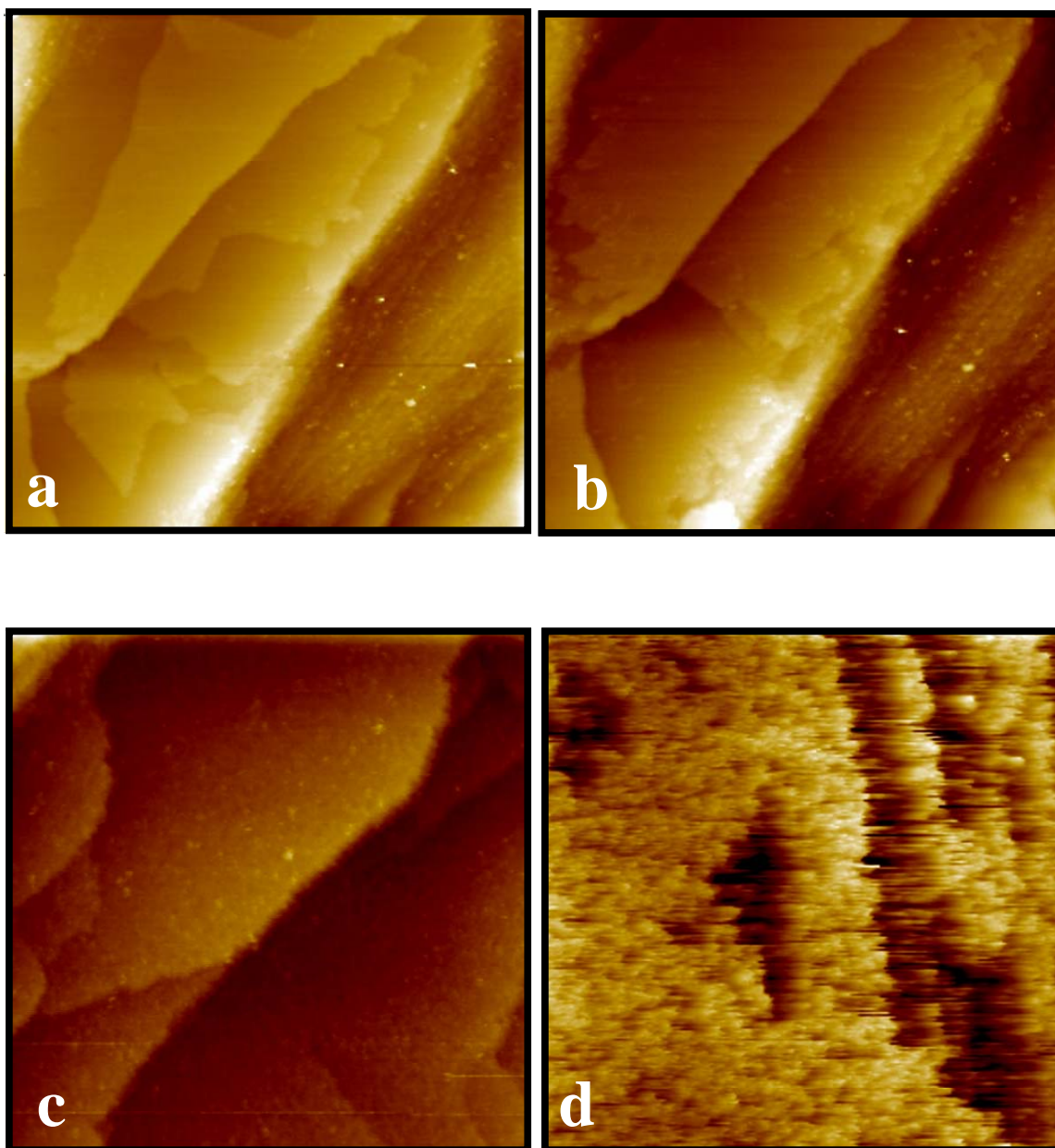


Figure 44. STM images of Rh (110) in (a) UHV at 300 K, (b) 12 Torr CO/O<sub>2</sub> (1:2) at 300 K, (c) UHV at 525 K, and (d) 8 Torr O<sub>2</sub> at 525 K. (a) and (b) are on the same area and have dimensions of 180 nm × 180 nm. The image size of (c) and (d) is 100 nm × 100 nm.

pressure change measured could be transformed into the TOF of CO<sub>2</sub> production. In 12 Torr CO/O<sub>2</sub> (1:2) mixture gases, the TOF could be as high as 1100 molecule/s on Rh(110) at 525 K. In the plot, the decrease of total pressure was approximately linear in the first 55 minutes. The linear slope turned steeper after 55 minutes of CO oxidation, indicating an increased production of CO<sub>2</sub>. The increased production of CO<sub>2</sub> lasted around 15 minutes before the rate became very slow due to the depletion of CO. In this plot, the reaction was divided into four time periods, labeled as “A”, “B”, “C” and “D”. Time period “A” represents the starting of CO oxidation. Time period “B” corresponds to the middle of CO oxidation. Time period “C” refers to the time period when the reaction rate was suddenly increased. Two dotted lines were marked in Figure 45 to show the beginning and end of the time period “C”. Time period “D” refers to the end of CO oxidation, when CO was depleted. STM images and I-V curves were taken during these time periods accordingly. During the time period “C”, the measured I-V curves varied over time. To better display the character of this time period, C<sub>1</sub> and C<sub>2</sub> were labeled to represent to the beginning and end of time period “C”.

Figure 46 demonstrates the surface morphology of Rh(110) before and during CO oxidation at 525 K. Figure 46a shows a clean Rh(110) surface with large terraces at room temperature. 12 Torr of CO/O<sub>2</sub> (1:2) were infused into the STM chamber at room temperature and the Rh(110) surface was then heated to 475 K. By staying at 475 K for 1 hour, huge thermal drifts, caused when the STM tip first approached a heated surface, could be compensated after reaching thermal equilibrium. This compensation enabled us to image the Rh(100) surface in a few minutes after we further increased the surface temperature to 525 K. Figure 46b shows the surface morphology of Rh(110) at 475 K in

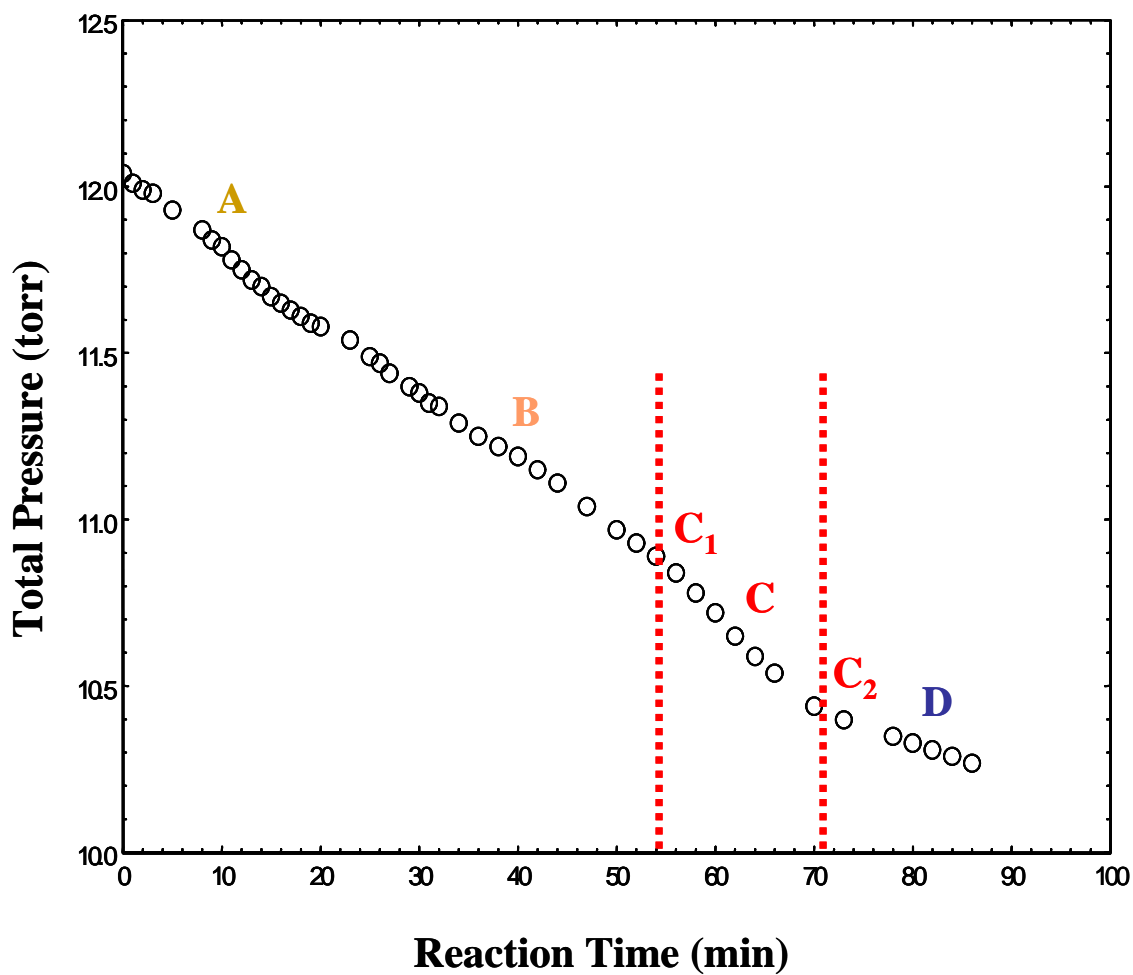


Figure 45. Plot of the total pressure versus time during CO oxidation on Rh(110) at 525 K. The ratio of CO:O<sub>2</sub> is 1:2. The reaction process is divided into four time periods, during which STM images and I-V curves are taken on the Rh(110) surface. These time periods are marked as A, B, C and D in the plot.

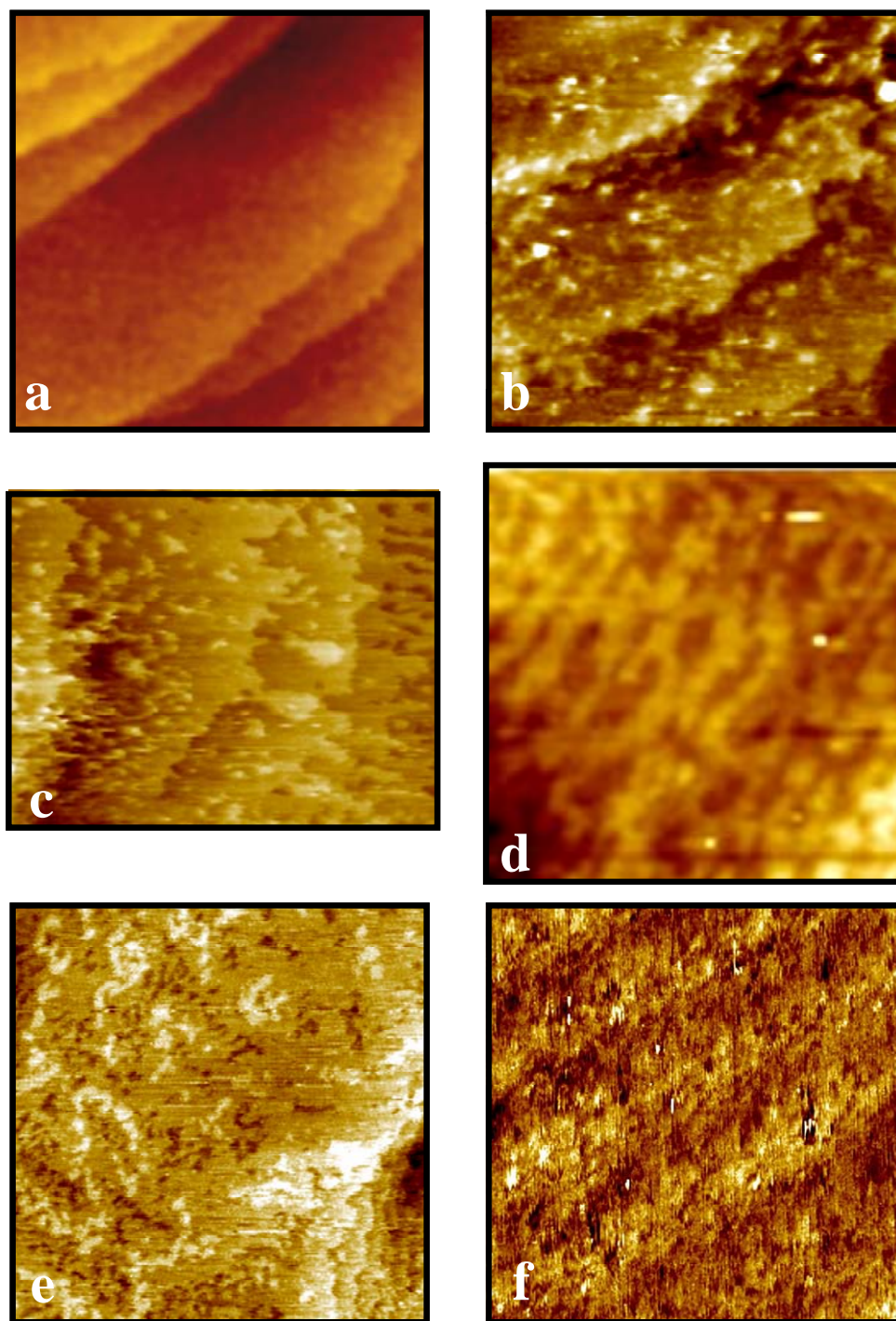


Figure 46. STM images of Rh(110) during CO oxidation. (a) Rh(110) in UHV at 300 K. (b) Rh(110) in 12 Torr CO/O<sub>2</sub> (1:2) at 475 K. (c) - (f) Rh(110) in 12 Torr CO/O<sub>2</sub> (1:2) at 525 K. (c) - (f) correspond to the time period A, B, C and D in Figure 45 respectively. (a), (b), (d), (e) and (f) have dimensions of 100 nm × 100 nm. The size of (c) is 80 nm × 110 nm.

12 Torr CO/O<sub>2</sub>. Small bright protrusions appeared on the Rh(110) surface. Similar protrusions were observed by Africh et al. [224] when Rh(110) was exposed to O<sub>2</sub> at room temperature. They assigned these protrusions as Rh clusters pulled out of the terrace by O<sub>2</sub> adsorption and dissociation. In our study, the CO oxidation reaction was slow at 475 K and the baratron did not show pressure decrease for ~ 1 hour. Accordingly, the surface morphology of Rh(110) remained similar as in Figure 46b during the hour when surface temperature was kept at 475 K. Figure 46c shows the surface of Rh(110) when the temperature was raised to 525 K. At 525 K, the change of surface morphology was drastic and continuous. Terraces decomposed starting from the step edges while holes and islands appeared on the Rh(110) surface. As the reaction continues, lamella structures were formed during the time period “B” (Figure 46d). The lamella structure has a height around 2 Å, which corresponds to the monolayer thickness of Rh(110). As the reaction proceeds to a hyperactive state, i.e., time period “C”, STM tip became very instable and kept dumping clusters on to the surface. To reveal the surface of time period “C”, we decreased the surface temperature to 475 K in the middle of time period “C”. STM image corresponding to the time period “C” was then obtained at 475 K in the presence of CO/O<sub>2</sub> (Figure 46e) and shows larger surface terraces with small and irregularly shaped islands and holes on the surface. During the time period “D”, the Rh(110) surface was roughened with 3D clusters, indicating the formation of Rh oxide (Figure 46f).

To reveal the oxidation state of Rh(110) surface during CO oxidation, we performed scanning tunneling spectroscopy (STS) throughout the CO oxidation. The results are depicted in Figure 47. To ensure only the electronic structure of the topmost

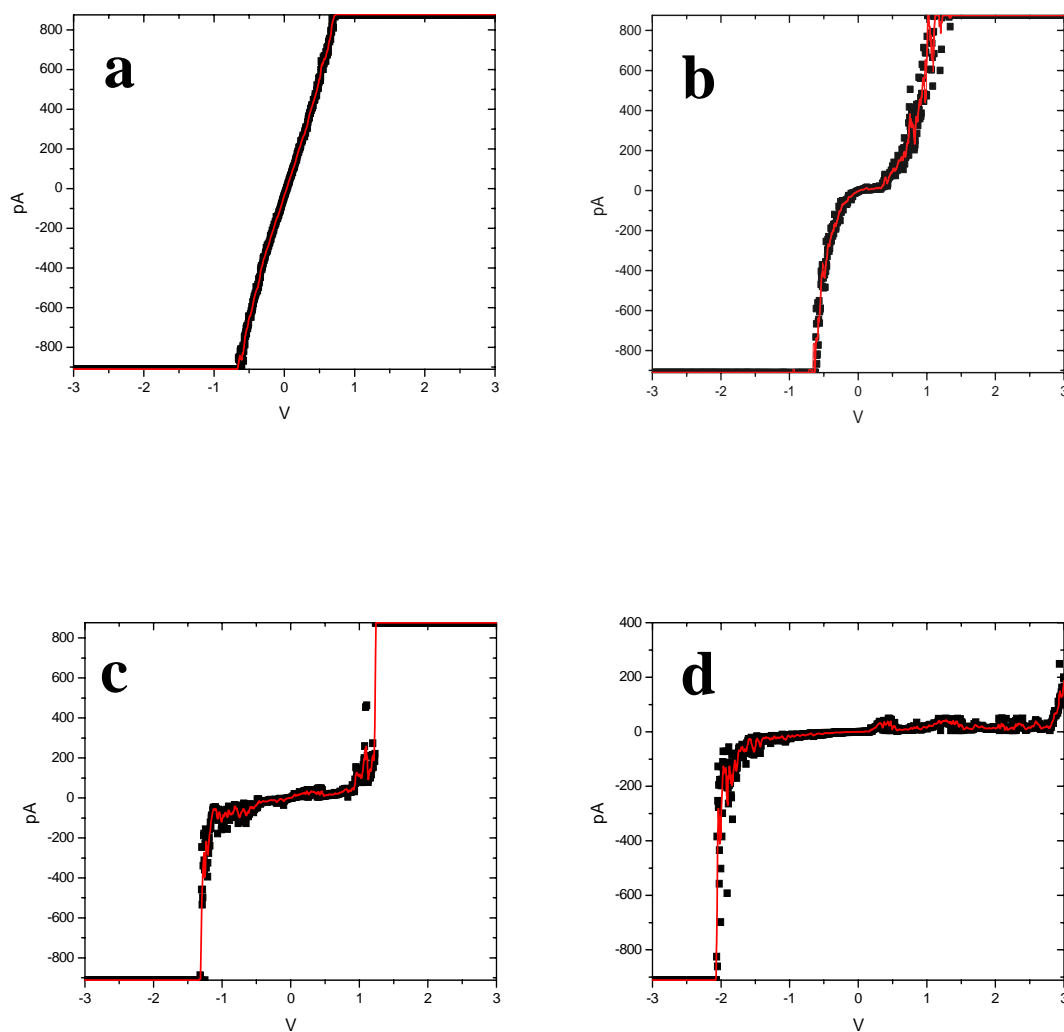


Figure 47. I-V curves measured during CO oxidation at 525 K. The total pressure is 12 Torr and the ratio of CO:O<sub>2</sub> is 1:2. (a) corresponds to the time period A and B in Figure 45. (b) corresponds to the time period C<sub>1</sub> in Figure 45. (c) corresponds to the time period C<sub>2</sub> in Figure 45. (d) corresponds to the time period D in Figure 45. The tunneling gap is fixed at  $I = 0.1$  nA and  $V_s = 1.1$  V. I-V curves for the different time periods of the reaction are based on the average behavior of I-V data sampled during each time period.

surface was probed, a high tunneling gap was fixed at  $V_s=1.1$  V and  $I=0.1$  nA throughout the measurement of I-V curves. During the time period of “A” and “B”, the I-V curve (Figure 47a) was characteristic for a metallic surface. During the time period of “C”, the I-V curves started to show band gap structures. At the beginning of time period “C”, the band gap remained small at around 0.3 eV (Figure 47b), whereas the gap increased to around 1.2 eV at the end of time period “C” (Figure 47c). Due to the short time period of “C”, collecting more I-V curves might be necessary to verify whether the increase of band gaps was due to surface inhomogeneity. Nonetheless, the appearance of band gaps suggests the introduction of surface oxidative state, which fits in between the metallic Rh and the bulk Rh oxide with a band gap of 3.5 eV [253]. During the time period “D”, Figure 47d shows a band gap of around 3.5 eV, suggesting a complete oxidation of the Rh(110) surface.

To reveal the nature of the hyperactive surface during time period “C”, three Rh(110) surfaces with well-defined surface structures were prepared for STM and STS measurements. Figure 48a shows a Rh(110) surface in the presence of  $10^{-6}$  Torr CO at 300 K. This surface was saturated with CO sitting on the bridging sites of Rh(110) [254]. The I-V curve of this surface (Figure 48b) did not reveal a band gap but show a much suppressed electronic states near the Fermi level. Comparison with the metallic I-V curve (Figure 47a) suggests 1) the Rh(110) surface is not covered by CO or 2) the CO binding is much weakened during CO oxidation. Figure 48c shows a Rh(110) surface in the presence of  $10^{-6}$  Torr  $O_2$  at 300 K. This surface was covered with chemisorbed oxygen sitting on the bridging sites of Rh(110) [233]. The I-V curve of this surface (Figure 48d) shows a band gap around 1.7 eV, close to that of the surface during time period “C”.

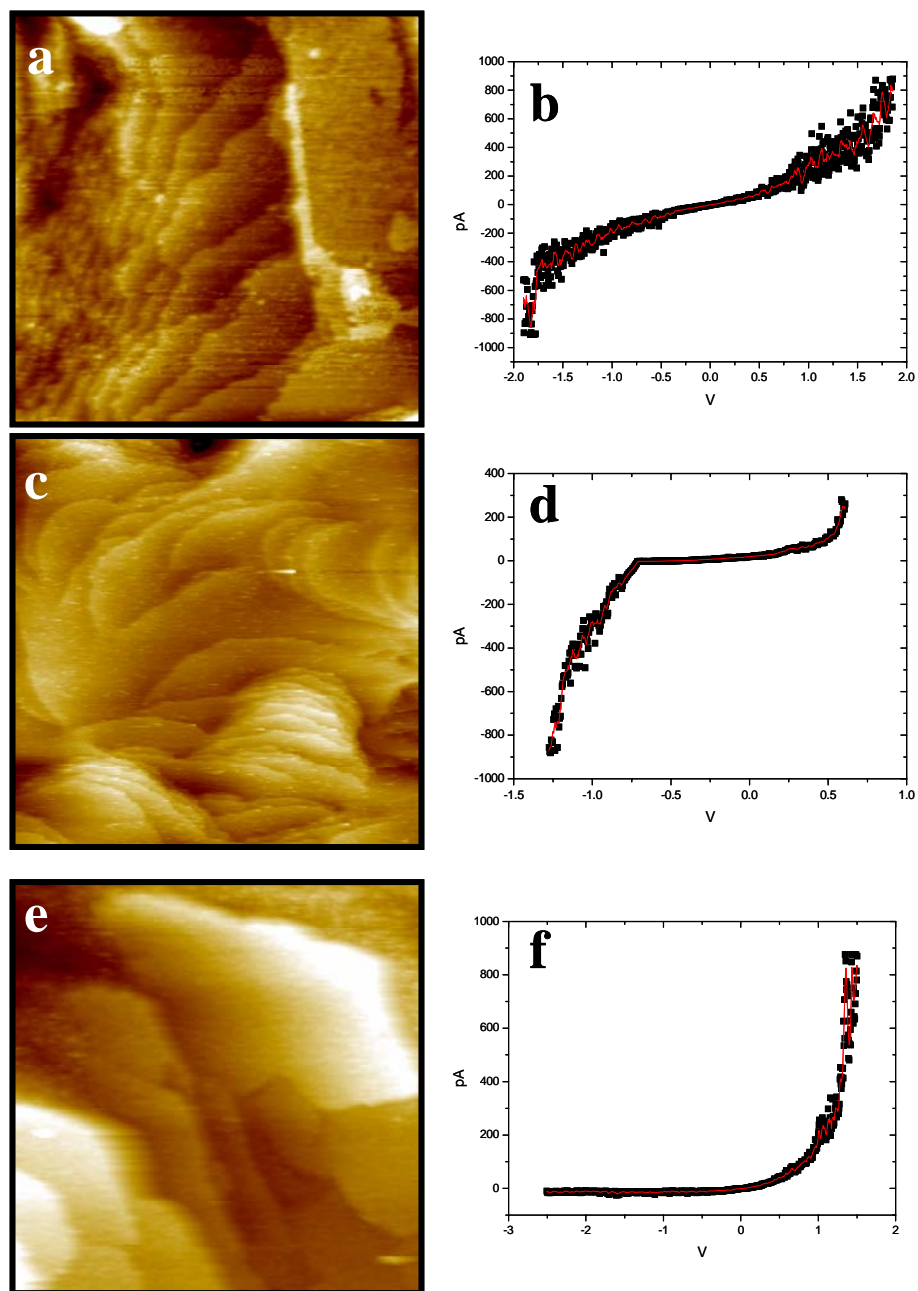


Figure 48. STM images and corresponding I-V curves of characteristic Rh (110) surfaces. (a) and (b) are Rh(110) in the presence of  $10^{-6}$  Torr CO at 300 K. (c) and (d) are Rh(110) in the presence of  $10^{-6}$  Torr O<sub>2</sub> at 300 K. (e) and (f) are on Rh(110) after being annealed in  $10^{-6}$  Torr O<sub>2</sub> at 750 K, when a surface oxide layer is produced. For I-V curve measurements, the tunneling gap is fixed at  $I = 0.1$  nA and  $V_s = 1.1$  V.



Figure 48e shows a Rh(110) surface after being annealed in  $10^{-6}$  Torr  $O_2$  at 750 K. This surface was covered with a  $c(2 \times 4)$  surface oxide layer, whose structure was recently characterized by Comelli et al.[220]. The I-V curve of this surface (Figure 48f) shows a band gap larger than 2.5 eV, close to that of the surface during time period “D”.

While the I-V curve measurements suggest the hyperactive surface of Rh(110) is similar to the surface of Rh(110) covered by chemisorbed oxygen in vacuum, the change of surface morphology of Rh(110) during CO oxidation suggests the hyperactive surface is more metallic like than in the form of oxide. The formation of surface oxides usually passivates the open metal surface and inhibits the diffusion of metal atoms due to the strong and directional covalent bonds in oxide. The rigidity of surface oxide is also evidenced in our study of Rh(110) in pure  $O_2$  (Figure 44d), as well as a series of STM studies by Varga et al. [255-257]. Moreover, we found the surface diffusion of Rh atoms is accelerated by CO oxidation reaction. The Rh(110) surface changed continuously during CO oxidation at 525 K, whereas the Rh(110) surface was relatively stable in UHV or  $CO/O_2$  mixture gas and at room temperature or 475 K. The correlation between surface diffusion of Rh atoms and the rate of CO oxidation is similar to what we observed in the sintering of supported Au clusters during CO oxidation. Therefore, we speculate the oxidation state of Au clusters during CO oxidation is similar to that of hyperactive Rh(110) surface, which is covered predominantly by chemisorbed oxygen.

**CHAPTER V**  
**THE STRUCTURE AND STABILITY OF**  
**ALLOY MODEL CATALYSTS**

In this chapter, we present our studies on the synthesis and structural characterization of alloy model catalysts, including Au-Pd alloy thin film supported on Rh(100), Au-Ag alloy clusters supported on TiO<sub>2</sub>(110), and Ru<sub>3</sub>Sn<sub>3</sub> clusters supported on the ultra-thin silica film. On the Au-Pd alloy thin film surface, we reveal the chemical contrast between Au and Pd atoms. On the supported Au-Ag clusters, we show how the growth kinetics influences the formation of Au-Ag alloy clusters. Of particular interest, we have focused on the synthesis and structural characterization of Ru<sub>3</sub>Sn<sub>3</sub> clusters supported on the ultra-thin silica film, which is prepared via solution deposition. The structure and adsorption sites of the ultra-thin silica film are also revealed, which explain why this silica film is superior in characterizing the atomic structure of supported Ru<sub>3</sub>Sn<sub>3</sub> clusters.

**The growth and structure of Au-Pd alloy on Rh(100)**

Au-Pd alloy catalysts are industrially important for a number of applications [258-261], such as hydrogen fuel cells [262] and pollution control [263]. The addition of Au to Pd can greatly enhance the performance and longevity of Pd catalysts. The promotion role of Au to Pd in the catalytic synthesis of vinyl acetate (VA) has recently been elucidated by Chen et al. [264, 265], who suggested surface Au atoms isolate Pd monomers that facilitate the coupling of critical surface species to form VA. Their study

demonstrated that Au-Pd alloy on an Au(100) surface exhibits a much higher catalytic reactivity for VA formation than that on an Au(111) surface. They thus suggested the formation of isolated Pd monomer pairs is responsible for VA synthesis while monomer pairs in the (100) surface lattice have the distance most close to the optimized distance for co-adsorption of reactant gases. To verify their suggestion, it is important to determine the surface atomic structure of Au-Pd alloy.

Previous STM studies have characterized the atomic structure of a few Au-Pd alloy surfaces. Maroun et al. [266] prepared and characterized a (111) surface of Au-Pd alloy through electrochemical deposition of the Au-Pd alloy film on an Au(111) surface. STM study by Aschoff et al. [267] resolved the atomic structure of Au<sub>3</sub>Pd(100) bulk alloy, which presents an Au-only surface at thermal equilibrium. Apparently, the surface of bulk alloy is not an ideal model for supported alloy clusters used in industry, because at reduced dimensions, the mixing properties of Au-Pd could be very different. Meanwhile, a planar alloy surface is desired for STM characterization of surface atomic structures. In this case, alloy thin films supported on a metal single crystal non-miscible with the alloy film become a better model system to study the active structure of alloy catalysts. Moreover, the thin film method provides the versatility to tune the surface composition of Au and Pd by varying the ratio of deposited Au and Pd, which thus could better approximate the structure of real alloy catalysts. In this study, Au-Pd alloy thin films supported on Rh(100) are selected to study the active structure of Au-Pd alloy catalysts. Rh single crystal is selected as the substrate to grow Au-Pd alloy thin films because 1) it is not miscible with Au and Pd at surface temperatures below 900 K [268], and 2) its atomic spacing (2.69 Å) is close to that of Au (2.88 Å) and Pd (2.75 Å).

We started by growing Au films on the Rh(100) surface. Figure 49a shows a clean surface of Rh(100) at room temperature, displaying smooth step edges with the expected monolayer step height of 2 Å. Deposition of 2 ML Au films on the Rh(100) surface leads to an epitaxial growth at room temperature and shows no apparent change on the terrace morphology. After annealing at 600 K for 10 min, the surface morphology underwent substantial changes, especially at the step edges (Figure 49b). Unlike the smooth step edges of the Rh(100) surface, the Au covered Rh(100) surface exhibits rectangular step edges after annealing at 600 K. Meanwhile, large vacancy islands of a few 10 nm width appeared on surface terraces. The rectangular step edges and the vacancy islands suggest Au is enriched near the step edges after 600 K annealing. Atomic scale STM images were then obtained on surface terraces and reveal the same (100)-(1 × 1) structure on both the top surface layer and vacancy islands (Figure 49b). The atomic distance is measured to be 2.9 Å, indicating only Au is present on the surface while Rh diffusion onto the surface is not thermodynamically favored. For 2ML Au on Rh(100), “added-row” structures appears near the step edges after annealing at 600 K (Figure 50a). The surface population of these “added-row” structures increases as the surface Au coverage increases. As the surface Au coverage reached 3 ML, the whole surface is covered by the “added-row” structure (Figure 50b). The atomic structure of these added rows are resolved in Figure 50c and 50d. On both 2 ML and 3 ML Au covered surfaces, the “added rows” exhibit the same structure and show a (9 × n) periodicity. Atoms in the added row show a quasi-hexagonal arrangement, rather than the square atomic arrangement supposed for (100) surfaces.

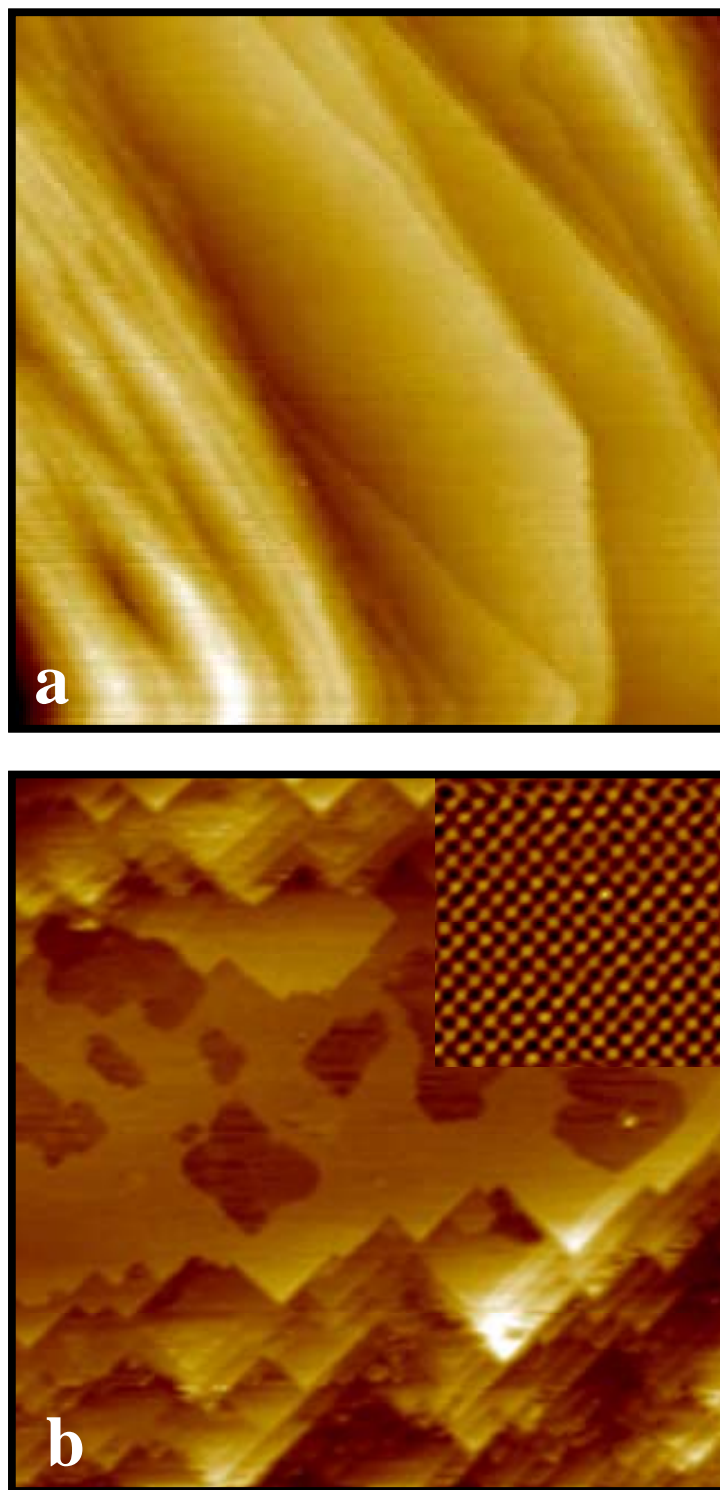


Figure 49. STM images of (a) Rh(100) and (b) 2 ML Au on Rh(100). Both (a) and (b) have dimensions of  $200 \text{ nm} \times 200 \text{ nm}$ . Inset is a zoom-in image of Au surface layer, which has a size of  $4.4 \text{ nm} \times 4.4 \text{ nm}$ . Tunneling parameters are  $V_s = -0.2 \text{ V}$  and  $I = 1 \text{ nA}$ .

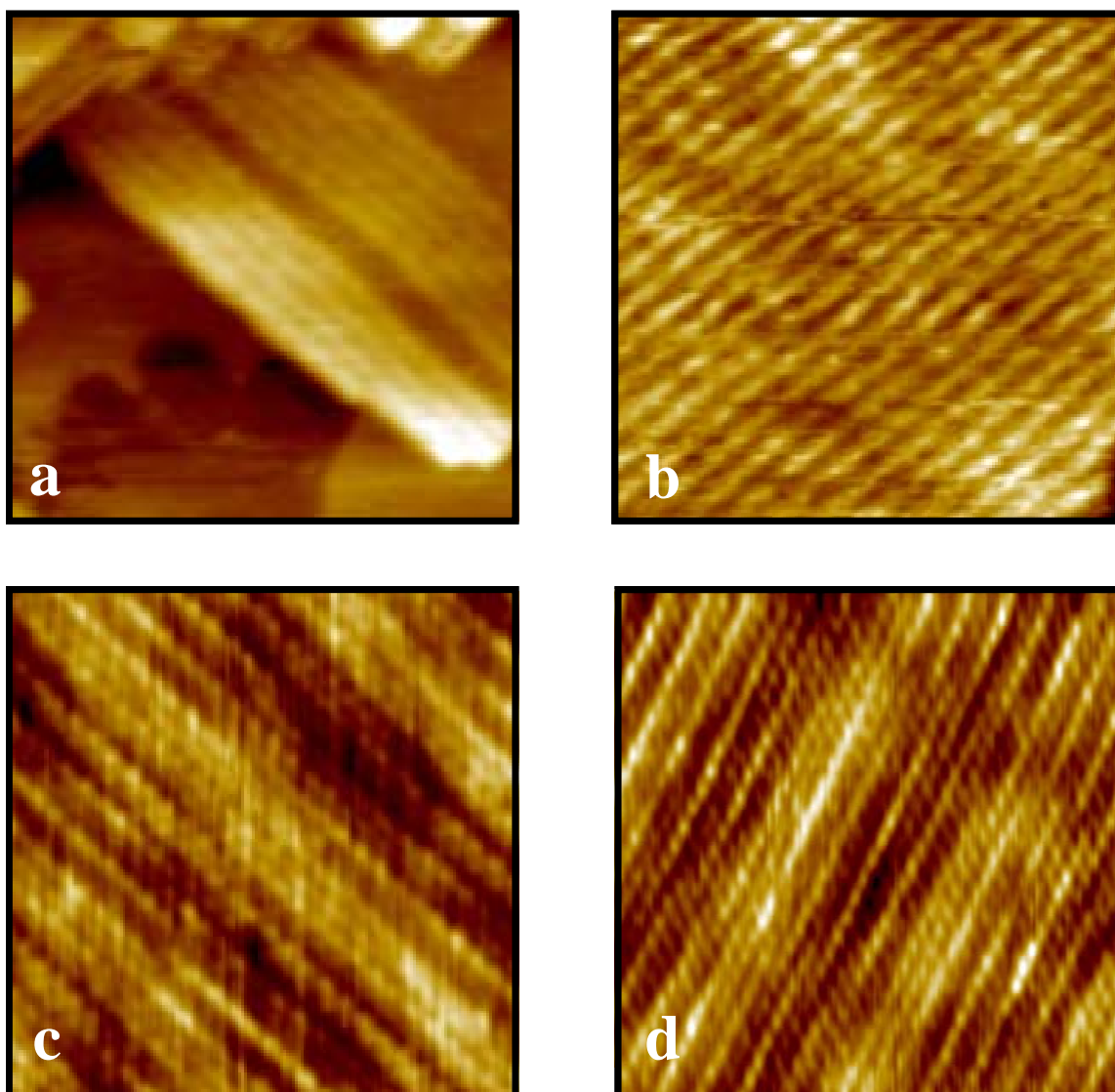


Figure 50. STM images of Au on Rh(100). (a) 2 ML Au on Rh(100). (b) 3 ML Au on Rh(100). (c) Zoom-in image in the reconstructed area of (a). (d) Zoom-in image of (b). (a) and (b) have dimensions of  $50 \text{ nm} \times 50 \text{ nm}$ . (c) and (d) have dimensions of  $7 \text{ nm} \times 7 \text{ nm}$ . Tunneling parameters are  $V_s = -0.1 \text{ V}$  and  $I = 2 \text{ nA}$ .

Indeed, the quasi-hexagonal reconstruction of (100) surfaces has been a unique surface characteristic for bulk Pt, Au, and Ir. The report of  $(5 \times 1)$  reconstruction of Pt(100) by Somorjai et al. [269] has been one of the first examples of clean transition metal surface reconstruction. Later on, LEED and STM studies showed late 5d metals, such as Pt, Au, and Ir, all exhibit the same  $(5 \times n)$  quasi-hexagonal surface reconstruction on the clean (100) surfaces where the unreconstructed surface should have square unit cells [8, 9, 270]. Scheffler et al. [271] elucidated the reconstruction mechanism of these late 5d metals through *ab initio* studies. They suggested the excess surface tension, which caused surface reconstruction, is due to d charge depletion from the surface layer. To reduce the surface tension, lattice spacing in the topmost layer is compressed, maximizing the overlap of surface atoms with the underneath layer. Radeke et al. [272] later conducted Monte Carlo studies on the reconstruction of Au multilayer on Rh(100). Their results suggest Au is more susceptible to hexagonal type surface reconstruction than pure Au(100) and the reconstruction takes place for surface Au coverage of 1.0 ML and above. No experimental measurements have been carried out so far to verify the surface reconstruction of Au on Rh(100).

In our study, a new type of surface reconstruction of Au has been observed when multilayer Au films are grown on Rh(100). Instead of the  $(5 \times n)$  reconstruction observed on bulk Au(100) surface, 2-3 ML Au on Rh(100) exhibits a larger  $(9 \times n)$  unit cell and less compression of the surface Au layer. In contrast to the theoretical prediction by Radeke et al. [272], our results suggest the lattice mismatch between Rh substrate and Au surface layers does not cause additional driving force for the  $(5 \times n)$  Au(100) surface reconstruction. The surface tension of unreconstructed Au films on Rh(100) is actually

lower than that of an unreconstructed Au(100) surface. The  $(9 \times n)$  quasi-hexagonal structure also provides additional evidence that Rh atoms do not diffuse onto the surface even after annealing, because surface Rh will reduce the surface tension of Au and cause surface transition back to  $(1 \times 1)$  phase.

Following the preparation of Au films on Rh(100) surface, we deposited Pd atoms on the 2 ML Au/Rh(100) surface to prepare alloy films. Figure 51a shows the surface morphology of 2 ML Pd deposited onto 2 ML Au/Rh(100) at room temperature. After Pd deposition, quasi-hexagonal reconstruction rows of Au were fully removed while many islands appeared on the surface. The appearance of islands suggests the surface diffusivity of Pd atoms is low at room temperature, resulting in the formation of small Pd islands instead of incorporating into step edges of surface Au layer. The surface in Figure 51a was then annealed at 800 K for 10 minutes, resulting in extended surface terraces with small holes (Figure 51b). This suggests, surface diffusion and interlayer transport of Pd atoms readily occur during annealing at 800 K. Pd atoms dissociated from the island edges to incorporate into Au terraces while Pd atoms in the islands could diffuse downwards to exchange with Au atoms from underneath layers. However, the surface diffusion of Pd and Au is probably slower than the interlayer transport of Pd, leading to the formation of small holes. The overall morphology of Figure 51a and 51b indicates that the growth of Au-Pd alloy films has kinetically been limited by surface diffusion. At room temperature, the deposited Pd atoms have low diffusivity on the surface and low probability to undergo place exchange with underneath Au atoms. As the surface population of Pd increases, Pd atoms coalesce with nearby Pd atoms and form islands on the surface. At elevated temperatures, both surface diffusion and interlayer transport are



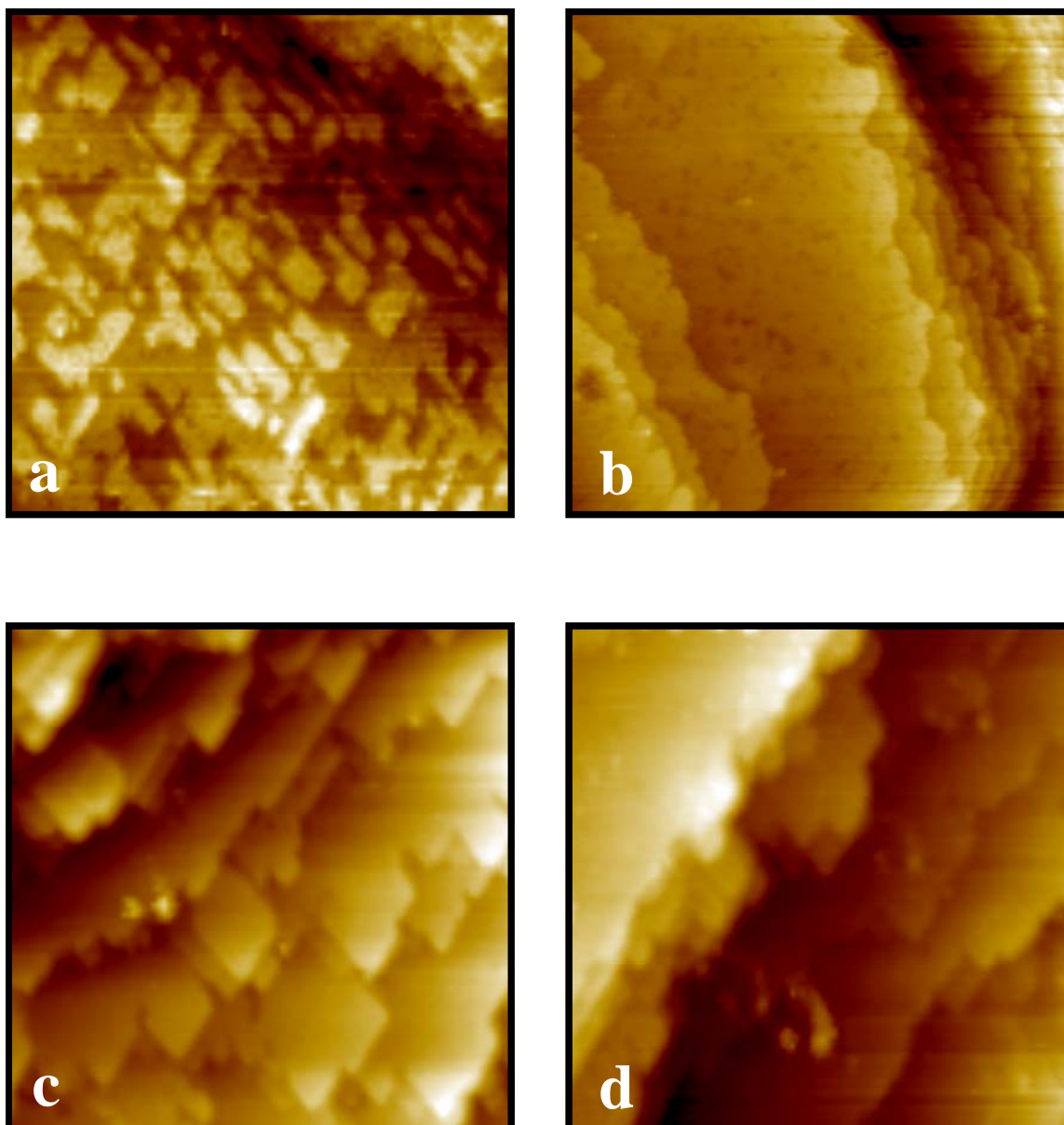


Figure 51. STM images of Au/Pd alloy on Rh(100). (a) 2 ML Pd deposited on 2 ML Au/Rh(100) at 300 K. (b) 2 ML Pd deposited on 2 ML Au/Rh(100) at 300 K and annealed at 800 K. (c) 0.5 ML Pd deposited on 2 ML Au/Rh(100) at 600 K. (d) 1 ML Pd deposited on 2 ML Au/Rh(100) at 600 K. All images have dimensions of  $100 \text{ nm} \times 100 \text{ nm}$ . Tunneling parameters are  $V_s = -0.1 \text{ V}$  and  $I = 1 \text{ nA}$ .

accelerated. However, the overall kinetics is limited by the surface diffusion of Pd and results in the formation of extended terraces with holes.

Room temperature deposition and subsequent annealing create an additional kinetic barrier for the mixing of Au and Pd, which is the detachment barrier for Pd to leave the islands formed at room temperature deposition. To remove this barrier, we facilitated the surface diffusion and interlayer transport by depositing Pd at 600 K. Figure 51c and 51d show the surface morphologies of 0.5 ML and 1 ML Pd deposited onto the 2ML Au/Rh(100) surface at 600 K, respectively. Unlike the room temperature Pd deposition, extended flat terraces maintained with rectangular step edges, revealing the rapid interlayer transport and the surface enrichment of Au atoms. The shape of step edges becomes smoothed with the increasing Pd coverage, suggesting the increased surface Pd ratio.

Figure 52 shows the high resolution STM images of Au/Pd alloy films prepared in Figure 51c and 51d. Two types of metal atoms with different apparent heights are present on top of the alloy film surface. The density of metal atoms with taller apparent height (bright protrusions) is less at a lower Pd coverage (0.5 ML Pd: 2 ML Au), suggesting the bright protrusions are Pd atoms. In the schematic representations in Figure 52, most Pd atoms appear isolated on the alloy film surface at a Pd:Au ratio of 0.5:2. When the concentration ratio of Pd:Au is increased to 1:2, the agglomeration form of Pd atoms, such as dimmers and trimers, also appear in the surface lattice. However, the surface concentration of Pd atoms remains low (~10%) at a Pd:Au ratio of 1:2. Figure 52 suggests Pd diffusion on the surface is the kinetic limiting step for the complete mixing of Au and Pd atoms to reach the thermodynamic equilibrium. At a Pd flux rate of 0.05

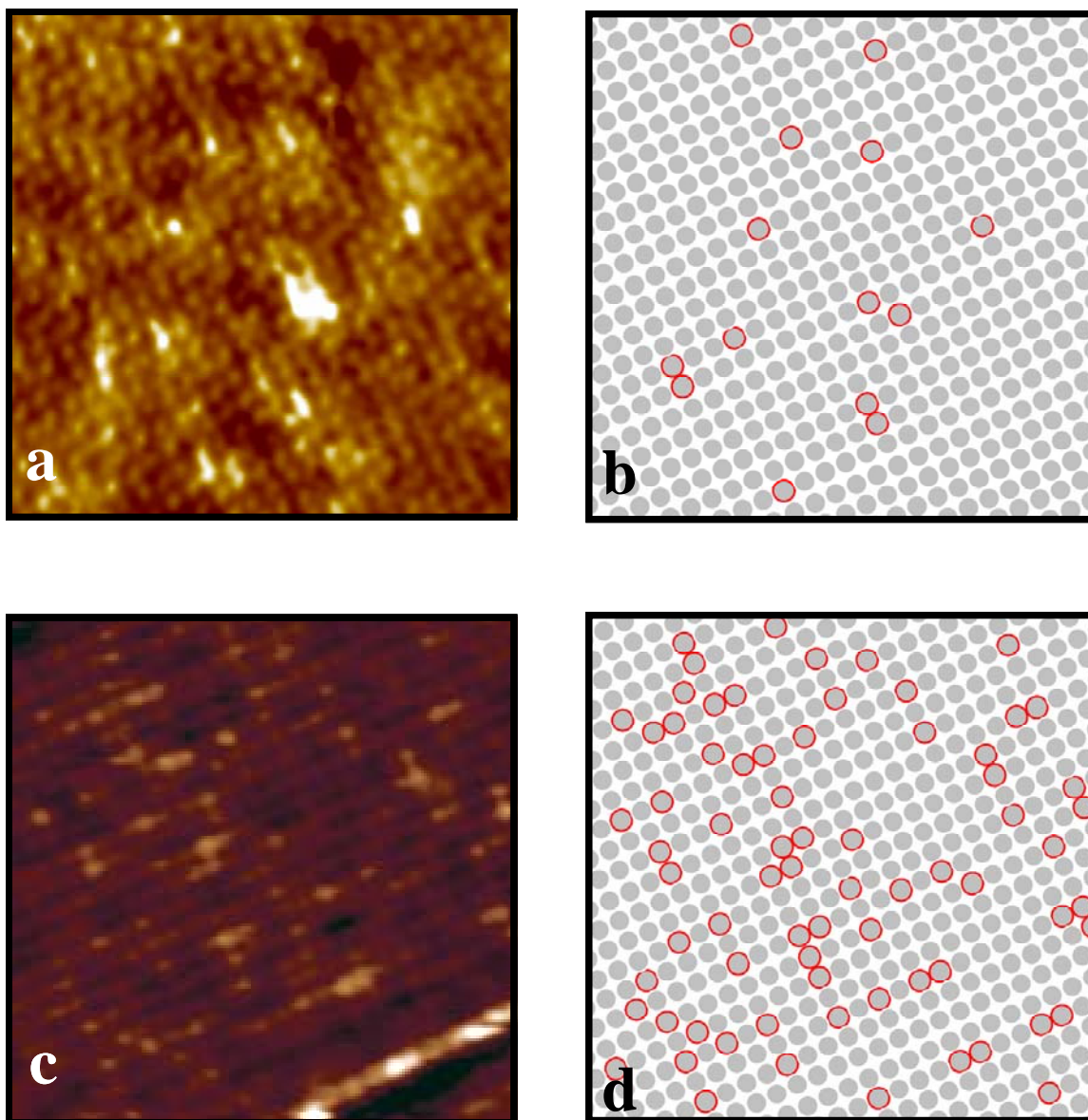


Figure 52. High resolution STM images of Au/Pd alloy on Rh(100). (a) 0.5 ML Pd deposited on 2 ML Au/Rh(100) at 600 K. (b) Schematic representation of (a) for clarity. The red circle corresponds to the bright spots in (a). (c) 1 ML Pd deposited on 2 ML Au/Rh(100) at 600 K. (d) Schematic representation of (c) for clarity. The red circle corresponds to the bright spots in (c). All images have dimensions of  $5 \text{ nm} \times 5 \text{ nm}$ . Tunneling parameters are  $V_s = -6 \text{ mV}$  and  $I = 5 \text{ nA}$ .

ML/min, the deposited Pd atoms are susceptible to surface nucleation and subsequent exchange with underneath Au atoms to stay in the agglomeration form in the surface lattice. Increasing the surface temperature should facilitate the surface diffusion of Pd atoms. However, our study also shows annealing at a surface temperature higher than 800 K facilitates the formation of thermodynamic equilibrium phase of Au-Pd alloy, which is incommensurate to the Rh(100) substrate (Figure 53).

Figure 53 displays the high resolution STM images of 2ML Pd/2 ML Au alloy film after 800 K and 1000 K annealing. Both surface moiré pattern and surface irregularity appeared after annealing, due to mismatch between the alloy Au-Pd film and the Rh(100) substrate. The non-planar, incommensurate alloy film brought difficulties for STM to reveal the chemical contrast between Au and Pd atoms. Therefore, the optimized method to grow planar Au-Pd alloy film is to deposit Pd onto the Au/Rh(100) surface at 600 K. Low flux rate is preferred in order to prevent the agglomeration of Pd islands.

### **The growth of Ag-Au alloy clusters on TiO<sub>2</sub>(110)**

The most simple and convenient way to synthesize supported alloy model catalysts is to evaporate metal atoms in UHV directly onto an oxide support surface. However, this method has an inherent problem, which is to prove that two metals mix together and form alloy clusters, rather than separating on the surface and forming two types of monometallic clusters. In this study, we applied *in-situ* STM to solve this problem and investigate the growth kinetics of Ag-Au alloy clusters supported on TiO<sub>2</sub>(110).

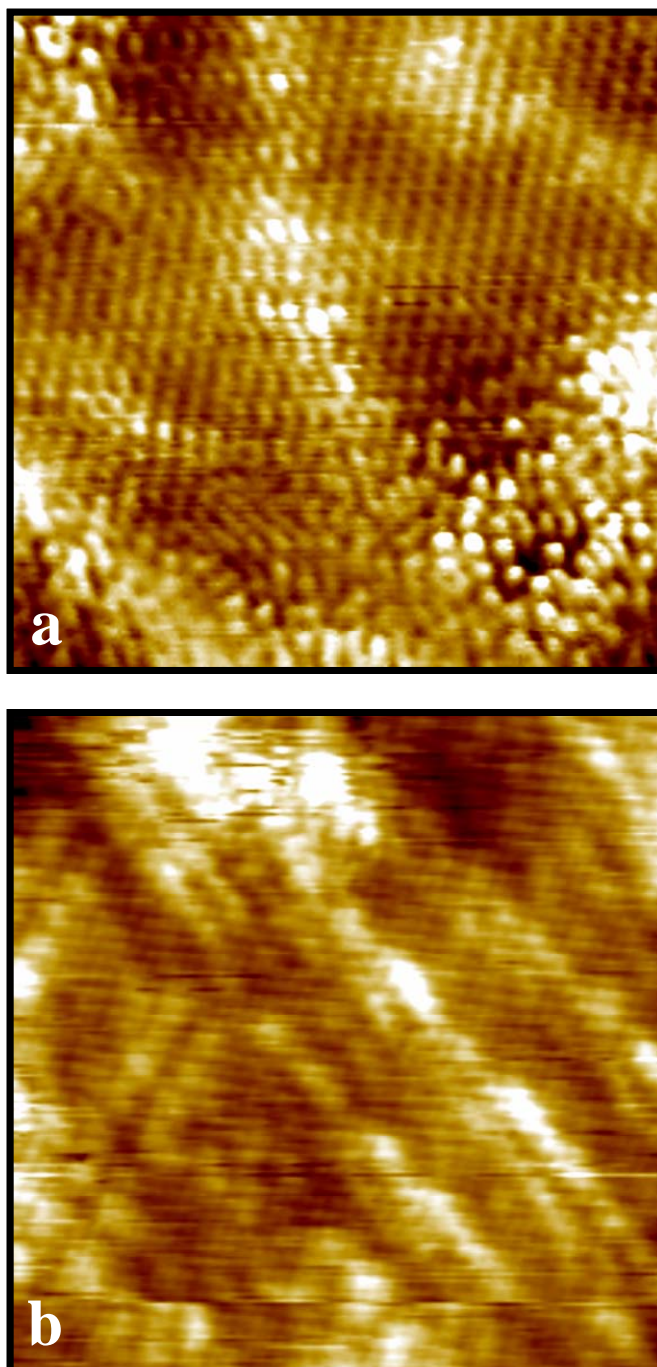


Figure 53. High resolution STM images of Au/Pd alloy on Rh(100). (a) 2 ML Pd deposited on 2 ML Au/Rh(100) at 300 K and annealed at 800 K for 10 min. (b) 2 ML Pd deposited on 2 ML Au/Rh(100) at 300 K and annealed at 1000 K for 10 min. The image sizes are: (a) 7 nm  $\times$  7 nm, (b) 10 nm  $\times$  10 nm. Tunneling parameters are  $V_s = -20$  mV and  $I = 5$  nA.

Similar to the promotion of Pd catalysts, the addition of Au can also enhance the activity and selectivity of Ag catalysts for alkene epoxidation [273-275]. In this study, we synthesize Ag-Au alloy clusters of varying ratios supported on  $\text{TiO}_2(110)$  and determine the growth kinetics for these Ag-Au clusters. The growth of Ag clusters on  $\text{TiO}_2(110)$  has been investigated in detail [95, 195, 276]. Studies reveal that Ag forms uniformly-sized and thermally-stable clusters that exhibit a “self-limiting” growth mechanism [276]. Furthermore, for Ag there is virtually no difference in the growth mode of clusters at step-edges relative to growth at terraces, in marked contrast to the growth of Au on  $\text{TiO}_2(110)$  as discussed above.

To understand the growth of Au clusters in the presence of Ag clusters, sequential *in-situ* STM measurements were carried out as a function of Au coverage on Ag pre-covered  $\text{TiO}_2(110)$  surface. A particular pre-coverage of 0.08 ML Ag (Figure 54a) was chosen to almost saturate the step edge sites with Ag clusters and thus allow the investigation of Au growth in the absence of their preferred nucleation sites. The series of *in-situ* STM images (Figure 54) show how the alloy clusters grow as a function of Au coverage on a cluster-by-cluster basis. It is noteworthy from these images (Figure 54a and 54b) that initially almost no new clusters form, however, with increased coverage, cluster size and number density gradually increase.

The histograms corresponding to these images are shown in Figure 55. The image of the Au-free surface (Figure 54a, 0.08 ML of Ag) shows: (i) a uniform distribution of Ag clusters with an average size distribution of 3.84 nm, and (ii) an average cluster size much larger than Au for a similar coverage. In other words, to obtain an equivalent average cluster size for Au, a much larger Au coverage is required. For the

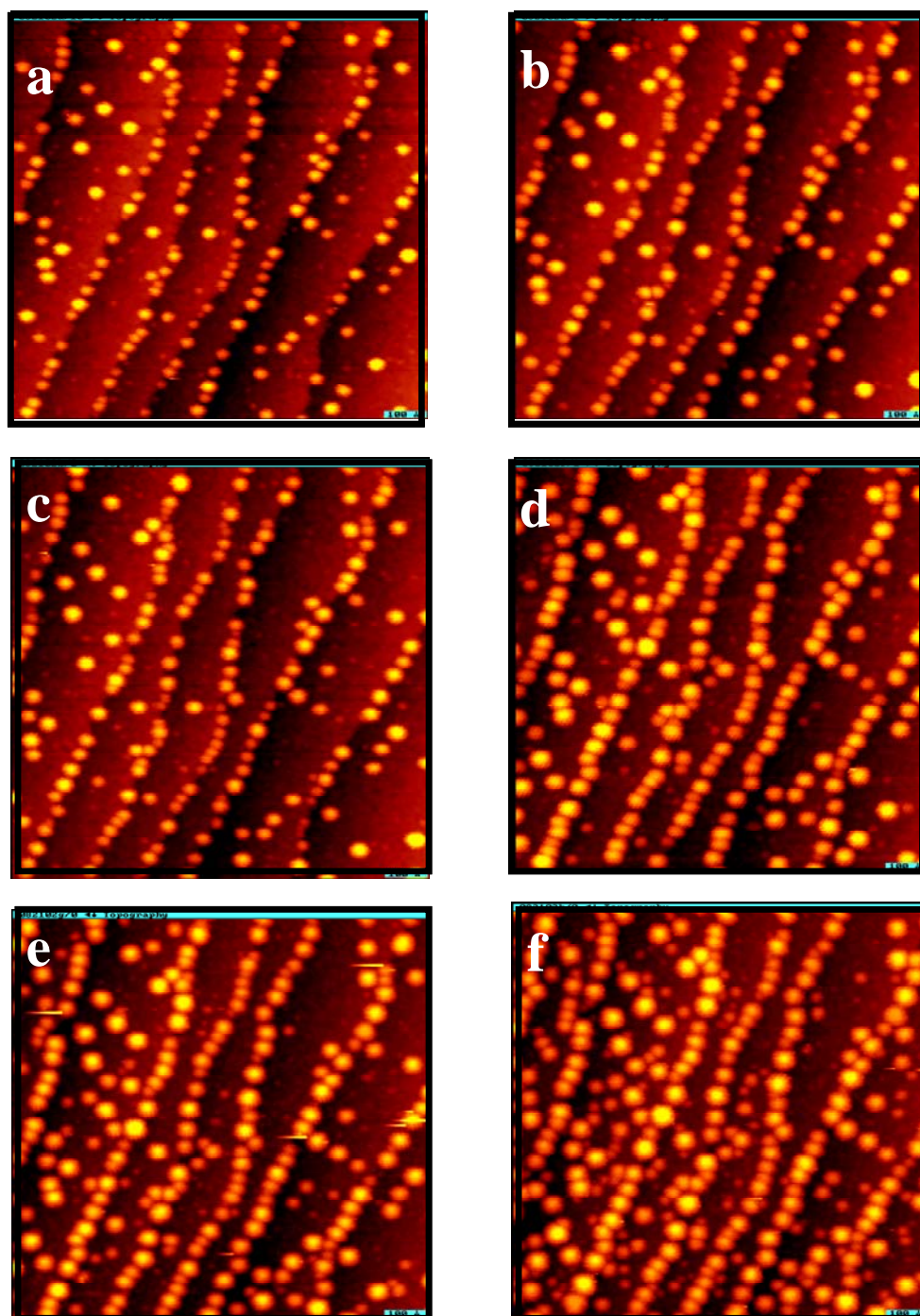


Figure 54. STM images ( $100 \text{ nm} \times 100 \text{ nm}$ ) during Au deposition on a Ag pre-covered (0.08 ML)  $\text{TiO}_2(110)$  surface after deposition of (a) 0.08 ML Ag, (b) 0.17, (c) 0.34, (d) 0.85, (e) 1.53 and (f) 2.04 ML Au.

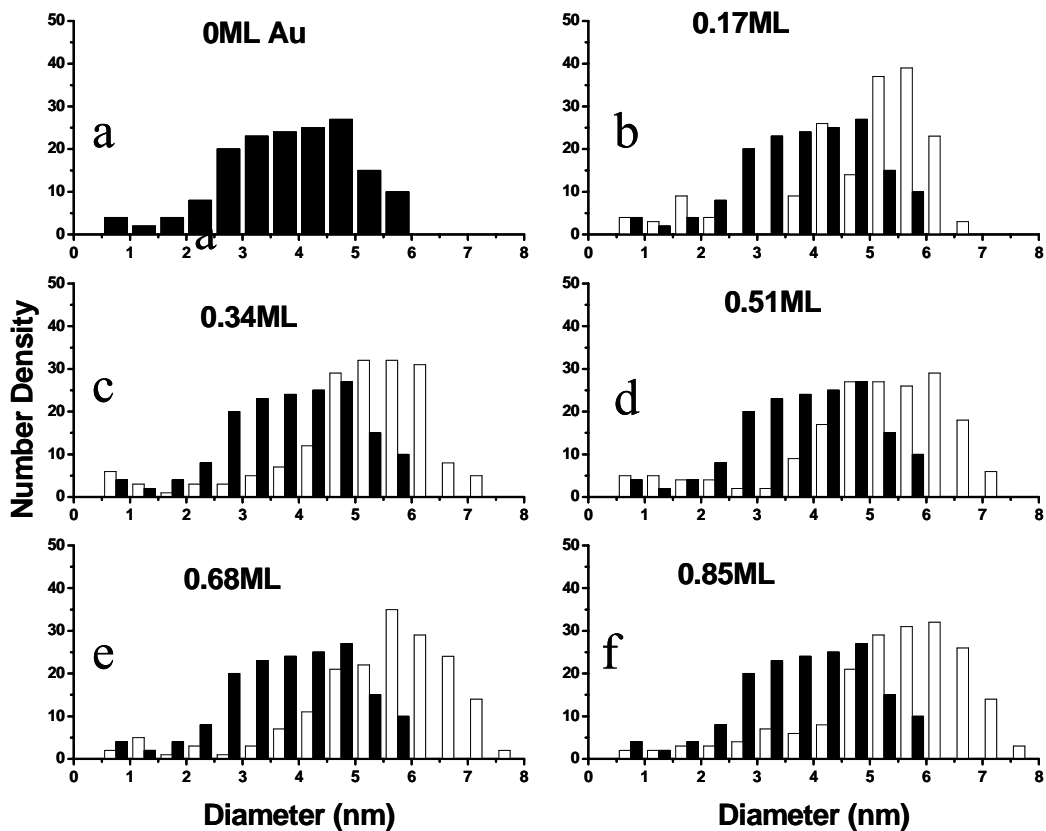


Figure 55. Histograms of the number density of clusters for various Au covered surfaces shown in Figure 54 as a function of their diameter. In plots (b) – (f), black bars are obtained from plot (a) and are shown side-by-side to demonstrate how the size distribution changes as a function of Au coverage with respect to that of a Ag pre-covered  $\text{TiO}_2(110)$  surface.



Au-covered surface, the cluster size distribution is indicated with unfilled bars, while the filled bars show the size distribution prior to Au deposition for reference. As Au coverage increases, the cluster size distribution gradually shifts towards larger diameters indicating preferential Au growth on existing clusters (Figure 54).

To understand the growth mode of Au on partially covered step edge sites, the  $\text{TiO}_2(110)$  surface was pre-covered with Ag (0.033 ML) such that a fraction of empty step edge sites remain (Figure 56a) for the nucleation of new Au clusters. This experiment was designed to contrast the Au growth in Figure 54, where almost no new Au clusters were found to nucleate until the Au coverage became relatively high. Such behavior can be (1) explained by a tendency to preferential alloy, or (2) because the pre-covered Ag clusters act as preferred nucleation sites. It is noteworthy that only after a small amount of Au deposition (0.17 ML), the STM image (Figure 56b, area marked with circle) shows nucleation of new Au clusters. However, with an increase in the Au coverage, the diameter and number density increase gradually, similar to the results of Figure 54.

The histograms of the size distribution corresponding to the STM images (Figure 56) are shown in Figure 57. The plot (Figure 58a) before starting Au deposition shows that the Ag clusters are uniform in size with an average size distribution of 3.8 nm. Although the coverage of Ag in Figure 54a (0.08 ML) is much larger than that shown in Fig. 56a (0.033 ML), the average cluster size in both cases is approximately the same ( $\sim 3.84$  nm). This is a clear indication of self-limiting growth [276]. Moreover, consistent with the previous case (Figure 54), with increased Au deposition, the size distribution

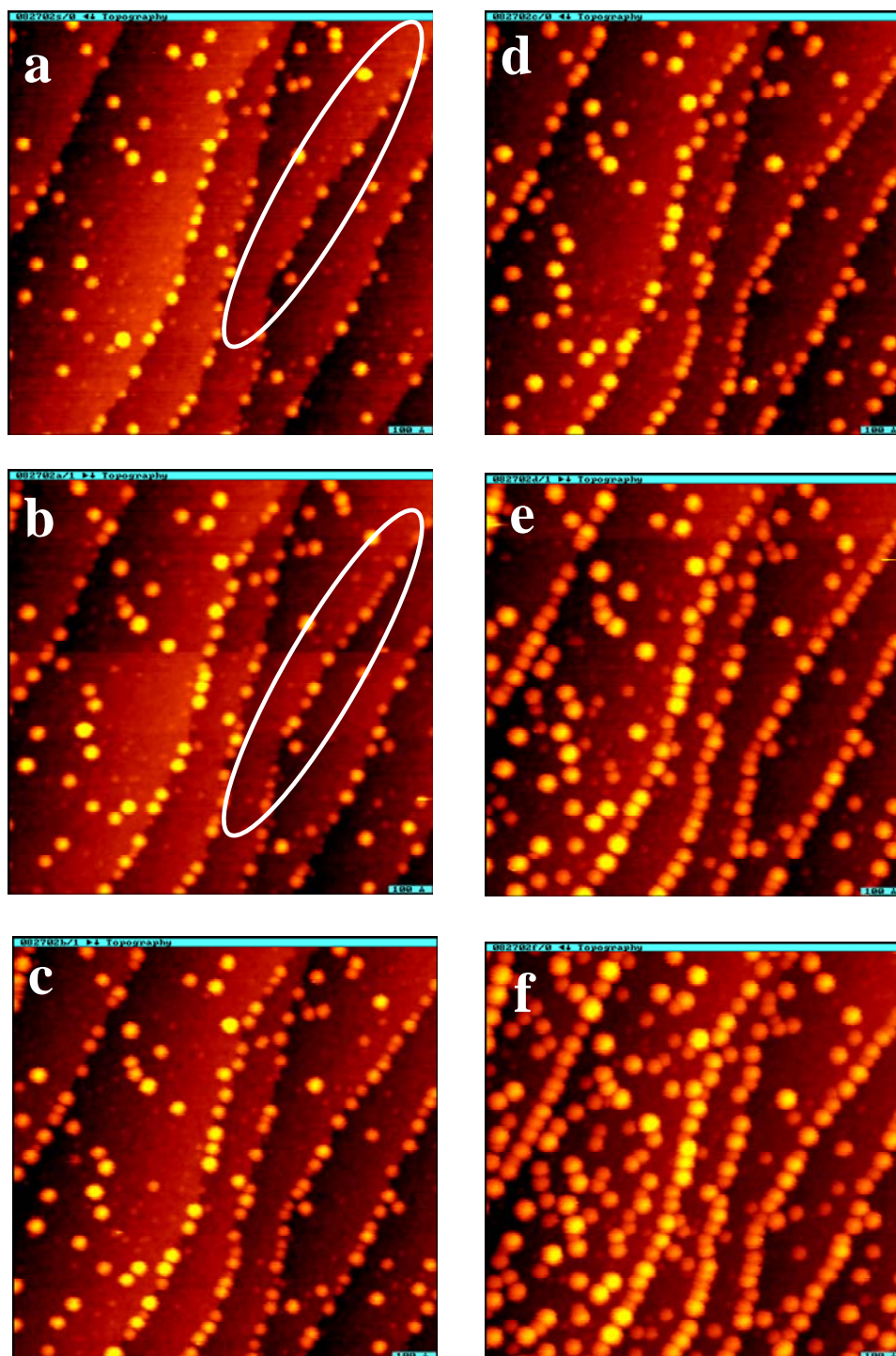


Figure 56. STM images (100 x 100 nm) during Au deposition on Ag pre-covered (0.033ML)  $\text{TiO}_2(110)$  surface after deposition of (a) 0.033ML Ag, (b) 0.17, (c) 0.34, (d) 0.51, (e) 0.85 and (f) 1.53 ML Au. The white circles in image (a) and (b) show the appearance of new Au clusters.

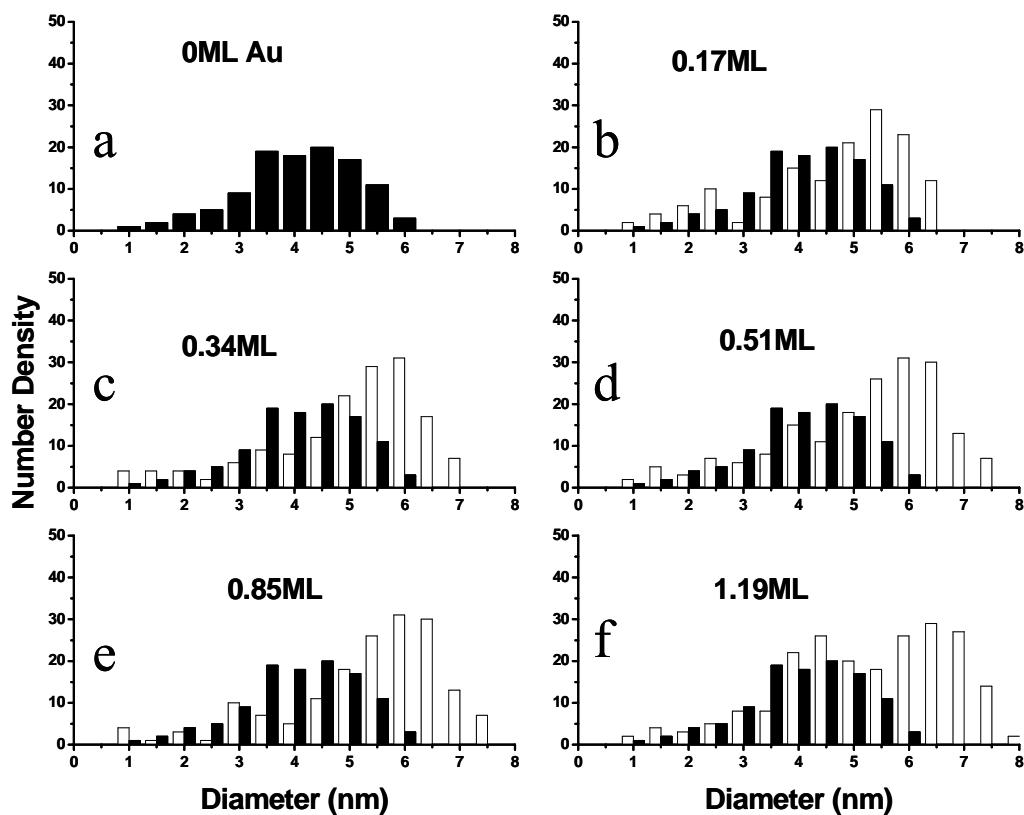


Figure 57. Histograms of the number density of clusters for various Au covered surfaces shown in Figure 56 as a function of their diameter. In plots (b) – (f), black bars are obtained from plot (a) and are shown side-by-side to demonstrate how the size distribution changes as a function of Au coverage with respect to that of a Ag pre-covered  $\text{TiO}_2(110)$  surface.

gradually shifts towards a higher value, indicating further growth of the existing clusters at the expense of the deposited Au.

The growth mode of clusters on steps is accelerated compared with that at terrace sites (Figure 58). The plots in Figure 58a-58c show remarkable contrast with the growth behavior of Au clusters supported on clean  $\text{TiO}_2(110)$ : (a) in terms of average diameter or height, almost no difference exist between the growth mode on step edge sites and those on terraces, and (b) the number density of alloy clusters does not increase continuously. However, in general, Figure 58c shows that the number density of clusters at the step edge sites are much higher compared to those on terraces, as is evident in Au growth on  $\text{TiO}_2(110)$ . A rapid increase in the number density of clusters (indicated by dotted line in Figure 58c) at step edge sites for a lower Ag pre-covered (0.033 ML) surface is apparent in Figure 56b.

These systematic experiments of Au growth on  $\text{TiO}_2(110)$  with Ag clusters blocking step edge sites to varying extent demonstrate the following findings. (a) On Ag pre-covered  $\text{TiO}_2(110)$  surfaces, competitive nucleation and growth on step edge sites as well as on pre-nucleated Ag clusters occur depending on the availability of the former sites. (b) Ag clusters on clean  $\text{TiO}_2(110)$  surface grow with uniform size distribution in a self-limiting fashion. (c) The average size of Ag clusters is much larger than that of Au clusters at the same metal coverage. Nevertheless, it is still not clear from these experiments why the pre-deposited Ag clusters act as active nucleation sites for Au. Is it due to the preferential alloying tendency of Ag or to the Ag clusters acting as a nucleation “seed crystal”?

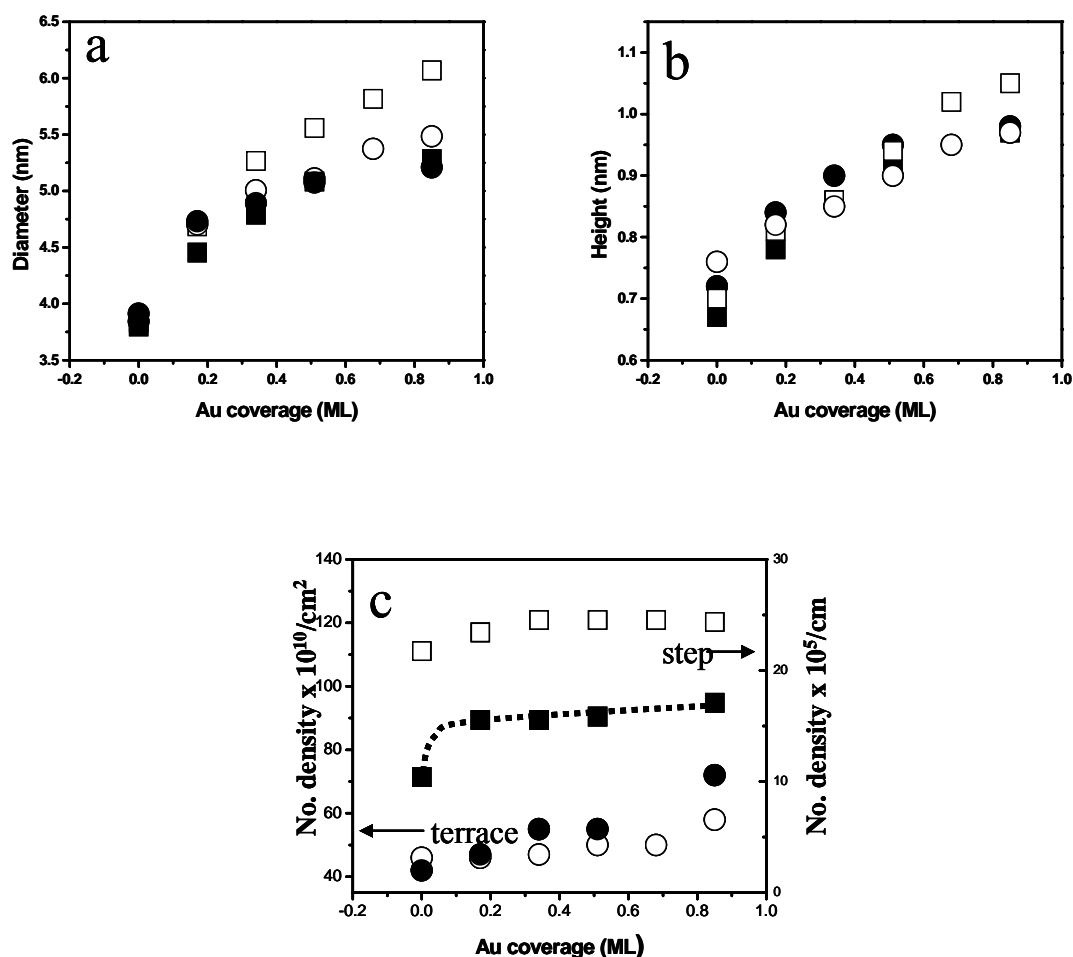


Figure 58. Au coverage dependent plots for two different Ag pre-covered (0.08 and 0.033 ML) TiO<sub>2</sub>(110) surfaces after isolating the contributions of edges from those of terraces as a function of: (a) number density, (b) diameter and (c) height. Open and solid symbols are used for the 0.08 and 0.033 ML Ag pre-covered surfaces, respectively. The dotted line indicates the sharp increase in the number of clusters after 0.17 ML of Au deposition. Number density at terraces is expressed in the number of clusters/cm<sup>2</sup> while that at steps is expressed in the number of clusters/cm (i.e., per unit length of the step).

### **The structure and adsorption sites of the ultra-thin silica film**

Silica ( $\text{SiO}_2$ ) is one of the most important oxide supports in catalysis. Surface science studies on bulk  $\text{SiO}_2$  have been limited because bulk  $\text{SiO}_2$  is an insulator and difficult to be characterized by electron or ion probes. In this case, thin silica films supported on single crystal metal surfaces are a good substitute and have been developed as the support for model catalytic studies. The first attempts to synthesize thin silica films for model catalytic studies dated back to the early 1990's, when Goodman and coworkers prepared amorphous  $\text{SiO}_2$  films on the Mo(100) and Mo(110) substrates [277, 278]. In the past five years, considerable attention has been paid to the well-ordered ultra-thin silica film (1 ML  $\text{SiO}_2$ ) which has  $c(2 \times 2)$  LEED pattern. Since Schroeder et al. [279] reported the synthesis of this well-ordered silica film supported on a Mo(112) substrate, a number of experimental and theoretical efforts have been devoted to reveal its atomic structure and apply the film as a support for model catalytic studies [280].

In spite of the extensive studies on the ultra-thin silica film supported on Mo(112), the atomic structure of this silica film is still under debate. Weissenrieder et al. [281] observed a honeycomb-like structure on the ultra-thin silica film using STM and suggested a 2D-network model based on their DFT calculations. Against this model, HREELS and STM studies by Chen et al. [282, 283] presented detailed information on the electronic structure of this silica film and suggested the  $[\text{SiO}_4]$  tetrahedra is isolated on the Mo(112) substrate. They proposed a different structural model, referred as the cluster model in a recent review by Kaya et al. [280] In the review, Kaya et al. suggested the discrepancy might be caused by the difference in the preparation procedures of ultra-thin silica films. Basically, the ultra-thin silica film can be prepared by the oxidization of

deposited Si atoms on Mo(112) and subsequent annealing to remove multi-layer SiO<sub>2</sub>. Subtle difference in the detailed preparation procedure remains between the above two groups. While Weissenrieder et al. desorbed the multi-layer SiO<sub>2</sub> film through UHV annealing, Chen et al. chose to anneal and remove the multi-layer SiO<sub>2</sub> film in an oxygen ambient ( $10^{-8}$ - $10^{-7}$  Torr O<sub>2</sub>). Therefore, Kaya et al. suggested the structure of the film annealed in UHV (“O-poor”) might differ with that of the film annealed in oxygen (“O-rich”), which has additional oxygen atoms adsorbed onto the Mo(112) substrate.

To resolve the discrepancy on the structure of this ultra-thin silica film, we conducted STM studies to resolve the atomic structure of both the “O-poor” film and the “O-rich” film adopting the preparation recipes by Weissenrieder et al. [281] and Chen et al. [282, 283]. Our STM study shows no difference between the two films in either the surface morphology or the atomic structure. Indeed, on the same ultra-thin silica film surface, we have observed all the surface electronic structures resolved by Weissenrieder et al. and Chen et al. In Figure 59, we show how the electronic structures observed by Weissenrieder et al. transit into the electronic structures observed by Chen et al. at a varying bias voltage.

Figure 59 shows the atomic resolution STM images consecutively obtained on the 1 ML SiO<sub>2</sub>/Mo(112) surface at varying bias voltages. Figure 59a - 59c all exhibit two bright protrusions along the  $[\bar{1}\bar{1}1]$  direction in a  $c(2 \times 2)$  unit. In particular, Figure 59a and 59c resolve a  $c(2 \times 2)$  surface with triangular protrusions. The two spots within the  $[\bar{1}\bar{1}1]$  row are brighter than the spot outside the row. Figure 59b resolves a  $c(2 \times 2)$  unit that contains only two bright spots lining along the  $[\bar{1}\bar{1}1]$  direction. Figure 59d also shows a  $c(2 \times 2)$  surface with triangular protrusions while no bright spots could be distinguished

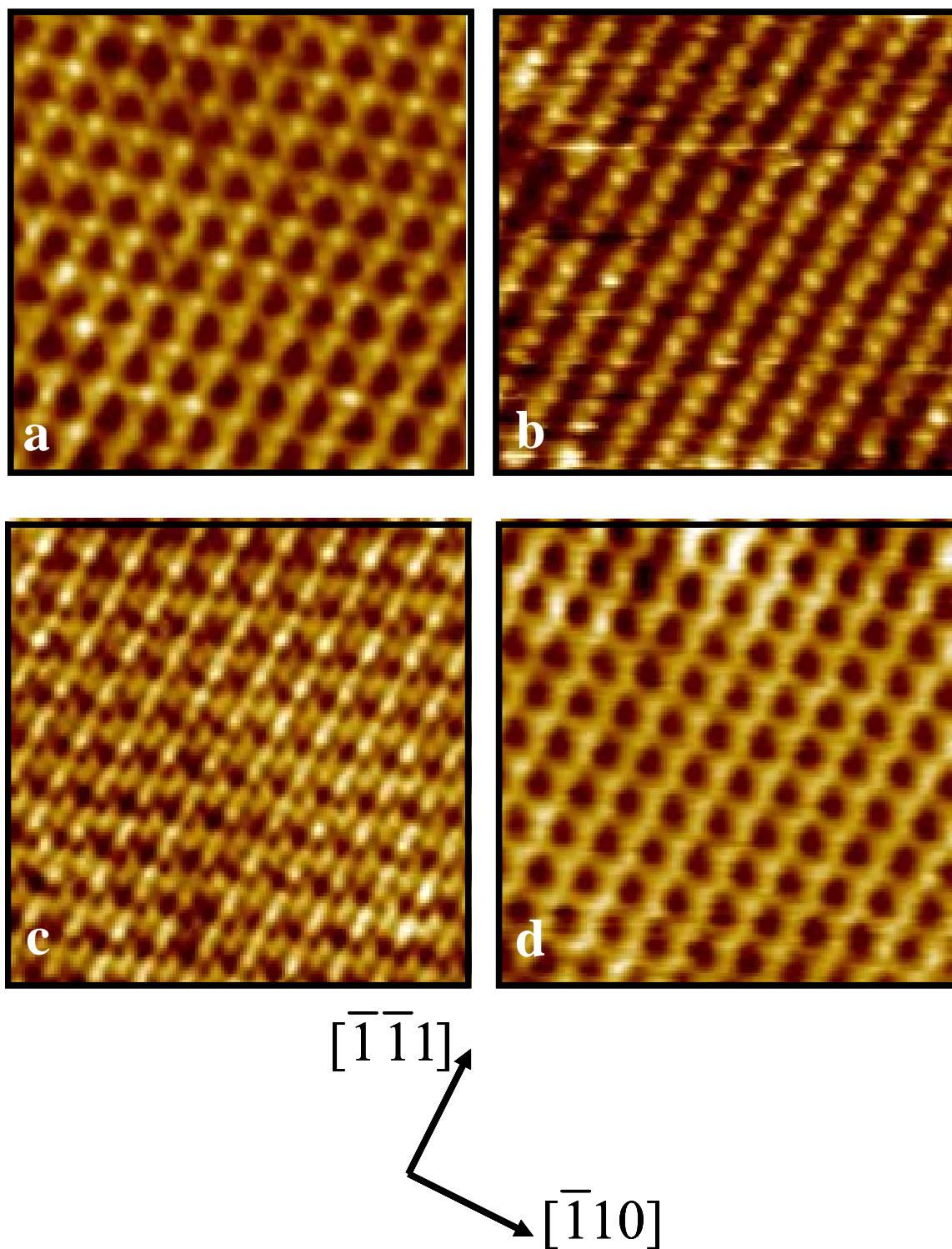


Figure 59. STM images of  $\text{SiO}_2(1\text{ML})/\text{Mo}(112)$  at various sample bias voltages. All images have dimensions of  $5\text{ nm} \times 5\text{ nm}$ . Tunneling parameters are (a)  $V_s = -0.6\text{ V}$ ,  $I = 2\text{ nA}$ , (b)  $V_s = -0.3\text{ V}$ ,  $I = 2\text{ nA}$ , (c)  $V_s = 0.3\text{ V}$ ,  $I = 2\text{ nA}$ , and (d)  $V_s = 1\text{ V}$ ,  $I = 2\text{ nA}$ .



within the protrusions. Further, through various-bias STM images, we found the two bright spots or the bright  $[\bar{1}\bar{1}1]$  row in Figure 59a are in the same line as those protrusions in Figure 59b-50d. There is no contrast reversal while varying the bias voltage. Therefore, the protrusions in Figure 59 correspond to the same surface features of the ultra-thin silica film. The evolution of electronic structures in Figure 59 suggests, within this small bias range, same surface features are probed while the resolution contrast varies with the bias dependent tip-surface separation.

Electronic structures in Figure 59a and 59c are similar to those reported by Weissenrieder et al., although those structures observed by Weissenrieder et al. did not show height difference within the triangular protrusions. They assigned the three spots in the triangular protrusions (Figure 59a and 59c) as oxygen atoms pointing out of the surface [281]. Figure 59d resembles the honeycomb structures reported by Weissenrieder et al., who derived the 2D-network model mainly based on this honeycomb structure and suggested each honeycomb consists of six Si atoms. The honeycomb-like structure resolved in Figure 59d is not a rigorous hexagonal pattern as observed by Weissenrieder et al., but very close to the structure in Figure 59a. All STM images in Figure 59 are raw images without filtering. It is possible the rigorous honeycomb structure reported by Weissenrieder et al. was caused by heavy filtering or fault drift correction.

Moreover, in their report, the assignment of honeycomb structures to Si hexagonal ring is arguable because the bias voltage (+1.2 V), they used to obtain the honeycomb structure, is close to the bias voltage (+0.65 V), they used to obtain the STM image with triangular protrusions, which they assigned as oxygen atoms. Generally, atoms with opposite charge states could not be resolved with similar apparent heights

within such a small bias range. Meanwhile, the electronic structure they calculated [281, 284], as well as the DFT calculation by Giordano et al.[285], suggests the DOS near the Fermi level is mainly contributed by the substrate Mo atoms. This means the observed electronic structures could not be directly assigned to either Si or O atoms. Instead, the topographic STM images should be interpreted with a combination of substrate electronic effect and surface geometric effect. In other words, STM probed the local DOS from hybridized orbitals of Mo while the length of local electronic waves protruding into the vacuum varies with the position of topmost surface atoms, i.e., O atoms. Therefore, the bright features in Figure 59 should always be assigned to O atoms.

The electronic structure shown in Figure 59b is the same as one of those observed by Chen et al. [282], who reported a series of bias-dependent STM images. STM images reported by Chen et al. demonstrate two characteristics: 1) at low bias voltages ( $-1 \text{ V} < V_s < 1 \text{ V}$ ), the STM images show electronic structures of either the  $(1 \times 1)$  Mo(112) substrate or the  $c(2 \times 2)$  units of silica with two bright protrusions (double-spot unit), and 2) at high bias voltages ( $|V_s| > 1 \text{ V}$ ), the STM images resolve electronic structures of the  $c(2 \times 2)$  units of silica with either one bright protrusion (single-spot unit) or four bright protrusions (quadruple-spot unit). These characteristics reported by Chen et al. were also observed in our STM study on the ultra-thin silica film.

The calculated electronic structures of the ultra-thin silica film [285] support the above characteristics seen by Chen et al. and us. Overall, STM probes the DOS contributed by Mo 5d electrons whereas, locally, the hybridized orbitals probed by STM have a shape according to the surface geometry of  $[\text{SiO}_4]$  tetrahedral. At small bias voltages, the tip-sample separation is reduced resulting in a better overlap between the tip

state and the surface state. STM images reveal the superimposed surface geometry of  $[\text{SiO}_4]$  tetrahedra on the  $(1 \times 1)$  Mo substrate. The position of two topmost oxygen atoms in the  $\text{SiO}_4$  tetrahedral is demonstrated as two protrusions in the STM image. The image contrast is dependent on the extent of overlapping between the tip state and the surface state. At large bias voltages, the tip-sample separation is increased so that the fine surface geometry of  $[\text{SiO}_4]$  tetrahedral could not be resolved. STM tip only overlaps with the outmost surface states of each Mo- $[\text{SiO}_4]$  unit and produces a single protrusion per  $[\text{SiO}_4]$  tetrahedral in STM images. The quadruple-spot STM image could be caused by two reasons: 1) at a sample bias of -3 V, the occupied states of oxygen are probed by STM, and 2) the STM tip adsorbs a molecule resulting in an extended tip state to overlap with surface states and revealing all oxygen atoms in the  $[\text{SiO}_4]$  tetrahedral.

No contrast reversal has been observed through our STM studies on the ultra-thin silica film surface, which suggests the DOS near Fermi level is mainly contributed by Mo substrate and supports our above interpretation of STM images based on the calculated electronic structures. Further, the single-spot and quadruple-spot STM images demonstrate the surface density of  $[\text{SiO}_4]$  tetrahedral, which is only half of the density described in the 2D-network model. The electronic structures we observed explicitly support the cluster model proposed by Chen et al., as shown in Figure 60. The detailed positions and tilted angles of oxygen atoms in Figure 60 might need be modified to better match the surface geometry of oxygen atoms observed in Figure 59.

In the preparation of ultra-thin silica film on Mo(112), the procedure of Si deposition and subsequent oxidation also varied in previous studies [282, 283, 286]. While Min et al. employed a single-step Si deposition procedure [286], Chen et al. used

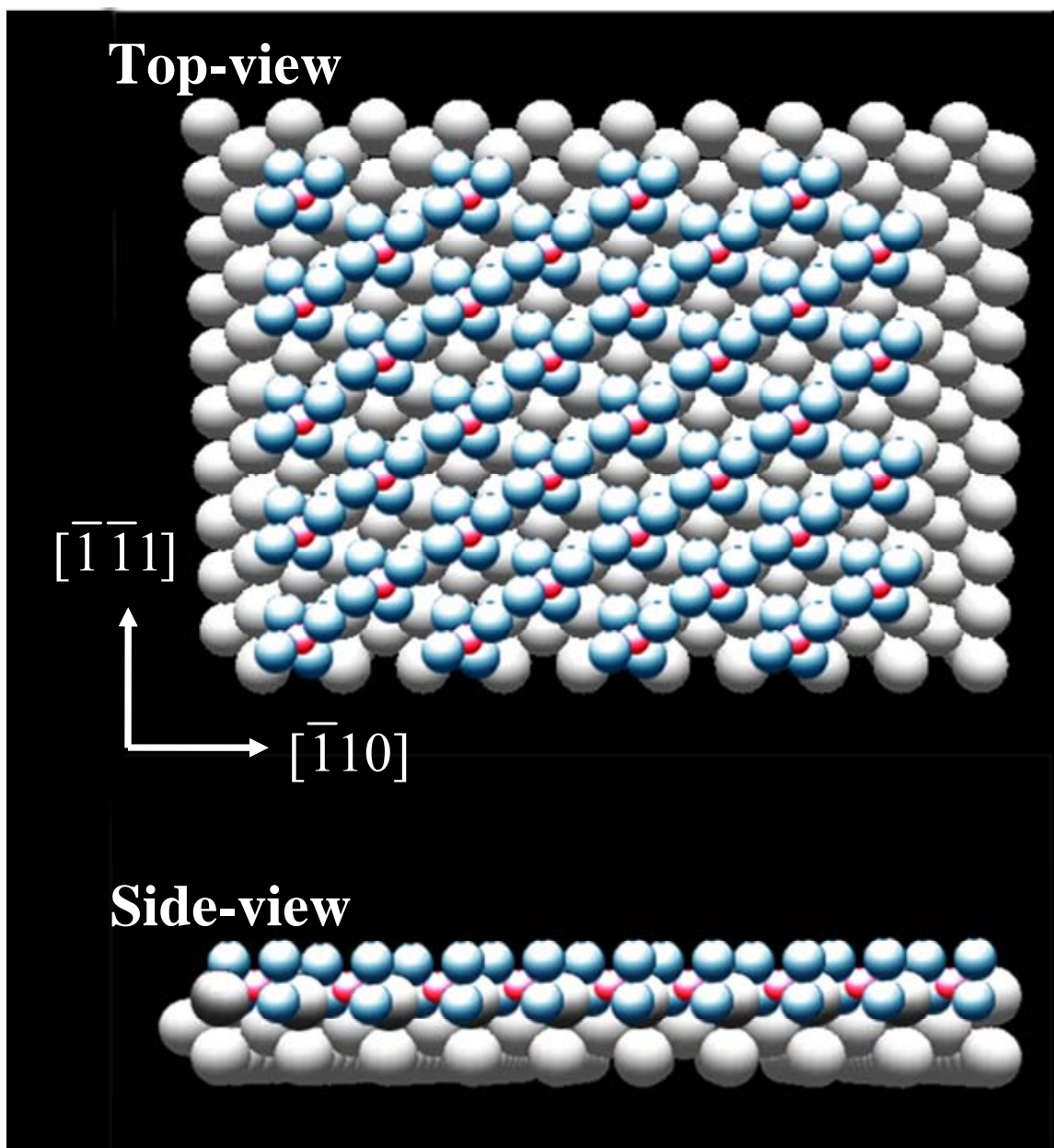


Figure 60. Top-view and side-view of the structural model of isolated  $[\text{SiO}_4]$  for  $\text{SiO}_2(1 \text{ ML})/\text{Mo}(112)$ . In the ball model, white represents Mo, red represents Si, and blue represents O.

repeated cycles of Si deposition with subsequent oxidation and annealing [282, 283]. We found the procedure of Si deposition and oxidation did not influence the surface structure of ultra-thin silica film. Indeed, the annealing temperature for desorption of multi-layer  $\text{SiO}_2$  is found most critical to the preparation of ultra-thin silica film. Our STM study shows, 1) when the annealing temperature is below 1250 K, insufficient surface diffusion and desorption caused  $\text{SiO}_x$  islands and clusters to remain on the planar  $\text{SiO}_2$  surface, and 2) when the annealing temperature is above 1250 K, the decomposition of ultra-thin silica film occurs and starts from the step edges. The decomposition caused an amorphous  $\text{SiO}_2$  layer on the surface, which evaporates away at above 1400 K. When the Si coverage is lower than 1 ML, sub-monolayer silica film forms with the same ordered structure as the ultra-thin silica film. Comparing the AES signal of the sub-monolayer silica film with that of the ultra-thin silica film provides the evidence that the ultra-thin silica film is of 1 ML thickness.

We then conducted STM studies using Pd atoms to probe the adsorption sites on the ultra-thin silica film supported on Mo(112). Figure 61 shows the surface morphology of 0.01 ML Pd deposited on the ultra-thin silica film at room temperature. Besides small Pd clusters, adsorption of Pd atoms on the extended surface of ultra-thin silica film were also observed, suggesting the limited diffusivity of Pd atoms on the silica surface, as well as the strong interaction between Pd and silica. In Figures 61, the Pd adsorption sites are demonstrated by varying the sample bias voltages to reveal the different electronic structures of the silica surface. The bias-dependent topographic images explicitly show Pd atoms are always adsorbed on the bright protrusions, which have been assigned as oxygen atoms or  $\text{SiO}_4$  units in the above discussions. Since Si atoms are at the center of

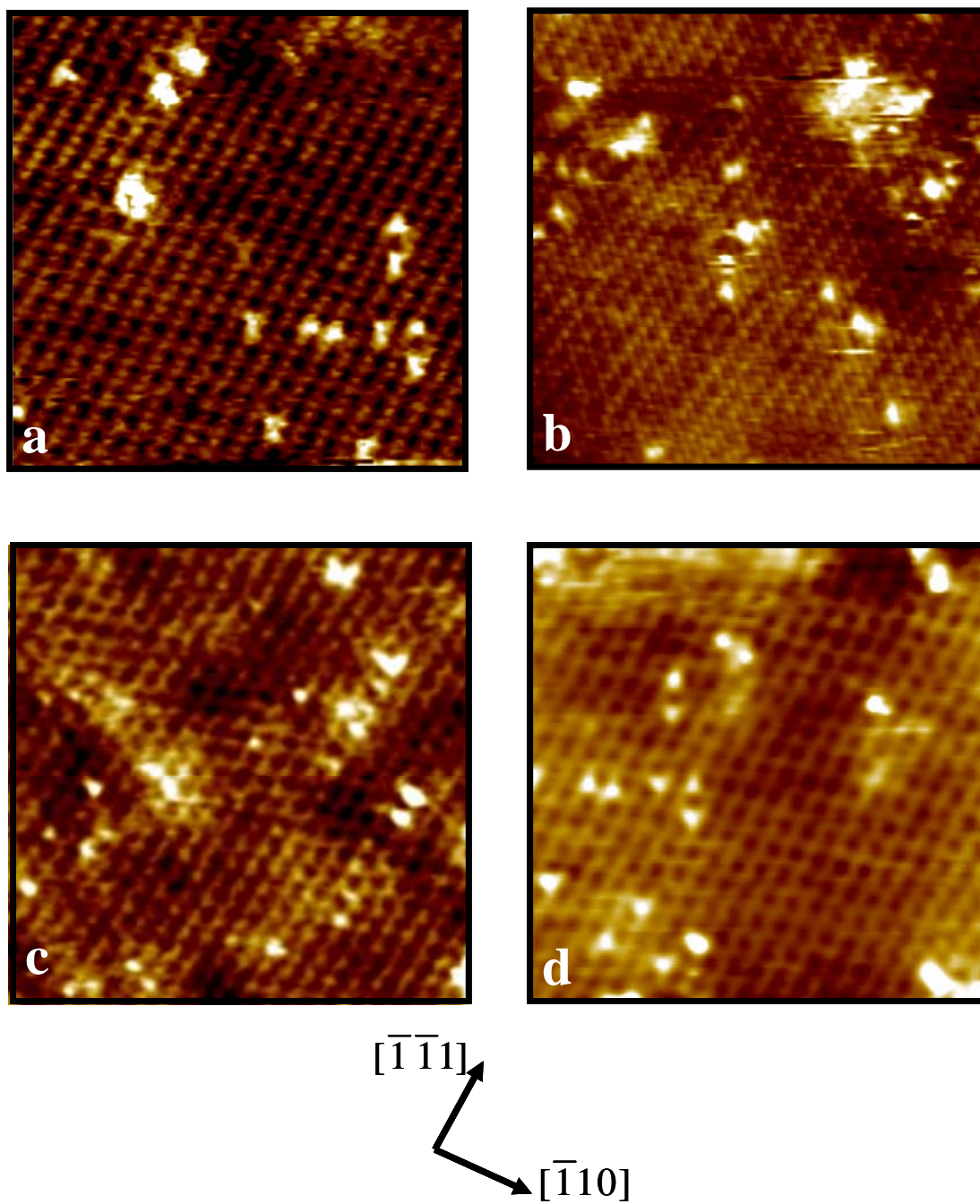


Figure 61. STM images of 0.01 ML Pd deposited on  $\text{SiO}_2(1 \text{ ML})/\text{Mo}(112)$ . All images have dimensions of  $10 \text{ nm} \times 10 \text{ nm}$ . Tunneling parameters are (a)  $V_s = -0.4 \text{ V}$ ,  $I = 1 \text{ nA}$ , (b)  $V_s = -0.2 \text{ V}$ ,  $I = 1 \text{ nA}$ , (c)  $V_s = 0.3 \text{ V}$ ,  $I = 1 \text{ nA}$ , and (d)  $V_s = 1 \text{ V}$ ,  $I = 1 \text{ nA}$ .

these oxygen atoms, these images so far can not conclude whether Pd is bonded to Si or oxygen atoms.

Figure 62 shows the surface morphology of Pd on the ultra-thin silica film when Pd coverage is increased to 0.03 ML. At increased coverage, the density of surface Pd atoms decreased accompanying the density increase of Pd clusters. Meanwhile, the inter-cluster distance is always less than 5 nm in Figure 62. This suggests Pd atoms adsorbed on the ultra-thin silica film are instable and would diffuse to and incorporate into nearby Pd clusters when their distance is less than 5 nm. Similar to Figure 61, Pd clusters always stayed on top of the bright protrusions while some Pd clusters elongated along the  $[\bar{1}\bar{1}1]$  direction. Figure 62a and 62d also show, during scanning, the honeycomb-like surface pattern of silica transformed into the single-spot surface pattern, suggesting a slightly increased tip-surface separation as the tip scan across the Pd clusters supported on the silica surface.

Figure 63 shows the zoom-in images of Pd nucleation on the ultra-thin silica film. Four typical electronic structures of the ultra-thin silica film are shown, which have a single-spot unit (Figure 63a), double-spot unit (Figure 63b), triple-spot unit (Figure 63c), and quadruple-spot unit (Figure 63d) respectively. Pd atoms and clusters grow exclusively on top of these bright spots. In Figure 63a, Pd atom grows on top of the  $[\text{SiO}_4]$  tetrahedral while slightly leaning toward neighbor oxygen atoms. Pd atom in Figure 63b grows in between the two bright spots, suggesting Pd is bonding to Si in the center of oxygen atoms. Figure 63c also shows Pd clusters grow at the center of three oxygen atoms, where Si locates in the tetrahedral. Figure 63d exhibits the nucleation of Pd clusters on a quadruple-spot unit, where Pd sits on top of  $\text{SiO}_4$  tetrahedral. Figure 63

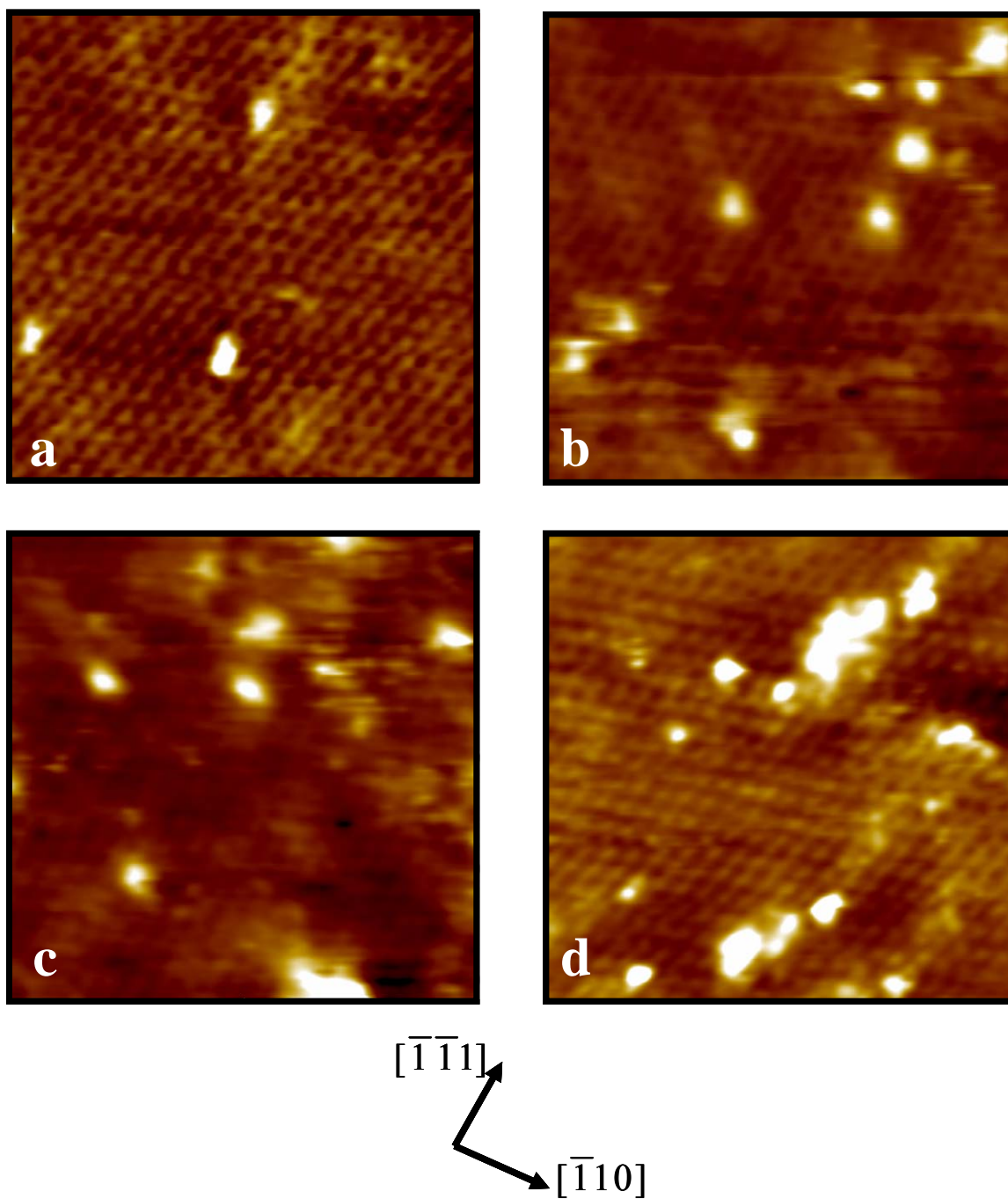


Figure 62. STM images of 0.03 ML Pd deposited on SiO<sub>2</sub>(1 ML)/Mo(112). All images have dimensions of 10 nm × 10 nm. Tunneling parameters are (a)  $V_s = -1$  V,  $I = 0.5$  nA, (b)  $V_s = 1$  V,  $I = 0.5$  nA, (c)  $V_s = 1$  V,  $I = 0.5$  nA, and (d)  $V_s = -1$  V,  $I = 0.5$  nA.



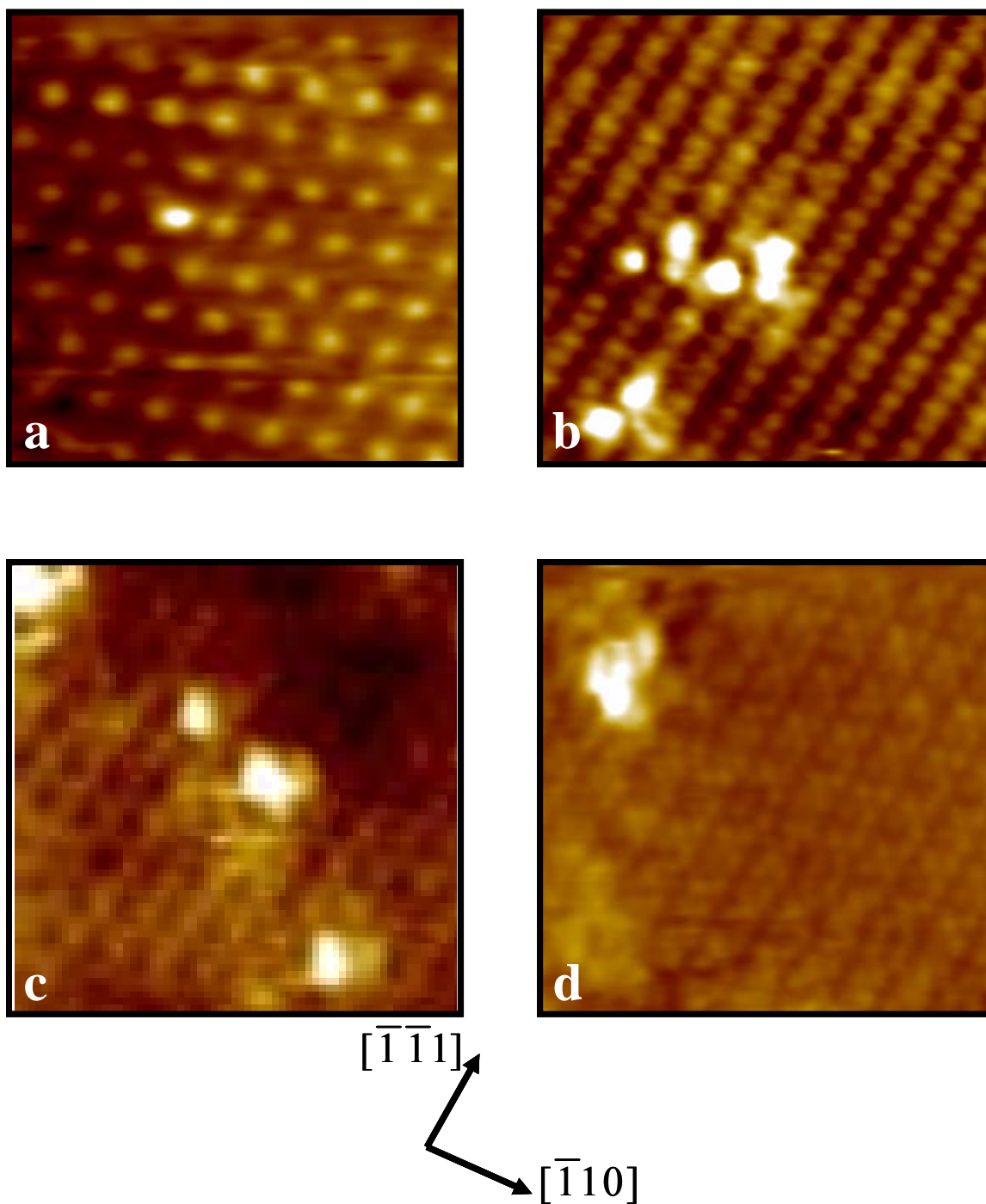


Figure 63. STM images of Pd adsorption on  $\text{SiO}_2(1 \text{ ML})/\text{Mo}(112)$  at various bias voltages. Size and tunneling parameters are (a)  $4 \text{ nm} \times 4 \text{ nm}$ ,  $V_s = -1.2 \text{ V}$ ,  $I = 4 \text{ nA}$ , (b)  $5 \text{ nm} \times 5 \text{ nm}$ ,  $V_s = -0.4 \text{ V}$ ,  $I = 4 \text{ nA}$ , (c)  $5 \text{ nm} \times 5 \text{ nm}$ ,  $V_s = -0.2 \text{ V}$ ,  $I = 4 \text{ nA}$ , and (d)  $5 \text{ nm} \times 5 \text{ nm}$ ,  $V_s = -1 \text{ V}$ ,  $I = 4 \text{ nA}$ .

suggests Pd binds to Si in the SiO<sub>4</sub> tetrahedral while oxygen also plays a role in the nucleation of Pd.

Giordano et al. [285] have recently reported a DFT study on the adsorption of Pd and Au atoms on the ultra-thin silica film, based on the 2D-network model. Their calculations suggest a low adsorption energy ( $\sim 0.3$  eV) of Pd atoms on Si and O sites of the silica film and thus a high diffusivity of Pd atoms across the silica surface. Their results also suggest the center of the honeycomb structure is the strongest binding site of Pd atoms. Our STM results, on the other hand, reveal Pd atoms can nucleate on the ultra-thin silica film without agglomeration and exhibit very low diffusivity on the silica surface at room temperature. Moreover, the nucleation of Pd atoms or clusters always prefers top sites of the [SiO<sub>4</sub>] tetrahedral at room temperature. The growth of Pd atoms or clusters at the center of the honeycomb structure was not observed through our studies. The drastic contrast between the experimental results and the prediction by Giordano et al. again suggest 2D-network model cannot represent the real structure of ultra-thin silica film.

Figure 64 shows the surface morphology of 0.1 ML Pd deposited on the ultra-thin silica film. Pd clusters nucleate homogeneously on the thin silica film while the cluster heights mainly range from 2-6 Å. Lu et al. [287] also observed similar growth behavior of Pd clusters on the ultra-thin silica film with high cluster densities. They assumed that the nucleation occurs on point defects present on the film, although their STM inspection of the film prior to Pd deposition did not reveal high density of surface point defects. Through our study, the homogeneous nucleation and high cluster density should indeed be explained by the strong interaction between Pd and the SiO<sub>4</sub> tetrahedral itself, rather

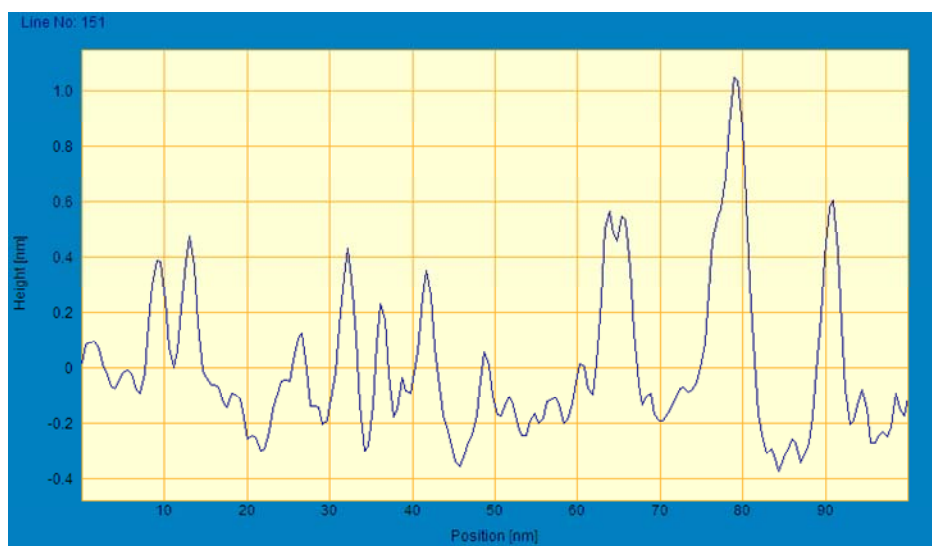
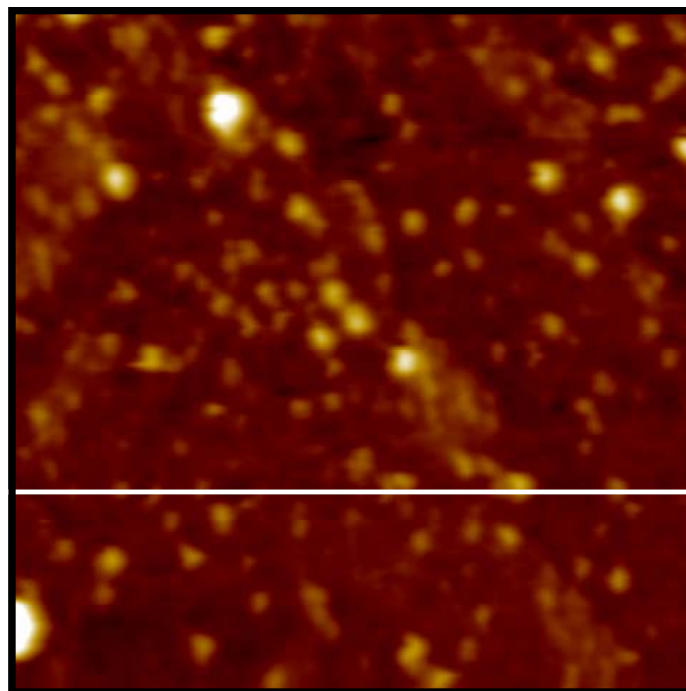


Figure 64. STM image of 0.1 ML Pd on SiO<sub>2</sub>(1 ML)/Mo(112). The image size is 80 nm × 80 nm. Tunneling parameters are  $V_s = -1.2$  V and  $I = 4$  nA. The line profile shows cross section along the white line in the STM image.

than surface defects of silica film, because line defects such as grain boundaries and step edges were present on the silica surface and did not show strong affinity with Pd clusters at room temperature.

### **The structure of Ru<sub>3</sub>Sn<sub>3</sub> clusters on the ultra-thin silica film**

The ultra-thin silica film supported on Mo(112) is a stable oxide support superior for preparation of supported model catalysts via wet impregnation for model catalytic studies. UHV studies on supported model catalysts prepared from wet-impregnation can provide structural information directly related to industrial catalysts. However, oxide support surfaces, such as TiO<sub>2</sub> single crystal [177] and oxide thin films, e.g., Al<sub>2</sub>O<sub>3</sub> [288] and MgO [289], are often roughened after being exposed to air or solutions, which presents the major challenge for determining the atomic structure of supported model catalysts prepared by wet-impregnation. The reason for surface roughening has often been attributed to the surface hydroxylation induced reconstruction, which starts at surface defect sites. UHV annealing at relatively high temperature can be used to recover the surface smoothness, but also caused the sintering or decomposition of supported metal clusters. Unlike those oxide support surfaces, so far neither silanol nor hydroxyl groups have been observed on the ultra-thin silica film in UHV [290, 291]. Our study further demonstrates that exposing this ultra-thin silica film to air or organic solution would not cause the roughening of silica surfaces. Our STM studies show that the surface remains unchanged after being exposed to air and the toluene solution.

Taking advantage of stable ultra-thin silica film, we investigated the atomic structure of Ru<sub>3</sub>Sn<sub>3</sub> alloy clusters prepared via solution deposition of a Ru<sub>3</sub>Sn<sub>3</sub> complex

( $\text{Ru}_3(\text{CO})_9(\text{SnPh}_2)_3$ ) on the ultra-thin silica film. The preparation of this model catalyst started with the synthesis of ultra-thin silica film on Mo(112) in the UHV chamber. After the synthesis of this ultra-thin silica film, a toluene solution containing  $\text{Ru}_3\text{Sn}_3$  complex was prepared before moving the film out of the chamber for solution deposition. The solid compound of  $\text{Ru}_3\text{Sn}_3$  complex was dissolved into toluene (Aldrich, HPLC grade) at room temperature. The  $\text{Ru}_3\text{Sn}_3$  solution, exhibiting orange color, was further diluted by toluene to make a  $2.9 \times 10^{-7}$  M  $\text{Ru}_3\text{Sn}_3$  solution. The Mo single crystal covered with an ultra-thin silica film was then moved out of the UHV chamber and applied with two drops of the diluted  $\text{Ru}_3\text{Sn}_3$  solution using a pipet. The  $\text{Ru}_3\text{Sn}_3$  solution wetted the ultra-thin silica film surface while the toluene solvent evaporated away very rapidly ( $< 10$  s) at room temperature. The ultra-thin silica film supported on Mo(112) was then moved back into the UHV chamber for characterization.

Figure 65 shows the surface morphology of the ultra-thin silica film supported on Mo(112) after solution deposition of  $\text{Ru}_3\text{Sn}_3$  complex and UHV annealing at 450 K for 10 minutes to remove the organic ligands. STM images reveal a flat and atomically resolved ultra-thin silica film surface after the film was exposed to the toluene solution. While the surface coverage of  $\text{Ru}_3\text{Sn}_3$  clusters was estimated to be  $\sim 0.09$  molecule/ $\text{nm}^2$  after solution deposition, STM measurements on this silica surface suggest a lower coverage of  $\text{Ru}_3\text{Sn}_3$  clusters. At the  $100 \text{ nm} \times 100 \text{ nm}$  scale, the flat silica surface appeared with small dots randomly dispersed on the surface (Figure 65a). The agglomeration of  $\text{Ru}_3\text{Sn}_3$  clusters was not apparent after 450 K annealing. Figure 65b demonstrates the triangular shape of these  $\text{Ru}_3\text{Sn}_3$  clusters and suggests the organic

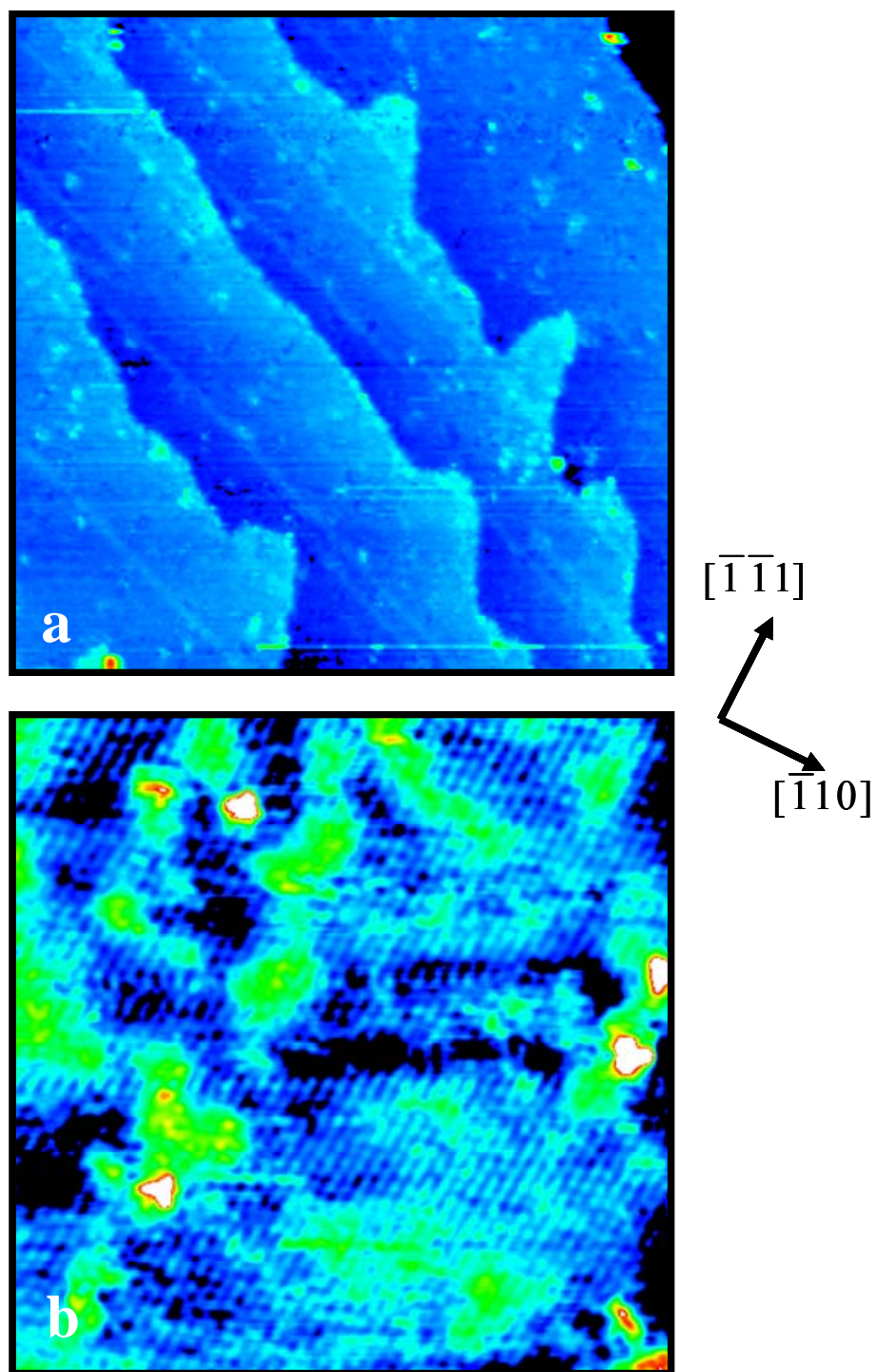


Figure 65. STM images of Ru<sub>3</sub>Sn<sub>3</sub> alloy clusters deposited on SiO<sub>2</sub>(1 ML)/Mo(112). The surface was annealed at 450 K for 10 min before STM images are taken at room temperature. Tunneling parameters and image sizes are (a)  $V_s = 1$  V,  $I = 0.1$  nA, 100 nm  $\times$  100 nm, and (b)  $V_s = 1$  V,  $I = 0.2$  nA, 20 nm  $\times$  20 nm.

ligands were completely removed after annealing at 450 K for 10 minutes. The triangular shape of  $\text{Ru}_3\text{Sn}_3$  clusters resolved on the silica surface is the same as the shape of the  $\text{Ru}_3\text{Sn}_3$  complex in crystalline form and determined by X-ray diffraction (Figure 66a). Figure 65b also shows substrate modulation in the corrugation amplitude on a large scale, which could be a surface moiré pattern caused by the lattice mismatch between the oxide film and the Mo substrate, or due to the introduction of sub-surface impurities. Figure 66b is a schematic illustration of a  $\text{Ru}_3\text{Sn}_3$  cluster supported on the ultra-thin silica surface. The cluster model (isolated  $[\text{SiO}_4]$  unit) is used to construct the silica substrate. Assuming the  $\text{Ru}_3\text{Sn}_3$  alloy cluster is stabilized by oxygen on the silica surface, Figure 66b shows both Ru and Sn atoms can be well accessed by surface oxygen atoms. Thus the nucleation of  $\text{Ru}_3\text{Sn}_3$  clusters on the silica surface should not alter the triangular structure of  $\text{Ru}_3\text{Sn}_3$  clusters, as proved in Figure 67.

Figure 67 shows the atomic structure of  $\text{Ru}_3\text{Sn}_3$  clusters supported on the ultra-thin silica film surface. High resolution images clearly demonstrate the structure of the  $\text{Ru}_3\text{Sn}_3$  clusters is well maintained after the  $\text{Ru}_3\text{Sn}_3$  complex is deposited onto the silica surface and the organic ligands removed by annealing. Figure 67b shows three Ru atoms are equally spaced in the Sn frame of  $\text{Ru}_3\text{Sn}_3$ . The line profile in Figure 67b shows the apparent height of Ru is smaller than Sn since the atomic radius of Ru is smaller than Sn. The atomic distance between Ru and Sn atoms is measured to be  $\sim 2.7 \text{ \AA}$ , suggesting the silica substrate did not alter the structure of the  $\text{Ru}_3\text{Sn}_3$  cluster. The nucleation of metal atoms on oxide thin film surfaces has been reported to be mediated by the substrate. Kulawik et al. [292] observed Au atoms evaporated in UHV onto a thin alumina film formed one-dimensional clusters with unusually large Au-Au distance of 5.6-6.0  $\text{Å}$ .

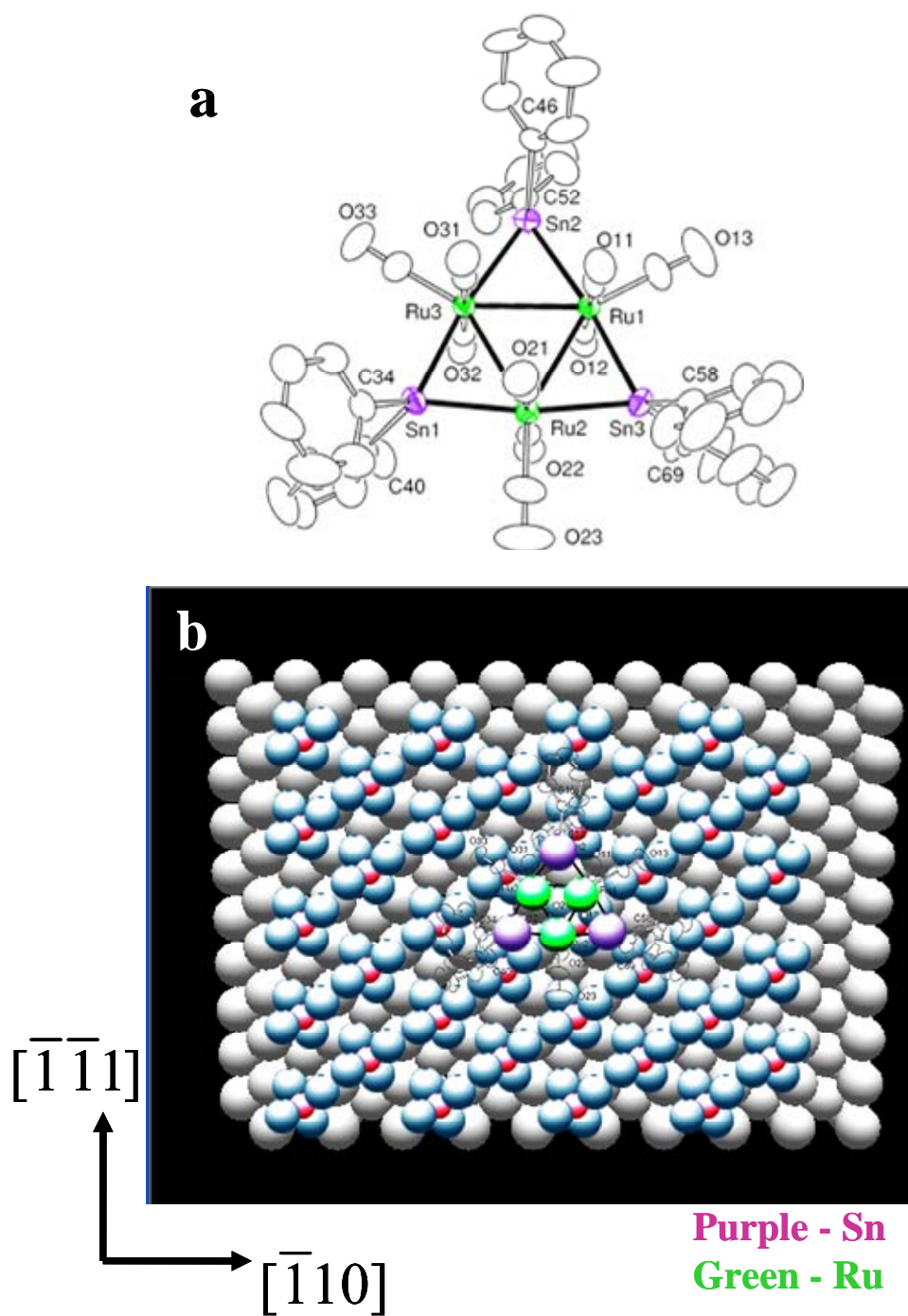


Figure 66. Schematics of (a) the structure of  $\text{Ru}_3(\text{CO})_9(\mu\text{-SnPh}_2)_3$  precursor, and (b) top-view of a  $\text{Ru}_3\text{Sn}_3$  cluster supported on  $\text{SiO}_2(1 \text{ ML})/\text{Mo}(112)$ . The isolated  $[\text{SiO}_4]$  model was used to construct the  $\text{SiO}_2$  substrate. Color representations of the ball model are: Mo – white; Si – red; O – blue; Sn – Purple; Ru – Green.



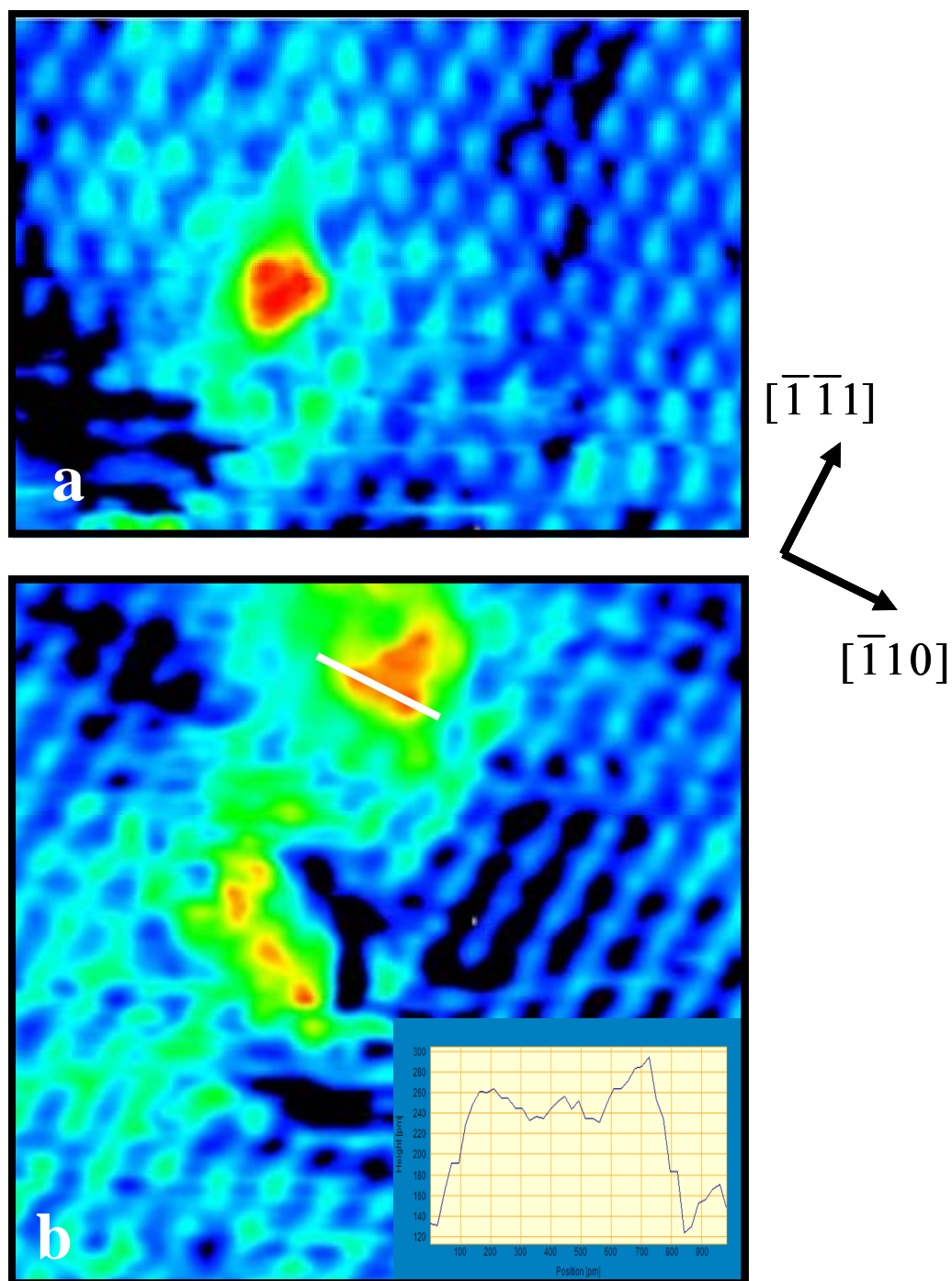


Figure 67. High resolution STM images of Ru<sub>3</sub>Sn<sub>3</sub> alloy clusters supported on SiO<sub>2</sub>(1 ML)/Mo(112). Tunneling parameters and image sizes are (a) V<sub>s</sub> = 0.6 V, I = 1 nA, 6 nm × 4 nm, and (b) V<sub>s</sub> = 1 V, I = 1 nA, 6 nm × 6 nm. Inset is the section profile of the line in (b).

These Au clusters were found to align with the [001] direction of the NiAl(110) substrate, leading to the suggestion that metal substrate mediates the adsorption of Au atoms.

Similar behavior was also observed in our above study on the nucleation of Pd clusters on ultra-thin silica film. Some small Pd clusters were found to elongate along the  $[\bar{1}\bar{1}1]$  direction of the Mo(112) substrate. In the case of  $\text{Ru}_3\text{Sn}_3$  clusters prepared by solution deposition, the effect of substrate mediation has not been observed, suggesting the  $\text{Ru}_3\text{Sn}_3$  cluster supported on the silica surface is mainly stabilized by the inherent metal-metal bonding.

Similar to other oxide surfaces, step edge sites on the ultra-thin silica film surface are preferred for the nucleation of alloy clusters after annealing. Figure 68a shows, after annealing at 700 K, most of  $\text{Ru}_3\text{Sn}_3$  clusters decomposed, moved to the step edges, and formed large clusters at step edge sites. Figure 68b displays dissociated atoms or some partial structure of the triangular  $\text{Ru}_3\text{Sn}_3$  cluster, providing evidence for the decomposition of  $\text{Ru}_3\text{Sn}_3$  clusters. Large Ru-Sn clusters are thus formed in the mode of Ostwald ripening through atom diffusion across the surface and subsequent nucleation at step edges. The formation of large Ru-Sn clusters suggests the diffusivity of Ru and Sn atoms are high enough for atoms to reach the step edge at 700 K. Figure 68b also shows a triangular cluster while Ru atoms inside the triangular Sn frame have disappeared. This suggests the triangular Sn frame is stabilized by surface oxygen whereas Ru atoms inside the Sn frame are not. Upon annealing, Ru atoms might dissociate from the triangular cluster first, leading to the decomposition of  $\text{Ru}_3\text{Sn}_3$  clusters. Sn atoms are more stable due to their stronger bonding with surface oxygen atoms. Extended annealing at high temperature would then destabilize Sn atoms, induce the breakdown of triangular Sn

frame, and lead to surface diffusion of Sn atoms towards the step edge to incorporate into large alloy clusters.

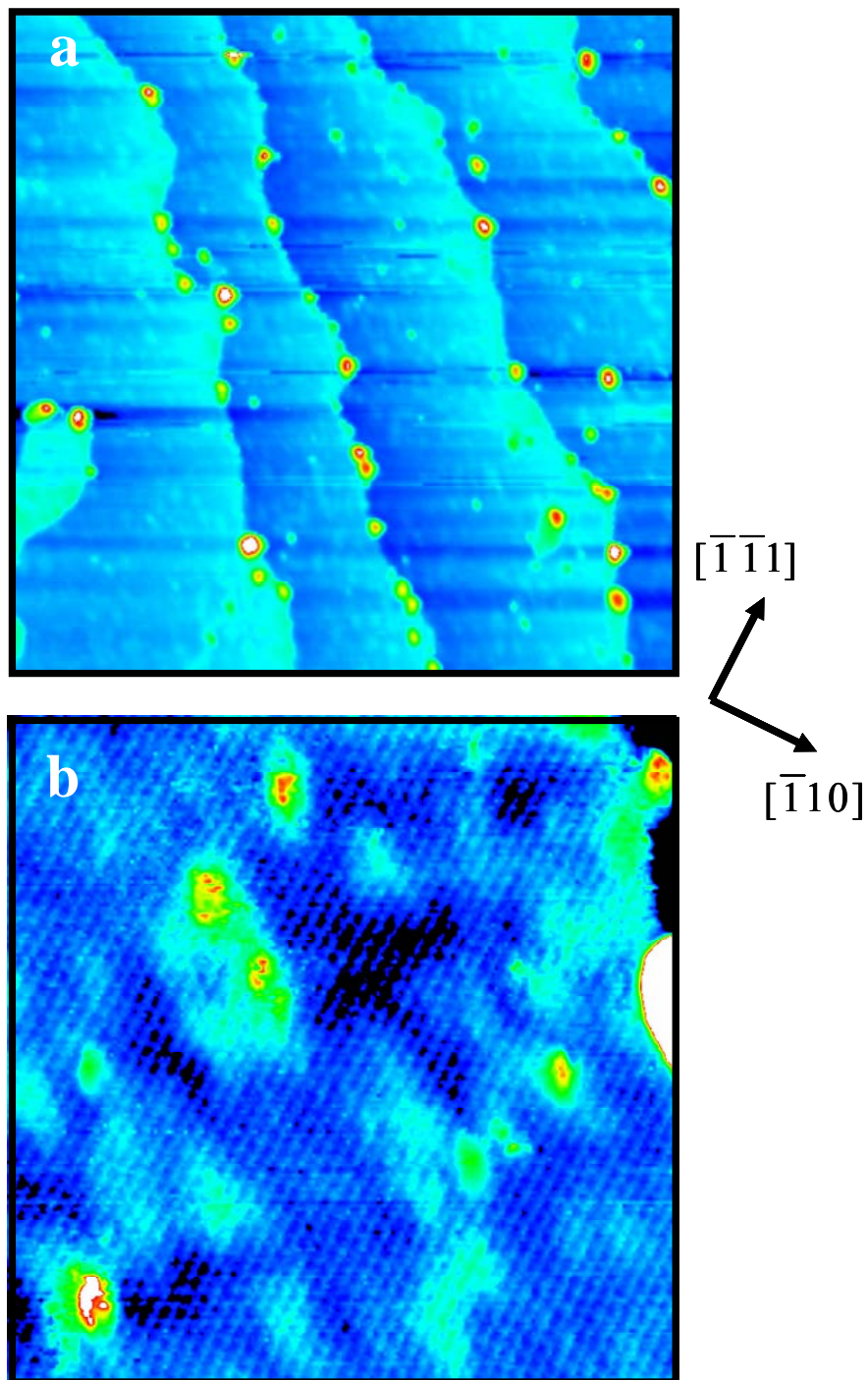


Figure 68. STM images of Ru<sub>3</sub>Sn<sub>3</sub> alloy clusters supported on SiO<sub>2</sub>(1 ML)/Mo(112) after annealing at 700 K for 10 min. Tunneling parameters and image sizes are (a)  $V_s = 1$  V,  $I = 0.1$  nA, 100 nm × 100 nm, and (b)  $V_s = 1$  V,  $I = 0.2$  nA, 20 nm × 20 nm.

## CHAPTER VI

### SUMMARY

The primary goals of the work presented in this dissertation are 1) to employ STM to investigate the structure and stability of model catalysts both in UHV and under reaction conditions, and 2) to determine the structure and stability of complex catalyst systems, such as model alloy catalysts.

To reach the first primary goal, Au clusters supported on  $\text{TiO}_2(110)$  have been used as a model to address primary issues for the understanding and development of supported Au catalysts. To determine the structure of catalytically active gold, it is important to reveal the binding sites of Au on  $\text{TiO}_2$ . The structure and stability of Au/ $\text{TiO}_2(110)$  has thus been investigated in UHV and at elevated temperatures. The surface structure of  $\text{TiO}_2(110)$  has been studied with its local electronic structure resolved with atomic resolution. Interstitial Ti cations are found to diffuse to the  $\text{TiO}_2(110)$  surface and form  $\text{TiO}_x$  species when the single crystal is either annealed at temperatures between 400-700 K or exposed to  $\text{O}_2$  at room temperature and above. These  $\text{TiO}_x$  species consist of undercoordinated Ti cations and have a structure dependent on the annealing temperature and oxygen exposure.

The undercoordinated Ti cations are found to play a critical role in the nucleation and stabilization of Au clusters supported on  $\text{TiO}_2(110)$ . Our studies show Au clusters grow preferentially at the step edges or the end of  $\text{TiO}_x$  strands on the  $\text{TiO}_2(110)$  surface. The Au nucleation sites at the step edges or  $\text{TiO}_x$  strands are found to be undercoordinated Ti cations. The formation of  $\text{TiO}_x$  species in the vicinity of Au clusters

is found to help stabilize supported Au clusters at elevated temperatures. Exposing the  $\text{TiO}_2(110)$  surface to water vapor causes the formation of hydroxyl groups at surface defect sites and induces the formation of  $\text{TiO}_x$  species in a way similar to  $\text{O}_2$ . These changes alter the growth kinetics of Au clusters on  $\text{TiO}_2(110)$ .

The preparation of planar Au films on  $\text{TiO}_2(110)$  has also been attempted by heavily reducing the  $\text{TiO}_2(110)$  surface using  $\text{H}_2$ . Au atoms were deposited onto the  $\text{TiO}_2(110)$  surface at 700 K in  $\text{H}_2$ , resulting in a better wetting of Au than Au deposition on  $\text{TiO}_2(110)$  in UHV. In addition, size selected  $\text{Au}_{400}$  clusters have been deposited on HOPG, with their morphology and structure characterized by STM.

The major obstacle in the commercialization of supported Au catalysts is the rapid catalyst deactivation, caused by the sintering of supported Au clusters. To reveal the nature of Au sintering, the surface morphology of Au/ $\text{TiO}_2(110)$  has been investigated in the presence of CO,  $\text{O}_2$  or CO/ $\text{O}_2$  mixture. Au clusters supported on  $\text{TiO}_2(110)$  are stable in CO and sinter very slowly in 0.1 Torr  $\text{O}_2$ . In the presence of 0.1 Torr CO/ $\text{O}_2$  mixture, supported Au clusters sinter rapidly, suggesting a reaction induced sintering mechanism. The sintering kinetics of individual Au clusters has been measured at temperatures between 300-410 K during CO oxidation. Supported Au clusters are found to sinter via Ostwald ripening. The sintering of Au clusters supported on  $\text{TiO}_2(110)$  does not fulfill the mean field assumption due to the prominent local effect. The activation energy of sintering for Au clusters around 3 nm tracks the activation energy of CO oxidation, which supports the reaction induced mechanism.

In comparison, the surface morphology of Rh(110) has been investigated during CO oxidation at 525 K. Similar to Au clusters supported on  $\text{TiO}_2(110)$ , surface diffusion

of Rh atoms is accelerated by CO oxidation reaction on Rh(110). The evolution of the surface morphology of both Au/TiO<sub>2</sub>(110) and Rh(110) clearly indicates a direct correlation between the reaction rate of CO oxidation and the diffusion rate of metal atoms.

To reach the second primary goal of this dissertation, several methods for the synthesis of model alloy catalysts have been devised and the corresponding atomic structures characterized. In particular, a molecular catalyst, namely Ru<sub>3</sub>Sn<sub>3</sub>, has been deposited on an ultra-thin silica film with its structure determined. The ultra-thin silica film was prepared on a Mo(112) surface. Bias dependent topographic images suggest the silica film has a surface unit of [SiO<sub>4</sub>] tetrahedral, which is isolated on the Mo(112) surface. A Ru<sub>3</sub>Sn<sub>3</sub> complex has then been deposited on the ultra-thin silica film via solution and with ligands removed by UHV annealing. The atomic structure of supported Ru<sub>3</sub>Sn<sub>3</sub> clusters has been successfully resolved and shows a triangular shape, essentially identical to the structure of Ru<sub>3</sub>Sn<sub>3</sub> in the Ru<sub>3</sub>Sn<sub>3</sub> complex. These Ru<sub>3</sub>Sn<sub>3</sub> clusters are not stable upon annealing at 700 K and sinter via Ostwald ripening. In addition, a planar Au-Pd alloy film has been synthesized on Rh(100). Chemical contrast has been obtained on the alloy film with Pd atoms appearing brighter and Au atoms appearing darker. The growth of Au-Ag alloy clusters have also been studied using *in-situ* STM. The kinetics of Au growth on an Ag pre-covered TiO<sub>2</sub>(110) surface shows a competition between Au growth at step edge sites and Au growth on pre-nucleated Ag clusters. With step edge sites saturated by Ag clusters, Au prefers to alloy with Ag clusters on TiO<sub>2</sub>(110).

**REFERENCES**

- [1] J. H. Sinfelt, *Surface Science* 500, 923 (2002).
- [2] I. Langmuir, *Physical Review* 6, 79 (1915).
- [3] M. Che, and C. O. Bennett, *Advances in Catalysis* 36, 55 (1989).
- [4] S. J. Tauster, *Accounts of Chemical Research* 20, 389 (1987).
- [5] S. J. Tauster, S. C. Fung, R. T. K. Baker, and J. A. Horsley, *Science* 211, 1121 (1981).
- [6] S. J. Tauster, S. C. Fung, and R. L. Garten, *Journal of the American Chemical Society* 100, 170 (1978).
- [7] R. J. Koestner, M. A. Vanhove, and G. A. Somorjai, *Surface Science* 121, 321 (1982).
- [8] M. A. Vanhove, R. J. Koestner, P. C. Stair, J. P. Biberian, L. L. Kesmodel *et al.*, *Surface Science* 103, 189 (1981).
- [9] M. A. Vanhove, R. J. Koestner, P. C. Stair, J. P. Biberian, L. L. Kesmodel *et al.*, *Surface Science* 103, 218 (1981).
- [10] M. Eiswirth, and G. Ertl, *Surface Science* 177, 90 (1986).
- [11] G. Ertl, *Berichte Der Bunsen-Gesellschaft-Physical Chemistry Chemical Physics* 90, 284 (1986).
- [12] P. Moller, K. Wetzl, M. Eiswirth, and G. Ertl, *Journal of Chemical Physics* 85, 5328 (1986).
- [13] D. W. Goodman, R. D. Kelly, T. E. Madey, and J. T. Yates, *Journal of Catalysis* 63, 226 (1980).



- [14] T. E. Madey, D. W. Goodman, and R. D. Kelley, *Journal of Vacuum Science & Technology* 16, 433 (1979).
- [15] D. W. Goodman, *Accounts of Chemical Research* 17, 194 (1984).
- [16] P. Stoltze, and J. K. Norskov, *Physical Review Letters* 55, 2502 (1985).
- [17] G. Ertl, *Crc Critical Reviews in Solid State and Materials Sciences* 10, 349 (1982).
- [18] H. J. Freund, M. Baumer, and H. Kuhlenbeck, *Advances in Catalysis*, Vol 45 45, 333 (2000).
- [19] C. R. Henry, *Surface Science Reports* 31, 235 (1998).
- [20] S. A. Chambers, *Surface Science Reports* 39, 105 (2000).
- [21] R. Franchy, *Surface Science Reports* 38, 199 (2000).
- [22] D. R. Rainer, and D. W. Goodman, *Journal of Molecular Catalysis A-Chemical* 131, 259 (1998).
- [23] D. W. Goodman, *Journal of Physical Chemistry* 100, 13090 (1996).
- [24] A. K. Santra, and D. W. Goodman, *Journal of Physics-Condensed Matter* 15, R31 (2003).
- [25] C. T. Campbell, *Surface Science Reports* 27, 1 (1997).
- [26] V. P. Zhdanov, and B. Kasemo, *Surface Science Reports* 39, 29 (2000).
- [27] D. F. Ogletree, H. Bluhm, G. Lebedev, C. S. Fadley, Z. Hussain *et al.*, *Review of Scientific Instruments* 73, 3872 (2002).
- [28] W. P. A. Jansen, A. W. D. van der Gon, G. M. Wijers, Y. G. M. Rikers, H. H. Brongersma *et al.*, *Review of Scientific Instruments* 73, 354 (2002).
- [29] T. W. Hansen, J. B. Wagner, P. L. Hansen, S. Dahl, H. Topsoe *et al.*, *Science* 294, 1508 (2001).

- [30] X. C. Su, P. S. Cremer, Y. R. Shen, and G. A. Somorjai, *Physical Review Letters* 77, 3858 (1996).
- [31] K. R. McCrea, and G. A. Somorjai, *Journal of Molecular Catalysis a-Chemical* 163, 43 (2000).
- [32] G. Rupprechter, H. Unterhalt, M. Morkel, P. Galletto, L. J. Hu *et al.*, *Surface Science* 502, 109 (2002).
- [33] G. Rupprechter, T. Dellwig, H. Unterhalt, and H. J. Freund, *Journal of Physical Chemistry B* 105, 3797 (2001).
- [34] T. Dellwig, G. Rupprechter, H. Unterhalt, and H. J. Freund, *Physical Review Letters* 85, 776 (2000).
- [35] E. Ozensoy, C. Hess, and D. W. Goodman, *Journal of the American Chemical Society* 124, 8524 (2002).
- [36] E. Ozensoy, B. K. Min, A. K. Santra, and A. W. Goodman, *Journal of Physical Chemistry B* 108, 4351 (2004).
- [37] E. Ozensoy, C. Hess, D. Loffreda, P. Sautet, and D. W. Goodman, *Journal of Physical Chemistry B* 109, 5414 (2005).
- [38] E. Ozensoy, and D. W. Goodman, *Physical Chemistry Chemical Physics* 6, 3765 (2004).
- [39] H. Isern, K. Peters, P. Steadman, O. Robach, J. Alvarez *et al.*, *Surface Science* 482, 101 (2001).
- [40] P. Steadman, K. Peters, H. Isern, J. Alvarez, and S. Ferrer, *Physical Review B* 62, R2295 (2000).

- [41] P. Bernard, K. Peters, J. Alvarez, and S. Ferrer, *Review of Scientific Instruments* 70, 1478 (1999).
- [42] M. D. Ackermann, T. M. Pedersen, B. L. M. Hendriksen, O. Robach, S. C. Bobaru *et al.*, *Physical Review Letters* 95 (2005).
- [43] B. J. McIntyre, M. Salmeron, and G. A. Somorjai, *Journal of Vacuum Science & Technology a-Vacuum Surfaces and Films* 11, 1964 (1993).
- [44] B. J. McIntyre, M. Salmeron, and G. A. Somorjai, *Review of Scientific Instruments* 64, 687 (1993).
- [45] B. J. McIntyre, M. B. Salmeron, and G. A. Somorjai, *Catalysis Letters* 14, 263 (1992).
- [46] B. J. McIntyre, M. Salmeron, and G. A. Somorjai, *Science* 265, 1415 (1994).
- [47] B. J. McIntyre, M. Salmeron, and G. A. Somorjai, *Surface Science* 323, 189 (1995).
- [48] B. J. McIntyre, M. Salmeron, and G. A. Somorjai, *Journal of Catalysis* 164, 184 (1996).
- [49] B. J. McIntyre, M. Salmeron, and G. A. Somorjai, *Catalysis Letters* 39, 5 (1996).
- [50] B. J. McIntyre, P. Sautet, J. C. Dunphy, M. Salmeron, and G. A. Somorjai, *Journal of Vacuum Science & Technology B* 12, 1751 (1994).
- [51] M. Montano, K. Bratlie, M. Salmeron, and G. A. Somorjai, *Journal of the American Chemical Society* 128, 13229 (2006).
- [52] M. Montano, M. Salmeron, and G. A. Somorjai, *Surface Science* 600, 1809 (2006).

- [53] X. C. Su, J. Jensen, M. X. Yang, M. B. Salmeron, Y. R. Shen *et al.*, *Faraday Discussions*, 263 (1996).
- [54] J. A. Jensen, K. B. Rider, M. Salmeron, and G. A. Somorjai, *Physical Review Letters* 80, 1228 (1998).
- [55] P. B. Rasmussen, B. L. M. Hendriksen, H. Zeijlemaker, H. G. Ficke, and J. W. M. Frenken, *Review of Scientific Instruments* 69, 3879 (1998).
- [56] J. A. Jensen, K. B. Rider, Y. Chen, M. Salmeron, and G. A. Somorjai, *Journal of Vacuum Science & Technology B* 17, 1080 (1999).
- [57] K. B. Rider, K. S. Hwang, M. Salmeron, and G. Somorjai, *Abstracts of Papers of the American Chemical Society* 219, U524 (2000).
- [58] K. B. Rider, K. S. Hwang, M. Salmeron, and G. A. Somorjai, *Physical Review Letters* 86, 4330 (2001).
- [59] B. L. M. Hendriksen, and J. W. M. Frenken, *Physical Review Letters* 89 (2002).
- [60] K. B. Rider, K. S. Hwang, M. Salmeron, and G. A. Somorjai, *Journal of the American Chemical Society* 124, 5588 (2002).
- [61] B. L. M. Hendriksen, S. C. Bobaru, and J. W. M. Frenken, *Surface Science* 552, 229 (2004).
- [62] E. Laegsgaard, L. Osterlund, P. Thostrup, P. B. Rasmussen, I. Stensgaard *et al.*, *Review of Scientific Instruments* 72, 3537 (2001).
- [63] E. K. Vestergaard, P. Thostrup, T. An, E. Laegsgaard, I. Stensgaard *et al.*, *Physical Review Letters* 88 (2002).
- [64] A. Kolmakov, and D. W. Goodman, *Catalysis Letters* 70, 93 (2000).
- [65] A. Kolmakov, and D. W. Goodman, *Surface Science* 490, L597 (2001).

- [66] R. Reichelt, S. Gunther, M. Rossler, J. Wintterlin, B. Kubias *et al.*, *Physical Chemistry Chemical Physics* 9, 3590 (2007).
- [67] M. Rossler, S. Gunther, and J. Wintterlin, *Journal of Physical Chemistry C* 111, 2242 (2007).
- [68] S. H. Kim, J. Mendez, J. Wintterlin, and G. Ertl, *Physical Review B* 72 (2005).
- [69] M. Rossler, P. Geng, and J. Wintterlin, *Review of Scientific Instruments* 76 (2005).
- [70] B. L. M. Hendriksen, S. C. Bobaru, and J. W. M. Frenken, *Catalysis Today* 105, 234 (2005).
- [71] R. Nowakowski, P. Grzeszczak, and R. Dus, *Surface Science* 507, 813 (2002).
- [72] T. Kobiela, and R. Dus, *Vacuum* 63, 267 (2001).
- [73] G. A. Somorjai, *Langmuir* 7, 3176 (1991).
- [74] G. A. Somorjai, *Catalysis Letters* 12, 17 (1992).
- [75] G. A. Somorjai, *Annual Review of Physical Chemistry* 45, 721 (1994).
- [76] G. A. Somorjai, *Journal of Molecular Catalysis a-Chemical* 107, 39 (1996).
- [77] G. A. Somorjai, and G. Rupprechter, *Journal of Chemical Education* 75, 161 (1998).
- [78] M. Haruta, *Catalysis Today* 36, 153 (1997).
- [79] M. Haruta, and M. Date, *Applied Catalysis A-General* 222, 427 (2001).
- [80] M. Valden, S. Pak, X. Lai, and D. W. Goodman, *Catalysis Letters* 56, 7 (1998).
- [81] M. Valden, X. Lai, and D. W. Goodman, *Science* 281, 1647 (1998).
- [82] M. Haruta, T. Kobayashi, H. Sano, and N. Yamada, *Chemistry Letters*, 405 (1987).

- [83] M. Haruta, S. Tsubota, T. Kobayashi, H. Kageyama, M. J. Genet *et al.*, *Journal of Catalysis* 144, 175 (1993).
- [84] A. C. Gluhoi, M. A. P. Dekkers, and B. E. Nieuwenhuys, *Journal of Catalysis* 219, 197 (2003).
- [85] R. J. H. Grisel, and B. E. Nieuwenhuys, *Journal of Catalysis* 199, 48 (2001).
- [86] M. M. Schubert, S. Hackenberg, A. C. van Veen, M. Muhler, V. Plzak *et al.*, *Journal of Catalysis* 197, 113 (2001).
- [87] M. S. Chen, and D. W. Goodman, *Catalysis Today* 111, 22 (2006).
- [88] M. S. Chen, and D. W. Goodman, *Science* 306, 252 (2004).
- [89] M. S. Chen, and D. W. Goodman, *Accounts of Chemical Research* 39, 739 (2006).
- [90] J. J. Pietron, R. M. Stroud, and D. R. Rolison, *Nano Letters* 2, 545 (2002).
- [91] U. Diebold, *Surface Science Reports* 48, 53 (2003).
- [92] K. Kosuge, *Chemistry of Non-stoichiometric Compounds* (Oxford University Press, Oxford, 1994).
- [93] X. Lai, T. P. St Clair, M. Valden, and D. W. Goodman, *Progress in Surface Science* 59, 25 (1998).
- [94] E. Wahlstrom, N. Lopez, R. Schaub, P. Thstrup, A. Ronnau *et al.*, *Physical Review Letters* 90 (2003).
- [95] D. Matthey, J. G. Wang, S. Wendt, J. Matthiesen, R. Schaub *et al.*, *Science* 315, 1692 (2007).
- [96] A. Berko, G. Menesi, and F. Solymosi, *Journal of Physical Chemistry* 100, 17732 (1996).
- [97] A. Berko, and F. Solymosi, *Surface Science* 411, L900 (1998).

- [98] A. Berko, and F. Solymosi, *Magy Kem Foly* 106, 7 (2000).
- [99] P. J. F. Harris, *Int.Mater.Rev.* 40, 97 (1995).
- [100] C. T. Campbell, A. W. Grant, D. E. Starr, S. C. Parker, and V. A. Bondzie, *Topics in Catalysis* 14, 43 (2001).
- [101] C. H. Bartholomew, *Studies in Surface Science and Catalysis* 111, 585 (1997).
- [102] C. H. Bartholemew, *Catalysis* 10, 41 (1993).
- [103] B. K. Chakraverty, *Journal of Physics and Chemistry of Solids* 28, 2401 (1967).
- [104] P. Wynblatt, and N. A. Gjostein, *Progress in Solid State Chemistry* 9, 21 (1975).
- [105] C. T. Campbell, S. C. Parker, and D. E. Starr, *Science* 298, 811 (2002).
- [106] A. Kolmakov, and D. W. Goodman, *Chemical Record* 2, 446 (2002).
- [107] A. K. Santra, A. Kolmakov, F. Yang, and D. W. Goodman, *Japanese Journal of Applied Physics* 42, 4795 (2003).
- [108] J. H. Sinfelt, *Journal of Catalysis* 29, 308 (1973).
- [109] L. Guzzi, G. N. Lu, and Z. Zsoldos, *Catalysis Today* 17, 459 (1993).
- [110] O. S. Alexeev, and B. C. Gates, *Industrial & Engineering Chemistry Research* 42, 1571 (2003).
- [111] J. H. Sinfelt, D. J. C. Yates, and J. L. Carter, *Journal of Catalysis* 24, 283 (1972).
- [112] J. H. Sinfelt, *Catalysis Today* 53, 305 (1999).
- [113] G. Meitzner, W. J. Mykytka, and J. H. Sinfelt, *Journal of Catalysis* 98, 513 (1986).
- [114] K. Besocke, *Surface Science* 181, 145 (1987).
- [115] G. Binnig, and H. Rohrer, *Surface Science* 126, 236 (1983).

- [116] G. Binnig, H. Rohrer, C. Gerber, and E. Weibel, *Physical Review Letters* 50, 120 (1983).
- [117] F. Besenbacher, *Reports on Progress in Physics* 59, 1737 (1996).
- [118] R. J. Hamers, *Annual Review of Physical Chemistry* 40, 531 (1989).
- [119] D. M. Eigler, P. S. Weiss, E. K. Schweizer, and N. D. Lang, *Physical Review Letters* 66, 1189 (1991).
- [120] G. V. Nazin, S. W. Wu, and W. Ho, *Proceedings of the National Academy of Sciences* 102, 8832 (2005).
- [121] P. Auger, *Journal De Physique Et Le Radium* 6, 205 (1925).
- [122] J. J. Lander, *Physical Review* 91, 1382 (1953).
- [123] L. A. Harris, *Journal of Applied Physics* 39, 1419 (1968).
- [124] M. J. Rost, L. Crama, P. Schakel, E. van Tol, G. B. E. M. van Velzen-Williams *et al.*, *Review of Scientific Instruments* 76 (2005).
- [125] A. Kolmakov, and D. W. Goodman, *Review of Scientific Instruments* 74, 2444 (2003).
- [126] A. J. Nam, A. Teren, T. A. Lusby, and A. J. Melmed, *Journal of Vacuum Science & Technology B* 13, 1556 (1995).
- [127] A. J. Melmed, *Journal of Vacuum Science & Technology B* 9, 601 (1991).
- [128] J. Mendez, M. Luna, and A. M. Baro, *Surface Science* 266, 294 (1992).
- [129] R. Zhang, and D. G. Ivey, *Journal of Vacuum Science & Technology B* 14, 1 (1996).
- [130] A. I. Oliva, A. Romero, J. L. Pena, E. Anguiano, and M. Aguilar, *Review of Scientific Instruments* 67, 1917 (1996).



- [131] V. Weinstein, M. Slutzky, A. Arenshtam, and E. Benjacob, *Review of Scientific Instruments* 66, 3075 (1995).
- [132] A. G. Guell, I. Diez-Perez, P. Gorostiza, and F. Sanz, *Analytical Chemistry* 76, 5218 (2004).
- [133] R. Fainchtein, and P. R. Zarriello, *Ultramicroscopy* 42, 1533 (1992).
- [134] M. C. Baykul, *Materials Science and Engineering B-Solid State Materials for Advanced Technology* 74, 229 (2000).
- [135] B. Ren, G. Picardi, and B. Pettinger, *Review of Scientific Instruments* 75, 837 (2004).
- [136] G. A. Fried, X. D. Wang, and K. W. Hipps, *Review of Scientific Instruments* 64, 1495 (1993).
- [137] M. Iwami, Y. Uehara, and S. Ushioda, *Review of Scientific Instruments* 69, 4010 (1998).
- [138] M. Li, W. Hebenstreit, U. Diebold, A. M. Tyryshkin, M. K. Bowman *et al.*, *Journal of Physical Chemistry B* 104, 4944 (2000).
- [139] U. Diebold, *Applied Physics a-Materials Science & Processing* 76, 681 (2003).
- [140] E. L. D. Hebenstreit, W. Hebenstreit, and U. Diebold, *Surface Science* 461, 87 (2000).
- [141] U. Diebold, W. Hebenstreit, G. Leonardelli, M. Schmid, and P. Varga, *Physical Review Letters* 81, 405 (1998).
- [142] H. Onishi, and Y. Iwasawa, *Chemical Physics Letters* 226, 111 (1994).
- [143] U. Diebold, J. F. Anderson, K. O. Ng, and D. Vanderbilt, *Physical Review Letters* 77, 1322 (1996).

- [144] U. Diebold, J. Lehman, T. Mahmoud, M. Kuhn, G. Leonardelli *et al.*, *Surface Science* 411, 137 (1998).
- [145] R. Schaub, P. Thostrup, N. Lopez, E. Laegsgaard, I. Stensgaard *et al.*, *Physical Review Letters* 87, 266104/1 (2001).
- [146] S. Wendt, R. Schaub, J. Matthiesen, E. K. Vestergaard, E. Wahlstrom *et al.*, *Surface Science* 598, 226 (2005).
- [147] S. Wendt, J. Matthiesen, R. Schaub, E. K. Vestergaard, E. Laegsgaard *et al.*, *Physical Review Letters* 96 (2006).
- [148] O. Bikondoa, C. L. Pang, R. Ithnin, C. A. Muryn, H. Onishi *et al.*, *Nat Mater* 5, 189 (2006).
- [149] O. Gulseren, R. James, and D. W. Bullett, *Surface Science* 377, 150 (1997).
- [150] C. Xu, X. Lai, G. W. Zajac, and D. W. Goodman, *Physical Review B* 56, 13464 (1997).
- [151] R. E. Tanner, M. R. Castell, and G. A. D. Briggs, *Surface Science* 413, 672 (1998).
- [152] R. Wiesendanger, in *Scanning Probe Microscopy and Spectroscopy: Methods and Applications* (Cambridge University Press, Cambridge, 1994).
- [153] S. Munnix, and M. Schmeits, *Physical Review B* 30, 2202 (1984).
- [154] H. Onishi, and Y. Iwasawa, *Physical Review Letters* 76, 791 (1996).
- [155] R. D. Smith, R. A. Bennett, and M. Bowker, *Physical Review B* 66 (2002).
- [156] M. Li, W. Hebenstreit, and U. Diebold, *Physical Review B* 61, 4926 (2000).
- [157] M. A. Henderson, *Surface Science* 419, 174 (1999).

- [158] K. T. Park, M. Pan, V. Meunier, and E. W. Plummer, *Physical Review B (Condensed Matter and Materials Physics)* 75, 245415 (2007).
- [159] K. T. Park, M. H. Pan, V. Meunier, and E. W. Plummer, *Physical Review Letters* 96, 226105 (2006).
- [160] M. Li, W. Hebenstreit, and U. Diebold, *Surface Science* 414, L951 (1998).
- [161] S. C. Parker, A. W. Grant, V. A. Bondzie, and C. T. Campbell, *Surface Science* 441, 10 (1999).
- [162] L. Zhang, R. Persaud, and T. E. Madey, *Physical Review B* 56, 10549 (1997).
- [163] S. Kielbassa, M. Kinne, and R. J. Behm, *Journal of Physical Chemistry B* 108, 19184 (2004).
- [164] S. Kielbassa, A. Habich, J. Schnaidt, J. Bansmann, F. Weigl *et al.*, *Langmuir* 22, 7873 (2006).
- [165] C. E. J. Mitchell, A. Howard, M. Carney, and R. G. Egdell, *Surface Science* 490, 196 (2001).
- [166] Y. Maeda, T. Fujitani, S. Tsubota, and M. Haruta, *Surface Science* 562, 1 (2004).
- [167] O. Dulub, W. Hebenstreit, and U. Diebold, *Physical Review Letters* 84, 3646 (2000).
- [168] M. Bowker, *Physical Chemistry Chemical Physics* 9, 3514 (2007).
- [169] M. Bowker, P. Stone, P. Morrall, R. Smith, R. Bennett *et al.*, *Journal of Catalysis* 234, 172 (2005).
- [170] R. A. Bennett, P. Stone, and M. Bowker, *Faraday Discussions*, 267 (1999).
- [171] M. J. J. Jak, C. Konstapel, A. van Kreuningen, J. Chrost, J. Verhoeven *et al.*, *Surface Science* 474, 28 (2001).

- [172] M. J. J. Jak, C. Konstapel, A. van Kreuningen, J. Verhoeven, and J. W. M. Frenken, *Surface Science* 457, 295 (2000).
- [173] M. A. Henderson, *Langmuir* 12, 5093 (1996).
- [174] M. A. Henderson, *Surface Science* 355, 151 (1996).
- [175] H. Uetsuka, A. Sasahara, and H. Onishi, *Langmuir* 20, 4782 (2004).
- [176] M. Chen, Y. Cai, Z. Yan, and D. W. Goodman, *Journal of the American Chemical Society* 128, 6341 (2006).
- [177] S. H. Overbury, P. A. Bertrand, and G. A. Somorjai, *Chemical Reviews* 75, 547 (1975).
- [178] F. Cosandey, and T. E. Madey, *Surface Review and Letters* 8, 73 (2001).
- [179] X. F. Lai, and D. W. Goodman, *Journal of Molecular Catalysis A-Chemical* 162, 33 (2000).
- [180] R. A. Bennett, P. Stone, and M. Bowker, *Catalysis Letters* 59, 99 (1999).
- [181] K. K. Nanda, A. Maisels, F. E. Kruis, H. Fissan, and S. Stappert, *Physical Review Letters* 91 (2003).
- [182] D. E. Starr, J. T. Ranney, J. H. Larsen, J. E. Musgrove, and C. T. Campbell, *Physical Review Letters* 87, 106102/1 (2001).
- [183] S. C. Parker, and C. T. Campbell, *Physical Review B* 75 (2007).
- [184] N. Lopez, J. K. Norskov, T. V. W. Janssens, A. Carlsson, A. Puig-Molina *et al.*, *Journal of Catalysis* 225, 86 (2004).
- [185] T. F. Buehrer, and W. E. Roseveare, *Journal of the American Chemical Society* 49, 1989 (1927).

- [186] M. S. Chen, K. Luo, D. Kumar, W. T. Wallace, C. W. Yi *et al.*, *Surface Science* 601, 632 (2007).
- [187] T. Minato, T. Susaki, S. Shiraki, H. S. Kato, M. Kawai *et al.*, *Surface Science* 566, 1012 (2004).
- [188] B. Yoon, H. Hakkinen, U. Landman, A. S. Worz, J. M. Antonietti *et al.*, *Science* 307, 403 (2005).
- [189] L. M. Molina, and B. Hammer, *Physical Review B* 69 (2004).
- [190] J. Guzman, S. Carrettin, J. C. Fierro-Gonzalez, Y. L. Hao, B. C. Gates *et al.*, *Angewandte Chemie-International Edition* 44, 4778 (2005).
- [191] J. Guzman, and B. C. Gates, *Journal of the American Chemical Society* 126, 2672 (2004).
- [192] L. Fu, N. Q. Wu, J. H. Yang, F. Qu, D. L. Johnson *et al.*, *Journal of Physical Chemistry B* 109, 3704 (2005).
- [193] E. A. Willneff, S. Braun, D. Rosenthal, H. Bluhm, M. Havecker *et al.*, *Journal of the American Chemical Society* 128, 12052 (2006).
- [194] J. G. Wang, and B. Hammer, *Topics in Catalysis* 44, 49 (2007).
- [195] X. F. Lai, T. P. St Clair, and D. W. Goodman, *Faraday Discussions*, 279 (1999).
- [196] J. Zhou, Y. C. Kang, S. Ma, and D. A. Chen, *Surface Science* 562, 113 (2004).
- [197] J. Zhou, Y. C. Kang, and D. A. Chen, *Journal of Physical Chemistry B* 107, 6664 (2003).
- [198] A. Berko, and F. Solymosi, *Journal of Catalysis* 183, 91 (1999).
- [199] A. Berko, and F. Solymosi, *Journal of Physical Chemistry B* 104, 10215 (2000).
- [200] A. Berko, J. Szoko, and F. Solymosi, *Surface Science* 566, 337 (2004).

- [201] C. H. Bartholomew, *Stud Surf Sci Catal* 111, 585 (1997).
- [202] A. K. Santra, A. Kolmakov, F. Yang, and D. W. Goodman, *Japanese Journal of Applied Physics Part 1-Regular Papers Short Notes & Review Papers* 42, 4795 (2003).
- [203] E. Wahlstrom, N. Lopez, R. Schaub, P. Thostrup, A. Ronnau *et al.*, *Physical Review Letters* 90, 26101 (2003).
- [204] J. D. Grunwaldt, and A. Baiker, *Journal of Physical Chemistry B* 103, 1002 (1999).
- [205] V. A. Bondzie, S. C. Parker, and C. T. Campbell, *Catalysis Letters* 63, 143 (1999).
- [206] M. A. Bollinger, and M. A. Vannice, *Applied Catalysis B-Environmental* 8, 417 (1996).
- [207] Z. P. Liu, X. Q. Gong, J. Kohanoff, C. Sanchez, and P. Hu, *Physical Review Letters* 91, 266012 (2003).
- [208] X. Z. Ji, A. Zuppero, J. M. Gidwani, and G. A. Somorjai, *Journal of the American Chemical Society* 127, 5792 (2005).
- [209] X. Z. Ji, and G. A. Somorjai, *Journal of Physical Chemistry B* 109, 22530 (2005).
- [210] X. Z. Ji, A. Zuppero, J. M. Gidwani, and G. A. Somorjai, *Nano Letters* 5, 753 (2005).
- [211] G. Rosenfeld, K. Morgenstern, I. Beckmann, W. Wulfhekel, E. Leagsgaard *et al.*, *Surface Science* 402-404, 401 (1998).
- [212] K. Morgenstern, G. Rosenfeld, G. Comsa, M. R. Sorensen, B. Hammer *et al.*, *Physical Review B: Condensed Matter and Materials Physics* 63, 045412/1 (2001).
- [213] N. C. Bartelt, W. Theis, and R. M. Tromp, *Physical Review B* 54, 11741 (1996).

- [214] W. Theis, N. C. Bartelt, and R. M. Tromp, *Physical Review Letters* 75, 3328 (1995).
- [215] K. Morgenstern, G. Rosenfeld, and G. Comsa, *Surface Science* 441, 289 (1999).
- [216] G. Rosenfeld, K. Morgenstern, M. Esser, and G. Comsa, *Applied Physics a-Materials Science & Processing* 69, 489 (1999).
- [217] X. Zheng, and B. Bigot, *J Phys II* 4, 743 (1994).
- [218] C. H. Bartholomew, *Applied Catalysis, A: General* 107, 1 (1993).
- [219] C. H. Bartholomew, *Studies in Surface Science and Catalysis* 88, 1 (1994).
- [220] C. Dri, C. Africh, F. Esch, G. Comelli, O. Dubay *et al.*, *Journal of Chemical Physics* 125 (2006).
- [221] C. Africh, and G. Comelli, *Journal of Physics-Condensed Matter* 18, R387 (2006).
- [222] S. Gunther, R. Hoyer, H. Marbach, R. Imbihl, F. Esch *et al.*, *Journal of Chemical Physics* 124 (2006).
- [223] A. Baraldi, S. Lizzit, F. Bondino, G. Comelli, R. Rosei *et al.*, *Physical Review B* 72 (2005).
- [224] C. Africh, H. P. Lin, M. Corso, F. Esch, R. Rosei *et al.*, *Journal of the American Chemical Society* 127, 11454 (2005).
- [225] P. Dudin, A. Barinov, L. Gregoratti, M. Kiskinova, F. Esch *et al.*, *Journal of Physical Chemistry B* 109, 13649 (2005).
- [226] S. Gunther, F. Esch, M. del Turco, C. Africh, G. Comelli *et al.*, *Journal of Physical Chemistry B* 109, 11980 (2005).
- [227] F. Bondino, G. Comelli, A. Baraldi, R. Rosei, S. Lizzit *et al.*, *Physical Review B* 66 (2002).

- [228] C. Africh, F. Esch, G. Comelli, and R. Rosei, *Journal of Chemical Physics* 116, 7200 (2002).
- [229] F. Bondino, A. Baraldi, H. Over, G. Comelli, P. Lacovig *et al.*, *Physical Review B* 6408 (2001).
- [230] C. Africh, F. Esch, G. Comelli, and R. Rosei, *Journal of Chemical Physics* 115, 477 (2001).
- [231] E. Vesselli, C. Africh, A. Baraldi, G. Comelli, F. Esch *et al.*, *Journal of Chemical Physics* 114, 4221 (2001).
- [232] F. Bondino, A. Baraldi, G. Comelli, and F. P. Netzer, *Surface Science* 461, 31 (2000).
- [233] S. W. Hla, P. Lacovig, G. Comelli, A. Baraldi, M. Kiskinova *et al.*, *Physical Review B* 60, 7800 (1999).
- [234] S. Lizzit, A. Baraldi, D. Cocco, G. Comelli, G. Paolucci *et al.*, *Surface Science* 410, 228 (1998).
- [235] A. Baraldi, S. Lizzit, D. Cocco, G. Comelli, G. Paolucci *et al.*, *Surface Science* 385, 376 (1997).
- [236] G. Comelli, A. Baraldi, S. Lizzit, D. Cocco, G. Paolucci *et al.*, *Chemical Physics Letters* 261, 253 (1996).
- [237] V. R. Dhanak, A. Baraldi, G. Comelli, K. C. Prince, R. Rosei *et al.*, *Physical Review B* 51, 1965 (1995).
- [238] G. Comelli, V. R. Dhanak, N. Pangher, G. Paolucci, M. Kiskinova *et al.*, *Surface Science* 317, 117 (1994).



- [239] L. Casalis, A. Baraldi, G. Comelli, V. R. Dhanak, M. Kiskinova *et al.*, *Surface Science* 306, 193 (1994).
- [240] C. Comicioli, V. R. Dhanak, G. Comelli, C. Astaldi, K. C. Prince *et al.*, *Chemical Physics Letters* 214, 438 (1993).
- [241] V. R. Dhanak, A. Baraldi, G. Comelli, G. Paolucci, M. Kiskinova *et al.*, *Surface Science* 295, 287 (1993).
- [242] A. Baraldi, V. R. Dhanak, G. Comelli, K. C. Prince, and R. Rosei, *Surface Science* 293, 246 (1993).
- [243] A. Baraldi, V. R. Dhanak, G. Comelli, M. Kiskinova, and R. Rosei, *Applied Surface Science* 68, 395 (1993).
- [244] A. Morgante, D. Cvetko, A. Santoni, K. C. Prince, V. R. Dhanak *et al.*, *Surface Science* 285, 227 (1993).
- [245] M. Kiskinova, S. Lizzit, G. Comelli, G. Paolucci, and R. Rosei, *Applied Surface Science* 64, 185 (1993).
- [246] G. Comelli, S. Lizzit, P. Hofmann, G. Paolucci, M. Kiskinova *et al.*, *Surface Science* 277, 31 (1992).
- [247] S. Lizzit, G. Comelli, P. Hofmann, G. Paolucci, M. Kiskinova *et al.*, *Surface Science* 276, 144 (1992).
- [248] G. Comelli, V. R. Dhanak, M. Kiskinova, G. Paolucci, K. C. Prince *et al.*, *Surface Science* 270, 360 (1992).
- [249] V. R. Dhanak, G. Comelli, G. Cauzero, G. Paolucci, K. C. Prince *et al.*, *Chemical Physics Letters* 188, 237 (1992).

- [250] G. Comelli, V. R. Dhanak, G. Paolucci, and R. Rosei, *Surface Science* 260, 1 (1992).
- [251] G. Comelli, V. R. Dhanak, M. Kiskinova, N. Pangher, G. Paolucci *et al.*, *Surface Science* 260, 7 (1992).
- [252] B. L. M. Hendriksen, S. C. Bobaru, and J. W. M. Frenken, *Topics in Catalysis* 36, 43 (2005).
- [253] K. Soo Young, B. Jeong Min, Y. Hak Ki, K. Kwang Young, T. Yoon-Heung *et al.*, *Applied Physics Letters* 87, 072105 (2005).
- [254] D. Alfe, and S. Baroni, *Surface Science* 382, L666 (1997).
- [255] J. Gustafson, A. Mikkelsen, M. Borg, E. Lundgren, L. Koehler *et al.*, *Physical Review Letters* 92, 126102/1 (2004).
- [256] J. Klikovits, M. Schmid, J. Gustafson, A. Mikkelsen, A. Resta *et al.*, *Journal of Physical Chemistry B* 110, 9966 (2006).
- [257] J. Gustafson, A. Mikkelsen, M. Borg, J. N. Andersen, E. Lundgren *et al.*, *Physical Review B* 71 (2005).
- [258] E. G. Allison, and G. C. Bond, *Catalysis Reviews-Science and Engineering* 7, 233 (1972).
- [259] P. N. Rylander, *Catalytic Hydrogenation in Organic Synthesis* (Academic Press, London, 1979).
- [260] P. C. R. Abel, K. Eichler, I. Nicolau, D. Peters, *Handbook of Heterogeneous Catalysis* (Wiley VCH, Weinheim, Germany, 1997), Vol. 5, pp. 2298.
- [261] A. M. Venezia, V. La Parola, V. Nicoli, and G. Deganello, *Journal of Catalysis* 212, 56 (2002).

- [262] D. L. Trimm, and Z. I. Onsan, *Catalysis Reviews-Science and Engineering* 43, 31 (2001).
- [263] M. Bonarowska, A. Malinowski, W. Juszczak, and Z. Karpinski, *Applied Catalysis B-Environmental* 30, 187 (2001).
- [264] M. S. Chen, K. Luo, T. Wei, Z. Yan, D. Kumar *et al.*, *Catalysis Today* 117, 37 (2006).
- [265] M. S. Chen, D. Kumar, C. W. Yi, and D. W. Goodman, *Science* 310, 291 (2005).
- [266] F. Maroun, F. Ozanam, O. M. Magnussen, and R. J. Behm, *Science* 293, 1811 (2001).
- [267] M. Aschoff, S. Speller, J. Kuntze, W. Heiland, E. Platzgummer *et al.*, *Surface Science* 415, L1051 (1998).
- [268] H. Okamoto, and T. B. Massalski, *Journal of Metals* 36, 57 (1984).
- [269] S. Hagstrom, H. B. Lyon, and G. A. Somorjai, *Physical Review Letters* 15, 491 (1965).
- [270] G. K. Binnig, H. Rohrer, C. Gerber, and E. Stoll, *Surface Science* 144, 321 (1984).
- [271] V. Fiorentini, M. Methfessel, and M. Scheffler, *Physical Review Letters* 71, 1051 (1993).
- [272] M. R. Radeke, and E. A. Carter, *Abstracts of Papers of the American Chemical Society* 209, 4 (1995).
- [273] D. I. Kondarides, and X. E. Verykios, *Journal of Catalysis* 158, 363 (1996).
- [274] N. Toreis, X. E. Verykios, S. M. Khalid, and G. B. Bunker, *Surface Science* 197, 415 (1988).
- [275] N. Toreis, and X. E. Verykios, *Journal of Catalysis* 108, 161 (1987).

- [276] D. A. Chen, M. C. Bartelt, S. M. Seutter, and K. F. McCarty, *Surface Science* 464, L708 (2000).
- [277] J. W. He, X. Xu, J. S. Corneille, and D. W. Goodman, *Surface Science* 279, 119 (1992).
- [278] X. P. Xu, and D. W. Goodman, *Surface Science* 282, 323 (1993).
- [279] T. Schroeder, M. Adelt, B. Richter, M. Naschitzki, M. Baumer *et al.*, *Surface Review and Letters* 7, 7 (2000).
- [280] S. Kaya, M. Baron, D. Stacchiola, J. Weissenrieder, S. Shaikhutdinov *et al.*, *Surface Science* In Press, Uncorrected Proof.
- [281] J. Weissenrieder, S. Kaya, J. L. Lu, H. J. Gao, S. Shaikhutdinov *et al.*, *Physical Review Letters* 95 (2005).
- [282] M. S. Chen, and D. W. Goodman, *Surface Science* 600, L255 (2006).
- [283] M. S. Chen, A. K. Santra, and D. W. Goodman, *Physical Review B* 69 (2004).
- [284] T. K. Todorova, M. Sierka, J. Sauer, S. Kaya, J. Weissenrieder *et al.*, *Physical Review B* 73 (2006).
- [285] L. Giordano, A. Del Vitto, and G. Pacchioni, *Journal of Chemical Physics* 124, 34701 (2006).
- [286] B. K. Min, W. T. Wallace, and D. W. Goodman, *Journal of Physical Chemistry B* 108, 14609 (2004).
- [287] J. L. Lu, S. Kaya, J. Weissenrieder, H. J. Gao, S. Shaikhutdinov *et al.*, *Surface Science* 600, L153 (2006).
- [288] F. Qin, N. P. Magtoto, and J. A. Kelber, *Surface Science* 565, L277 (2004).
- [289] S. Altieri, S. F. Contri, S. Agnoli, and S. Valeri, *Surface Science* 566, 1071 (2004).

- [290] T. Schroeder, J. B. Giorgi, M. Baumer, and H. J. Freund, *Physical Review B* 66, 165422 (2002).
- [291] S. Wendt, M. Frerichs, T. Wei, M. S. Chen, V. Kempter *et al.*, *Surface Science* 565, 107 (2004).
- [292] M. Kulawik, N. Nilius, and H. J. Freund, *Physical Review Letters* 96, 036103 (2006).

## VITA

Fan Yang received his B.S. in chemistry in 2001 from Peking University, Beijing, P. R. China. He then joined the graduate school at the Department of Chemistry, Texas A&M University in September 2001. He graduated with a Ph.D. in Chemistry under the direction of Dr. D. Wayne Goodman in December 2007. His hobbies include photography, movies, and playing basketball. His permanent address is Guomai Garden C-502, Wenzhou, Zhejiang province, P. R. China, 325000.